iv

| **Correspondence Address** |

Gazi University Graduate School of Natural and Applied Sciences
Emniyet Neighborhood, Bandırma Avenue, No:6/20B, 06560, Yenimahalle - ANKARA
B Block, Auxiliary Building

| **e-mail** |

gujsa06@gmail.com

| **web page** |

https://dergipark.org.tr/tr/pub/gujsa

Gazi University Journal of Science Part A: Engineering and Innovation
is a peer-reviewed journal.

| INDEXING |

| ACCESSIBILITY |

| CONTENTS |

| CONTENTS |

| CONTENTS |

| CONTENTS |

Gazi University
Journal of Science
PART A: ENGINEERING AND INNOVATION
http://dergipark.org.tr/gujsa

Comparison of Experimental and Monte Carlo Efficiencies of 0.5g/cc Epoxy Matrix Marinelli Source with Multiple Radioactive Nuclides

Gülper AKSOY[1] (ID) Hasan ÜNLÜ[1] (ID) Nilgün ORHAN[2] (ID) Mustafa Hicabi BÖLÜKDEMİR[3*] (ID)

[1]Gazi University, Graduate School of Natural and Applied Sciences, Advanced Technologies, Ankara, Türkiye
[2]Turkish Energy, Nuclear and Mining Research Authority, Nuclear Energy Research Institute, İstanbul, Türkiye
[3]Gazi University, Faculty of Sciences, Department of Physics, Ankara, Türkiye

Keywords	Abstract
Epoxy Marinelli Source Efficiency Monte Carlo	Using the gamma spectroscopy system, it can be determined whether environmental samples or standard radioactive sources are radioactive, and from which elements their radioactivity originates. The purpose of Monte Carlo (MC) simulation is to model a real-life system with its inputs and evaluate the outputs with real results. This study calculates the experimental efficiency of a p-type HPGe detector using a 0.5 g/cc Epoxy Matrix Marinelli beaker and compares these results with GESPECOR and PHITS MC Simulation programs. Thus, the thickness of the dead layer, which thickens over time and affects the detector efficiency, was determined from the most compatible result of the MC calculations made repeatedly at various alternative thicknesses to the experimental results. For 1.5 mm dead layer thickness, less than 2 % error was found between the test and MC results, especially at energies above 165 keV. As a result, it was determined that the dead layer thickness of the detector reached 1.5 mm with an increase of 114 % after its production. The current value of the dead layer thickness of each detector should be checked, as the efficiency affects the determination of the activity.

1. INTRODUCTION

Marinelli beakers are sample containers that fit into the end cap of the detector, designed in such a way that the sample material is close to both the top and sides of the detector crystal for the highest sensitive counting of large sample volumes (Gilmore, 2008). In gamma spectrometry, when the radioactivity detected is low, Marinelli beakers can be used. These beakers maximize the counting efficiency of the detector because of their geometry that almost surrounds the detector (Ahmed et al., 2009). Note that to make quantitative measurements, it is necessary to obtain the full energy peak efficiency (FEPE) curve of the detection systems. The FEPE curve is affected the sample geometry, the sample matrix, and the density of the matrix as well as the detection system (Harb et al., 2008). The FEPE curve can be obtained either by using a known radioactive standard source homogeneously distributed in a Marinelli beaker of the same size and composition (Vasconcelos et al., 2011), or by accurately modeling the source geometry, matrix, the position of the source, and the detection system using MC-based simulations (Azli & Chaoui, 2015; Lépy et al., 2019). Using the Monte Carlo method, the detection process can be simulated and applied to obtain efficiency values for each geometry (Ródenas et al., 2003). It is a convenient tool for situations where it is not always possible to perform experimental calibrations due to expensive standard gamma sources (Bölükdemir et al., 2021), and no radioactive waste is generated in this process (Vasconcelos et al., 2011). This study aims to find the current dead layer (DL) thickness of a p-type HPGe detector with 30 % relative efficiency by using a Marinelli type

source. DL thickness, which affects the detector efficiency as it changes, was investigated with GESPECOR and PHITS MC codes.

2. MATERIAL AND METHOD

2.1. Experimental Setup

A p-type coaxial HPGe (GCD-30185) detector with a 0.7 mm Al end cap thickness was used for the experiments (Figure 1a). The detector has a relative efficiency of 30 % and a peak to Compton ratio of 58:1 at 1.33 MeV. The resolutions of given energies are 1.85 keV at 1.33 MeV and 0.875 keV at 0.122 MeV. The size information of the detector used in the experiment is given in Table 1. The detector has a connection with a digital signal processing analyzer operating through Gamma Vision spectroscopy software. The experimental efficiency was calculated using a Marinelli beaker with reference multi-radioactive nuclides dispersed in a 0.5 g/cc epoxy matrix. The Marinelli beaker snugged on the detector has a volume of 1 liter that is comprised of radionuclides in the energy range of 46 - 1836 keV (Figure 1b).

Table 1. Geometric dimensions of the detector (mm)

Basic Detector dimensions		
Detector diameter	57.3	
Detector length	57.3	
Hole diameter	7	
Hole depth	40.8	
Detector dimensions and materials		
Description	**Dimension**	**Material**
End cap to crystal cap	7.5	N.A.
End cap diameter	83	Aluminum
End cap window	0.6	Aluminum
Insulator/shield	0.01	Aluminized/ Mylar
Outside contact layer	0.7	Lithium
Hole contact layer	0.003	Boron
Mount cap wall	1.5	Aluminum
End cap wall	1.5	Aluminum

(a)   (b)

Figure 1. a) HPGe Detector, b) Marinelli beaker with 0.5 g/cc density used in the experiment

$$\varepsilon(E) = \frac{N_p(E)/t}{A.f_\gamma(E)} \ F_{coi} \tag{1}$$

Where Np(E) is the full energy peak net area, t is the gamma acquisition live time in seconds, A is the source activity in Bequerrels at the measurement date, fγ, and F_{coi} are the gamma-ray emission probability of the interested energy (%) and TCS correction factor, respectively. To obtain the coincidence summing factors, GESPECOR, a program that can also calculate coincidence-summing effects with cascade gamma photons, coincidence losses, K_α, K_β, and multiple X-rays, was used.

2.2. PHITS

In this study, HPGe detector was modeled using PHITS version 3.26 (Particle and Heavy Ion Transport Code System) and Marinelli beaker that snugs on the detector. PHITS, which has recently gained increasing popularity, is a Monte Carlo particle transport simulation code and was developed by the Japanese Atomic Energy Agency in collaboration with various institutions in Japan and Europe (Sato et al., 2018). PHITS can transport most types of particles with an energy of up to 1 TeV using several nuclear reaction models and data libraries. While modeling the experimental setup with this simulation, first the given geometric parameters of the detector and its surroundings, such as crystal dimensions, the thickness of the end cap window, the DL thickness, the structure of the detector components, etc. are defined (Ordóñez et al., 2019; Zamzamian et al., 2020). Marinelli beaker with its dimensions, its wall thickness, and the material (EPOXY) inside it was also modeled in the simulation (Figure 2). T-deposit tally reveals the deposited energy distribution in a specified location by ionization of charged particles. It is used to calculate FEPE values for the energy of interest. The history number in this simulation is 10^6 for each energy value, a sufficient amount for the required counting statistics to obtain an uncertainty of around 1 %.
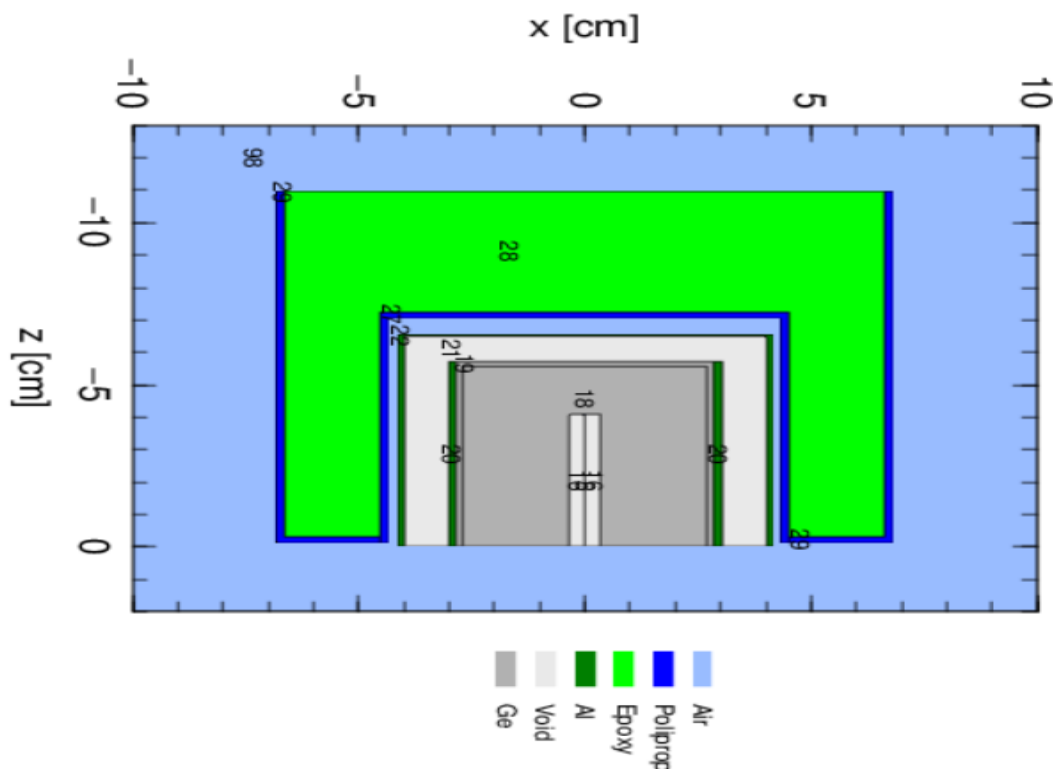
Figure 2. *Two-dimensional view of the detector and Marinelli beaker modeled in PHITS*

2.3. GESPECOR

Another MC simulation program used in this study is GESPECOR version 4.2, which is a practical and useful code commonly used in Gamma Measurement Laboratories. The efficiency computation, self-absorption effects, and coincidence summing can be calculated by just entering the parameters into its user-friendly interface. GESPECOR is easily applicable to various sample geometries such as point, cylindrical, and Marinelli measured using well-type, closed-end coaxial HPGe detectors (Sima et al., 2001; Murphy et al., 2020). While creating the model of the experiment using GESPECOR, first the detector was modeled by entering the relevant parameters in the interface, then the source geometry was selected as Marinelli and the experimental setup was simulated by entering the dimensional parameters of the Marinelli beaker, the components and density of the epoxy material in the container (Figure 3). The number of photons in this simulation was again taken 10^6. The DL thickness was increased to 1.7 mm in 0.1 mm steps from the 0.7 mm provided by the manufacturer to determine the optimum DL thickness that was consistent with the experimental efficiency. As the DL thickness increased, the efficiency values decreased and the agreement with the experiment was observed.
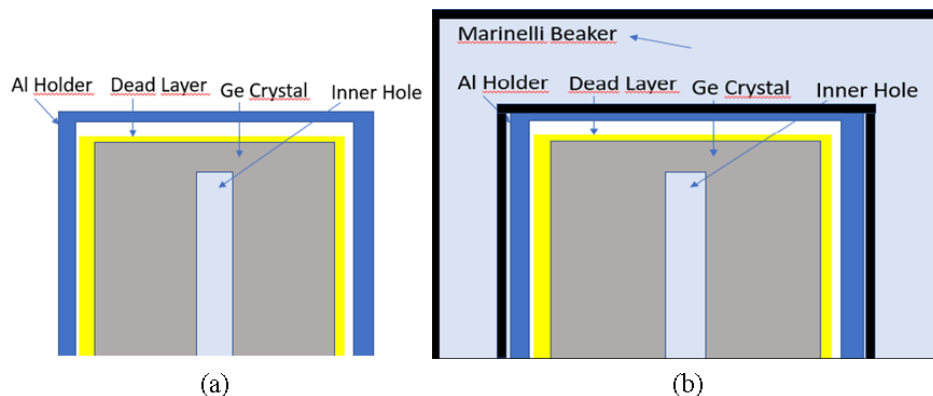
Figure 3. *Two-dimensional view of the detector and Marinelli beaker modeled in GESPECOR*

3. RESULTS AND DISCUSSION

The experiment was carried out with a Marinelli beaker containing a multi-energy point radioactive source in an epoxy matrix with a density of 0.5 g/cc attached to the detector. The elemental composition of the epoxy used was 62.040 % C, 27.547 % O, and 10.413 % H by weight. The radionuclides used in the experiment, the energy values of the gamma rays emitted from these nuclides, the source activity, the error percentage of the source activity, the half-life (days) of the radioactive sources, the gamma density, the experimental efficiency, the total count rate, and absolute error uncertainties are given in Table 2.

Table 2. *The energy (keV) values, activities (µCi), half-lives, gamma emission probabilities, net count rate, experimental efficiency values, and percentage error of the multiple radioactive Marinelli sources used in the experiment*

Nuclide	Energy (keV)	A_0 (µCi)	A_0(µCi) U_{Total}%	$t_{1/2 \text{ (day)}}$	$f(\gamma)$	Net Count	ε-Exp	U_{exp}%
^{210}Pb	46.54	0.30320	4.0	8140	4.252	1.1	0.00229	4.4
^{241}Am	59.54	0.03014	3.0	157740	35.920	4.0	0.01008	3.4
^{109}Cd	88.03	0.42430	3.0	462.6	3.660	14.8	0.02750	3.1
^{57}Co	122.06	0.01661	3.0	271.79	85.490	16.1	0.03431	3.1
^{139}Ce	165.86	0.02051	3.0	137.64	79.900	16.1	0.03335	3.1
^{203}Hg	279.20	0.06153	3.0	46.595	81.480	23.3	0.02418	3.1
^{113}Sn	391.70	0.07979	3.0	115.09	64.970	27.5	0.01868	3.0
^{85}Sr	514.00	0.10000	3.0	64.849	98.500	33.7	0.01481	3.1
^{137}Cs	661.66	0.07143	3.0	11012	84.990	27.3	0.01218	3.0
^{88}Y	898.04	0.16840	3.0	106.63	93.700	40.5	0.00969	3.0
^{60}Co	1173.23	0.08579	3.0	1924.3	99.850	23.2	0.00786	3.0
^{60}Co	1332.49	0.08579	3.0	1924.3	99.983	21.0	0.00710	3.1
^{88}Y	1836.07	0.16840	3.0	106.603	99.346	24.3	0.00553	3.0

The experimental setup was modeled using GESPECOR and PHITS MC programs. The DL thickness was increased from 0.7 mm given by the manufacturer to 1.7 mm in 0.1 mm steps. As the DL thickness was increased, a decrease was observed in the efficiency values. Except for 46.5 keV, 59 keV, and 88 keV energies, the photopic efficiency closest to the experimental efficiency was obtained at 1.5 mm thickness in both GESPECOR (Figure 4) and PHITS MC (Figure 5) simulations. This mismatch in the low-energy region is due to the DL thickness in p-type HPGe detectors (Ješkovský et al., 2019). The DL thickness is due to lithium

intrusiveness on the outer surface of the Germanium crystal in high-purity germanium detectors (Modarresi et al., 2018). Even at room temperature, lithium atoms are aggressive to the crystal surface (Huy et al., 2007). The reason is that the manufacturer does not explain the DL thickness with precise measurements and that it reaches this thickness randomly during the lifetime of the detector. Even the millimeter variation in DL thickness must be carefully considered to arrive at an accurate calculation of the experimental efficiency. Discrepancies in the low energy region have also been reported for both Marinelli geometries and point sources in the literature (Ródenas et al., 2003; Huy, 2011; Britton et al., 2013).
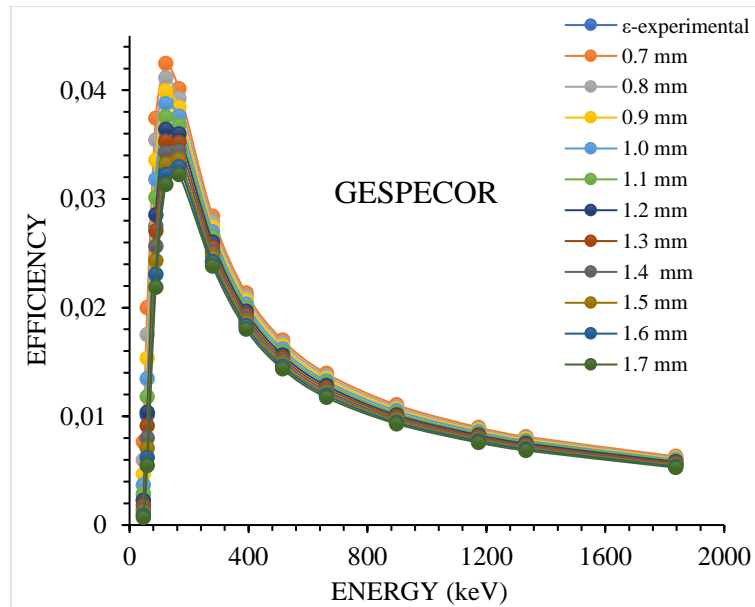
Figure 4. *Energy dependence of efficiency from GESPECOR for DL thicknesses between 0.7 - 1.7 mm*
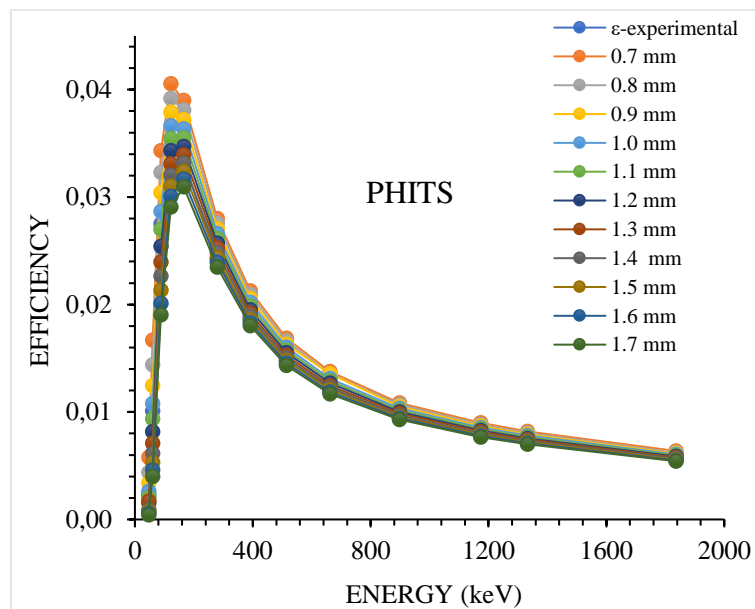
Figure 5. *Energy dependence of efficiency from PHITS for DL thicknesses between 0.7 - 1.7 mm*

The photon energy of 59.54 keV is insufficient to reach the crystal just through the detector's outer top dead layer, but the photon energy of 662 keV is sufficient to reach both the outer lateral and inner dead layers of the crystal (Azli & Chaoui, 2015). At energies above 122.06 keV, the results of both GESPECOR (Table 3) and PHITS MC (Table 4) codes are in good agreement with experimental efficiencies with a maximum deviation of 2 % and 2.8 % respectively, at 1.5 mm dead layer. These DL thicknesses can be determined effortlessly using simulation programs.

Table 3. *The percentage difference in the efficiency values calculated using GESPECOR according to the dead layer change in the experimental efficiency*

Energy (keV)	ε_{exp}	0.7 mm	0.8 mm	0.9 mm	1.0 mm	1.1 mm	1.2 mm	1.3 mm	1.4 mm	1.5 mm	1.6 mm	1.7 mm
46.54	0.00229	233.8	160.6	103.9	59.8	25.4	1.4	22.4	38.8	51.7	61.9	69.9
59.54	0.01008	98.3	73.6	52.0	33.3	17.0	2.8	9.7	20.6	30.1	38.5	45.8
88.03	0.02750	36.1	28.8	22.0	15.6	9.6	3.8	1.7	6.8	11.6	16.2	20.5
122.06	0.03431	23.7	19.9	16.3	12.9	9.4	6.0	2.8	0.2	3.2	6.0	8.7
165.86	0.03334	20.3	17.7	15.2	12.8	10.3	7.9	5.5	3.2	1.0	1.1	3.3
279.20	0.02418	17.5	15.4	13.4	11.5	9.5	7.6	5.7	3.8	2.0	0.3	1.6
391.70	0.01868	14.2	12.5	10.6	8.8	6.9	5.2	3.4	1.6	0.1	1.9	3.6
514.00	0.01481	14.9	13.0	11.1	9.3	7.4	5.6	3.8	2.1	0.2	1.4	3.0
661.66	0.01218	14.5	12.6	10.7	8.8	7.1	5.2	3.4	1.6	0.3	2.0	3.7
898.04	0.00968	14.1	12.2	10.4	8.6	6.5	4.6	3.1	1.4	0.2	2.0	3.5
1173.23	0.00786	14.3	12.5	10.8	9.1	7.2	5.5	3.9	2.1	0.6	1.2	3.1
1332.49	0.00710	14.5	12.9	11.0	9.3	7.7	6.0	4.0	2.3	0.6	1.1	2.9
1836.07	0.00552	14.3	12.1	10.4	8.7	7.2	5.4	3.4	1.5	0.3	2.0	3.8

Table 4. *The percentage difference in the efficiency values calculated using PHITS according to the dead layer change in the experimental efficiency*

Energy (keV)	ε_{exp}	0.7 mm	0.8 mm	0.9 mm	1.0 mm	1.1 mm	1.2 mm	1.3 mm	1.4 mm	1.5 mm	1.6 mm	1.7 mm
46.54	0.00229	152.6	91.2	48.7	13.7	11.1	32.3	25.4	60.7	68.1	75.4	81.2
59.54	0.01008	65.3	42.6	23.4	7.1	7.4	19.1	29.6	39.3	47.3	54.4	60.3
88.03	0.02750	24.8	17.5	10.7	4.2	1.9	7.6	12.9	17.7	22.4	26.9	30.8
122.06	0.03431	18.1	14.2	10.4	6.8	3.3	0.0	3.5	6.7	9.6	12.4	15.3
165.86	0.03333	16.9	14.3	11.6	9.1	6.6	4.1	1.8	0.5	2.8	5.0	7.1
279.20	0.02418	15.9	13.9	11.8	10.0	8.1	6.3	4.5	2.6	0.8	1.0	2.9
391.70	0.01868	13.8	11.8	10.0	8.1	6.3	4.5	2.8	1.0	0.7	2.1	3.6
514.00	0.01481	13.9	12.1	10.2	8.3	6.5	4.7	3.0	1.5	0.2	1.7	3.3
661.66	0.01218	13.0	11.2	11.2	7.5	5.8	4.1	2.3	0.7	0.9	2.6	4.3
898.04	0.00968	12.0	10.5	8.6	6.9	5.1	3.6	1.9	0.2	1.3	2.3	3.8
1173.23	0.00785	14.3	12.4	10.7	9.1	7.5	5.7	4.0	2.4	0.9	0.8	2.2
1332.49	0.00709	15.1	13.5	11.6	10.0	8.1	6.5	5.1	3.5	1.9	0.5	1.0
1836.07	0.00552	15.1	12.9	11.1	9.5	8.1	6.3	4.8	3.2	1.5	0.0	1.4

4. CONCLUSION

In this study, the FEPE curve of the detector for this Marinelli geometry was experimentally obtained using a Marinelli source containing an epoxy matrix with a density of 0.5 g/cc. Experimental efficiencies were obtained by counting a multi-energy point radioactive source in the range of 46.5 - 1836 keV in the HPGe detector. The experimental efficiency values of the detector at 0.7 mm dead layer thickness given by the manufacturer were calculated with Monte Carlo. Experimental efficiency results were compared with Monte Carlo efficiency values. In comparison, a difference between the experimental efficiency value of 233.8 % and 14.1 % was observed in the GESPECOR program in the range of 46.5 - 1836 keV. Likewise, a difference of 152.6 % - 12 % was observed in this energy range in the PHITS program. In order to obtain the correct dead layer thickness and to understand the change in the active volume of the crystal after eight years of use, when Modeling was done using Monte Carlo simulation codes GESPECOR and PHITS, the most compatible results with the experiment were obtained at 1.5 mm DL thickness for both GESPECOR and PHITS. In the GESPECOR program, a difference of 51.7 %, 30.1 %, 11.6 %, 122 keV and 3.2 % was obtained at 46.5 keV, 59 keV and 88 keV, and 122 keV, respectively, while this difference was found between 2 % and 0.1 % from 165 keV. In the PHITS program, 46.5 keV, 59 keV, 88 keV and 122 keV are 68.1 %, 47.3 %, 22.4 % and 9.6 %, respectively, while the difference from the experimental efficiency is between 2.8 % and 0.2 % in the 165 - 1836 keV range. In addition, while the simulations are being run, it has been determined that the active volume of the detector crystal decreases as the dead layer thickness increases and thus the efficiency values decrease. Good agreement was obtained at 1.5 mm DL in the high energy region, although inconsistency was observed between simulations and experiments in the low energy region of 46.5 keV and 122 keV. Marinelli beakers are almost completely they cover the detector crystal, are very useful geometries for calculating experimental efficiency against energy values. The compatibility between the detector's efficiency calculation and the Monte Carlo simulation for multi-energy radioactive sources was studied in an epoxy Marinelli beaker with a density of 0.5 g/cc. Inconsistencies in the low energy region such as 46.5, 59, 88 and 122 keV are due to the detector being p-type. This incompatibility is explained by the random and time-time diffusion of lithium on the crystal surface in high purity germanium detectors (Modarresi et al., 2017). It can be caused by errors in the position of the Marinelli beaker on the detector or by the wall thickness of the Marinelli beaker.

ACKNOWLEDGEMENT

CONFLICT OF INTEREST

The authors declare no conflict of interest.

REFERENCES

Ahmed, A. S., Capello, K., Chiang, A., Cardenas-Mendez, E., & Kramer, G. H. (2009). Optimization of geometric parameters for Marinelli beaker to maximize the detection efficiency of an HPGe detector. *Nuclear Instruments and Methods in Physics Research Section A: Accelerators, Spectrometers, Detectors and Associated Equipment*, 610(3), 718-723. doi:10.1016/j.nima.2009.09.020

Azli, T., & Chaoui, Z.-E.-A. (2015). Performance Revaluation of a N-Type Coaxial HPGe Detector with Front Edges Crystal Using MCNPX. *Applied Radiation and Isotopes*. *97*, 106-112. doi:10.1016/j.apradiso.2014.12.027

Bölükdemir, M. H., Uyar, E., Aksoy, G., Ünlü, H., Dikmen, H., & Özgür, M. (2021). Investigation of Shape Effects and Dead Layer Thicknesses of a Coaxial HPGe Crystal on Detector Efficiency by Using PHITS Monte Carlo Simulation. *Radiation Physics and Chemistry*, *189*, 109746. doi:10.1016/j.radphyschem.2021.109746

Britton, R., Burnett, J., Davies, A., & Regan, P. H. (2013). Determining the Efficiency of a Broad-Energy HPGe Detector Using Monte Carlo Simulations. *Journal of Radioanalytical and Nuclear Chemistry*, *295*(3), 2035-2041. doi:10.1007/s10967-012-2203-2

Gilmore, G. (2008). *Practical Gamma-Ray Spectrometry: Second Edition*. John Wiley and Sons.

Harb, S., Salahel Din, K., & Abbady, A. (2008, February 19-23). *Study of Efficiency Calibrations of HPGe Detectors for Radioactivity Measurements of Environmental Samples*. In: Proceedings of the 3rd Environmental Physics Conference, (pp. 207-218), Aswan, Egypt.

Huy, N. Q., Binh, D. Q., & An, V. X. (2007). Study on the Increase of Inactive Germanium Layer in a High-Purity Germanium Detector after a Long Time Operation Applying MCNP Code. *Nuclear Instruments and Methods in Physics Research, Section A: Accelerators, Spectrometers, Detectors and Associated Equipment*, *573*(3), 384-388. doi:10.1016/j.nima.2006.12.048

Huy, N. Q. (2011). Dead-Layer Thickness Effect for Gamma Spectra Measured in an HPGe p-Type Detector. *Nuclear Instruments and Methods in Physics Research, Section A: Accelerators, Spectrometers, Detectors and Associated Equipment*, *641*(1), 101-104. doi:10.1016/j.nima.2011.02.097

Ješkovský, M., Javorník, A., Breier, R., Slučiak, J., & Povinec, P. P. (2019). Experimental and Monte Carlo Determination of HPGe Detector Efficiency. *Journal of Radioanalytical and Nuclear Chemistry*, *322*(3), 1863-1869. doi:10.1007/s10967-019-06856-4

Lépy, M. C., Thiam, C., Anagnostakis, M., Galea, R., Gurau, D., Hurtado, S., Karfopoulos, K., Liang, J., Liu, H., Luca, A., Mitsios, I., Potiriadis, C., Savva, M. I., Thanh, T. T., Thomas, V., Townson, R. W., Vasilopoulou, T., & Zhang, M. (2019). A Benchmark for Monte Carlo Simulation in Gamma-Ray Spectrometry. *Applied Radiation and Isotopes*, *154*, 108850. doi:10.1016/j.apradiso.2019.108850

Modarresi, S. M., Masoudi, S. F., & Karimi M. (2017). A Method for Considering the Spatial Variations of Dead Layer Thickness in HPGe Detectors to Improve the FEPE Calculation of Bulky Samples. *Radiation Physics and Chemistry*, *130*, 291-296. doi:10.1016/j.radphyschem.2016.08.020

Modarresi, S. M., Masoudi, S. F., & Karimi M. (2018). A Method for Self-Attenuation and Sample-Height Correction for Counting Efficiency of HPGe Using Marinelli Beaker Geometry. *Journal of Radioanalytical and Nuclear Chemistry*, *316*(1), 129-137. doi:10.1007/s10967-018-5725-4

Murphy, N. M., León Vintró, L., Burbidge, C. I., & Currivan, L. (2020). An Automated Programme for the Optimisation of HPGe Detector Parameters Using an Evolutionary Algorithm with GESPECOR. *Applied Radiation and Isotopes*, *156*, 108883. doi:10.1016/j.apradiso.2019.108883

Ordóñez, J., Gallardo, S., Ortiz, J., Sáez-Muñoz, M., & Martorell, S. (2019). Intercomparison of Full Energy Peak Efficiency Curves for an HPGe Detector Using MCNP6 and GEANT4. *Radiation Physics and Chemistry*, *155*(2), 248-251. doi:10.1016/j.radphyschem.2018.06.049

Ródenas, J., Pascual, A., Zarza, I., Serradell, V., Ortiz, J., & Ballesteros, L. (2003). Analysis of the Influence of Germanium Dead Layer on Detector Calibration Simulation for Environmental Radioactive Samples Using the Monte Carlo Method. *Nuclear Instruments and Methods in Physics Research, Section A: Accelerators, Spectrometers, Detectors and Associated Equipment*, *496*(2-3), 390-399. doi:10.1016/S0168-9002(02)01748-5

Sato, T., Iwamoto, Y., Hashimoto, S., Ogawa, T., Furuta, T., Abe, S., Kai, T., Tsai, P.E., Matsuda, N., Iwase, H., Shigyo, N., Sihver, L., & Niita, K. (2018). Features of Particle and Heavy Ion Transport Code System (PHITS) Version 3.02. *Journal of Nuclear Science and Technology*, *55*(6), 684-690. doi:10.1080/00223131.2017.1419890

Sima, O., Arnold, D., & Dovlete, C. (2001). GESPECOR: A Versatile Tool in Gamma-Ray Spectrometry. *Journal of Radioanalytical and Nuclear Chemistry*, *248*, 359-364. doi:10.1023/A:1010619806898

Vasconcelos, D. C., Pereira, C., Gallardo, S., Rocha, Z., & Santos, T. O. (2011, October 24-28). Efficiency Simulation of a HPGE Detector for the Environmental Radioactivity Laboratory / CDTN Using a MCNP-Gammavision Method. International Nuclear Atlantic Conference (INAC 2011).

Zamzamian, S. M., Hosseini, S. A., Feghhi, S. A., & Samadfam, M. (2020). Determining of the Optimized Dimensions of the Marinelli Beaker Containing Source with Inhomogeneous Emission Rate by Using Genetic Algorithm Coupled with MCNP and Determining Distribution Type by Neural Networks. *Applied Radiation and Isotopes*, *157*, 109039. doi:10.1016/j.apradiso.2020.109039

Sample Size Estimation of Nonparametric Tests with Ordered Alternatives for Longitudinal Data in Randomized Complete Block Designs

Melike BAHCECITAPAR[1*] (iD)   Hatice Tul Kubra AKDUR[2] (iD)

[1]Hacettepe University, Faculty of Science, Department of Statistics, Ankara, Türkiye
[2]Gazi University, Faculty of Science, Department of Statistics, Ankara, Türkiye

Keywords	Abstract
Nonparametric Tests Autocorrelated Longitudinal Data Randomized Complete Block Designs	Longitudinal studies involve repeated measurements from the same subjects or blocks over short or an extended periods of time. In longitudinal studies, usually the most important step is to decide how many experimental units to use. There are no closed form equations for determining sample size in many complex designs. Monte Carlo simulation method is an effective tool in complex designs to estimate power or sample size. This paper introduces estimating sample size for the number of blocks or experimental units based on a fixed number of treatment/time in randomized complete block designs with correlated longitudinal responses analyzed by nonparametric tests against ordered alternatives. The sample size of subjects is estimated for each test statistics by taking into account the autocorrelation structure of the error terms which form either a stationary first-order moving average or autoregressive with non-normally distributed white noise terms. An extensive sample size/power comparison among the recently proposed Modification of S test and the other two well-known nonparametric tests such as the Page test and the generalized Jonckheere test against ordered alternatives in randomized complete block designs is carried out under stationary first-order autoregressive and moving average error structures with white noise terms distributed with either Laplace or Weibull distributions. Simulation study indicates that the distribution of white noise and the error structure have an important role on sample size estimation for each nonparametric test. The Modification of S test requires large sample size in contrast to other tests for longitudinal data in the specified simulation setting.

1. INTRODUCTION

Longitudinal data taken from same subjects over time can occur within the randomized complete block designs (RCBDs). In RCBDs with longitudinal data, homogeneous subjects are blocks and a complete set of treatments/time points are randomly assigned to each block. Testing the trend/direction change of responses over time can be assessed by nonparametric tests for assessing the efficiency of treatment in a RCBD which is often expected to increase or decrease with the ordering of treatments. Many studies have examined the behavior of nonparametric tests in independent situations. Although longitudinal studies are quite popular today, the use of nonparametric tests in these studies is quite rare and nonparametric trend tests' behavior has almost never been investigated. In some clinical trials, it is reasonable to observe that the efficiency of treatment may increase or decrease based on the dose value of a drug throughout the study (Dmitrienko et al., 2007). The case that responses would incline or decline over time leads to the statistical testing problem with ordered alternatives and many nonparametric tests have been developed for this problem in RCBDs (Hollander, 1967; Shan et al., 2014; Best & Rayner, 2015). The Page (*P*) test is a well-known distribution-free tests for ordered alternatives on treatments in RCBDs (Page, 1963). The generalized Jonckheere (*GJ*) test was proposed for repeated measures in RCBDs (Zhang & Cabilio, 2012). The Modification of S (*MS*) test is a new

*Corresponding Author, e-mail: mlk@hacettepe.edu.tr

nonparametric test based on the rank differences within each block to detect monotonic trend of treatments in RCBDs (Akdur et al., 2019). All of these nonparametric tests assume that the within-block responses are independent and error terms follow an identical continuous distribution with known parameters. However, in some situations, such as when the blocks/subjects have repeated measures, the existence of autocorrelated errors and distribution of responses should be taken into account commonly. Recently, Akdur (2020) has investigated power performances of some nonparametric trend tests in RCBDs when randomized blocks contain dependent observations by using the circular block bootstrap method. The defining feature of longitudinal data is that repeated measures are likely to be autocorrelated over time. It is unreasonable to assume that the within-block responses or repeated measurements are independent over time in the analysis of this kind of popular statistical experimental designs. In RCBDs with longitudinal data, let Y_{ij} be the measurement of the ith subject at jth time point, where $i = 1,2, \ldots, b$ and $j = 1,2, \ldots, n$. A model for RCBDs with balanced and equally spaced longitudinal data can be written as

$$Y_{ij} = \mu + \beta_i + \tau_j + \varepsilon_{ij}, i = 1, \ldots, b; j = 1, \ldots, n; \tag{1}$$

where μ is a common mean, β_i are block (subject) effects, τ_j are time (treatment) effects, b is the number of blocks (subjects) and n is the number of time points (treatments) at which subjects (blocks) are measured. The error terms ε_{ij} are here assumed to follow popular stationary time series processes, a stationary first-order moving average (MA1) or a stationary first-order autoregressive (AR1) model. The null hypothesis on the treatment effect is as

$$H_0: \tau_1 = \tau_2 = \cdots = \tau_n = 0 \tag{2}$$

against the increasing ordered alternative

$$H_0: \tau_1 \leq \tau_2 \leq \cdots \leq \tau_n \tag{3}$$

or the decreasing ordered alternative

$$H_0: \tau_n \leq \tau_{n-1} \leq \cdots \leq \tau_1 \tag{4}$$

with at least one inequality. When the ordering of treatments is already known, the ordered alternative is a natural choice as in Equation (3) or Equation (4). Nonparametric tests are useful for statistical testing problem with the ordered alternative, when longitudinal data are not distributed normally or quite small to satisfy assumptions of traditional ANOVA models in RCBDs. Zhang and Cabilio (2012) proposed the *GJ* test against ordered alternatives for longitudinal data in RCBDs which are assumed to be autocorrelated in AR1 and second-order autoregressive (AR2) model to test the direction of change over treatments/time, when the errors follow $N(0,1)$ or Student-t distribution. Akdur et al. (2019) modified the *S* test for ordered alternative hypothesis in RCBDs for two-way ANOVA layout under the assumption of independent errors. However, they do not investigate the most general case in which the responses are assumed to be autocorrelated and non-normally distributed in RCBDs. Before starting clinical studies, it is an indispensable prerequisite to determine a suitable sample size according to the structure of the data. For the intended power value of the statistical test of interest, in recent years, many statistical studies have been carried out especially for the parametric tests with various effect sizes under independence assumption (Aslan et al., 2021; Serdar et al., 2021; Unalan, 2021). This paper proposes a new idea for calculating sample sizes (i.e. number of blocks) of *P*, *GJ* and *MS* test statistics for a target power against ordered alternatives for longitudinal data in RCBDs, when the error terms form either a stationary MA1 or AR1 model under Laplace and Weibull distributions. A broad set of Monte Carlo simulations is performed to model autocorrelated non-normally distributed responses and to compare these three nonparametric tests in terms of sample sizes and power values under a wide range of conditions. The remainder of this paper is organized as follows. The *P*, *GJ* and *MS* test statistics are briefly introduced in Section 2. In Section 3, the performance of *MS* test is compared with other commonly used nonparametric tests with regard to sample size under various conditions. In Section 4, a real example from a clinical trial is given to illustrate sample size calculations for the *MS*, *P* and *GJ* tests to obtain required 80% power. Section 5 is given to discussion and further works.

2. MATERIAL AND METHOD

This paper focuses on the P and GJ tests, well-known rank-based nonparametric tests for ordered alternatives in RCBDs. The MS test is a recently proposed nonparametric test which is an alternative to the GJ test for the ordered alternative problem in RCBDs.

2.1. Page's Test Statistics

For an ordered alternative hypothesis, Page's test statistics has been proposed as a nonparametric test based on within-block ranks, in which responses are ranked within each block (subject) (Page, 1963). The Page (P) test statistics is given as $P = \sum_{j=1}^{n} j r_j$, where $r_j = \sum_{j=1}^{b} R_{ij}$ is the sum of ranks of the j th treatment (time point) for block (subject) i and R_{ij} is the rank of response within block i at treatment j. Under the null hypothesis in Equation (2), the P test asymptotically follows a normal distribution with the mean $E(P) = \frac{bn(n+1)^2}{4}$ and the variance $V(P) = \frac{b(n-1)n^2(n+1)^2}{144}$ (Page, 1963). The null hypothesis would be rejected for a large value of the P test. Thas et al. (2012) provided a new version of Page test $PL = \sqrt{c} \sum_{j=1}^{n} \frac{l_j \overline{R_J}}{d}$ statistic using orthogonal trend contrast for tied and untied data where $\overline{R_J}$ is the mean of the ranks for treatment j, l_j are the linear trend coefficients, $d^2 = \sum_{j=1}^{n} l_j^2$. Here, $c = b(n-1)/(nV)$ for tied $V = \left\{ \sum_{i,j} R_{ij}^2 /(bn) \right\} - (n+1)^2/4$ whereas for untied data, $V = (n^2 - 1)/12$. Additionally, Best and Rayner (2015) suggested a new test statistic which developed upon the idea of orthogonal trend analysis used in ANOVA and provided as $PT = \sqrt{b} \sum_{j=1}^{n} l_j \overline{R_J} /dS$ where S^2 is the mean square error of a randomized block ANOVA of the R_{ij}.

2.2. Generalized Jonckheere Test Statistics

The GJ test statistics is an alternative nonparametric test to the P test for the problem of testing the ordered alternative hypothesis in RCBDs (Zhang & Cabilio, 2012). It is based on the Kendall's Tau correlation that measures the association between responses within each block and the alternative ordering where each block is ranked within itself over treatment or time (Kendall, 1938). The J test statistics was generalized for RCBDs as given $GJ = \frac{1}{b} \sum_{i=1}^{b} T_K(i)$, where $T_K(i) = \binom{n}{2}^{-1} A_K(i)$ is a Mann-Kendall statistics for testing the direction of change in responses (repeated measures over time for subject i and $A_K(i) = \sum_{l<m}^{n} (R_{im} - R_{il})$ is the non-standardized Kendall's tau correlation where $sgn(R_{im} - R_{il})$ is either 1 or -1, depending on whether $R_{im} > R_{il}$ or $R_{im} < R_{il}$ (Skillings & Wolfe, 1978; Zhang & Cabilio, 2012).

2.3. Modification of S Test Statistics

The Modification of S (MS) test statistics is the recently proposed nonparametric test based on the S test for RCBDs. Rank differences within each block are calculated in the MS test to compose an overall test statistic (Shan et al., 2014; Akdur et al., 2019). The MS test statistic is defined as $MS = \frac{1}{b} \sum_{i=1}^{b} T_K(i)$, where $T_K(i) = \binom{n}{2}^{-1} S_K(i)$ and $S_K(i) = \sum_{l<m}^{n} (R_{im} - R_{il}) I(R_{im} > R_{il})$ for subject i. $I((R_{im} > R_{il})$ is the indicator function which is either 1 or 0, depending on whether $R_{im} > R_{il}$ or $R_{im} < R_{il}$.

3. SIMULATION-BASED SAMPLE SIZE ESTIMATION

In this section, Monte Carlo simulations are conducted to compare the performances of the three nonparametric tests against ordered alternatives in RCBDs when observations are autocorrelated longitudinal data: 1) the P test; 2) the GJ test; and 3) the MS test. These tests are compared with each other in terms of sample sizes required to obtain 80% empirical power. Laplace and Weibull distributions are taken into account for longitudinal data. The nominal value of α is set to be as 0.05 for all simulation scenarios. Total 10000 iterations are utilized to obtain the 95% cutpoint for all tests. Giving the number of repeated measures over time, sample sizes are computed from simulated data based on the 95% cutpoint and 80% power. These are estimated for both AR1 and MA1 error models with parameter values ρ or $\theta = 0.20, 0.40, 0.60$ and 0.80 under various approximations to the distribution of longitudinal data and the whole is carried out for $n = 4, 5, 7, 10$. Additionally, sample sizes are also estimated for independent errors (ρ or $\theta = 0$) over time/treatment. For

random block and error distributions, Laplace distribution with location parameter 0 and dispersion parameter 1 (L(0,1)) and Weibull distribution with shape parameter 1 and scale parameter 1 (W(1,1)) are considered. In order to compare sample size calculations for the *MS*, *P* and *J* tests, the model with a linear trend alternative with individual block (subject) effects is considered here is written as

$$Y_{ij} = \beta_i + \phi j + \varepsilon_{ij}, i = 1,\ldots,b; j = 1,\ldots,n \tag{5}$$

assuming that for each subject, ε_{ij} are time series and they represent AR1 or MA1 errors. In Equation (5), ϕ is the slope term to generate an increasing order of treatments. For the linear trend model in Equation (5), ϕ is set to be as 0.2, 0.3 and 0.4 to assess the effect of different trends of longitudinal data on nonparametric tests. In such a model as in Equation (5), the repeated measures are considered to be from a linear model with errors following a AR1 or MA1 process over time and non-normal white noise terms. It is assumed that the error terms form either a stationary AR1 model

$$\varepsilon_{ij} = \rho \varepsilon_{ij-1} + e_{ij}, \tag{6}$$

or a stationary MA1 model

$$\varepsilon_{ij} = e_{ij} - \theta e_{ij-1}, \tag{7}$$

where ρ and θ are autocorrelation coefficients for AR1 and MA1 process, respectively and e_{ij} are independent and non-normally distributed white noise terms. In AR1 error model (Equation 6), it is assumed that $\rho > 0$ and the magnitude of correlation among responses declines as they become farther apart. In MA1 error model (Equation 7), the correlation is the same for any two consecutive responses. The results of 10000 Monte Carlo iterations generated by the model in Equation (5) for each combination of n, ρ, θ and error distributions are summarized in Table 1-3. All simulations are performed for the *P*, *J* and *MS* tests against increasing ordered alternatives for repeated measures over time in RCBDs. Simulation studies are conducted in Cran R 3.4.3. The steps of this algorithm are inspired by the bi-section method and a sample size can be estimated based on a Monte Carlo simulation for the model in Equation (5) through the following steps:

(1) Obtain the pre-specified parameters through either historical data or previous clinical trials.
(2) Specify a desired statistical power (i.e. 80%) and a type-1 error rate (i.e. 5%).
(3) Simulate correlated responses within blocks for a fixed sample size *n* of treatment/time within each block under null hypothesis to obtain critical values of each trend test and record them.
(4) Simulate correlated responses within blocks for a fixed sample size *n* of treatment/time within each block under alternative hypothesis. From the obtained data set, estimate each nonparametric test statistics value based on the simulated data set.
(5) Repeat steps 3 to 4, M (i.e. M=10 000) times under various conditions explained through of this section.
(6) Then, using critical values record if a *p*-value is smaller than 0.05. Estimate the empirical power of the model based on the fraction of *p*-values that are smaller than 0.05.
(7) If the power calculated is less than the targeted power, divide the sample size into half and add it to itself and estimate the new power with this new sample size. If the power obtained is greater than the targeted power, divide the sample size in half and subtract it from itself and estimate the new power with this new sample size. Go to first step and repeat them through Step 7.
(8) Stop the simulation if the desired statistical power is obtained with a small tolerance value, i.e. 0.009.

Table 1 displays sample size calculations to obtain 80% empirical power of tests for longitudinal data generated by the model in Equation (5) with uncorrelated error terms within blocks for $n = 4, 5, 7, 10$. It can be seen that sample sizes estimated for Laplace distribution are greater than those for Weibull distribution. For each test, under all combinations for *n* and ϕ, the smallest sample size is obtained for Weibull distribution. Under uncorrelated error terms over time, sample sizes for 80% power are same for the *MS* and *P* tests for Weibull distribution. On the other hand, under both distributions, for each *n*, sample sizes of the *GJ* test are smaller than the others. As *n* increases, sample size decreases for all values of ϕ. Additionally, as shown in Figure 1, for fixed *n*, as ϕ increases, sample size estimated to obtain 80% empirical power of tests decreases.

Table 1. *Simulated sample size and power study based on uncorrelated errors following Laplace or Weibull distribution (α =0.05)*

ϕ	n	Laplace distribution			Weibull distribution		
		MS	*P*	*GJ*	*MS*	*P*	*GJ*
0.2	4	59 (0.799)	53 (0.808)	54 (0.809)	59 (0.807)	53 (0.793)	41 (0.794)
	5	41 (0.808)	41 (0.794)	36 (0.807)	41 (0.797)	41 (0.793)	32 (0.799)
	7	32 (0.804)	32 (0.800)	27 (0.793)	27 (0.802)	27 (0.797)	21 (0.807)
	10	24 (0.799)	24 (0.796)	20 (0.799)	20 (0.800)	21 (0.804)	17 (0.806)
0.3	4	24 (0.795)	24 (0.797)	20 (0.792)	21 (0.799)	21 (0.806)	17 (0.802)
	5	18 (0.795)	18 (0.799)	17 (0.808)	17 (0.806)	17 (0.794)	14 (0.797)
	7	14 (0.795)	14 (0.801)	11 (0.797)	11 (0.794)	11 (0.796)	9 (0.801)
	10	11 (0.802)	11 (0.796)	9 (0.799)	9 (0.805)	9 (0.793)	8 (0.806)
0.4	4	14 (0.799)	14 (0.792)	11 (0.791)	11 (0.798)	11 (0.792)	9 (0.808)
	5	11 (0.802)	11 (0.804)	9 (0.794)	9 (0.795)	10 (0.800)	8 (0.799)
	7	8 (0.794)	8 (0.796)	6 (0.799)	6 (0.793)	6 (0.795)	5 (0.796)
	10	6 (0.800)	6 (0.880)	5 (0.795)	4 (0.793)	4 (0.799)	3 (0.801)
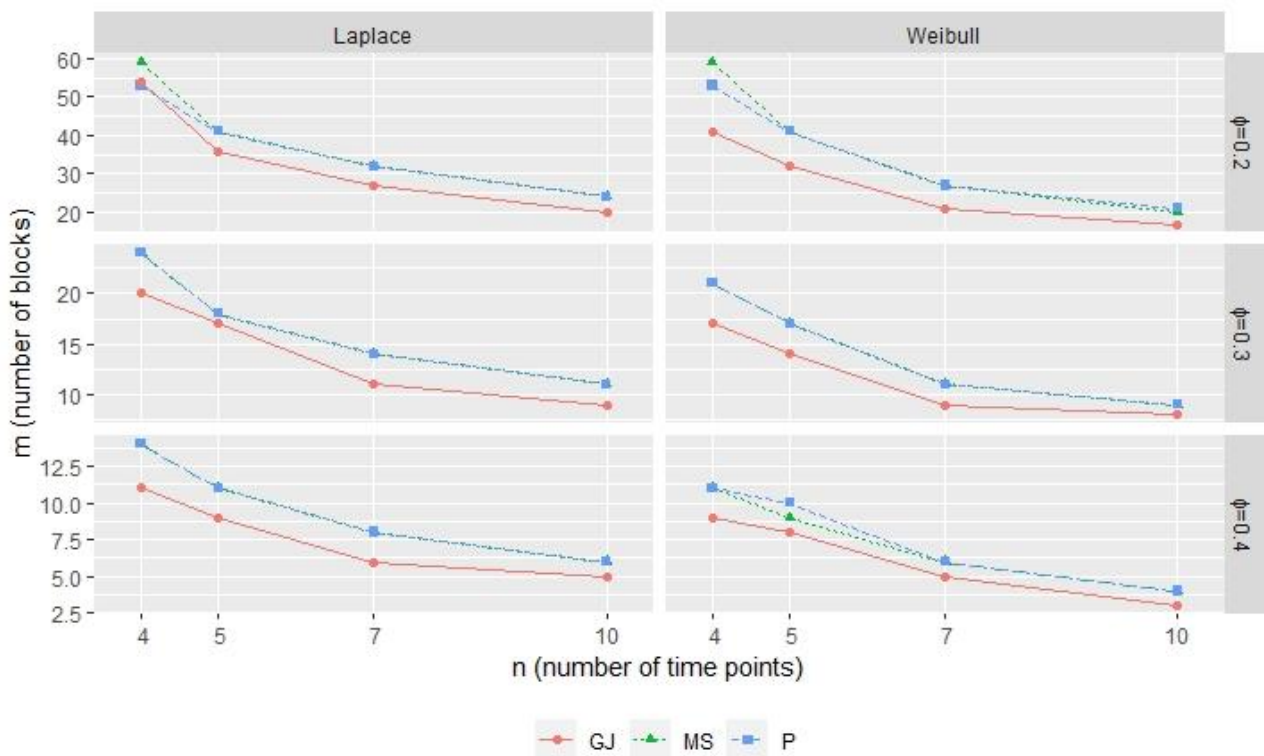
Figure 1. *Sample size (number of blocks) required to obtain 80% power curves of the MS, P and GJ tests for longitudinal data with uncorrelated errors following L(0,1) and W(1,1) distribution (α = 0.05)*

Table 2. *Simulated sample size and power study based on MA1 and AR1 error models following L(0,1) for*
α=0.05

			L(0,1)					
			MA1			AR1		
ϕ	ρ or θ	n	MS	P	GJ	MS	P	GJ
0.2	0.20	4	47 (0.809)	47 (0.796)	41 (0.793)	47 (0.806)	47 (0.808)	41 (0.806)
		5	35 (0.796)	36 (0.796)	32 (0.807)	36 (0.801)	35 (0.798)	32 (0.808)
		7	27 (0.791)	27 (0.804)	24 (0.807)	27 (0.802)	27 (0.808)	24 (0.799)
		10	21 (0.791)	21 (0.805)	17 (0.806)	21 (0.795)	21 (0.798)	18 (0.797)
	0.40	4	47 (0.792)	47 (0.798)	41 (0.807)	41 (0.801)	41 (0.803)	36 (0.806)
		5	32 (0.796)	35 (0.802)	32 (0.807)	32 (0.808)	35 (0.808)	27 (0.802)
		7	27 (0.804)	27 (0.799)	21 (0.806)	24 (0.793)	24 (0.797)	20 (0.802)
		10	23 (0.808)	21 (0.794)	18 (0.799)	21 (0.797)	21 (0.808)	17 (0.804)
	0.60	4	47 (0.802)	47 (0.795)	41 (0.799)	35 (0.793)	36 (0.804)	35 (0.807)
		5	35 (0.808)	32 (0.803)	32 (0.803)	32 (0.803)	27 (0.792)	24 (0.797)
		7	27 (0.795)	27 (0.795)	21 (0.792)	21 (0.795)	21 (0.793)	20 (0.798)
		10	21 (0.795)	24 (0.807)	18 (0.806)	18 (0.806)	18 (0.801)	14 (0.799)
	0.80	4	51 (0.797)	51 (0.793)	47 (0.803)	36 (0.793)	41 (0.806)	35 (0.803)
		5	41 (0.808)	41 (0.801)	32 (0.794)	27 (0.800)	27 (0.796)	24 (0.803)
		7	27 (0.794)	32 (0.808)	24 (0.807)	21 (0.799)	21 (0.808)	17 (0.796)
		10	24 (0.802)	24 (0.796)	20 (0.804)	18 (0.808)	18 (0.805)	14 (0.795)
0.3	0.20	4	21 (0.792)	21 (0.794)	18 (0.806)	21 (0.805)	21 (0.799)	17 (0.803)
		5	17 (0.803)	17 (0.808)	14 (0.799)	17 (0.805)	18 (0.808)	14 (0.806)
		7	11 (0.796)	14 (0.807)	11 (0.806)	11 (0.805)	14 (0.809)	9 (0.796)
		10	11 (0.808)	11 (0.808)	8 (0.793)	11 (0.805)	11 (0.809)	8 (0.793)
	0.40	4	20 (0.804)	21 (0.795)	18 (0.802)	18 (0.792)	20 (0.806)	18 (0.807)
		5	14 (0.799)	17 (0.808)	14 (0.802)	14 (0.805)	17 (0.807)	14 (0.796)
		7	11 (0.801)	11 (0.795)	9 (0.795)	11 (0.800)	11 (0.793)	9 (0.796)
		10	9 (0.794)	9 (0.791)	8 (0.792)	9 (0.803)	9 (0.792)	8 (0.799)
	0.60	4	23 (0.805)	24 (0.805)	20 (0.793)	18 (0.803)	18 (0.792)	17 (0.806)
		5	17 (0.808)	17 (0.800)	14 (0.807)	14 (0.805)	14 (0.804)	11 (0.804)
		7	11 (0.794)	11 (0.793)	11 (0.806)	11 (0.799)	11 (0.806)	9 (0.798)
		10	9 (0.800)	11 (0.808)	8 (0.807)	9 (0.800)	9 (0.803)	8 (0.800)
	0.80	4	24 (0.801)	27 (0.803)	21 (0.792)	18 (0.792)	18 (0.797)	17 (0.799)
		5	17 (0.794)	18 (0.802)	14 (0.808)	14 (0.801)	14 (0.802)	11 (0.793)
		7	14 (0.805)	14 (0.798)	11 (0.797)	11 (0.808)	11 (0.808)	9 (0.809)
		10	11 (0.793)	11 (0.801)	9 (0.796)	9 (0.806)	9 (0.807)	6 (0.794)
0.4	0.20	4	14 (0.805)	14 (0.807)	11 (0.800)	14 (0.806)	14 (0.803)	11 (0.808)
		5	9 (0.791)	9 (0.798)	8 (0.794)	9 (0.794)	9 (0.795)	8 (0.792)
		7	8 (0.799)	8 (0.808)	6 (0.805)	8 (0.805)	8 (0.805)	6 (0.894)
		10	6 (0.797)	6 (0.808)	5 (0.796)	6 (0.806)	6 (0.806)	5 (0.793)
	0.40	4	14 (0.806)	14 (0.808)	11 (0.806)	11 (0.793)	11 (0.798)	11 (0.801)
		5	9 (0.808)	9 (0.803)	8 (0.799)	9 (0.795)	9 (0.802)	8 (0.794)
		7	6 (0.791)	6 (0.793)	6 (0.802)	6 (0.801)	6 (0.793)	6 (0.801)
		10	6 (0.803)	6 (0.800)	5 (0.800)	5 (0.798)	5 (0.795)	5 (0.800)
	0.60	4	14 (0.805)	14 (0.803)	12 (0.798)	11 (0.808)	11 (0.801)	9 (0.793)
		5	9 (0.793)	9 (0.799)	8 (0.800)	8 (0.799)	8 (0.805)	8 (0.804)
		7	8 (0.809)	8 (0.797)	6 (0.796)	6 (0.796)	6 (0.794)	5 (0.795)
		10	6 (0.802)	6 (0.807)	5 (0.805)	5 (0.801)	4 (0.794)	5 (0.806)
	0.80	4	17 (0.805)	14 (0.793)	14 (0.794)	11 (0.804)	11 (0.797)	9 (0.792)
		5	11 (0.806)	11 (0.797)	9 (0.803)	8 (0.805)	9 (0.802)	8 (0.809)
		7	8 (0.797)	8 (0.808)	6 (0.792)	6 (0.793)	6 (0.800)	5 (0.794)
		10	6 (0.796)	6 (0.801)	5 (0.802)	5 (0.792)	5 (0.793)	5 (0.806)

Table 3. *Simulated sample size and power study based on MA1 and AR1 error models following W(1,1)*
distribution for α=0.05

			W(1,1)					
			MA1			AR1		
ϕ	ρ or θ	n	MS	P	GJ	MS	P	GJ
0.2	0.20	4	195 (0.803)	173 (0.793)	80 (0.796)	135 (0.799)	131 (0.801)	59 (0.798)
		5	135 (0.806)	131 (0.799)	68 (0.794)	153 (0.805)	153 (0.798)	68 (0.798)
		7	80 (0.791)	87 (0.803)	41 (0.793)	116 (0.806)	116 (0.802)	53 (0.793)
		10	53 (0.792)	47 (0.799)	32 (0.804)	60 (0.797)	60 (0.792)	35 (0.801)
	0.40	4	456 (0.793)	456 (0.802)	131 (0.806)	99 (0.794)	102 (0.808)	47 (0.802)
		5	405 (0.795)	386 (0.802)	102 (0.791)	401 (0.801)	405 (0.805)	87 (0.803)
		7	281 (0.799)	270 (0.795)	80 (0.795)	597 (0.794)	597 (0.793)	168 (0.802)
		10	132 (0.805)	135 (0.799)	51 (0.808)	339 (0.803)	339 (0.801)	120 (0.802)
	0.60	4	867 (0.803)	827 (0.807)	162 (0.796)	32 (0.797)	32 (0.807)	18 (0.803)
		5	591 (0.794)	608 (0.798)	113 (0.794)	87 (0.798)	87 (0.806)	36 (0.802)
		7	584 (0.802)	566 (0.796)	106 (0.792)	196 (0.799)	196 (0.796)	93 (0.799)
		10	249 (0.806)	249 (0.791)	77 (0.808)	138 (0.798)	138 (0.801)	63 (0.800)
	0.80	4	2228 (0.793)	2228 (0.792)	356 (0.806)	11 (0.807)	11 (0.797)	9 (0.798)
		5	734 (0.802)	699 (0.801)	131 (0.799)	14 (0.801)	14 (0.806)	9 (0.798)
		7	734 (0.793)	684 (0.796)	128 (0.804)	32 (0.804)	32 (0.793)	17 (0.800)
		10	239 (0.805)	230 (0.793)	77 (0.803)	17 (0.802)	17 (0.807)	8 (0.793)
0.3	0.20	4	41 (0.804)	36 (0.792)	24 (0.804)	27 (0.804)	27 (0.802)	17 (0.799)
		5	27 (0.803)	32 (0.806)	20 (0.804)	14 (0.801)	14 (0.804)	11 (0.803)
		7	20 (0.791)	21 (0.809)	14 (0.803)	21 (0.796)	24 (0.799)	14 (0.794)
		10	14 (0.808)	14 (0.809)	9 (0.807)	17 (0.808)	14 (0.794)	11 (0.800)
	0.40	4	53 (0.800)	51 (0.797)	32 (0.804)	27(0.802)	27 (0.807)	18 (0.800)
		5	41 (0.807)	41 (0.799)	21 (0.796)	41 (0.806)	36 (0.796)	21 (0.798)
		7	21 (0.802)	32 (0.793)	17 (0.795)	47 (0.803)	47 (0.797)	21 (0.804)
		10	14 (0.803)	21 (0.796)	14 (0.806)	36 (0.793)	36 (0.799)	18 (0.806)
	0.60	4	68 (0.800)	77 (0.804)	36 (0.804)	14 (0.805)	14 (0.801)	11 (0.806)
		5	47 (0.807)	47 (0.806)	27 (0.800)	20 (0.804)	21 (0.808)	11 (0.805)
		7	41 (0.804)	41 (0.792)	21 (0.796)	53 (0.8069	53 (0.796)	20 (0.798)
		10	27 (0.796)	27 (0.803)	14 (0.797)	135 (0.801)	135 (0.803)	27 (0.798)
	0.80	4	111 (0.802)	116 (0.806)	53 (0.791)	8 (0.793)	8 (0.804)	5 (0.799)
		5	60 (0.793)	60 (0.796)	32 (0.804)	8 (0.804)	8 (0.804)	5 (0.801)
		7	47 (0.809)	47 (0.792)	27 (0.808)	9 (0.800)	9 (0.804)	6 (0.792)
		10	32 (0.802)	32 (0.808)	17 (0.799)	27 (0.800)	27 (0.797)	11 (0.797)
0.4	0.20	4	18 (0.791)	18 (0.799)	14 (0.809)	17 (0.806)	17 (0.806)	11 (0.809)
		5	14 (0.807)	14 (0.804)	9 (0.793)	14 (0.808)	14 (0.808)	9 (0.794)
		7	9 (0.791)	9 (0.800)	6 (0.800)	11 (0.799)	11 (0.808)	6 (0.793)
		10	6 (0.800)	6 (0.791)	5 (0.804)	8 (0.806)	8 (0.809)	5 (0.796)
	0.40	4	21 (0.804)	21 (0.800)	14 (0.794)	14 (0.808)	14 (0.798)	9 (0.791)
		5	17 (0.807)	17 (0.800)	11 (0.798)	14 (0.801)	14 (0.798)	9 (0.795)
		7	11 (0.792)	11 (0.794)	8 (0.808)	14 (0.797)	14 (0.794)	8 (0.808)
		10	9 (0.804)	8 (0.792)	6 (0.806)	11 (0.798)	11 (0.792)	6 (0.798)
	0.60	4	27 (0.798)	27 (0.805)	15 (0.805)	8 (0.801)	8 (0.794)	5 (0.793)
		5	18 (0.791)	18 (0.799)	11 (0.798)	9 (0.805)	9 (0.808)	6 (0.806)
		7	14 (0.808)	14 (0.797)	9 (0.803)	14 (0.796)	14 (0.802)	8 (0.804)
		10	11 (0.809)	11 (0.806)	6 (0.792)	17 (0.797)	18 (0.796)	8 (0.807)
	0.80	4	36 (0.792)	36 (0.800)	24 (0.808)	6 (0.802)	6 (0.803)	5 (0.794)
		5	24 (0.805)	24 (0.800)	14 (0.807)	6 (0.800)	6 (0.798)	5 (0.799)
		7	17 (0.799)	17 (0.799)	11 (0.808)	5 (0.803)	5 (0.802)	3 (0.792)
		10	11 (0.808)	11 (0.792)	8 (0.804)	9 (0.799)	9 (0.803)	5 (0.808)

As can be seen in Table 2, the *GJ* test provides the smallest sample size even with small *n*. Additionally, for each ϕ and fixed correlation coefficient of either AR1 or MA1 structure, when *n* increases, sample sizes required to obtain 80% decreases for each test. It can be also seen that for each ϕ, sample size of each test under AR1 structure is smaller than sample size estimated under MA1 structure, when ρ or θ is greater than 0.40 for fixed values of *n*. In some simulation combinations, sample sizes are found to be same for the *MS* and *P* tests. When error terms have AR1 or MA1 structure, as *n* increases, sample size required to obtain at least 80% power of each test decreases for fixed ρ or θ. Additionally, for fixed *n* and ρ or θ, sample sizes estimated by AR1 error model are much smaller. For all combinations, the sample size of the *GJ* test is smaller than that of other tests. Figure 2 displays the plots of sample sizes required to obtain 80% power of the tests, when error terms have AR1 or MA1 structure and follows L(0,1) distribution.
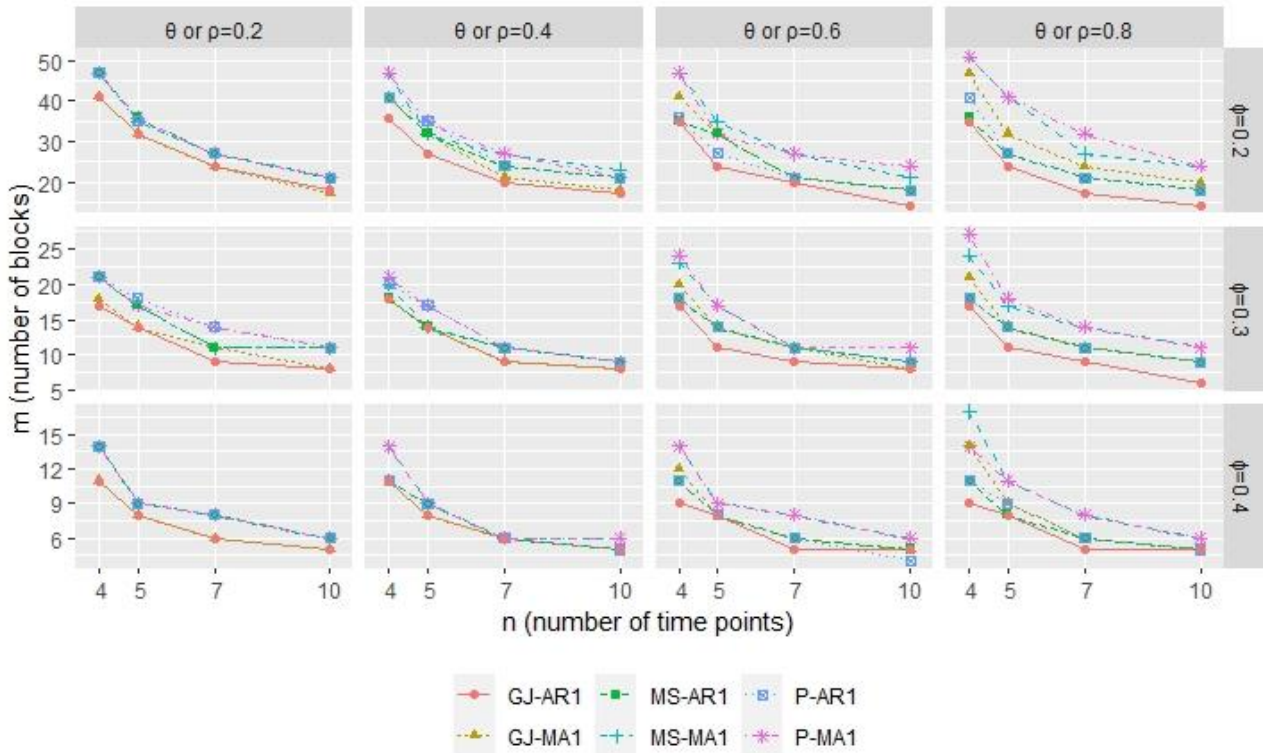
Figure 2. *Sample size (number of blocks) required to obtain 80% power curves of the MS, P and GJ tests for longitudinal data, when errors are autocorrelated in MA1 or AR1 structures and distributed in L(0,1) (α =0.05)*

Table 3 presents sample sizes for the *P*, *GJ* and *MS* tests required to obtain 80% power under the MA1 and AR1 models with white noise terms following Weibull distribution. The results of simulations under Weibull distribution are not completely similar with those under the Laplace distribution. For ρ from 0.4 to 0.8, as *n* increases from 4 to 7, sample sizes of all tests increase. Under AR1 structure, for all ρ, sample sizes for *n* = 10 are smaller than those for *n* = 7. On the other hand, when errors terms have MA1 structure, for all θ, as *n* increases from 4 to 10, sample size decreases. Also, sample sizes of the all tests under MA1 error model are larger than those provided under AR1 error model for Weibull distribution. The greatest sample size in this simulation study is obtained for θ = 0.80, *n* = 4 and ϕ = 0.2, when errors terms have MA1 model with white noise terms following W(1,1) distribution. The sample size of the *GJ* test has been observed to be the smallest in comparison to the other two tests. The smallest sample sizes for each combination of *n*, ϕ and ρ or θ are obtained by the *GJ* test. Usually, sample sizes of the *MS* and *P* tests are same. Figure 3 represents estimated sample sizes to obtain 80% power for the tests in RCBDs with longitudinal data, when error terms have either MA1 or AR1 model with W(1,1) distributed white noise terms.
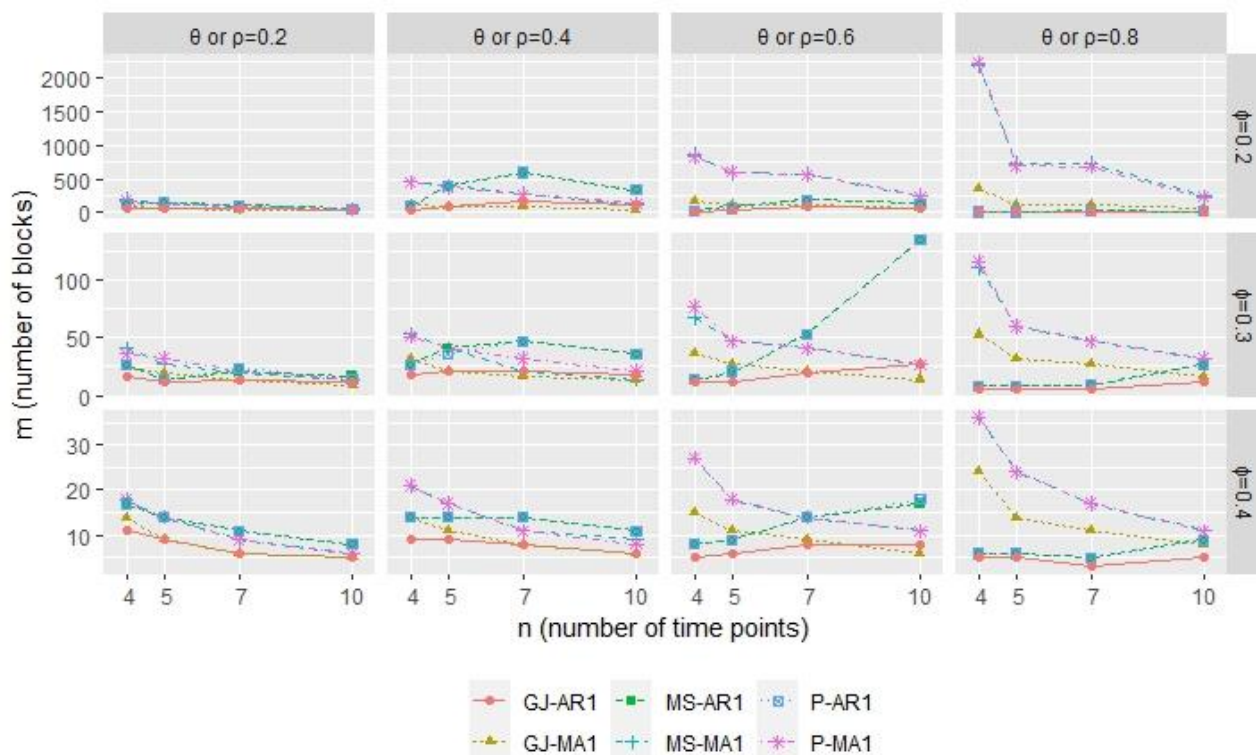
Figure 3. *Sample size (number of blocks) required to obtain 80% power curves of the MS, P and GJ tests for longitudinal data, when errors are autocorrelated in MA1 or AR1 structures and distributed in W(1,1)*
(α=0.05)

4. DATA EXAMPLE

Data set in (Zhang & Cabilio, 2012) is taken into consideration to estimate sample sizes required to obtain 80% power of the *MS*, *P* and *GJ* tests for analyzing longitudinal data in RCBDs. This data set from a self-report survey was containing the total scores (0 (worst)-100 (best)) of pain, stiffness, and disability scores for each knee using the Western Ontario and McMasters Osteoarthritis Index (WOMAC). The longitudinal data set analyzed in (Zhang & Cabilio, 2012) includes 88 participants ($b = 88$) who have no missing pain records at the baseline and three 12-month interval visits ($n = 4$). They were concerned with changes of the total score over time in order to illustrate the implementation of the *GJ* test. The total WOMAC scores are appeared to be L-shaped with a long tail to the right and a declining trend in terms of medians for the left knee. Zhang and Cabilio (2012) analyzed these scores assuming AR(1) error terms with $\rho = 0.5$ and standard normal white noise. Here, the data are investigated for the *MS*, *P* and *GJ* tests for the AR(1) error model with white noise terms following W(1,1) and $\rho = 0.5$. At α = 0.05, sample sizes required for 80% power of the *MS*, *P* and *GJ* test statistics based on 10 000 MC simulations are estimated as 60 (0.806), 59 (0.7983) and 36 (0.8053), respectively.

5. DISCUSSION AND CONCLUSION

In the case of independent error terms, the distribution of the *GJ* statistics developed for RCBDs only depends on *n* and *b* and has an asymptotic normal distribution (Zhang & Cabilio, 2012). The expected values and variances of nonparametric tests depend on the error model parameters and distribution. Even if the parameters and distributions of the error terms are known, it is quite difficult to determine the asymptotic distributions of nonparametric tests, especially in the case of a dependent response variable. Therefore, it is almost impossible to obtain the exact formulas for the power and sample size of these tests. In this case, it will be inevitable for practitioners to estimate the power and sample size with simulation-based methods. This study is the first study in the literature that estimates the number of experimental units, that is, the number of blocks, which should be included in a research in an increasing or decreasing order for nonparametric tests to reach 0.80 power for testing the ordered alternatives hypothesis in the case of longitudinal data in two-way ANOVA form of

RCBDs. This study shows that, in the autocorrelated error models for RCBDs with longitudinal data, the number of blocks, i.e. sample size of subjects depends on the number of time points, the magnitude of autocorrelation coefficient, the slope term of the linear model and the distribution of errors. The fewer experimental units involved in clinical trials, the less costly it is, so choosing the trend test that requires a small sample size is very important. Monte Carlo simulations are conducted in this paper, because asymptotic distributions of tests are not known due to non-normal distributions and auto correlated error, even when the error term model is known. The sample size performance of nonparametric tests under various non-normal distributions is examined through an extensive simulation study in this paper. It is assumed that the error terms form either a stationary AR1 or MA1 model with independent white noise terms from Laplace or Weibull distribution. However, all simulations based on the fact that blocks are independent. The main purpose of this study is to investigate how sample size is affected by the distributions of errors and blocks, autocorrelation structure and the magnitude of trend in RCBDs with longitudinal data. The sample sizes for the *P*, *GJ* and *MS* tests under each non-normal distribution assuming that each subject has the same autocorrelation structure over time/ treatment were estimated by Monte Carlo simulations. When the error distribution follows laplace or weibull distributions under AR1 or MA1 correlation structures, the required sample size of GJ test is smaller than the required sample size of MS and Page tests in this study. For fixed ϕ and the coefficient parameter θ in the MA1 error model, as the number of time points n increases, sample size appears to be decreasing for each test under both non-normal error distributions. However, under Weibull distribution, when errors are autocorrelated in AR1 model, as n increases, sample sizes of all tests are increasing. For fixed n and ϕ, when the coefficient parameter ρ in the AR1 model approaches to 1, even for large n, sample size required for 80% power values of the *P*, *GJ* and *MS* tests appears to be decreasing under both distributions. However, for fixed n and ϕ, when the coefficient parameter θ in the MA1 model approaches to 1, sample sizes of the *P*, *GJ* and *MS* tests appears to be increasing under both distributions. In the light of simulation results, it can be seen that for RCBDs with longitudinal data, sample size of subjects is closely associated with the underlying error model, the values of its parameters, the distribution of data and the direction of time, all of which are unknown in practice. In comparison of sample sizes in terms of error distributions, for all combinations of correlation coefficient, number of time points and direction of time, the sample sizes estimated under Weibull distribution are much greater than those under Laplace distribution. Under Laplace distribution of errors, the more time points involved in the study and the larger correlation coefficient, the smaller sample size tends to be. The *MS*, *P* and *GJ* tests depend on the error distribution, the error correlation model and the direction of time/treatments. As a future study, the performance of alternative Page tests can be investigated in terms of sample size requirements for a target power in a Monte Carlo simulation study. In conclusion, we provide a simulation-based tool for situations in which the response variable is correlated within/ blocks and for which the accuracy of normal approximations is not sufficient in RCBDs.

CONFLICTS OF INTEREST

No conflict of interest was declared by the authors.

REFERENCES

Akdur, H. T. K., Ozonur, D., Gul, H. H., & Bayrak, H. (2019). Comparison of rank-based tests for ordered alternative hypotheses in randomized complete block designs. *Gazi University Journal of Science*, *32*(2)*,* 705-716.

Akdur, H. T. K. (2020). Comparison of non-parametric tests of ordered alternatives for repeated measures in randomized blocks. *Communications in Statistics - Simulation and Computation*, *51*(7), 4146-4158. doi:10.1080/03610918.2020.1740262

Aslan, E., Koskan, O., & Altay, Y. (2021). Determination of the Sample Size on Different Independent K Group Comparisons by Power Analysis. *Turkish Journal of Agricultural Research, 8*(1), 34-41. doi:10.19159/tutad.792694

Best, D. J., & Rayner, J. C. W. (2015). An alternative to page's test permitting both tied and missing data. *Journal of Statistical Theory and Practice*, *9*(3), 524-536. doi:10.1080/15598608.2014.940098

Dmitrienko, A., Chuang-Stein, C., & D'Agostino Sr, R. B. (2007). *Pharmaceutical statistics using SAS: a practical guide*. SAS Institute.

Hollander, M. (1967). Rank tests for randomized blocks when the alternatives have an a priori ordering. *Annals of the Institute of Statistical Mathematics*, *38*(3), 867-877. doi:10.1214/aoms/1177698880

Kendall, M. G. (1938). A new measure of rank correlation. *Biometrika*, *30*(1/2), 81-93. doi:10.2307/2332226

Page, E. B. (1963). Ordered hypotheses for multiple treatments: a significance test for linear ranks. *Journal of the American Statistical Association*, *58*(301), 216-230. doi:10.1080/01621459.1963.10500843

Shan, G., Young, D., & Kang, L. (2014). A new powerful nonparametric rank test for ordered alternative problem. *PloS one*, *9*(11), e112924. doi:10.1371/journal.pone.0112924

Serdar, C. C., Cihan, M., Yücel, D., & Serdar, M. A. (2021). Sample size, power and effect size revisited: simplified and practical approaches in pre-clinical, clinical and laboratory studies. *Biochemia Medica*, *31*(1), 27-53. doi:10.11613/bm.2021.010502

Skillings, J. H., & Wolfe, D. A. (1978). Distribution-free tests for ordered alternatives in a randomized block design. *Journal of the American Statistical Association*, *73*(362), 427-431. doi:10.1080/01621459.1978.10481595

Thas, O., Best, D. J., & Rayner, J. C. W. (2012). Using orthogonal trend contrasts for testing ranked data with ordered alternatives. *Statistica Neerlandica*, *66*(4), 452-471. doi:10.1111/j.1467-9574.2012.00525.x

Unalan, A. (2021). Sample Size in Clinical Researches: Power of the Test and Effect Size. *Black Sea Journal of Health Science*, *4*(3), 221-227. doi:10.19127/bshealthscience.866556

Zhang, Y., & Cabilio, P. (2012). A generalized Jonckheere test against ordered alternatives for repeated measures in randomized blocks. *Statistics in Medicine*, *32*(10), *Special Issue*, 1635-1645. doi:10.1002/sim.5606

Machine Learning Techniques for the Classification of IoT-Enabled Smart Irrigation Data for Agricultural Purposes

Aamo IORLIAM[1*] (iD) Sylvester BUM[2] (iD) Iember S. AONDOAKAA[3] (iD) Iveren Blessing IORLIAM[4] (iD) Yahaya SHEHU[5] (iD)

[1,4]Centre for Food Technology and Research, BSU, Makurdi, Nigeria
[1,2,3]Department of Mathematics & Computer Science, BSU, Makurdi, Nigeria
[5]Shehu Shagari College of Education, Sokoto, Nigeria

Keywords	Abstract
IoT Agriculture Smart Irrigation Machine Learning Techniques	To support farming year-round, a variety of smart IoT irrigation devices have recently been developed. It is crucial to forecast the soil moisture of agricultural farms so as to produce high yields since the high yields depends on the efficiency of water supply on farmlands. In smart irrigation, anytime water is needed on the farms, the smart pumps switch on to pump the required water so as to prevent the crops from drying up. The smart pumps also shut down if the farms have the ideal level of soil moisture, preventing over-flooding of the fields. Data is generated when the smart pumps are ON or OFF at any given time. Therefore, it is crucial to classify the data produced by smart IoT-enabled irrigation devices when these devices are ON or OFF. In this paper, the soil moisture, temperature, humidity, and time are used as inputs into machine learning techniques for classification. These machine learning techniques include logistic regression, random forest, support vector machine, and convolutional neural network. According to experimental findings, the accuracy of the logistic regression was 71.76%, that of the random forest was 99.98%, that of the support vector machine was 90.21%, and that of the convolutional neural network was 98.23. Based on the high accuracy that the random forest attained, it has more potential to help in assessing smart irrigation conditions (wet or dry) in an optimized manner.

1. INTRODUCTION

Crop growth is now severely hampered by the relative scarcity of water brought on by drought or insufficient rainfall throughout the world (Goap et al., 2018). Irrigation is the process of delivering the necessary amount of water to plants at predetermined intervals. It is necessary for both farming and raising agricultural output and it has historically been the solution to the problem of water scarcity on farms (Surendran et al., 2015). Prior to today, farms have relied on conventional irrigation techniques including furrow irrigation, check basin irrigation, strip irrigation, and basin irrigation to lessen the impact of water scarcity. To irrigate crops, traditional irrigation techniques included buckets, pumps, canals, and watering cans. This approach frequently requires a lot of labor to convey water to the roots of the plants (Janani & Jebakumar, 2019).

Research has produced better irrigation techniques known as "smart irrigation" using the Internet of Things (IoT) to control water scarcity on farms. Utilizing sprinklers, pipes, ditches, and other similar equipment, smart irrigation distributes a controlled amount of water at the proper moment (Adam et al., 2020). This aims to increase crop yields while conserving water and money (Iorliam et al., 2021). Smart irrigation systems that use machine learning are more accurate at estimating how much water plants need (Çetin & Beyhan, 2022). In order to successfully address the issue of inadequate or excessive irrigation, these machine learning techniques

consider agricultural parameters to effectively curtail the issue of under or over irrigation (Çetin & Beyhan, 2022). Different machine learning techniques have been created or adopted by researchers in order to create smart irrigation systems that make use of wireless sensor networks, big data, cloud computing, and the internet of things in order to efficiently manage the water requirements of crops on smart farms (Sanjeevi et al., 2020).

In order to replicate human behaviors and make informed choices, decision-support tools have used irrigation data from human specialists to comprehend the scheduling patterns of irrigation systems (Pluchinotta et al., 2018). These tools continuously learn from their experiences and improve their performances. For the goal of smart irrigation management, machine learning methods such as artificial neural networks, support vector regressions, decision trees, random forests, and naive bayes have been applied (Goap et al., 2018; Romero et al., 2018; Nawandar & Satpute, 2019). By utilizing computational tools to learn from irrigation data, these machine learning algorithms or techniques play significant roles in smart irrigation systems. The main goal of this learning process is to train IoT-enabled data in order to carry out smart irrigation operations (Janani & Jebakumar, 2019). The collection of the training data is determined by some features, which may be binary, nominal, or numeric (Janani & Jebakumar, 2019). Therefore, to classify IoT-generated data from smart irrigation systems, this research uses machine learning techniques such as logistic regression (LR), random forest (RF), support vector machine (SVM), and convolutional neural network (CNN) algorithms. In order to identify when the IoT-enabled device is malfunctioning, under attack from malware, or has the potential to destroy farms that they are supposed to properly irrigate for the effective and efficient growth of crops, it is crucial to classify the IoT-generated data from smart irrigation based on whether it is ON or OFF. Therefore, the inability of machine learning techniques to classify the data produced by these devices could indicate that they are unsuitable for use in smart irrigation. Four algorithms (LR, RF, SVM, and CNN) were selected for this study because they are the machine learning techniques that have been used the most frequently in the literature (Torres-Sanchez et al., 2020; Dhasaradhan et al., 2021). We evaluated our proposed approach using datasets from Mittal (2020).

2. RELATED WORKS

Automation technology is being used in agriculture more often to reduce costs and increase yields. Automation of irrigation systems is essential for controlling water and electricity usage in rice cultivation while preserving grain quality. To develop a rice irrigation system, Pfitscher et al. (2011) utilized wireless connectivity and Supervisory Control and Data Acquisition (SCADA). It demonstrated a completely automated irrigation system for rice. They used an ultrasonic sensor to monitor and control crop water levels, and a GPRS communication system to enable system remote control. Both water and power can be supplied by this gadget. By using soil moisture to determine when to turn ON or OFF the irrigation system, Tyagi et al. (2017) created an automated smart irrigation system. The developed system has benefits including minimal human intervention, great affordability, and simplicity of deployment (Tyagi et al., 2017).

On the basis of precise real-time farm data, Gondchawar and Kawitkar (2016) proposed a smart irrigation system with certain sensor modules for measuring light, soil moisture, humidity, and temperature. Furthermore, an automated watering system was developed by Shekhar et al. (2017) using Raspberry Pi 3 and Arduino Uno integrated electronics that are inexpensive. Shekhar et al. (2017) developed an intelligent IoT-based system that records and analyzes sensor data related to soil moisture and temperature for irrigation forecasting. This is an entirely automated system that uses irrigation intelligence and interacts with other devices. The Raspberry Pi 3 edge level processor receives the sensor data serially and employs the K-NN machine learning method to make an estimation of the soil quality based on a training set of data. In a direct connection to smart farming, several academics have argued for scalable network designs for managing and monitoring farms in rural areas (Monaco et al., 2016). Such systems enhance communication by utilizing technologies like the cross-layer-based channel access and routing solution for sensing and actuation to improve coverage range, throughput, and latency (Dholu & Ghodinde, 2018).

Reviewing the viability of using several proposed/developed automatic irrigation systems for rice irrigation were Kumar et al. (2018). The researchers chose rice because it requires a lot of water and is frequently produced underwater. According to the study, an autonomous irrigation system can make use of several cutting-edge irrigation approaches, including time-based systems, volume-based systems, real-time feedback

mechanisms, and computer-based irrigation control systems (Kumar et al., 2018). A comprehensive IoT irrigation design was put up by Fernández-Ahumada et al. (2019) for the automation of irrigation networks for agricultural use. The developed system has shown to be extremely reliable and stable. A recent proposal for the detection and classification of intrusions on networks created and utilized for agricultural purposes was made by Raghuvanshi et al. (2022). For the purpose of classifying preprocessed data such as NSL, KDD, and NSL-KDD, they used machine learning techniques. These datasets are not generated by IoT smart irrigation systems, even though they are used for anomaly detection.

Iorliam et al. (2020) proposed a unique approach based on artificial neural networks for classifying soil data from IoT-enabled soil nutrients. Between 81.33% and 97.13% of accuracy was attained by their proposed approach. For the effective irrigation of crop areas, Roy et al. (2020) created an IoT automatic and manual irrigation system. Their research revealed that the AgriSens technology they developed increased crop output by 10.21% (Roy et al., 2020). Roy et al. (2020) proposed that in the future, machine learning should be used to analyze how factors like wind, humidity, temperature, and UV rays affect crop yields. Neforawati et al. (2019) classified the Paddy growth stage into seeding, transplanting, flowering, and maturity using CNN and found that their classifications had an overall accuracy of 82%. Also, Nindam et al. (2019) classified normal and abnormal Jasmine rice germination using CNN. According to experimental findings, their suggested method had a validation accuracy of 96.43%. Inspired by Iorliam et al. (2020), Roy et al. (2020), Neforawati et al. (2019) and Nindam et al. (2019), the researchers proposed using machine learning methods such as LR, RF, SVM, and CNN for the classification of IoT-enabled data generated while the smart irrigation devices are either ON or OFF.

3. PROPOSED METHOD

3.1. Dataset Description and Pre-Processing

As pointed out by Cheng et al. (2022), there is a general lack of public labelled IoT smart irrigation datasets for performing supervised learning experiments. This experiment therefore used publicly available data from Mittal (2020), which includes features like soil moisture (SM), temperature (T), humidity (H), and time (t). The algorithms employed in this experiment use each of these features as an input. The status column's "ON" or "OFF" values acted as class labels (ON = 1, OFF = 0).

The Kaggle dataset used to produce the smart irrigation IoT dataset is available at: http://autoirrigationdataforricecrop.herokuapp.com/. It is critical to classify the secondary data produced by IoT smart irrigation devices since it may include extremely intriguing statistical information that can characterize the device whether it is ON or OFF. Failure to classify these data points could indicate that the designed smart irrigation pump is failing or has been compromised by malware. Figure 1 displays the input data we used for this experiment, which includes columns for soil moisture (column A), temperature (column B), humidity (column C), time (column D), and status (column E).

	A	B	C	D	E
1	Soil Moisture	Temperature	Humidity	Time	Status
2	54	22	70	21	ON
3	12	20	40	104	OFF
4	34	26	35	62	ON
5	7	44	44	93	OFF
6	50	38	23	92	OFF
7	4	26	52	6	ON
8	15	34	58	82	ON
9	45	30	43	85	ON
10	47	4	42	2	OFF
11	19	41	22	0	ON
12	63	44	65	75	ON
13	88	34	41	71	ON
14	39	20	70	82	ON
15	65	43	44	93	OFF

***Figure 1.** Input Data*

Machine learning algorithms (LR, RF, SVM, and CNN) were utilized to analyze and categorize the smart irrigation dataset based on the device status (ON = 1, OFF = 0). There are 100,000 samples in the overall dataset. 70% of the dataset is used for training, while 30% is used for testing. In a Google Colaboratory, Python is utilized for programming. The "dropna ()" method in Python is used to remove any rows with NULL values during data pre-processing.

3.2. Methodology

The proposed model gathers raw data from smart irrigation systems, pre-processes it to extract SM, T, H, and t, and then uses this processed data as input into four separate algorithms (LR, RF, SVM, CNN). The outcomes of these algorithms' classifications are subsequently produced as confusion matrices. Figure 2 summarizes the proposed model's functionality as a whole.
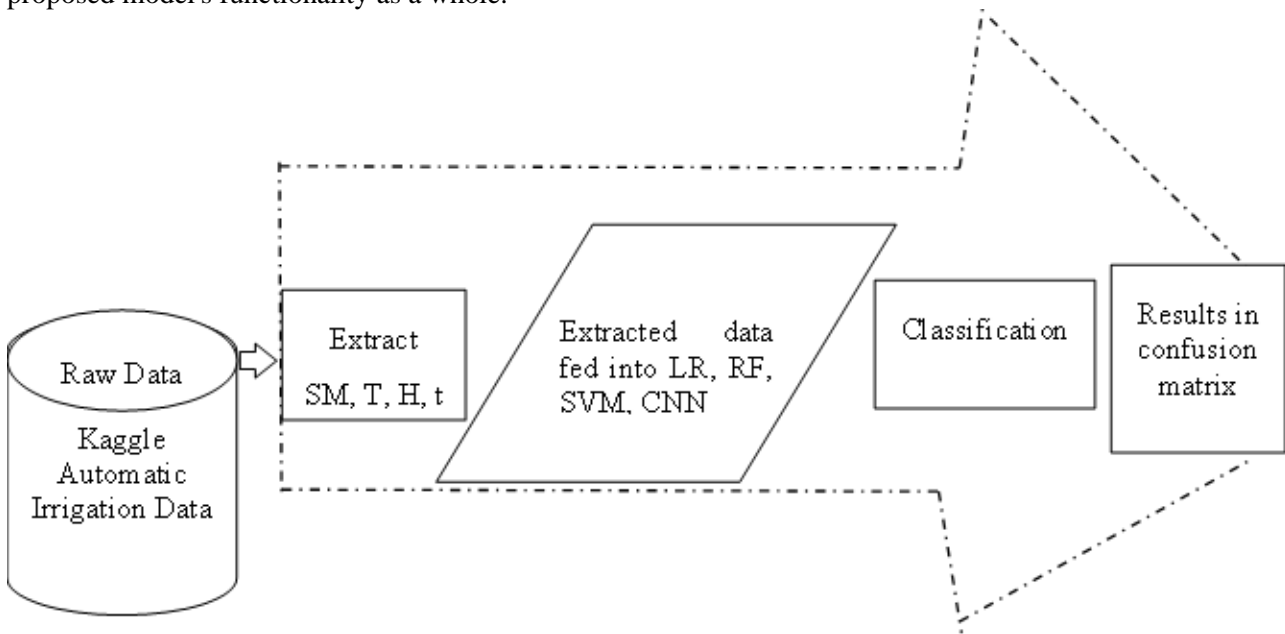
Figure 2. Machine Learning Techniques for Classification of IOT-Enabled Smart Irrigation

The following is a description of the machine learning techniques used in this paper:

i. Logistic regression (LR)

In this instance, the LR is used to classify data that is generated depending on whether the smart irrigation equipment is turned "ON" or "OFF." Since the LR technique uses supervised learning, labels are given for "ON = 1" and "OFF = 0". Either our dependent or target class is "ON" or it is "OFF." The variables that are independent are SM, T, H, and t.

Taking π as the probability of the event occurring, the LR model is therefore represented as:

$$\pi = P(Y = 1|X_1 \ldots X_n = x_n) \tag{1}$$

$$= \frac{1}{1 + e^2} \tag{2}$$

where $z = \beta_0 + \beta_1 x_1 + \cdots + \beta_n x_n$

and $\beta_0, \beta_1 \ldots \beta_n$ are model parameters (estimators).

In our case, Y represents the outcome of our prediction (ON or OFF). $X_1, X_2, \ldots, X_n$ are a set of n explanatory variables (SM, T, H, and t) (Bhowmik et al., 2011).

ii. Random forest (RF)

The RF has shown to improve the prediction performance of decision tree classifiers and controls over-fitting. As a result, it is chosen for the classification of data produced by smart irrigation devices.

The number of trees chosen for the forest (n-estimators) in our experiment was set to default = 100. The RF formula utilized for the classification task is based on the Gini index, which is mathematically stated as:

$$\text{Gini Index} = 1 - \sum_{k=1}^{n} (P_k)^2 \tag{3}$$

where P_k = the probability of an object being classified to a particular class (class 1 = "ON", or class 0 = "OFF") in the dataset

n = number of classes (2, ON or OFF) (Qi, 2012).

iii. Support vector machine (SVM)

Both separable and non-separable instances can be handled by the linear SVM. In our case, the radial basis function, or "RBF," was employed as the default kernel.

The following illustration shows a two-dimensional data set that can be divided along a line:

$$y = ax + b \tag{4}$$

if $y = x_2$, and $x = x_1$, the we get:

$$ax_1 - x_2 + b = 0 \tag{5}$$

When $x = (x_1, x_2), and\ w = (a, -1)$

We therefore get:

$$w * x_i + b = 0 \tag{6}$$

Based on the hyperplane, we can make predictions using the hypothesis function (h), defined as:

$$h(x_i) = \begin{cases} +1, & if\ w * x_i + b \geq 0 \\ -1, & if\ w * x_i + b < 0 \end{cases} \tag{7}$$

Therefore, any point above the hyperplane will be classified as +1 class, whereas any point below the hyperplane will be considered as -1 class (Fan, 2018).

iv. Convolutional Neural Network (CNN)

The CNN (Krizhevsky et al., 2017) is used in this paper since it has been demonstrated in literature to be one of the most often used artificial neural networks. The objective of this experiment is to use CNN to categorize IoT-smart irrigation data according to whether the device is "ON" or "OFF." The first class is denoted by the number 1 for "ON," and the second class, "class 0," is denoted by the number 0 for "OFF." The following steps illustrate the CNN setup used in this paper:

1. The dataset described in 3.1 is used
2. The sequential model "sequential ( )" is used as the first layer due to the fact that we are using linear stack of layers
3. Our model added the first hidden layer with 4 input parameters, and 480 neurons. The rectified linear activation function (ReLu) is first chosen due to its ability to achieve higher performance
4. Additional two dense layers are added with 240, and 120 neurons, respectively
5. Our model is ended with a dense layer, no activation, and a sigmoid activation function. The sigmoid activation function is chosen because we are considering a binary classification (ON or OFF) and the sigmoid activation function best fits our case in order to acquire our score
6. Our compiled model is done using the binary crossentropy, the Adam optimizer, and accuracy.
7. The training data of X, training data of Y are fit to our model using 1000 epochs, and a batch size of 128. The test data of X, and test data of Y are validated as well using the same epochs and batch size.

Based on the above setup, the results achieved are presented in Section 4 D.

3.3. Evaluation Metrics

To evaluate the proposed approach, the following evaluation measures are used:

i. **Accuracy**: Expressed mathematically as:

$$\text{Accuracy} = \frac{(TP + TN)}{(TP + TN + FP + FN)} \tag{8}$$

ii. **Precision**: Expressed mathematically as:

$$\text{Precision} = \frac{(TP)}{(TP + FP)} \tag{9}$$

iii. **Recall**: Expressed mathematically as:

$$\text{Recall} = \frac{(TP)}{(TP + FN)} \tag{10}$$

iv. **F1-Score**: Expressed mathematically expressed as:

$$F1 - \text{Score} = \frac{(2 \text{ x Precision x Recall})}{(\text{Precision} + \text{Recall})} \tag{11}$$

where:

True Positive (TP): The outcome of the developed model correctly predicts the positive class.

True Negative (TN): The outcome where the negative class is correctly predicted by the developed model.

False Positive (FP): The outcome where the positive class is incorrectly predicted by the developed model.

False Negative (FN): The outcome where the negative class is incorrectly predicted by the developed model.

4. RESULTS AND DISCUSSIONS

To classify data from IoT-enabled smart irrigation devices, four algorithms were used (LR, RF, SVM, and CNN). Based on the information produced by the IoT smart irrigation system, the machine learning algorithms were able to divide the dataset into two classes. Class 0 (information while the smart irrigation pump is off)

384

Aamo IORLIAM, Sylvester BUM, Iember S. AONDOAKAA, Iveren Blessing IORLIAM, Yahaya SHEHU
GU J Sci, Part A, 9(4): 378-391 (2022)

and Class 1 (data when the smart irrigation pump is ON). The data (100,000 rows) are divided at random into 70% training and 30% testing, with the results displayed and discussed in 4 A–D.

A. Performance of Logistic Regression

The pre-processed IoT-enabled smart irrigation data given in 3.1 are supplied into the LR algorithm. As can be seen in Figure 3, the logistic regression technique achieved 71.76% accuracy, 0.7155 F1 score, 0.7303 precision value, and 0.7501 recall, respectively.

```
***LOGISTIC REGRESSION RESULTS***
Accuracy: 71.76%
F1 Score: 0.715479
Precision:  0.7302731181493369
Recall:  0.7500777508241587
```

Figure 3. Results of Logistic Regression

Again, Figure 4 shows the result of the confusion matrix for the LR algorithm. The LR algorithm correctly classified 9469 as class 0 (OFF) and wrongly classified 4454 samples of class 0 as class 1 (ON). Furthermore, the LR algorithm correctly classified 12059 samples of class 1 (ON), and wrongly classified 4018 samples of class 1 as class 0 (OFF).
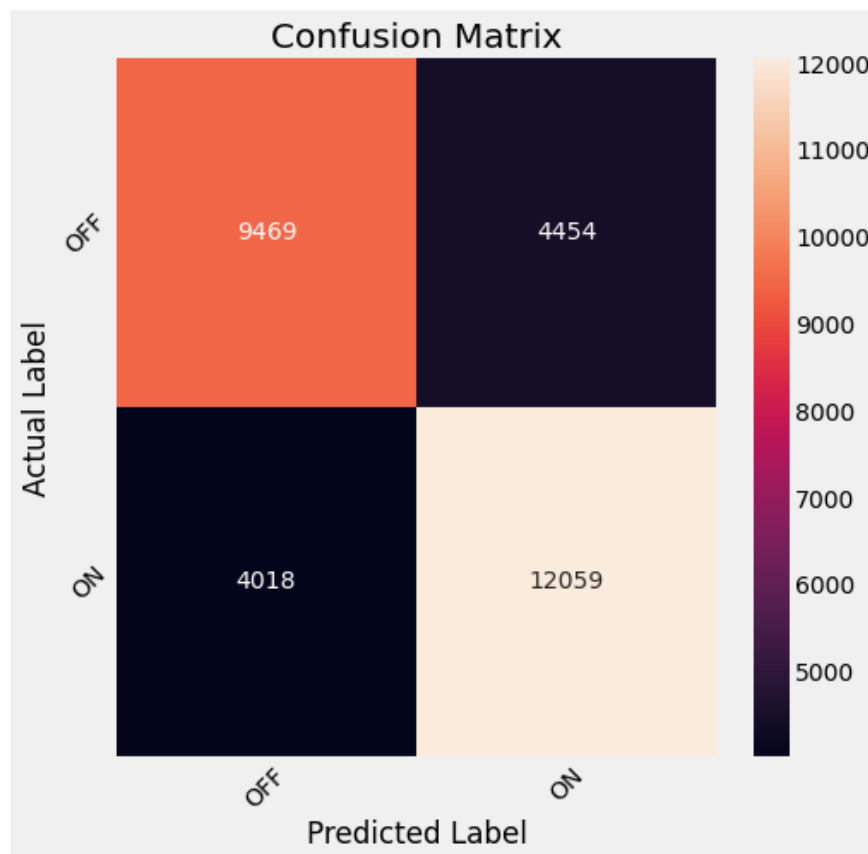
Figure 4. Confusion Matrix for Logistic Regression

Recent research by Raghuvanshi et al. (2022) showed that the LR's classification accuracy on intrusion detection datasets like NSL, KDD, and NSL-KDD was less than 78%. Our classification accuracy using LR on a realistic smart irrigation dataset is 71.76%, which is quite similar to the outcome in Raghuvanshi et al. (2022).

B. Performance of Random Forest

As can be observed in Figure 5, the Random Forest (RF) algorithm achieved 99.98%, 0.9998, 0.9996, and 0.9999 for the Accuracy, F1 score, Precision value, and Recall, respectively.

```
***RANDOM FOREST RESULTS***
Accuracy: 99.98%
F1 Score: 0.999765
Precision:  0.9996269120756125
Recall:  0.9999377993406731
```

Figure 5. *Results for Random Forest*

The RF's confusion matrix shows that the algorithm correctly classified 13917 as class 0 (OFF) and wrongly classified 6 samples of class 0 as class 1 (ON). Furthermore, the RF algorithm correctly classified 16076 samples of class 1 (ON), and wrongly classified only 1 sample of class 1 as class 0 (OFF) as seen in Figure 6.
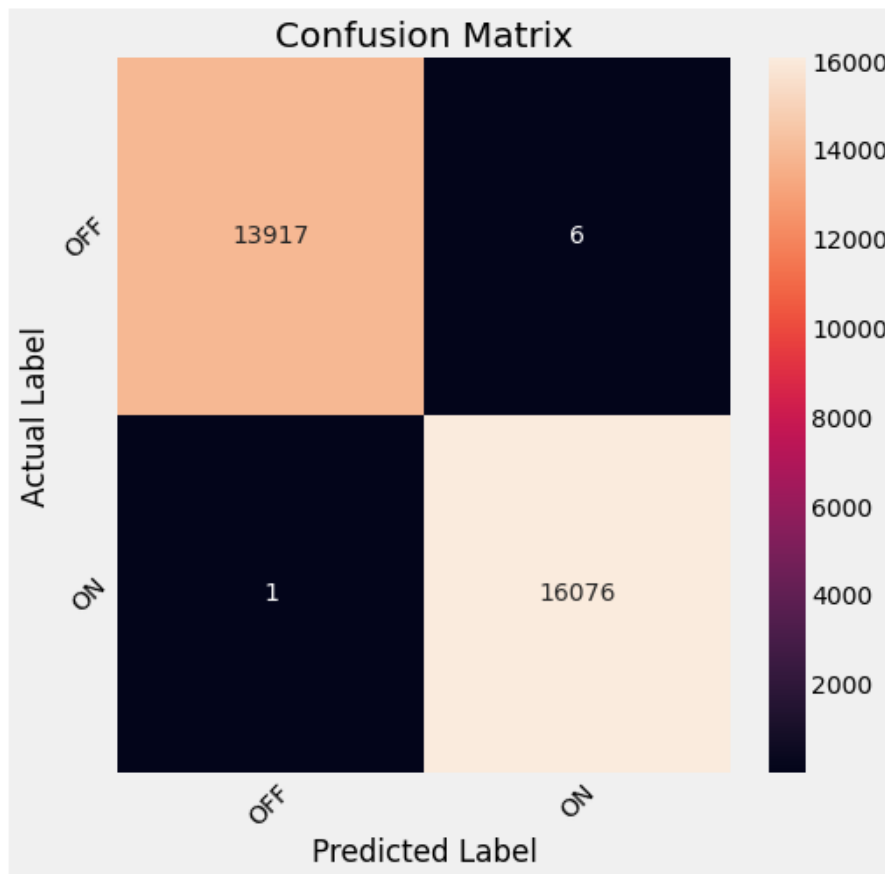
Figure 6. *Confusion Matrix for Random Forest*

This shows that the RF algorithm accurately classified data generated by IOT smart irrigation device up to 99.98%. Our accuracy outperformed that of Raghuvanshi et al. (2022), when they used the RF algorithm on intrusion detection datasets such as NSL, KDD, and NSL-KDD and achieved an accuracy of less than 78% (Raghuvanshi et al., 2022). Moreover, our accuracy also outperformed that of Ok et al. (2012) when they utilized the random forest algorithm for agricultural crop classification and achieved an accuracy of 85.89%.

C. Performance of Support Vector Machine

As shown in Figure 7, the Support Vector Machine (SVM) algorithm achieved 90.21% Accuracy, 0.9014 F1 scores, 0.9019 Precision value, and 0.9170 Recall.

```
***SVM RESULTS***
Accuracy: 90.21%
F1 Score: 0.901423
Precision:  0.9018780204318835
Recall:  0.9170243204577968
```

Figure 7. *Support Vector Machine Results*

Again, the confusion matrix for the SVM shows that it correctly classified 12319 samples as class 0 (OFF) and wrongly classified 1604 samples of class 0 as class 1 (ON). Furthermore, the SVM algorithm correctly classified 14743 samples of class 1 (ON), and wrongly classified 1334 samples of class 1 as class 0 (OFF) as seen in Figure 8.
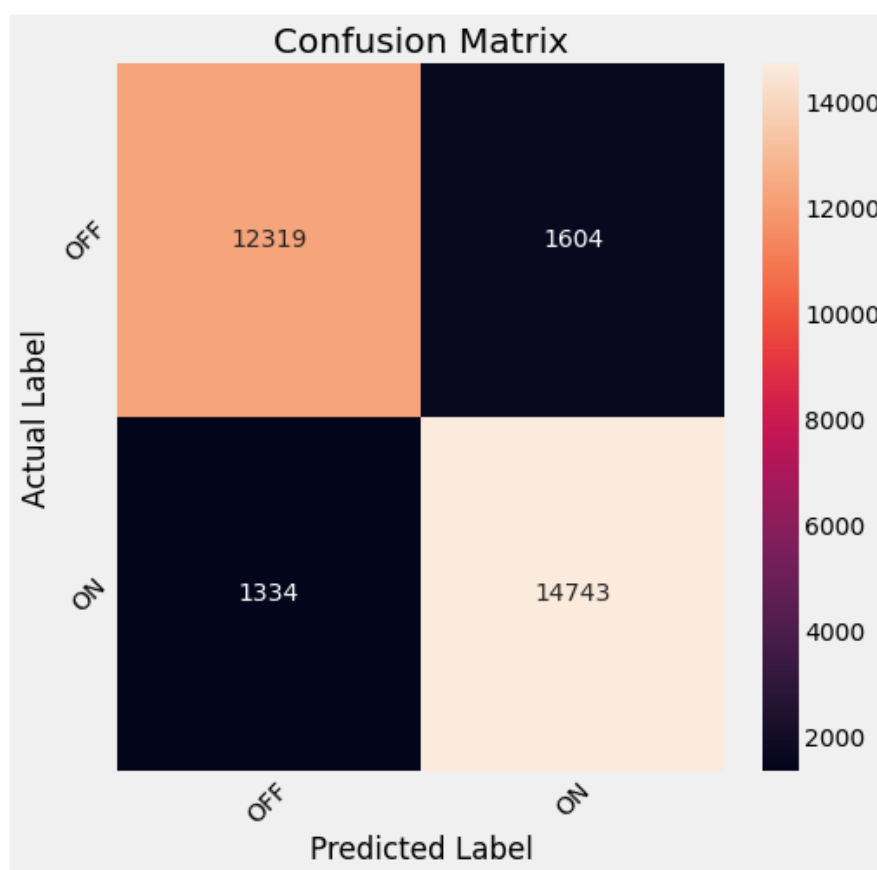
Figure 8. *Confusion Matrix for Support Vector Machine*

This further proves that our proposed method can effectively be applicable for the separability of smart irrigation IoT data using SVM with a high accuracy of 90.21%. Our proposed method performs a bit lesser as compared to Raghuvanshi et al. (2022), when they used the SVM algorithm on intrusion detection datasets such as NSL, KDD, and NSL-KDD and achieved an accuracy of more than 98% (Raghuvanshi et al., 2022). Interestingly, our proposed method achieved a slightly higher result to that of Jagtap et al. (2022) when they applied the SVM in the classification of crop images and achieved an accuracy that was less than 90%.

D. Performance of Convolutional Neural Network (CNN)

The Convolutional Neural Network (CNN) algorithm achieved an accuracy of 0.9823, precision of 0.98, recall of 0.98, and F1 score of 0.98. Furthermore, the training loss vs the epochs for the CNN classification of the IoT-enabled dataset is presented in Figure 9.
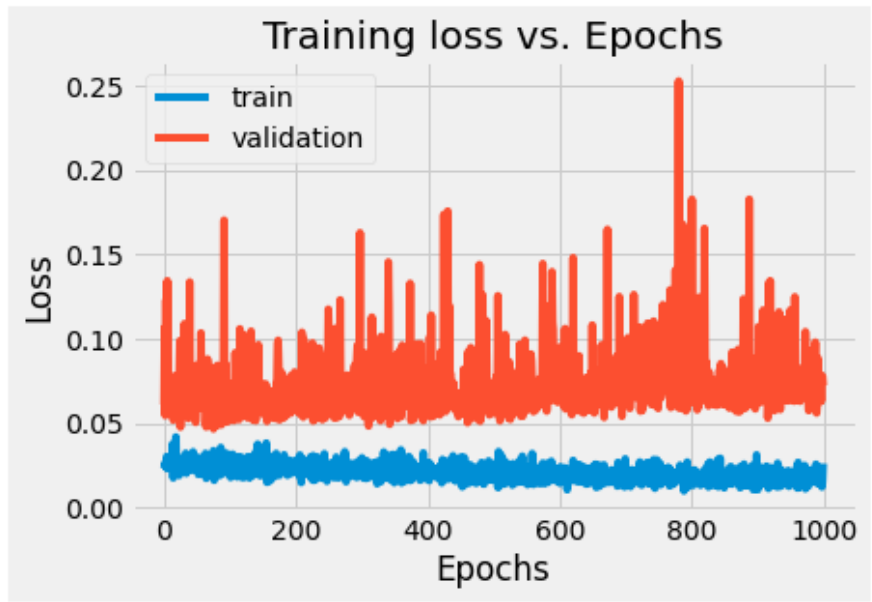
Figure 9. *Training Loss Vs Epochs for the CNN*

Generally, when the Loss Vs Epochs graph is taken into account, lower Loss values result in a good performance. Figure 9 shows that the graph was more consistent for the train datasets. The Loss values got closer to zero as the number of Epochs tends towards 1000. Additionally, as Epoch values tends towards 1000, the Loss values tends more towards zero (0) for the validation dataset.

Once more, while examining the training accuracy vs. epochs for this experiment as shown in Figure 10, it can be seen that the accuracies for the train dataset and test dataset were over 0.98 when the epochs were closer to 1000.
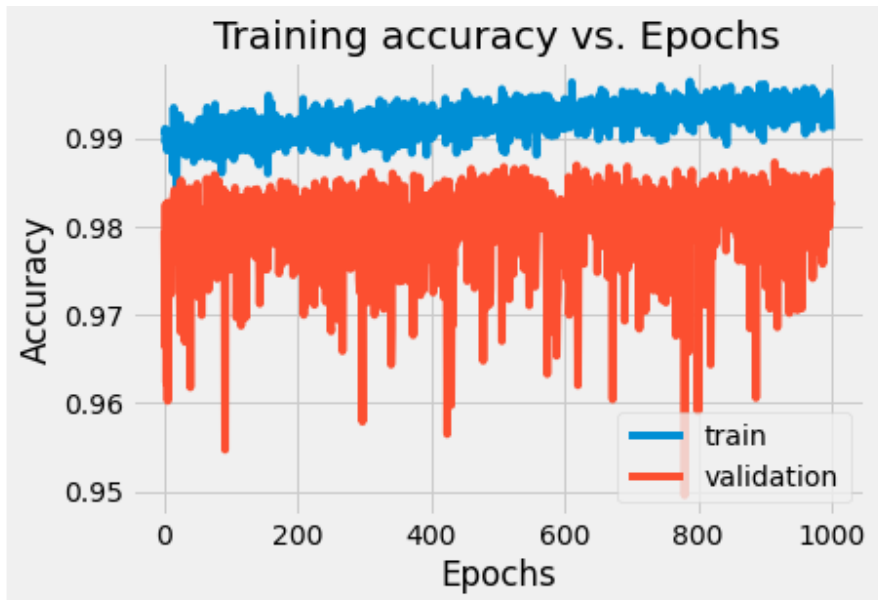
Figure 10. *Training Accuracy Vs Epochs for the CNN*

This demonstrates that for this experiment, epochs of over 1000 were well suited for the effective classification of IoT enabled data.

The confusion matrix is shown in Figure 11 to clearly demonstrate the number of samples that were classified using CNN based on the "ON" or "OFF" of the smart irrigation device.
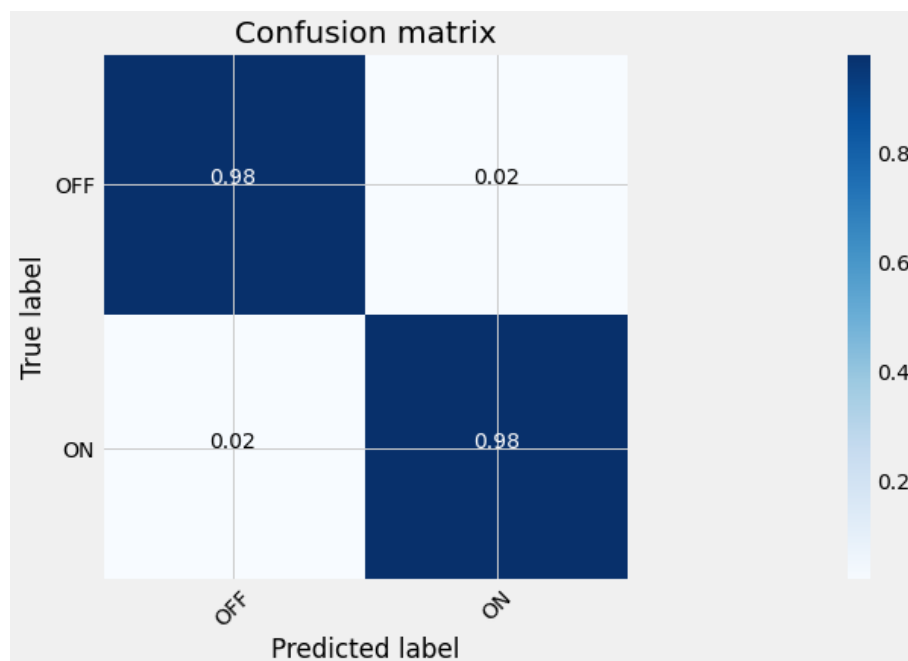
Figure 11. *Confusion Matrix for the CNN*

It can be seen from Figure 11 that the CNN algorithm correctly classified 0.98 (98%) samples as class 0 (OFF) and wrongly classified 0.02 (2%) samples of class 0 as class 1 (ON). Furthermore, the CNN algorithm correctly classified 0.98 (98%) samples of class 1 (ON), and wrongly classified 0.02 (2%) samples of class 1 as class 0 (OFF). With an accuracy of up to 98% shown in the confusion matrix, it proved that the proposed method of using the CNN for the classification of IoT-enabled data was very successful.

The accuracy of our proposed method (98.23%) outperformed that of Neforawati et al. (2019), when they used the CNN to classify Paddy growth level and achieved an overall accuracy of 82%. Furthermore, the accuracy of our proposed method outperformed that of Nindam et al. (2019) when they utilized the CNN for the classification of normal and abnormal Jasmine rice germination and achieved a validation accuracy of 96.43%.

In summary, Table 1 and Figure 12 compares the results of the machine learning techniques achieved in this paper.

Table 1. *Comparison Performance of Algorithms*

Algorithm	Accuracy	F1 score	Precision Value	Recall
LR	71.760	0.715	0.730	0.750
RF	99.980	0.999	0.999	0.999
SVM	90.210	0.901	0.901	0.917
CNN	98.230	0.980	0.980	0.980

Applying machine learning techniques for the separability of data produced by IoT-enabled smart irrigation devices is necessary because, if an IoT smart irrigation pump is supposed to go "OFF" but does not, this could result in flooding of the farm that is receiving irrigation, and vice versa. Therefore, the precise classification of data derived from whether the smart irrigation pump is "OFF" or "ON" can help in identifying when such a device is faulty (malfunctioning), under attack from malware, and has a potential of destroying farms which they are supposed to properly irrigate for the effective and efficient growth of crops.

In this study, the RF algorithm outperformed the SVM, LR, and CNN in all the evaluation metrics employed. The classification accuracy of the RF is 99.98%, followed by the CNN which is 98.23%, then the SVM which is 90.21%, and the LR which is 71.76%. From the comparative analysis, it can also be deduced that the LR performed least in all evaluation metrics used in this study.
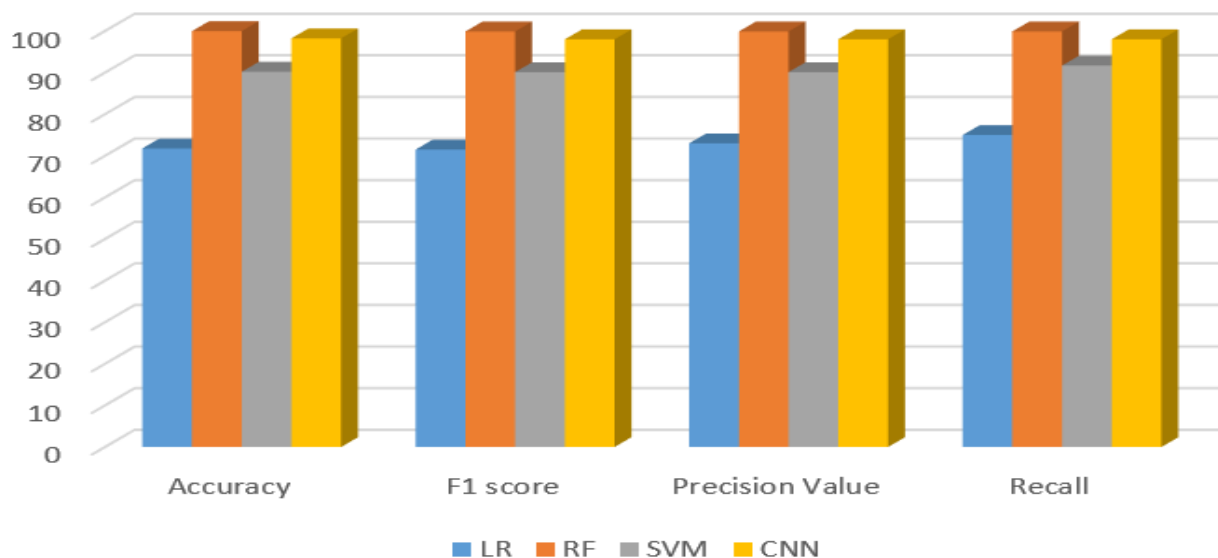
Figure 12. Graph Showing the Performance of Algorithms

5. CONCLUSION AND FUTURE WORK

This study examines how to classify (separate) data produced by IoT-enabled smart irrigation devices using machine learning approaches. The researchers concluded that smart irrigation device pre-processed IoT-generated datasets can be employed as input data into machine learning algorithms to understand patterns and carry out classification tasks. The RF algorithm, which was one of the four machine learning algorithms (LR, RF, SVM, and CNN) used in this study, was judged to be the most successful because it accurately distinguished between the times when the smart irrigation device was "ON" and "OFF" with 99.98%, 0.9998, 0.9996, and 0.9999 for the Accuracy, F1 score, Precision value, and Recall, respectively. The precise classification of IoT smart irrigation data by machine learning algorithms may indicate that the IoT devices that produced such data are particularly effective and efficient in the irrigation of crop farms, which may result in improved crop yields. In the future, we intend to classify IoT-enabled smart irrigation data for agricultural purposes using Benford's law and Zipf's law.

CONFLICT OF INTEREST

The authors declare no conflict of interest.

REFERENCES

Adam, M. S. A., Osman, A. A., Omer, E. A., & Abdallah, A. M. B. (2020). *Automatic Irrigation Implementation*. PhD Thesis, Supervised by Ust. Jafer Babiker, Sudan University of Science & Technology.

Bhowmik, A., Ramasubramanian, V., & Kumar, A. (2011). Logistic regression for classification in agricultural ergonomics. *Advances in Applied Science Research*, *3*(2):163-170.

Çetin, M., & Beyhan, S. (2022). Smart Irrigation Systems Using Machine Learning and Control Theory. In: R. Bhatnagar, N. K. Tripathi, N. Bhatnagar, & C. K. Panda (Eds.), *The Digital Agricultural Revolution: Innovations and Challenges in Agriculture through Technology Disruptions* (pp. 57-85). Scrivener Publishing LLC. doi:10.1002/9781119823469.ch3

390

Aamo IORLIAM, Sylvester BUM, Iember S. AONDOAKAA, Iveren Blessing IORLIAM, Yahaya SHEHU
GU J Sci, Part A, 9(4): 378-391 (2022)

Cheng, W., Ma, T., Wang, X., & Wang, G. (2022). Anomaly Detection for Internet of Things Time Series Data Using Generative Adversarial Networks with Attention Mechanism in Smart Agriculture. *Frontiers in Plant Science*, *13*. doi:10.3389/fpls.2022.890563

Dhasaradhan, K., Jaichandran, R., Shunmuganathan, K. L., Usha Kiruthika, S., & Rajaprakash, S. (2021). Hybrid machine learning model using decision tree and support vector machine for diabetes identification. In: V. Bhateja, S. C. Satapathy, C. M. Travieso-González, V. N. M. Aradhya (Eds.), *Data Engineering and Intelligent Computing* (Proceedings of ICICC 2020) (pp. 293-305). Springer. doi:10.1007/978-981-16-0171-2_28

Dholu, M., & Ghodinde, K. A. (2018, May). *Internet of things (IoT) for precision agriculture application*. In: Proceedings of the 2018 2nd International Conference on Trends in Electronics and Informatics (ICOEI) (pp. 339-342). IEEE. doi:10.1109/ICOEI.2018.8553720

Fan, S. (2018, May 7). Understanding the mathematics behind Support Vector Machines. (Accessed: 30/06/2022) URL

Fernández-Ahumada, L. M., Ramírez-Faz, J., Torres-Romero, M., & López-Luque, R. (2019). Proposal for the design of monitoring and operating irrigation networks based on IoT, cloud computing and free hardware technologies. *Sensors*, *19*(10), 2318. doi:10.3390/s19102318

Goap, A., Sharma, D., Shukla, A. K., & Krishna, C. R. (2018). An IoT based smart irrigation management system using Machine learning and open source technologies. *Computers and Electronics in Agriculture*, *155*, 41-49. doi:10.1016/j.compag.2018.09.040

Gondchawar, N., & Kawitkar, R. S. (2016). IoT based smart agriculture. *International Journal of Advanced Research in Computer and Communication Engineering*, *5*(6), 838-842.

Iorliam, A., Adeyelu, A., Otor, S., Okpe, I., & Iorliam, I. B. (2020). A Novel Classification of IoT-Enabled Soil Nutrients Data Using Artificial Neural Networks. *International Journal of Innovative Research in Electrical, Electronics, Instrumentation and Control Engineering*, 8(4), 103-109. doi:10.17148/IJIREEICE.2020.8418

Iorliam, A., Iorliam, I. B., & Blum, S. (2021). Internet of Things for Smart Agriculture in Nigeria and Africa: A Review. *International Journal of Latest Technology in Engineering, Management & Applied Science*, *10*(2), 7-13.

Jagtap, S. T., Phasinam, K., Kassanuk, T., Jha, S. S., Ghosh, T., & Thakar, C. M. (2022). Towards application of various machine learning techniques in agriculture. *Materials Today: Proceedings*, *51*(1), 793-797. doi:10.1016/j.matpr.2021.06.236

Janani, M., & Jebakumar, R. (2019). A study on smart irrigation using machine learning. *Cell & Cellular Life Sciences Journal*, *4*(1), 1-8. doi:10.23880/cclsj-16000141

Krizhevsky, A., Sutskever, I., & Hinton, G. E. (2017). ImageNet classification with deep convolutional neural networks. *Communications of the ACM*, *60*(6), 84-90. doi:10.1145/3065386

Kumar, M., Sahni, R. K., Waghaye, A. M., Nayak, A. K., & Kumar, D. (2018). Automated Irrigation System for Rice: A Review. *The Andhra Agric. Journal*, *65 (spl)*, 324-329.

Mittal, R. (2020). Automatic Irrigation Data for Rice Crop. (Accessed: 30/06/2022) URL

Monaco, F., Sali, G., Ben Hassen, M., Facchi, A., Romani, M., & Valè, G. (2016). Water management options for rice cultivation in a temperate area: A multi-objective model to explore economic and water saving results. *Water*, *8*(8), 336. doi:10.3390/w8080336

Nawandar, N. K., & Satpute, V. R. (2019). IoT based low cost and intelligent module for smart irrigation system. *Computers and Electronics in Agriculture*, *162*, 979-990. doi:10.1016/j.compag.2019.05.027

Neforawati, I., Herman, N. S., & Mohd, O. (2019, April). Precision agriculture classification using convolutional neural networks for paddy growth level. *Journal of Physics: Conference Series*, *1193*, 012026. doi:10.1088/1742-6596/1193/1/012026

391

Aamo IORLIAM, Sylvester BUM, Iember S. AONDOAKAA, Iveren Blessing IORLIAM, Yahaya SHEHU
GU J Sci, Part A, 9(4): 378-391 (2022)

Nindam, S., Sung, T. L., Manmai, T.-O., & Lee, H. J. (2019, June*). Collection and Classification of Jasmine Rice Germination Using Convolutional Neural Networks*. In: Proc. International Symposium on Information Technology Convergence (ISITC 2019) (pp. 105-108).

Ok, A. O., Akar, O., & Gungor, O. (2012). Evaluation of random forest method for agricultural crop classification. *European Journal of Remote Sensing*, *45*(1), 421-432. doi:10.5721/EuJRS20124535

Pfitscher, L. L., Bernardon, D. P., Kopp, L. M., Ferreira, A. A. B., Heckler, M. V. T., Thome, B. A., Montani, P. D. B., & Fagundes, D. R. (2011, May). *An automated irrigation system for rice cropping with remote supervision*. In: J. A. Aguado, & A. Pires (Eds.), 2011 International Conference on Power Engineering, Energy and Electrical Drives. 2011 International Conference on Power Engineering, Energy and Electrical Drives (POWERENG). IEEE. doi:10.1109/PowerEng.2011.6036452

Pluchinotta, I., Pagano, A., Giordano, R., & Tsoukiàs, A. (2018). A system dynamics model for supporting decision-makers in irrigation water management. *Journal of Environmental Management*, *223*, 815-824. doi:10.1016/j.jenvman.2018.06.083

Qi, Y. (2012). Random Forest for Bioinformatics. In: C. Zhang, & Y. Ma (Eds.), *Ensemble Machine Learning Methods and Application* (pp. 307-323). Springer, Boston, MA. doi:10.1007/978-1-4419-9326-7_11

Raghuvanshi, A., Singh, U. K., Sajja, G. S., Pallathadka, H., Asenso, E., Kamal, M., Singh, A., & Phasinam, K. (2022). Intrusion Detection Using Machine Learning for Risk Mitigation in IoT-Enabled Smart Irrigation in Smart Farming. In: M. F. Manzoor, A. Hussain, & R. M. Aadil (Eds.), *Journal of Food Quality*, *2022 (Special Issue)*, 3955514. doi:10.1155/2022/3955514

Romero, M., Luo, Y., Su, B., & Fuentes, S. (2018). Vineyard water status estimation using multispectral imagery from an UAV platform and machine learning algorithms for irrigation scheduling management. *Computers and Electronics in Agriculture*, *147*, 109-117. doi:10.1016/j.compag.2018.02.013

Roy, S. K., Misra, S., Raghuwanshi, N. S., & Das, S. K. (2020). AgriSens: IoT-based dynamic irrigation scheduling system for water management of irrigated crops. *IEEE Internet of Things Journal*, *8*(6), 5023-5030. doi:10.1109/JIOT.2020.3036126

Sanjeevi, P., Prasanna, S., Siva Kumar, B., Gunasekaran, G., Alagiri, I., & Vijay Anand, R. (2020). Precision agriculture and farming using Internet of Things based on wireless sensor network. *Transactions on Emerging Telecommunications Technologies*, *31*(12), e3978. doi:10.1002/ett.3978

Shekhar, Y., Dagur, E., Mishra, S., Tom, R. J., Veeramanikandan, M., & Sankaranarayanan, S. (2017). Intelligent IoT based automated irrigation system. *International Journal of Applied Engineering Research*, *12*(18), 7306-7320.

Surendran, U., Sushanth, C. M., Mammen, G., & Joseph, E. J. (2015). Modelling the crop water requirement using FAO-CROPWAT and assessment of water resources for sustainable water resource management: A case study in Palakkad district of humid tropical Kerala, India. *Aquatic Procedia*, *4*, 1211-1219. doi:10.1016/j.aqpro.2015.02.154

Torres-Sanchez, R., Navarro-Hellin, H., Guillamon-Frutos, A., San-Segundo, R., Ruiz-Abellón, M. C., & Domingo-Miguel, R. (2020). A decision support system for irrigation management: Analysis and implementation of different learning techniques. *Water*, *12*(2), 548. doi:10.3390/w12020548

Tyagi, A., Gupta, N., Navani, J. P., Tiwari, R., & Gupta, A. (2017). Smart irrigation system. *International Journal for Innovative Research in Science & Technology*, *3*(10).

Experimental Investigation of Hydro-Mechanical Soil Properties of a Slope Failure

Seda DURUKAN[1]* [iD]   Ender BAŞARI[2] [iD]

[1]Manisa Celal Bayar University, Manisa Vocational School of Technical Sciences, Department of Construction Technology, Manisa, Türkiye
[2]Manisa Celal Bayar University, Engineering Faculty, Department of Civil Engineering, Manisa, Türkiye

Keywords	Abstract
Unsaturated Soils Matric Suction Landslides Slope Stability	A sudden slope failure occurred in Manisa possibly due to the effect of water infiltration because of a slightly damaged sewage pipe. Considering that there was no other evidence such as rainfall or any loading conditions to trigger the slope failure, a laboratory investigation on the soil's unsaturated hydro-mechanical properties was initiated. Slopes are naturally unsaturated soils, and they may lose their stability with increased saturation degrees with water infiltration. Thus, for a proper investigation, the unsaturated hydro-mechanical properties of soils should be determined. The results presented in this study are focused on determining the key parameters to evaluate the slope failure for unsaturated soil conditions. In this regard, hydraulic conductivity and suction characteristics and the shear strength parameters were determined as well as the classical geotechnical properties of the soil. Classification of soil was determined as silty sand which is known to have slight to moderate suction stresses and mostly affected suddenly by water infiltration. A flexible-wall permeability test was run with a falling head procedure and the saturated hydraulic conductivity of the soil sample was measured as 1×10^{-7} m/s. Suction characteristics were detected by filter paper method, besides, the soil water retention curve of the soil was constructed. The maximum matric suction of the soil was measured as 2887 kPa for an air-dried sample. Following, the shear strength parameters were measured by conventional direct shear test for both dry and soaked conditions. Finally, the friction angle due to suction was calculated to be 1.7 degrees from the results of dry and saturated shear strength parameters.

1. INTRODUCTION

Slope failures can occur due to many reasons, but one is particularly the interest of this study which is slope failures triggered by water infiltration. Slopes are naturally unsaturated soils; however, the conventional soil mechanics principles handle the slope stability analyses regarding the saturated conditions. Slopes can be stable even at very steep angles when they are unsaturated, and when subjected to an infiltration caused by rainfall, snowmelt or any leakage, then, the same slope may suddenly lose its stability due to the increase in its saturation degree which causes decrease in capillary forces. In literature, there are many examples of failures caused by infiltration (Oh & Lu, 2015; Batali & Andreea, 2016; Xian et al., 2022) and also many studies to predict the event before it happens like early warning systems (Intrieri et al., 2012; Naidu et al., 2018). In addition, there are such modeling studies which aims understanding the behavior of the infiltration caused slope failures (Vanapalli et al., 1996; Zhang et al., 2014; Tang et al., 2018). In fact, using laboratory data is the most convenient way to investigate the stability of a certain slope, it is not very common for practical purposes. Some of the theoretical studies used imaginary soil properties where some of them used real laboratory data or data from unsaturated soil hydraulic database (UNSODA, 2022). The main characteristic properties which affect the slope stability and failure mechanism are known as the matric suction and hydraulic

*Corresponding Author, e-mail: seda.durukan@cbu.edu.tr

conductivity (HC). Concerning the unsaturated soil mechanics, matric suction is a key parameter to enhance the strength and the unsaturated soil strength relations are suggested by Fredlund et al. (1978) as a modified equation given in Equations 1 and 2, in addition, the graphical forms of the relation for both saturated (Figure 1a) and unsaturated soils (Figure 1b) are also given in Figure 1.

$$\tau_f = c' + \left(\sigma_f - u_a\right)_f \tan \emptyset' + (u_a - u_w) \tan \emptyset^b \qquad (1)$$

$$c = c' + (u_a - u_w) \tan \emptyset^b \qquad (2)$$

where;

$\left(\sigma_f - u_a\right)_f$ is net normal stress

$(u_a - u_w)$ is the matric suction

$\emptyset^b$ is the angle which gives the rate of change in shear strength related to the changes in matric suction.

c' and $\emptyset'$ are classical effective cohesion and angle of internal friction, respectively.

(a) Saturated soils

(b) Unsaturated soils
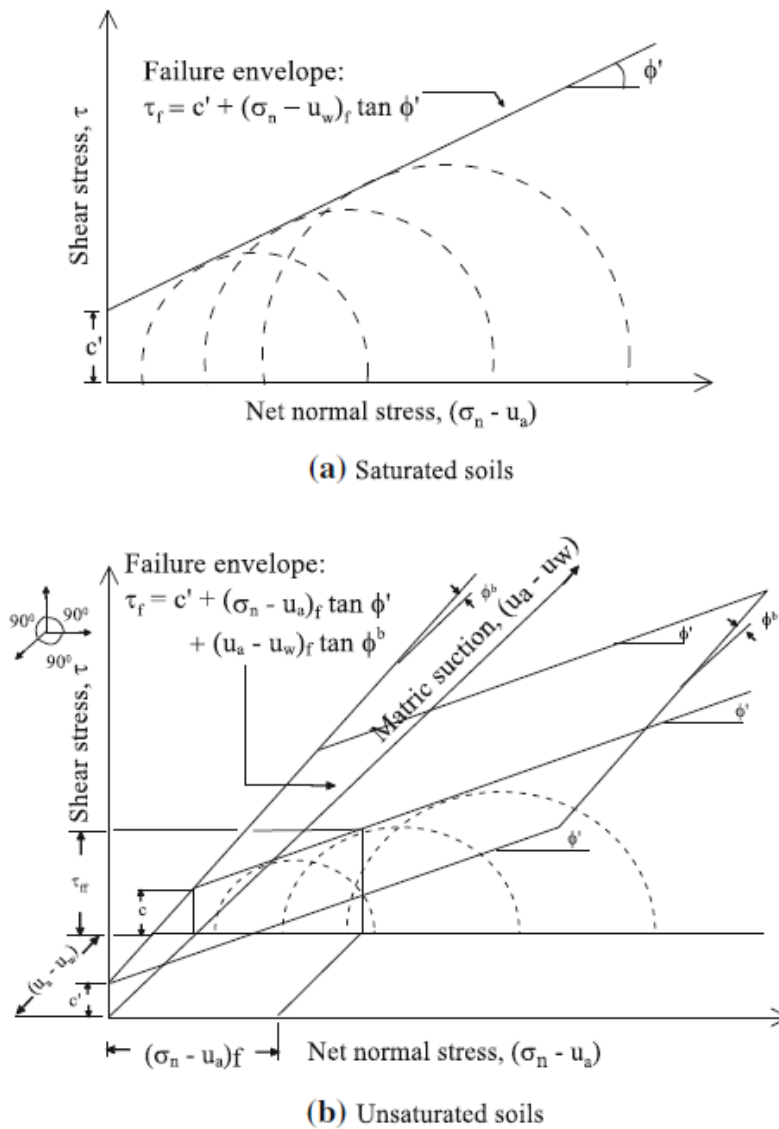
Figure 1. *Classical and modified failure criteria of*
a) *saturated soils and* ***b)*** *unsaturated soils (after Chowdhury & Azam, 2016)*

The friction angle due to suction, ϕ^b, is accepted to be constant as shown in Equation1 and Figure 1 and in literature it is generally used as a constant called as the average rate of increase in shear strength relating to matric suction. The results from many reported studies (Gan & Fredlund, 1995; Bai & Lui, 2012; Chowdhury & Azam, 2016) ϕ^b is found to be smaller than ϕ' in addition, according to Gan and Fredlund (1995) ϕ^b approaches to ϕ' with increasing saturation and finally equals when the soil approaches full saturation.

When studying with unsaturated soils it is very important to measure their suction values in order to properly obtain their strength characteristics. The shear strength measurements can be done by modified forms of test apparatus such as direct and ring shear tests and triaxial tests. The modification usually includes a controlled suction measurement system; however, the modifications are mostly expensive and time-consuming so that, separate measurements of suction characteristics and shear strength are still accepted. Oh and Vanapalli (2010) used a modified triaxial apparatus to measure the unsaturated shear strength parameters and investigated the factor of safety of a glacial soil under the rainfall conditions. The axis translation method was applied, and the study also reported a constant ϕ^b although, the change in shear strength relating to matric suction was not linear. Bai and Liu (2012) performed conventional direct shear tests and then, combined the shear strength results with the suction characteristics of findings from filter paper tests. The findings of the study showed the relation between ϕ^b and matric suction, the results implied that, with increasing matric suction ϕ^b decreased and reached very smaller values where it was equal to ϕ' when there was no suction. To combine suction and shear strength tests, a soil water retention curve (SWRC) is usually constructed by measured suction values for corresponding volumetric water contents or saturation degrees to find the desired suction value for a specific volumetric water content or a saturation degree (Fattah et al., 2017). Then, this suction value is related to the strength parameters using Equation1. Thus, an appropriate laboratory work to properly study a stability problem for an unsaturated soil is the key initial situation. The objective of this study is to investigate and find out the hydro-mechanical properties of a soil picked up from a failed slope in Manisa triggered by water infiltration. In this regard, index properties, sieve analysis, Atterberg limits, HC test and direct shear tests (dry and soaked) were conducted. Besides, matric suction measurements were done and SWRC was also constructed.

2. MATERIAL AND METHOD

A slope failure occurred in Manisa after a leakage from a slightly damaged sewage pipe (Figure 2). Considering that there was not any other evidence to trigger the slope failure, an investigation on the soil hydro-mechanical properties was initiated. Sieve analyses was done and Atterberg limits were determined along with the index properties such as unit weight and specific gravity and all the basic geotechnical descriptive properties were presented in Table 1.
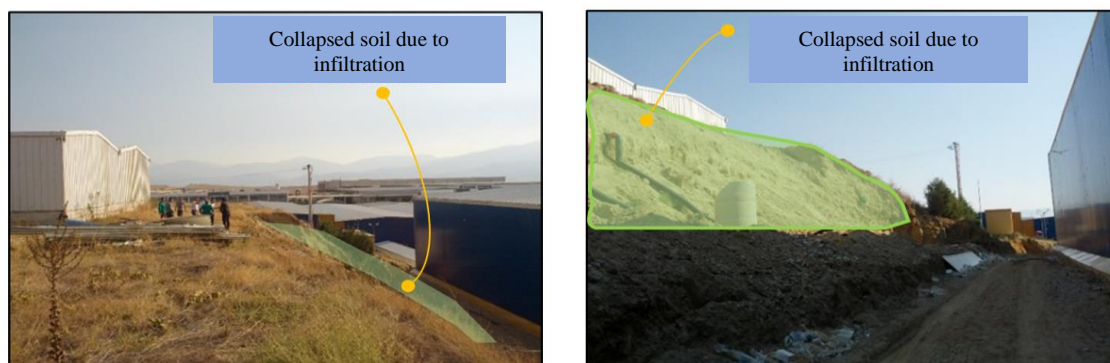
Figure 2. Condition of the slope

The saturated HC of the soil was measured by a flexible wall permeameter with falling head procedure (ASTM D5084-16). A soil sample was taken directly from the slope origin and cut into dimensions to fit in the permeameter (Figure 3) and then carefully trimmed to a diameter of 10 cm and a height of 9.6 cm thus, no compaction procedure was followed and, the soil was in its air-dried state. Geotextiles of 10 cm diameter were used as porous material and the HC of the geotextiles were initially found to be 10^{-4} m/s which was convenient

to use to determine the HC of the slope soil. During the test, the confining stress was 35 kPa, the average hydraulic gradient was 11 and no backpressure was applied. The flow direction was upwards to avoid any air bubbles and tap water was used during the permeation in addition, the inflow path itself was also flushed avoiding any air bubbles. For the first 24 h, the inflow valves were kept open while the outflow valves were closed which helped the prehydration of the soil specimen for a homogeneous diffusion. The test was lasted at least for 3 pore volumes of flow (PVF) and terminated when the outflow and inflow remained constant for the last 5 consecutive measurements while the ratio of consecutive hydraulic conductivities were in the range of ±25%.

Table 1. *Some geotechnical properties of the soil*

Property	Quantitiy or Definition
Gravel %	13
Sand %	58
Fines %	29
Soil Classification	SM
PI	Non-Plastic
Specific Gravity (Gs)	2.68
Unit weight, γ (kN/m^3)	18
Natural water content, w (%)	6.5
Void ratio, e	0.43

Figure 3. *Setup and process of the hydraulic conductivity test*

The suction measurements were done by using filter paper method (ASTM D5298-16). Filter paper method is known to be an easy, cost-effective method and the only method to measure matric and total suction together (Bulut & Leong, 2008). Filter papers were directly used from box as air dried and no pre-treatment was made. A bio-incubator type incubator (Santez SI-150K) was used during the equilibrium process and the equilibrium time was 1 week. The temperature of the incubator was held constant at 20°C with a sensitivity of ±0.1 where the relative humidity was 65%. During the matric suction measurements, the contact filter paper is buried between two soil layers. This study followed the description in Durukan and Akıncı (2017) which suggests placing the filter paper between two separately compacted soil layers in order to have a smooth contact surface between the soil layers and the filter paper. Following the suction measurements, the SWRC of the soil was also constructed by using a free program SWRC-Fit (Seki, 2007; Seki et al., 2022) and the van Genuchten parameters were determined. SWRC-Fit can fit several soil hydraulic unimodal or bimodal models to measured soil water retention data and the model of van Genuchten is one of those models.

To obtain the mechanical properties of the soil, conventional direct shear tests were run for both dry and soaked conditions (ASTM D3080-11). An original soil sample was directly taken from the slope as it was in hydraulic conductivity test thus, no compaction process was needed. The box size was 60x60 mm and for soaked samples, the soil was saturated at least 24h under surcharge loading conditions. The vertical change in the specimen height was observed and when no further increase was achieved in the vertical displacement then, full saturation was also assumed to be achieved. Three tests for both dry and saturated samples were run with three different dead loading conditions and the shearing rate was 0.02 mm/min. At the end of the test, the water content of the saturated test sample was measured to be 16%. The friction angles were obtained based on the assumption of Jewell and Wroth (1987) where the horizontal plane was assumed to be the plane of maximum stress ratio (τ/σ_n)

3. RESULTS AND DISCUSSION

The hydromechanical properties of a soil from a slope failure were investigated. Thus, saturated hydraulic conductivity, suction characteristics and mechanical properties were determined along with basic geotechnical properties previously presented in Table 1. Hydraulic conductivity test results were presented in Figure 4 in terms of hydraulic conductivity (HC), the ratio of outlet and inlet fluid (q_{out}/q_{in}) and the change in hydraulic conductivity (ΔHC) as a function of PVF. The test lasted at least for 3 PVF and the hydraulic conductivity was found to be 1×10^{-7} m/s. The HC behavior of the soil sample was stable and q_{out}/q_{in} values scatter was in a narrow interval around 1 after 1 PVF (Figure 4a). Similarly, the wide scatter of ΔHC stabilized after 1.5 PVF and reached the acceptable variation limits and, after 2.6 PVF the scatter became narrower resulting in termination of the test (Figure 4b).

In order to construct a SWRC, the matric suction characteristics were detected by filter paper method. During the test there were 6 soil samples having different water contents which varied between 0 and 13%. Five of these specimens were compacted to have the same unit weight which the original sample had, for varying water contents. The 6th sample was the original air-dried sample which was also used in direct shear tests. The data was shown as dots in Figure 5 as well as the SWRC seen in dashed lines. The data showed good agreement and the coefficient of determination (R^2) was found to be 0.98. The matric suction value of the air-dried original soil sample was 2887 kPa. The suction and volumetric water content data measured from filter paper test were entered in SWRC-Fit program to obtain the van Genuchten parameters (Seki, 2007; Seki et al., 2022). The van Genuchten parameters of the soil sample which are saturated water content (cm^3/cm^3) (Θ_s), residual water content (cm^3/cm^3) (Θ_r), the soil water characteristic curve index (shape parameter of the curve) (n), a scaling parameter which is inversely proportional to mean pore diameter (cm^{-1}) (α) were presented in Table 2. These fitting parameters, n and α, are the key estimated parameters to construct a SWRC. The van Genuchten equation presenting the effective saturation (S_e) is given in Equation 3.

$$S_e = \left[\frac{1}{1 + (\alpha h)^n} \right]^m \qquad and \qquad m = 1 - 1/n \qquad\qquad (3)$$
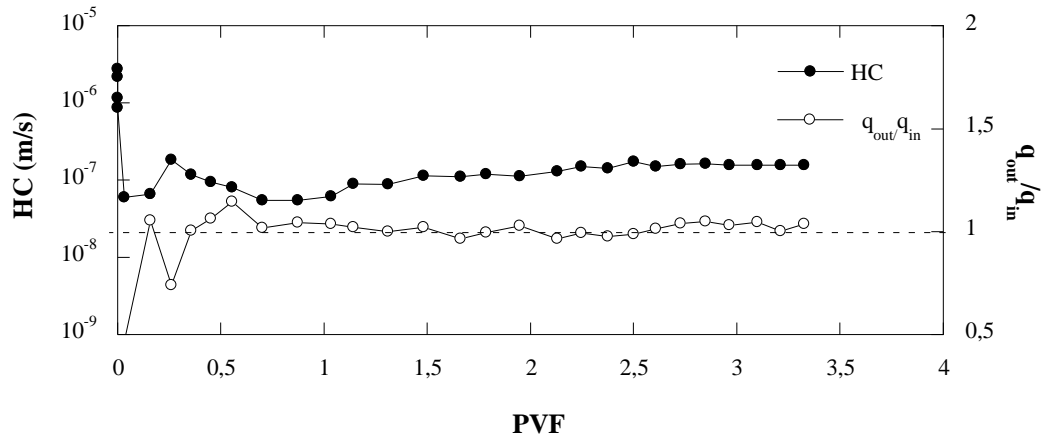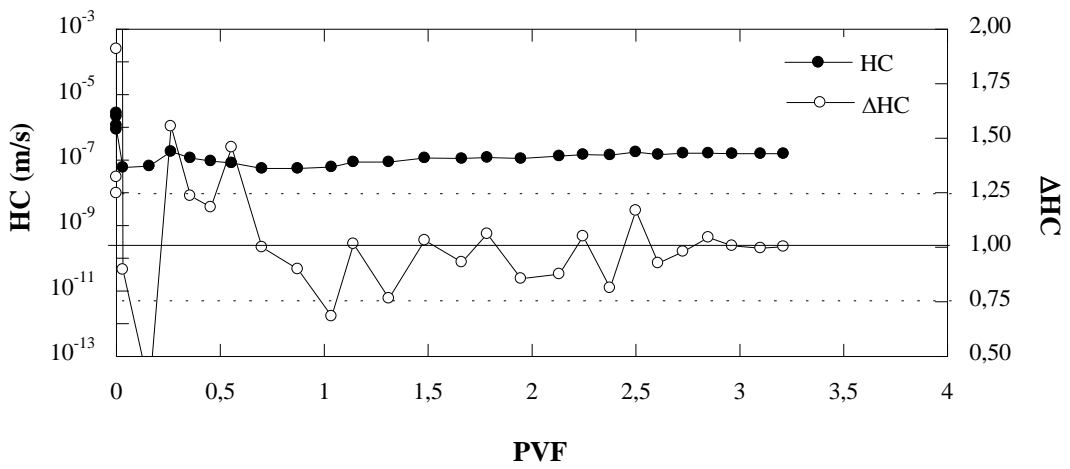
Figure 4. *HC characteristics of the soil sample*
a) *along with q_{out}/q_{in} and* **b)** *along with ΔHC as a function of PVF*
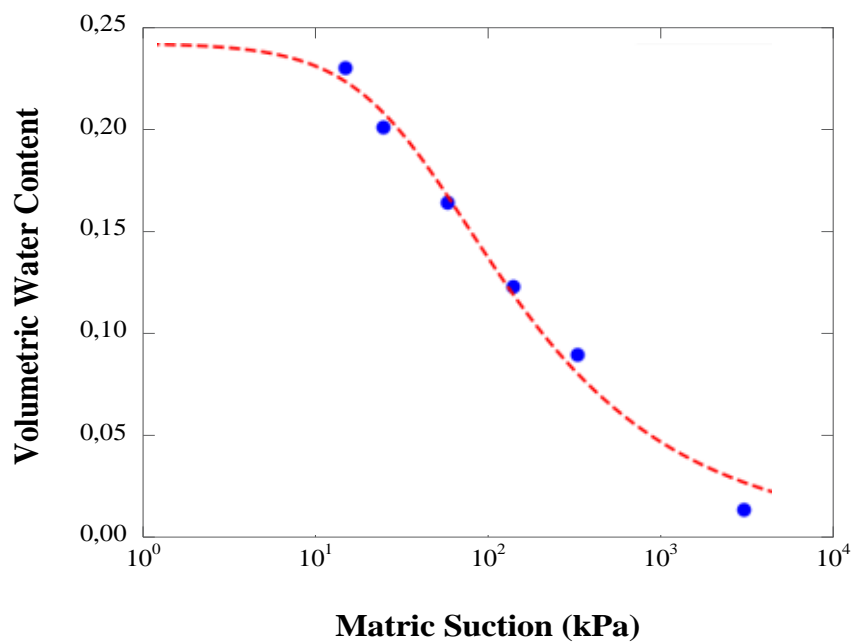
Figure 5. *SWRC of the soil sample*

Table 2. *Van Genuchten parameters of the soil*

Parameters	Quantitiy
Θ_s (cm³/cm³)	0.24474
Θ_r (cm³/cm³)	7.2E-16
α (cm⁻¹)	0.028653
n	1.5039

Constructing a SWRC provides to obtain any suction value for a specific water content and/or saturation degree. Combining the suction characteristics with hydraulic conductivity lets one to obtain a hydraulic conductivity function (HCF). McCartney et al. (2007) investigated estimation of HCF using infiltration column tests and declared that the HCF was sensitive to any change in the moisture content and suction, which could cause inaccuracy in the gradient and also in negative pore pressures. The authors also added that the HCF predicted from the SWRC was found to underestimate the values of hydraulic conductivity. In this study, each hydraulic conductivity values (K_{Se}) were calculated using the relative hydraulic conductivity (K_r) relations defined in van Genuchten (1980) (Equation 4) related to the matric suction, saturated hydraulic conductivity, effective saturation (Se) and fitting van Genuchten parameters as mentioned in the study of van Genuchten (1980) and placed in a graph and presented in Figure 6. The hydraulic conductivity values decreased with increasing matric suction as expected.

$$K_r = S_e^{(1/2)} \left[1 - \left(1 - S_e^{(1/m)} \right)^m \right]^2 \tag{4}$$
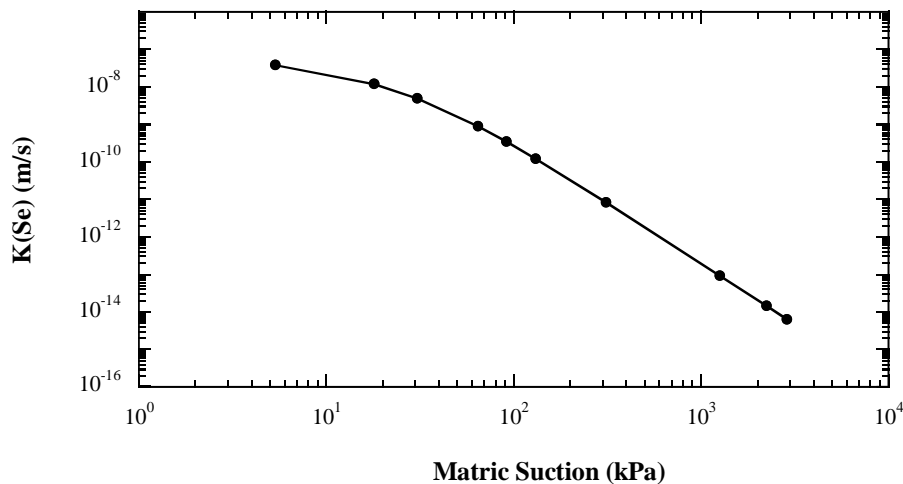
Figure 6. *The change in HC with matric suction of the soil sample*

Direct shear tests were conducted on two saturation states, dry and soaked states, and soaked state was assumed to be saturated in the study. Test results were given in Figure 7, the angle of internal friction for saturated and dry samples were 18 and 23.5 degrees, respectively. Results are in harmony with those of Bai and Liu (2012) where the angle of internal friction decreased while the water content increased. The cohesion intercepts of the dry and saturated samples were found to be 10.5 kPa and 95.5 kPa, respectively. The matric suction of the dry sample was measured as 2887 kPa. Regarding Equations 1 and 2, the friction angle due to suction, ϕ^b, referencing the change in saturated and dry states, was found as 1.7 degrees. The friction angle due to suction is expected to increase with increasing saturation and at full saturation ϕ^b to reach ϕ' as mentioned in Gan and Fredlund (1995) and Bai and Lui (2012). The shear test equipment used in this study was not modified to measure the mechanical properties for controlled suction situations so, other comparisons for ϕ^b was not done.
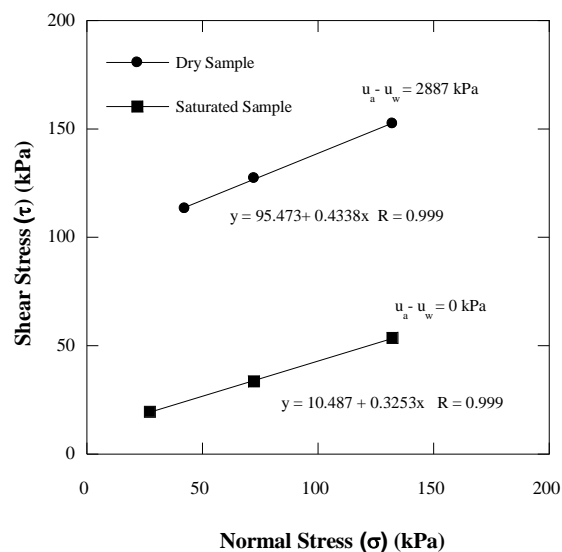
Figure 7. *Direct shear results of the soil sample*

4. CONCLUSION

The hydro-mechanical properties of a soil concerning a slope failure associated with water infiltration were investigated. In this regard, an experimental study was conducted, and hydraulic conductivity, suction characteristics and shear strength were measured along with classical geotechnical properties. Because the measured characteristics could be used in modelling the slope failure. The hydraulic conductivity and direct shear tests were done with original soil samples and saturated HC of the soil sample was found to be 1×10^{-7} m/s. Matric suction values were detected by filter paper method and the results gathered from suction tests were used to construct the SWRC of the soil. The maximum suction value was 2887 kPa for the air-dried original sample. Finally, the van Genuchten characteristics were found to be 0.24474 for Θ_s, 7.2E-16 for Θ_r, 0.028653 for α and 1.5039 for n. The shear strength characteristics were measured for both dry and saturated states in order to compare and calculate ϕ^b which was found to be 1.7 degrees. The angle of internal friction for saturated and dry samples were 18 and 23.5 degrees, respectively. The results were compatible with those given in literature. In addition, the cohesion intercepts of the dry and saturated samples were found to be 10.5 kPa and 95.5 kPa, respectively.

CONFLICT OF INTEREST

The authors declare no conflict of interest.

REFERENCES

ASTM D3080-11 (2011). Standard test method for direct shear test of soils under consolidated drained conditions. American Society for Testing and Materials, Withdrawn Standart.

ASTM D5084-16 (2016). Standard test method for measurement of hydraulic conductivity of saturated porous materials using a flexible wall permeameter. American Society for Testing and Materials, Active Standart.

ASTM D5298-16 (2016). Standard test method for measurement of soil potential (suction) using filter paper. American Society for Testing and Materials, Active Standart.

Batali, L., & Andreea, C. (2016). Slope Stability Analysis Using the Unsaturated Stress Analysis. Case Study. *Procedia Engineering*, *143*, 284-291. doi:10.1016/j.proeng.2016.06.036

Bai, F. Q., & Liu, S. H. (2012). Measurement of the Shear Strength of an Expansive Soil by Combining a Filter Paper Method and Direct Shear Tests. *Geotechnical Testing Journal*, *35*(3), 451-459. doi:10.1520/GTJ103342

Bulut, R., & Leong, C. (2008). Indirect Measurement of Suction. *Geotechnical and Geological Engineering*, *26*, 633-644. doi:10.1007/s10706-008-9197-0

Chowdhury, R. H., & Azam, S. (2016). Unsaturated shear strength properties of a compacted expansive soil from Regina, Canada. *Innovative Infrastructure Solutions*, 1, 47. doi:10.1007/s41062-016-0047-2

Durukan, S., & Akıncı, G. (2017). Assessment and statistical evaluation of suction characteristics obtained via filter paper technique on zeolite – bentonite mixtures. *Environmental Earth Sciences*, *76*, 685, 1-13. doi:10.1007/s12665-017-7032-8

Gan, JK-M, & Fredlund D. G., (1995, September 6-8). *Shear Strength Behavior of Two Saprolitic Soils*. In: Proceedings of the First International Conference on Unsaturated Soils (UNSAT'95), Paris, France.

Fattah, M. Y., Salim, N. M., & Irshayyid, E. J. (2017). Determination of the soil–water characteristic curve of unsaturated bentonite–sand mixtures. *Environmental Earth Sciences*, *76*(5), 201. doi:10.1007/s12665-017-6511-2

Fredlund, D. G., Morgenstern, N. R., & Widger, R. A. (1978). The shear strength of unsaturated soils. *Canadian Geotechnical Journal*, *15*(3), 313-321. doi:10.1139/t78-029

Intrieri, E., Gigli, G., Mugnai, F., Fanti, R., & Casagli, N. (2012). Design and implementation of a land-slide early warning system. *Engineering Geology*. *147-148*, 124-136. doi:10.1016/j.enggeo.2012.07.017

Jewell, R. A. & Wroth, C. P. (1987). Direct shear tests on reinforced sand. *Geotechnique*, *37*(1), 53-68. doi:10.1680/geot.1987.37.1.53

McCartney, J. S., Villar, L. F. S., & Zornberg, J. G. (2007, November 1-3). *Estimation of the Hydraulic Conductivity Function of Unsaturated Clays using Infiltration Column Tests*. In: Proceedings of the Sixth Brazilian Symposium on Unsaturated Soils, (pp. 321-328), Salvador, Brazil.

Naidu, S., Sajinkumar, K. S., Oommen, T., Anuja, V. J., Samuel, R. A., & Muraleedharan C. (2018). Early warning system for shallow landslides using rainfall threshold and slope stability analysis. *Geoscience Frontiers*, *9*(6), 1871-1882. doi:10.1016/j.gsf.2017.10.008

Oh, S., & Lu, N. (2015). Slope stability analysis under unsaturated conditions: Case studies of rainfall-induced failure of cut slopes. *Engineering Geology*, *184*, 96-103. doi:10.1016/j.enggeo.2014.11.007

Oh, W. T., & Vanapalli, S. K. (2010). Influence of rain infiltration on the stability of compacted soil slopes. *Computers and Geotechnics*, *37*(5), 649-657. doi:10.1016/j.compgeo.2010.04.003

Seki, K. (2007) SWRC fit - a nonlinear fitting program with a water retention curve for soils having unimodal and bimodal pore structure. Hydrology and Earth System Sciences, *4*, 407-437. doi:10.5194/hessd-4-407-2007

Seki, K., Toride, N., & van Genuchten, M. Th. (2022). Closed-form hydraulic conductivity equations for multimodal unsaturated soil hydraulic properties. *Vadose Zone Journal*, *21*(1), e20168. doi:10.1002/vzj2.20168

Tang, G., Huang, J., Sheng, D., & Sloan, S. W. (2018). Stability analysis of unsaturated soil slopes under random rainfall patterns. *Engineering Geology*, *245*, 322-332. doi:10.1016/j.enggeo.2018.09.013

UNSODA. (2022). Unsaturated Soil Hydraulic Database. Database and program for indirect methods of estimating unsaturated hydraulic properties (Accessed: 06/10/2022) URL

van Genuchten, M. Th. (1980). A closed Form Equation for Predicting the Hydraulic Conductivity of Unsaturated Soils. *Soil Science Society of American Journal*, *44*(5), 892-898.

Vanapalli, S. K., Fredlund, D. G., & Pufahl, D. E. (1996). The Relation Between the Soil-Water Characteristic Curve and the Unsaturated Shear Strength of a Compacted Glacial Till. *Geotechnical Testing Journal*, *19*(3), 259-268. doi:10.1520/GTJ10351J

Xian, Y., Wei, X., Zhou, H., Chen, N., Liu, Y., Liu, F., & Sun, H. (2022). Snowmelt-triggered reactivation of a loess landslide in Yili, Xinjiang, China: mode and mechanism. *Landslides*, *19*(8), 1843-1860 doi:10.1007/s10346-022-01879-7

Zhang, L. L., Fredlund, D. G., Fredlund, M. D., & Wilson, G. W. (2014). Modeling the unsaturated soil zone in slope stability analysis. *Canadian Geotechnical Journal*, *51*(12), 1384-1398. doi:10.1139/cgj-2013-0394

Discretization of Fractional Order Operator in Delta Domain

Sujay Kumar DOLAI[1] [iD] Arindam MONDAL[2*] [iD] Prasanta SARKAR[3] [iD]

[1]Department of Electrical Engineering, Dream Institute of Technology, West Bengal, India
[2]Department of Electrical & Electronics Engineering, Pailan College of Management &Technology, West Bengal, India
[3]Department of Electrical Engineering, National Institute of Technical Teachers Training & Research, West Bengal, India

Keywords	Abstract
Continuous Fraction Expansion Direct Discretization Delta Operator Fractional Order Operator Fractional Order System	The fractional order operator is the backbone of the fractional order system (FOS). The fractional order operator (FOO) is generally represented as $s^{\pm\mu} (0 < \mu < 1)$. Discrete time FOS can be obtained through the discretization of the fractional order operator. The FOO is the general form of either fractional order differentiator (FOD) or integrator (FOI) depending upon the values of μ. Out of the two discretization methods, direct discretization outperforms the method of indirect discretization. The mapping between the continuous time and discrete time domain is done with the development of generating function. Continuous fraction expansion (CFE) is used expand the generating function for the rational approximation of the FOO. There is an inherent problem associated with the discretization of FOO in discrete z-domain particularly at very fast sampling rate. In the other hand, discretization using delta operator parameterization provides the continuous time and discrete time results in hand to hand, when the continuous time systems are sampled at very fast sampling rate and circumventing the problem with shift operator parameterization at fast sampling rate. In this work, a new generating function is proposed to discretize the FOO using the Gauss-Legendre 3-point quadrature rule and generating function is expanded using the CFE to form rational approximation of the FOO in delta domain. The benchmark fractional order systems are considered in this work for the simulation purpose and comparison of results are made to prove the efficacy of the proposed method using MATLAB.

1. INTRODUCTION

Nowadays, scientists and researchers are paying much more attention to the theory and application of fractional calculus (Oldham & Spanier, 1974; Miller & Ross, 1993), though it was invented more than 300 years back. The researchers are really overwhelmed to rediscover the untouched and undiscovered part of engineering application as well as in the diversified classes of science using fractional calculus (Sun et al., 1984a, 1984b; Skaar et al., 1988; Caponetto et al., 2010). Fractional calculus plays the most important role in fractional order control study. Analytical design Fractional order PID controller for fractional order or integer order plant has been studied in (Yumuk et al., 2019). Robust fractional order controller was designed by (Yumuk et al., 2022) using the ideal Bode transfer functions using the fundamental property of fractional order calculus. The fractional order calculus extends its horizon even in the field of electromagnetics. In the study of plane wave diffraction by two strips, (Tabatadze et al., 2020) have applied fractional boundary conditions on strips having different fractional order. For the analysis of complex system, fractional order derivative and partial differential equations are widely used in the field of science and technology. Caputo version (Caputo, 1967) as well as Atangana-Baleanu derivative (Atangana & Baleanu, 2016) version of fractional order derivatives are used in the literature. Garden equation is a kind of nonlinear partial differential equation, commonly used to describe

complex systems. To solve this garden equation, (Dokuyucu, 2020) have expanded the garden equation to Caputo derivative sense in order to make it fractional order.

The fundamental part of the fractional order calculus or fractional order differential equation is the fractional order operator (FOO), generally represented by $s^{\pm\mu}$. The operator can be termed as fractional order differentiator (FOD) or fractional order integrator (FOI) considering the positive and negative values of μ (Nakagawa & Sorimachi, 1992; Podlubny, 1999). The FOO needs to be converted into rational transfer function for the realization of the fractional order system (FOS). The rationalization may be done in continuous time domain or in discrete time domain. There are bench mark solutions for conversion of FOO into rational approximation in continuous time domain (Vinagre et al., 2000; Xue et al., 2006; Khanra et al., 2010).

Nowadays, there is a call for paradigm shift from the continuous time domain to discrete time domain realization of every system. This results in a serious attempt to get the FOS to be realized in discrete time domain. Therefore, the continuous time (Oustaloup, 1995) rational approximation of the FOO is to be converted into the discrete domain to realize FOS in the discrete time domain. This method is known as indirect discretization (Chen & Moore, 2002; Krishna, 2011; 2015; Maione, 2011; Keyser & Muresan, 2016) and it is having certain flaws. The problems associated with the indirect discretization is overcome with the direct discretization method.

In direct discretization method, generating functions are used to get the relationship between the s -domain and z -domain in shift operator parameterization. Euler, Tustin, Al-Alauoi are some of the renowned mathematicians to propose the new generating functions for the aforesaid application and finally the generating functions are expanded using continued fraction expansion (CFE) method (Chen et al., 2009).

As the demand is increasing day by day for the digital realization of the fractional order controller or fractional order system, the systems to be designed for maximum accuracy. To implement any FOS in discrete time domain, the continuous time systems need to be sampled with very high sampling rate. The increased sampling rate will make the results ill conditioned when implemented in discrete z -domain and also there will be issue with finite word length effect (Middleton & Goodwin, 1990a, 1990b; Chen & Moore, 2002). Therefore, the considerable features of the traditional continuous-time system cannot be produced by shift operator parameterization of discrete time systems at high sample rates. In other way around, delta operator parameterization (Middleton & Goodwin, 1990a, 1990b) provides meaningful outcome at very high sampling frequency and the results are found for both continuous time and discrete time in hand to hand rather than two special cases. The problems associated with traditional shift operator parameterization thus can be avoided using delta operator parameterization and is used in numerous application (Middleton & Goodwin, 1986; Cortés-Romero et al., 2013; Sarkar et al., 2016; Zhao & Zhang, 2017; Swarnakar et al., 2017; Gao et al., 2018; Lamrabet et al., 2020; Quezada-Téllez et al., 2020; Ganguli et al., 2021).

In this paper, the FOO is directly discretized using delta operator parameterization though direct discretization of the FOO using shift operator parameterization (Vinagre et al., 2003; Pan & Das, 2013) has been worked out in earlier work. The 3-point Gauss-Legendre quadrature rule (Khattri, 2009) is a powerful computational tool for numerical computation and this is capitalized in this paper to form the new generating function for direct discretization of FOO in delta domain. The developed generating function is expanded using the traditional CFE tool to get the rational approximation of the FOO in delta domain.

The following section discusses the significant contributions of this work. It can be observed from literature that the discretization of the fractional order system was made through the discretization of the fractional order operator in shift operator parameterization. This paper deals with the direct discretization of FOS using delta operator parameterization. At a very high sampling rate, the shift operator parameterized discrete time system fails to provide meaningful information whereas, delta operator parameterized discrete time system provides the same result as that of the continuous time system making the approach a unified one. A direct relationship between the continuous time variable and discrete delta domain variable is developed and that gives rise to a new generating function for rational approximation of the fractional order operator. The results obtained are compared with the results obtained using the other standard methods, to prove the efficacy of the proposed method.

The paper is organized as follows: Introduction to fractional order operator and direct discretization of FOO in delta domain are illustrated in section 2. In Section 3, three different examples are considered for simulation purpose to analyze the results. The section 4 is devoted for conclusion.

2. MATERIAL AND METHOD

2.1. Fractional order operator and fractional order system

A non-integer order system is literally said to be a fractional order system. Like the integer order system, any fractional order system can be described by its fractional order differential equation. A fractional order differential equation is described below (Pan & Das, 2013).

$$a_n D^{\alpha_n} y(t) + a_{n-1} D^{\alpha_{n-1}} y(t) + ... + a_0 D^{\alpha_0} y(t) = b_m D^{\beta_m} u(t) + b_{m-1} D^{\beta_{m-1}} u(t) + ... + b_0 D^{\beta_0} u(t) \tag{1}$$

where, a_i and b_j are the coefficients. D signifies the fractional derivative operator. The generalized operator used in (1) is known as integro-diffrerentiator operator and expressed as (Boubaker & Jafary, 2018):

$$_g D_t^\eta = \begin{cases} \dfrac{d^\eta}{dt^\eta} & (\eta > 0) \\ 1 & (\eta = 0) \\ \displaystyle\int_g^\eta (dt)^\eta & (\eta < 0) \end{cases} \tag{2}$$

Taking the Laplace transform on both sides of (1) considering initial condition zero, the transfer function of the fractional order system is taking the form as:

$$G(s) = \frac{Y(s)}{U(s)} = \frac{b_m D^{\beta_m} + b_{m-1} D^{\beta_{m-1}} + ... + b_0 D^{\beta_0}}{a_n D^{\alpha_n} + a_{n-1} D^{\alpha_{n-1}} + ... + a_0 D^{\alpha_0}} \tag{3}$$

where, $L[y(t)] = Y(s), L[u(t)] = U(s)$. L stands for Laplace trasform.

Mathematical representations of integro-diffrerentiator operator are usually done with the help of Grünwald-Letnikov (GL), Riemann-Liouville (RL) and Caputo derivative based approach. R-L definition is utilized in this paper to represent any fractional order system.

The RL definition is mathematically represented as:

$$_g D_t^\eta f(t) = \frac{1}{\Gamma(n-\eta)} \frac{d^n}{dt^n} \int_g^t (t-\tau)^{n-\eta-1} f(\tau) d\tau \tag{4}$$

where, g and t are the operating limits, n is an integer and $\Gamma(n-\alpha)$ is the gamma function of $(n-\alpha)$.

Taking the Laplace transform of (4) with initial condition zero, the transfer function of a FOS is obtained.

$$L\left\{ _g D_t^\eta f(t) \right\} = s^\eta F(s) \quad \text{for } 0 < \eta < 1 \tag{5}$$

From (5), it is observed that s^η plays the pivotal role for the realization of a FOS and this is known as fractional order operator (FOO), conceptualized using R-L definition.

2.2. Discretization of fractional order operator in delta domain

The delta operator is defined as:

$$\delta = \frac{q-1}{\Delta} \tag{6}$$

q is the forward shift operator and Δ is termed as sampling time. It is nothing but the scaled and shifted version of the forward shift operator. Applying the delta operator (δ) on any differentiable signal $\xi(t)$ gives the following relationship at high sampling limit ($\Delta \to 0$).

$$\underset{\Delta \to 0}{Lt} \, \delta\xi(t) = \underset{\Delta \to 0}{Lt} \, \frac{\xi(t+\Delta)-\xi(t)}{\Delta} \approx \frac{d\xi(t)}{dt} \tag{7}$$

In complex delta domain, γ is used to represent the frequency domain variable similar to z in shift operator parameterization. The relationship between these two variables are represented by (8) (Middleton & Goodwin, 1990a, 1990b)

$$\gamma = \frac{z-1}{\Delta} = \frac{e^{s\Delta}-1}{\Delta} \tag{8}$$

At high sampling time limits ($\Delta \to 0$), (8) is rewritten as

$$\underset{\Delta \to 0}{Lt}\gamma = \underset{\Delta \to 0}{Lt}\frac{e^{s\Delta}-1}{\Delta} \approx \underset{\Delta \to 0}{Lt}\frac{1+s\Delta+\frac{s^2\Delta^2}{2!}+....-1}{\Delta} = s \tag{9}$$

From (9), the relationship between the frequency domain variable γ in delta domain and frequency domain variable s in continuous time domain is established at fast sampling rate. It is observed that at fast sampling rate two domain results coincide making the approach a unified one and this philosophy is capitalized in this work. Equation (10) is established by rearranging (8).

$$e^{s\Delta} = \gamma\Delta+1$$

$$\text{or, } s = \frac{1}{\Delta}\ln(1+\gamma\Delta) \tag{10}$$

For the discretization of fractional order operator in delta domain, (10) acts as the pivotal equation. CFE is used to get the rational transfer function using the generating function in delta domain. $\ln(1+\gamma\Delta)$ has to be approximated in its closed form such that CFE can be utilized for expansion. One of the best close form approximation of $\ln(1+x)$ is 3P -GILOG which is done using trapezoidal quadrature rule (Khattri, 2009) Applying 3P -GILOG rule, $\ln(1+x)$ is approximated with an error of 0.00002548744.

$$\ln(1+x) \approx \frac{60x+60x^2+11x^3}{60+90x+36x^2+3x^3} \tag{11}$$

Equation (10) is re-established in (12) by using (11)

$$s = \left\{\frac{1}{\Delta}\ln(1+\gamma\Delta)\right\} \approx \frac{1}{\Delta}\left\{\frac{60\Delta\gamma+60\Delta^2\gamma^2+11\Delta^3\gamma^3}{60+90\gamma\Delta+36\Delta^2\gamma^2+3\Delta^3\gamma^3}\right\}$$

$$\text{or, } \quad s \approx \left\{\frac{60\gamma+60\Delta\gamma^2+11\Delta^2\gamma^3}{60+90\gamma\Delta+36\Delta^2\gamma^2+3\Delta^3\gamma^3}\right\} \tag{12}$$

The discrete-time frequency variable (γ) in delta domain coincides with the continuous-time frequency variable (s) at fast sampling limit ($\Delta \rightarrow 0$) which is again established from (12). Therefore, the direct relasionship between (γ) and (s) can be expressed by (12). Equation (12) is used as the generating function for rest of the paper.

Consider the general form of a fractional order differentiator (FOD):

$$G(s) = s^r \left(0 < r < 1\right) \tag{13}$$

Equation (13) can be used as the fractional order integrator (FOI) if r is replaced by $-r$. In general $s^{\pm r}$ is the representation of a FOO. For the direct discretization of the FOO in delta domain, generating function developed in (12) is used. This will be called as CFE3P-GILOG method. The delta domain rational is expressed by (14).

$$s^r \approx G_\delta(\gamma) \approx CFE\left\{\left(\frac{60\gamma + 60\Delta\gamma^2 + 11\Delta^2\gamma^3}{60 + 90\gamma\Delta + 36\Delta^2\gamma^2 + 3\Delta^3\gamma^3}\right)^r\right\} \tag{14}$$

The CFE approximation is mathematically formulated using (15).

$$(1+p)^q = 1 + \cfrac{qp}{1 + \cfrac{(1-q)p}{2 + \cfrac{(1+q)p}{3 + \cfrac{(2-q)p}{2 + \cfrac{(2+q)p}{5 + \cfrac{(3-q)p}{2 + \dots}}}}}} \tag{15}$$

To obtain the standard form of CFE as given in (15), p is replaced by $\left\{\left(\frac{60\gamma + 60\Delta\gamma^2 + 11\Delta^2\gamma^3}{60 + 90\gamma\Delta + 36\Delta^2\gamma^2 + 3\Delta^3\gamma^3}\right) - 1\right\}$ to get the rational approximation of fractional order trasfer function as described by (13).

Third and fifth order approximation of the rth order FOO in delta domain are obtained in this study and corresponding integer order transfer functions are given by (16) and (17) respectively.

$$s^r \approx G_{\delta3}(\gamma) = CFE\left\{\left(\frac{60\gamma + 60\Delta\gamma^2 + 11\Delta^2\gamma^3}{60 + 90\gamma\Delta + 36\Delta^2\gamma^2 + 3\Delta^3\gamma^3}\right)^r\right\} = \frac{a^0\gamma^{-3} + a^1\gamma^{-2} + a^2\gamma^{-1} + a^3}{b^0\gamma^{-3} + b^1\gamma^{-2} + b^2\gamma^{-1} + b^3} \tag{16}$$

$$s^r \approx G_{\delta5}(\gamma) = CFE\left\{\left(\frac{60\gamma + 60\Delta\gamma^2 + 11\Delta^2\gamma^3}{60 + 90\gamma\Delta + 36\Delta^2\gamma^2 + 3\Delta^3\gamma^3}\right)^r\right\} = \frac{a_0\gamma^{-5} + a_1\gamma^{-4} + a_2\gamma^{-3} + a_3\gamma^{-2} + a_4\gamma^{-1} + a_5}{b_0\gamma^{-5} + b_1\gamma^{-4} + b_2\gamma^{-3} + b_3\gamma^{-2} + b_4\gamma^{-1} + b_5} \tag{17}$$

The coefficients of fifth order approximation as given in (17) are tabulated in Table 1 and Table 2. Third order coefficients can also be generated using same method.

Table 1. *Numerator coefficients in Delta Domain (Fifth order approximation)*

$$D = \begin{pmatrix} 0.0000000000009*r^{20} +0.0000000002*r^{19}+0.0000000007*r^{18} \\ -0.0000000125*r^{17}-0.0000000938*r^{16}+0.0000002678*r^{15} \\ +0.0000041147*r^{14}+0.0000023404*r^{13}-0.0000832278*r^{12} \\ -0.0001815327*r^{11}+0.0008236971*r^{10}+0.0028742227*r^{9} \\ -0.0037642038*r^{8}-0.0219278504*r^{7}+0.0029948516*r^{6} \\ +0.0913906642*r^{5}+0.0456801094*r^{4}-0.1882914088*r^{3} \\ -0.1659256439*r^{2}+0.1311668715*r+0.1407588614 \end{pmatrix}$$

Coefficients	Numerator
a_0	$(11/3)^{\wedge}r*(-0.0000000008*r^{\wedge}(19)+0.0000808873*r^{\wedge}(13)$ $-0.0000000118*r^{\wedge}(18)+0.0189329987*r^{\wedge}(7)-0.0006421643*r^{\wedge}(11)$ $+0.0000064551*r^{\wedge}(14)-0.1370707737*r^{\wedge}(5)+0.0000000002*r^{\wedge}(20)$ $+0.3542170527*r^{\wedge}(3)-0.00000000000083*r^{\wedge}(21)-0.0347587723*r^{\wedge}(2)$ $+0.0008899811*r^{\wedge}(9)-0.0002647606*r^{\wedge}(12)+0.0000001739*r^{\wedge}(16)$ $+0.0943855158*r^{\wedge}(6)-0.2719257329*r-0.1426112993*r^{\wedge}(4)-0.0256920542*r^{\wedge}(8)$ $-0.0000043825*r^{\wedge}(15)+0.0036979198*r^{\wedge}(10)+0.0000001064*r^{\wedge}(17)$ $+0.1407588613)/(r+1)/(D)$
a_1	$(11/3)^{\wedge}r*(0.1644443976*\Delta*r^{\wedge}(4)+0.0918686023*r^{\wedge}(7)*\Delta$ $-0.0003734650*\Delta*r^{\wedge}(12)+0.0000000593*\Delta*r^{\wedge}(17)$ $-0.3878961892*r^{\wedge}(5)*\Delta-0.0000000008*\Delta*r^{\wedge}(19)+0.0007351380*\Delta*r^{\wedge}(11)$ $-0.0000066339*\Delta*r^{\wedge}(13)-0.0118943514*\Delta*r^{\wedge}(9)+0.0000000024*\Delta*r^{\wedge}(18)$ $+0.0000000004*\Delta*r^{\wedge}(20)-0.0000013710*\Delta*r^{\wedge}(15)+0.0239456455*\Delta*r^{\wedge}(6)$ $+0.0037394061*\Delta*r^{\wedge}(10)-0.5508586034*r*\Delta+0.5687601324*\Delta-0.0000004127*\Delta*r^{\wedge}(16)$ $+0.0000185012*\Delta*r^{\wedge}(14)-0.6689646772*\Delta*r^{\wedge}(2)+0.8039575376*\Delta*r^{\wedge}(3)$ $-0.0180971662*\Delta*r^{\wedge}(8))/(r+1)/(D)$
a_2	$(11/3)^{\wedge}r*(-0.0000001311*r^{\wedge}(16)*\Delta*2-0.0000027603*r^{\wedge}(13)*\Delta*2$ $+0.3130657428*r^{\wedge}(4)*\Delta*2+0.4267807131*r^{\wedge}(3)*\Delta*2+0.0000044924*r^{\wedge}(14)*\Delta*2$ $+0.0006386468*r^{\wedge}(11)*\Delta*2-0.0000629870*r^{\wedge}(12)*\Delta*2-0.0000000009*\Delta\Delta2*r^{\wedge}(19)$ $+0.0536655937*r^{\wedge}(7)*\Delta*2+0.0000000015*r^{\wedge}(18)*\Delta*2-0.0077595346*\Delta\Delta2*r^{\wedge}(9)$ $-0.0000000005*r^{\wedge}(17)*\Delta*2+0.0051773501*\Delta\Delta2*r^{\wedge}(8)+0.0000005116*r^{\wedge}(15)*\Delta*2$ $-0.2848454910*r*\Delta r2-0.7146110314*r^{\wedge}(2)*\Delta*2-0.2137256757*r^{\wedge}(5)*\Delta*2$ $+0.5083225658*\Delta\Delta2+0.0001514540*r^{\wedge}(10)*\Delta*2-0.061671367*r^{\wedge}(6)*\Delta*2)/(r+1)/(D)$
a_3	$(11/3)^{\wedge}r*(0.0001204050*r^{\wedge}(11)*\Delta^{\wedge}3+0.0000001372*\Delta^{\wedge}3*r^{\wedge}(15)$ $-0.0014131743*r^{\wedge}(9)*\Delta^{\wedge}3+0.0000093853*r^{\wedge}(12)*\Delta^{\wedge}3$ $+0.0766858880*r^{\wedge}(3)*\Delta^{\wedge}3-0.0000000204*\Delta^{\wedge}3*r^{\wedge}(14)-0.0000057087*r^{\wedge}(13)*\Delta^{\wedge}3$ $-0.0000000056*\Delta^{\wedge}3*r^{\wedge}(16)+0.15779943*\Delta^{\wedge}3+0.0000000001*r^{\wedge}(18)*\Delta^{\wedge}3$ $-0.0000000014*\Delta^{\wedge}3*r^{\wedge}(17)-0.0509720473*r*\Delta^{\wedge}3+0.1140054487*\Delta^{\wedge}3*r^{\wedge}(4)$ $+0.0096773395*r^{\wedge}(7)*\Delta^{\wedge}3-0.2337211260*\Delta^{\wedge}3*r^{\wedge}(2)-0.0002793147*r^{\wedge}(10)*\Delta^{\wedge}3$ $-0.0384625577*r^{\wedge}(5)*\Delta^{\wedge}3+0.0037561161*r^{\wedge}(8)*\Delta^{\wedge}3$ $-0.0275056629*\Delta^{\wedge}3*r^{\wedge}(6))/(r+1)/(D)$
a_4	$(11/3)^{\wedge}r*(-0.0029236890*r*\Delta^{\wedge}4+0.0000064494*r^{\wedge}(11)*\Delta^{\wedge}4$ $-0.0000465989*r^{\wedge}(10)*\Delta^{\wedge}4+0.0043795008*r^{\wedge}(3)*\Delta^{\wedge}4-0.0300922900*\Delta^{\wedge}4*r^{\wedge}(2)$ $-0.0000770354*r^{\wedge}(9)*\Delta^{\wedge}4+0.0150541247*\Delta^{\wedge}4*r^{\wedge}(4)+0.0000000005*\Delta^{\wedge}4*r^{\wedge}(16)$ $+0.0000000070*\Delta^{\wedge}4*r^{\wedge}(15)-0.0037739418*\Delta^{\wedge}4*r^{\wedge}(6)-0.0000003008*r^{\wedge}(13)*\Delta^{\wedge}4$ $+0.0005489612*r^{\wedge}(8)*\Delta^{\wedge}4+0.0005371903*r^{\wedge}(7)*\Delta^{\wedge}4+0.0000022018*r^{\wedge}(12)*\Delta^{\wedge}4$ $-0.0000000007*\Delta^{\wedge}4*r^{\wedge}(17)+0.0200212359*\Delta^{\wedge}4-0.0000000526*\Delta^{\wedge}4*r^{\wedge}(14)$ $-0.0021709653*r^{\wedge}(5)*\Delta^{\wedge}4)/(r+1)/(D)$
a_5	$(11/3)^{\wedge}r*(-0.0000000021*\Delta^{\wedge}5*r^{\wedge}(14)+0.0006633505*\Delta^{\wedge}5*r^{\wedge}(4)$ $+0.0000000002*\Delta^{\wedge}5*r^{\wedge}(16)+0.0000000919*\Delta^{\wedge}5*r^{\wedge}(12)-0.0001641415*\Delta^{\wedge}5*r^{\wedge}(6)$ $+0.0000235385*\Delta^{\wedge}5*r^{\wedge}(8)-0.0000019706*\Delta^{\wedge}5*r^{\wedge}(10)+0.0008933494*\Delta^{\wedge}5$ $-0.0013381808*\Delta^{\wedge}5*r^{\wedge}(2))/(r+1)/(D)$

Table 2. *Denominator coefficients in Delta Domain (Fifth order approximation)*

Coefficients	Denominator
b_0	$(0.0000000000008*r\char94(21)+0.0000000002*r\char94(20)+0.0000000008*r\char94(19)$ $-0.0000000118*r\char94(18)-0.0000010632*r\char94(17)+0.0000001739*r\char94(16)+0.0000043825*r\char94(15)$ $+0.0000064551*r\char94(14)-0.0000808873*r\char94(13)-0.0002647606*r\char94(12)+0.0006421643*r\char94(11)$ $+0.0036979198*r\char94(10)-0.0008899811*r\char94(9)-0.0256920542*r\char94(8)-0.0189329987*r\char94(7)$ $+0.0943855158*r\char94(6)+0.1370707737*r\char94(5)-0.1426112993*r\char94(4)-0.3542170527*r\char94(3)$ $-0.0347587723*r\char94(2)+0.2719257329*r+0.1407588613)/(r+1)/(D)$
b_1	$(0.1644434976*\Delta*r\char94(4)-0.9186860239*r\char94(7)*\Delta-0.0003734650*\Delta*r\char94(12)$ $-0.0000000593*\Delta*r\char94(17)+0.3878961892*r\char94(5)*\Delta+0.0000000009*\Delta*r\char94(19)$ $-0.0007351380*\Delta*r\char94(11)+0.0000066339*\Delta*r\char94(13)+0.0118943514*\Delta*r\char94(9)$ $+0.0000000023*\Delta*r\char94(18)+0.0000000004*\Delta*r\char94(20)+0.0000013710*\Delta*r\char94(15)$ $+0.0239456455*\Delta*r\char94(6)+0.0037394061*\Delta*r\char94(10)+0.5508586034*r*\Delta$ $+0.5687601324*\Delta-0.0000004127*\Delta*r\char94(16)+0.0000185012*\Delta*r\char94(14)$ $-0.6689646772*\Delta*r\char94(2)-0.8039575376*\Delta*r\char94(3)$ $-0.0180971662*\Delta*r\char94(8))/(r+1)/(D)$
b_2	$(-0.0000001311*r\char94(16)*\Delta\char94 2+0.0000276031*r\char94(13)*\Delta\char94 2$ $+0.3130657428*r\char94(4)*\Delta\char94 2-0.4267807131*r\char94(3)*\Delta\char94 2+0.0000044924*r\char94(14)*\Delta\char94 2$ $-0.0006386468*r\char94(11)*\Delta\char94 2-0.0000062987066*r\char94(12)*\Delta\char94 2+0.0000000009*\Delta\char94 2*r\char94(19)$ $-0.0536655937*r\char94(7)*\Delta\char94 2+0.0000000014807*r\char94(18)*\Delta\char94 2+0.0077595346*\Delta\char94 2*r\char94(9)$ $+0.0000000009*r\char94(17)*\Delta\char94 2+0.0051773501*\Delta\char94 2*r\char94(8)-0.0000005116*r\char94(15)*\Delta\char94 2$ $+0.2848454910*r*\Delta\char94 2-0.7146110314*r\char94(2)*\Delta\char94 2+0.2137256757*r\char94(5)*\Delta\char94 2$ $+0.5083225658*\Delta\char94 2+0.0001514540*r\char94(10)*\Delta\char94 2$ $-0.0616713*r\char94(6)*\Delta\char94 2)/(r+1)/(D)$
b_3	$(-0.0001204050*r\char94(11)*\Delta\char94 3-0.0000001372*\Delta\char94 3*r\char94(15)+0.0014131743*r\char94(9)*\Delta\char94 3$ $+0.0000093853*r\char94(12)*\Delta\char94 3-0.0766858880*r\char94(3)*\Delta\char94 3-0.0000000204*\Delta\char94 3*r\char94(14)$ $+0.0000057087*r\char94(13)*\Delta\char94 3-0.0000000056*\Delta\char94 3*r\char94(16)+0.1577994381*\Delta\char94 3$ $+0.0000000010*r\char94(18)*\Delta\char94 3+0.0000000014*\Delta\char94 3*r\char94(17)+0.0509720473*r*\Delta\char94 3$ $+0.1140054487*\Delta\char94 3*r\char94(4)-0.0096773395*r\char94(7)*\Delta\char94 3-0.2337211260*\Delta\char94 3*r\char94(2)$ $-0.0002793147*r\char94(10)*\Delta\char94 3+0.0384625577*r\char94(5)*\Delta\char94 3+0.0037561161*r\char94(8)*\Delta\char94 3$ $-0.0275056629*\Delta\char94 3*r\char94(6))/(r+1)/(D)$
b_4	$(0.0029236890*r*\Delta\char94 4-0.0000064494*r\char94(11)*\Delta\char94 4$ $-0.0000465989*r\char94(10)*\Delta\char94 4-0.0043795008*r\char94(3)*\Delta\char94 4-0.0300922900*\Delta\char94 4*r\char94(2)$ $+0.0000770354*r\char94(9)*\Delta\char94 4+0.0150541247*\Delta\char94 4*r\char94(4)+0.0000000006*\Delta\char94 4*r\char94(16)$ $-0.0000000054*\Delta\char94 4*r\char94(15)-0.0037739418*\Delta\char94 4*r\char94(6)+0.0000003008*r\char94(13)*\Delta\char94 4$ $+0.0005489612*r\char94(8)*\Delta\char94 4-0.0005371903*r\char94(7)*\Delta\char94 4+0.00000022011*r\char94(12)*\Delta\char94 4$ $+0.0000000007*\Delta\char94 4*r\char94(17)+0.0200212359*\Delta\char94 4-0.0000000526*\Delta\char94 4*r\char94(14)$ $+0.0021709653*r\char94(5)*\Delta\char94 4)/(r+1)/(D)$
b_5	$(-0.0000000021*\Delta\char94 5*r\char94(14)+0.0006633505*\Delta\char94 5*r\char94(4)+0.0000000002*\Delta\char94 5*r\char94(16)$ $+0.0000000919*\Delta\char94 5*r\char94(12)-0.0001641415*\Delta\char94 5*r\char94(6)+0.0000235385*\Delta\char94 5*r\char94(8)$ $-0.0000001970*\Delta\char94 5*r\char94(10)+0.0008933494*\Delta\char94 5$ $-0.0013381808*\Delta\char94 5*r\char94(2))/(r+1)/(D)$

3. SIMULATION AND RESULT ANALYSIS

Here, three different fractional order transfer functions are considered as examples for simulation study to find the efficacy of the proposed method.

Example 1:

A half order differentiator ($1/2^{nd}$) is considered in this example (Swarnakar et al., 2017) with transfer function as shown below:

$$G(s) = s^{0.5} \tag{18}$$

In delta domain, the mathematical formulation of the $1/2^{nd}$ order differentiator is expressed by (19) where, the sampling rate is considered as $\Delta = 0.01 \, \text{sec}$.

$$s^{0.5} \approx G_{CFE\text{-}3P\text{-}GILOGdel}(\gamma) \approx CFE\left\{ \left(\frac{60\gamma + 60\Delta\gamma^2 + 11\Delta^2\gamma^3}{60 + 90\gamma\Delta + 36\Delta^2\gamma^2 + 3\Delta^3\gamma^3} \right)^{0.5} \right\}_{\Delta=0.01} \tag{19}$$

For a sampling rate of $\Delta = 0.01$ sec, The third and fifth order approximation of $s^{0.5}$ in delta domain after continued fraction expansion of $\left(\frac{60\gamma + 60\Delta\gamma^2 + 11\Delta^2\gamma^3}{60 + 90\gamma\Delta + 36\Delta^2\gamma^2 + 3\Delta^3\gamma^3} \right)^{0.5}$ results in Eq. (20) and Eq. (21) respectively.

$$s^{0.5} \approx G_{CFE\text{-}3P\text{-}GOLOGdel3}(\gamma) \approx$$

$$CFE\left\{ \left(\frac{60\gamma + 60\Delta\gamma^2 + 11\Delta^2\gamma^3}{60 + 90\gamma\Delta + 36\Delta^2\gamma^2 + 3\Delta^3\gamma^3} \right)^{0.5} \right\}_{\Delta=0.01} = \frac{0.3932\,\gamma^3 + 0.01202\,\gamma^2 + 3.91e\text{-}05\,\gamma^1 + 3.191e\text{-}08}{\gamma^3 + 0.01114\,\gamma^2 + 2.587e\text{-}05\,\gamma^3 + 1.667e\text{-}08} \tag{20}$$

$$s^{0.5} \approx G_{CFE\text{-}3P\text{-}GILOGdel5}(\gamma) \approx$$

$$CFE\left\{ \left(\frac{60\gamma + 60\Delta\gamma^2 + 11\Delta^2\gamma^3}{60 + 90\gamma\Delta + 36\Delta^2\gamma^2 + 3\Delta^3\gamma^3} \right)^{0.5} \right\}_{\Delta=0.01} \tag{21}$$

$$= \frac{0.2495\,\gamma^5 + 0.001962\,\gamma^4 + 2.198e\text{-}06\,\gamma^3 + 7.738e\text{-}10\,\gamma^2 + 1.078e\text{-}13\,\gamma + 5.195e\text{-}18}{\gamma^5 + 0.002716\,\gamma^4 + 2.013e\text{-}06\,\gamma^3 + 5.587e\text{-}10\,\gamma^2 + 6.517e\text{-}14\,\gamma + 2.713e\text{-}18}$$

For $G_{CFE\text{-}3P\text{-}GILOGdel5}(\gamma)$, Table 1 and Table 2 are used to compute the coefficients for the numerator and denominator taking $r = 0.5$ and $\Delta = 0.01$ sec. The frequency responses of delta domain transfer functions for both 3rd order and 5th order approximations are demonstrated in Figure 1. The magnitude and phase error in frequency responses for $G_{CFE\text{-}3P\text{-}GILOGdel3}(\gamma)$ and $G_{CFE\text{-}3P\text{-}GILOGdel5}(\gamma)$ are shown in Figure 2. The error in magnitude and phase are calculated with respect to the frequency response characteristics of the continuous time half order differentiator. It can be observed that the higher order approximation gives more closer result to the original half order differentiator.
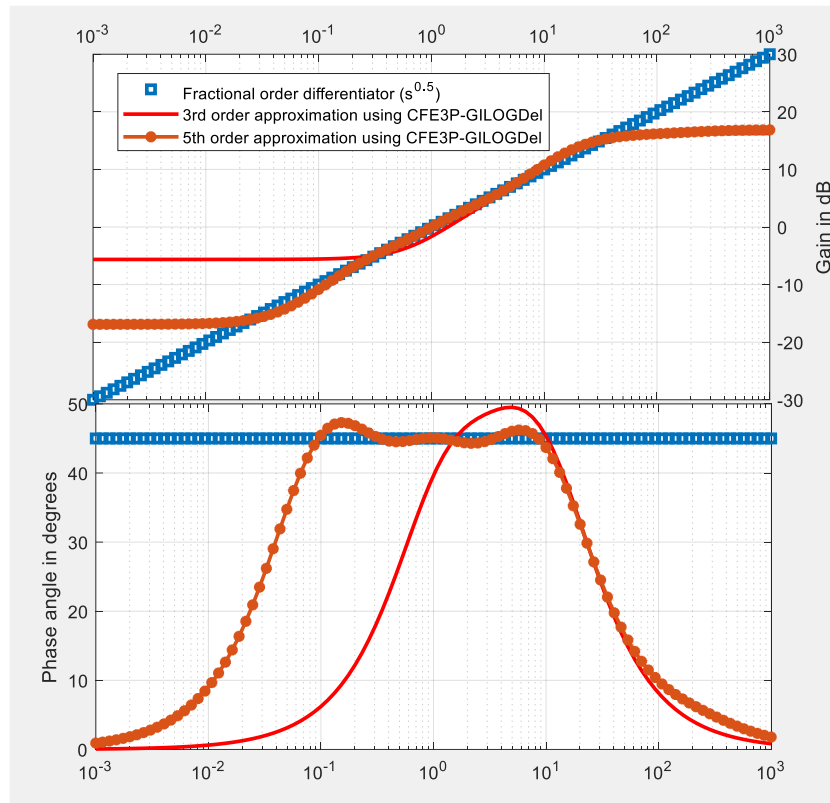
Figure 1. *Fifth order and third order approximation of $s^{0.5}$ in delta domain using proposed method (Frequency Response)*
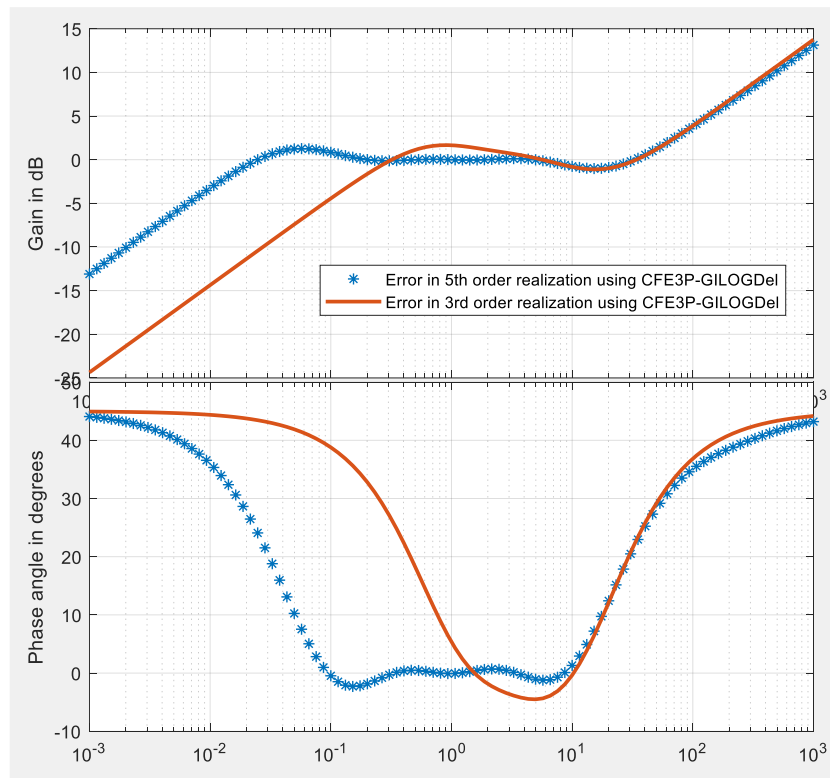

Figure 2. *Error comparison between fifth order and third order approximation of $s^{0.5}$ in delta domain using proposed method (magniude error and phase error)*

The magnitude response is more closer to the original half order diffrentiator than the phase response characteristics for a wide range of frequency. The error in frequency response characteristics between original system and rational approximation is compared on the basis of the maximum absolute values of magnitude and phase error and these values are tabulated in Table 3.

Table 3. *Absolute maximum phase error and magnitude error for discretization of 0.5th- order differentiator using CFE-3P-GILOGDel*

| Approximation order	Maximum magnitude error (dB)	Maximum phase error (Degree)
Fifth	0.862	4.563
Third	1.02	27.5

The fifth order CFE approximation has been employed to develop the frequency responses for the various systems taken into consideration in this study since the approximation findings for the fifth order are more evident than those for the third order. At a sampling time of $\Delta = 0.01s$, the fifth order rational approximation of $1/2^{nd}$ order differentiator is considered to be realized in discrete time domain based upon the four methods described in this paper namely CFE of Euler (CFEEuler), CFE of Tustin (CFETust), CFEDO and CFE of 3P-GILOG in Delta domain (CFE-3P-GILOGdel) and following rational transfer functions are obtained.

$$G_{CFEEuler5}(z)\big|_{\Delta=0.01} = \frac{3940 - 6402\,z^{-1} + 1724\,z^{-2} + 1116\,z^{-3} - 324.2\,z_{-4} - 23.69\,z^{-5}}{124.6 - 109\,z^{-1} - 38.94\,z^{-2} + 30.9\,z^{-3} + 3.62\,z^{-4} - z^{-5}} \qquad (22)$$

$$G_{CFETust5}(z)\big|_{\Delta=0.01} = \frac{5572 - 9054\,z^{-1} + 2438\,z^{-2} + 1578\,z^{-3} - 458.4\,z^{-4} - 33.5\,z^{-5}}{124.6 - 109\,z^{-1} - 38.94\,z^{-2} + 30.9\,z^{-3} + 3.62\,z^{-4} - z^{-5}} \qquad (23)$$

$$G_{CFEDO5}(\gamma)\big|_{\Delta=0.01} = \frac{1.641e\text{-}06\,\gamma^6 + 0.001001\gamma^5 + 0.2051\gamma^4 + 14.45\gamma^3 + 66.61\gamma^2 + 39.43\gamma + 1.875}{2.344e\text{-}07\,\gamma^6 + 0.0001505\gamma^5 + 0.03308\gamma^4 + 2.676\gamma^3 + 41.02\gamma^2 + 66.02\gamma + 13.13} \qquad (24)$$

$$G_{CFE\text{-}3P\text{-}GILOGdel5}(\gamma\gamma)\big|_{\Delta=0.01} = \frac{\gamma^5 + 0.02716\gamma^4 + 0.0002013\gamma^3 + 5.587e\text{-}07\,\gamma^2 + 6.517e\text{-}10\,\gamma\gamma + 2.713e\text{-}13}{0.2495\,\gamma^5 + 0.01962\gamma^4 + 0.0002198\gamma^3 + 7.738e\text{-}07\,\gamma^2 + 1.078e\text{-}09\,\gamma\gamma + 5.195e\text{-}13} \qquad (25)$$
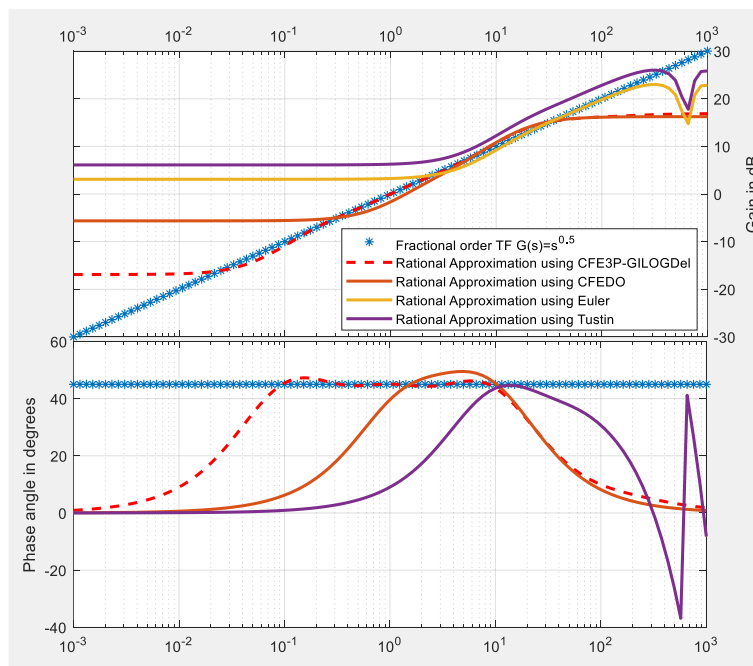
Figure 3. *Frequency response comparison after discretization of G*(s) *using four methods for r=0.5 and Δ=0.01*

Example 2: A fractional order system is considered (Baranowski et al., 2015).

$$G_1(s) = \frac{0.5863}{0.2318s^{0.958}+1} \tag{26}$$

For the discretization of the above system, sampling time considered is $\Delta = 0.0001$ sec. The discretization of this fractional order transfer function results in four rational approximation T.F. as given by (27), (28), (29) and (30) by using four methods as mentioned in earlier section.

$$G_{1CFEEuler5}(z)\big|_{\Delta=0.0001} = \frac{14.33 + 11.93\,z^{-1} - 10.72\,z^{-2} - 8.061\,z^{-3} + 1.169\,z^{-4} + 0.5863\,z^{-5}}{3.85e04 - 4.01e04\,z^{-1} - 2.275e04\,z^{-2} + 2.489e04\,z^{-3} + 1182\,z^{-4} - 1665\,z^{-5}} \tag{27}$$

$$G_{1CFETust5}(z)\big|_{\Delta=0.0001} = \frac{14.33 + 11.93\,z^{-1} - 10.72\,z^{-2} - 8.061\,z^{-3} + 1.169\,z^{-4} + 0.5863\,z^{-5}}{7.476e04 - 7.792e04\,z^{-1} - 4.417e04\,z^{-2} + 4.837e04\,z^{-3} + 2294\,z^{-4} - 3236\,z^{-5}} \tag{28}$$

$$G_{1CFEDO5}(\gamma)\big|_{\Delta=0.0001} = \frac{20.57\,\gamma^5 - 946.2\,\gamma^4 + 1.435e005\,\gamma^3 + 2.697e005\,\gamma^2 + 1.311e005\,\gamma + 1.27e004}{5061\,\gamma^5 + 5.024e004\,\gamma^4 + 3.515e005\,\gamma^3 + 5.168e005\,\gamma^2 + 2.233e005\,\gamma\gamma + 2.168e004} \tag{29}$$

$$G_{1\,CFE-3P-GILOGdel5}(\gamma)\big|_{\Delta=0.0001} = \frac{0.5863\,\gamma^5 + 0.0001124\gamma^4 + 6.915e\text{-}09\,\gamma^3 + 1.719e\text{-}13\,\gamma^2 + 1.852e\text{-}18\,\gamma\gamma + 7.24e\text{-}24}{1.003\,\gamma^5 + 0.0002162\gamma^4 + 1.506e\text{-}08\,\gamma^3 + 4.202e\text{-}13\,\gamma^2 + 5.079e\text{-}18\,\gamma\gamma + 2.229e\text{-}23} \tag{30}$$
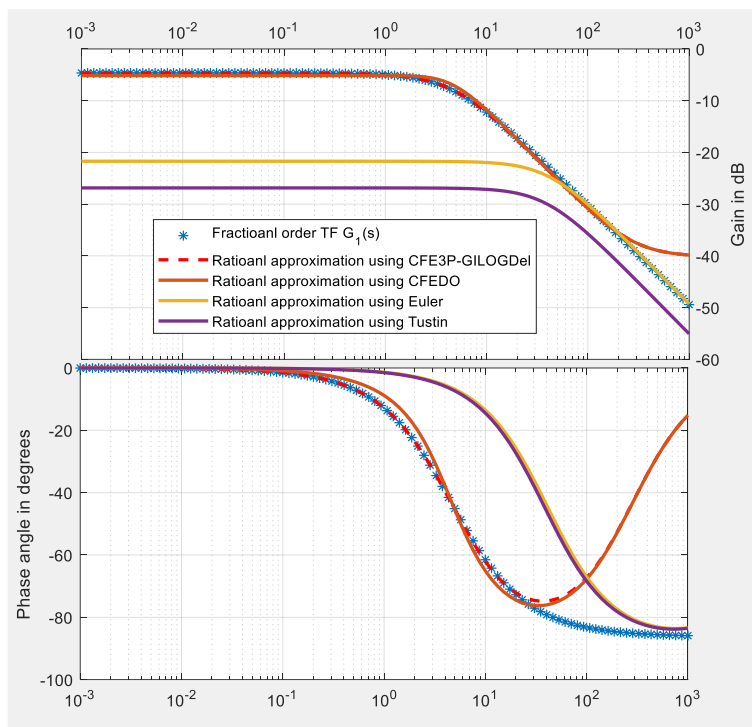
Figure 4. *Frequency response comparison after discretization of $G_1(s)$ using four methods for r=0.958 and Δ=0.0001*

Example 3:

The FO system (Kothari et al., 2019) is chosen and the transfer function is given as:

$$G_2(s) = \frac{0.979}{0.997s^{0.716}+0.9} \tag{31}$$

A higher sampling rate is considered in this case to discretize the system function represented by (31). The sampling rate is considered as $\Delta = 0.00001s$. CFEEuler, CFE Tust, CFEDO and CFE-3P-GILOGdel are the

four methods used to discretize this continuous time transfer function results in four rational approximation T.F. as given by (32), (33), (34) and (35) respectively.

$$G_{2CFEEuler5}(z)\big|_{\Delta=0.00001} = \frac{23.92 + 19.93\,z^{-1} - 17.9\,z^{-2} - 13.46\,z^{-3} + 1.953\,z^{-4} + 0.979\,z^{-5}}{1.655e05 - 1.726e05\,z^{-1} - 9.778e04\,z^{-2} + 1.071e05\,z^{-3} + 5076\,z^{-4} - 7165\,z^{-5}} \tag{32}$$

$$G_{2CFETustin5}(z)\big|_{\Delta=0.00001} = \frac{23.92 + 19.93\,z^{-1} - 17.9\,z^{-2} - 13.46\,z^{-3} + 1.953\,z^{-4} + 0.979\,z^{-5}}{3.215e05 - {}^3.352e05\,z^{-1} - 1.899e05\,z^{-2} + 2.081e05\,z^{-3} + 9858\,z^{-4} - 1.392e04\,z^{-5}} \tag{33}$$

$$G_{2CFEDO5}(\gamma)\big|_{\Delta=0.00001} = \frac{925.4\,\gamma^5 + 4.38e004\,\gamma^4 + 3.058e005\,\gamma^3 + 4.274e005\,\gamma^2 + 1.527e005\gamma + 1.018e004}{1.13e004\,\gamma^5 + 1.995e005\,\gamma^4 + 7.43e005\,\gamma^3 - 2.905e030\,\gamma^2 + 1.982e005\,\gamma + 1.118e004} \tag{34}$$

$$G_{2\ CFE-3P-GILOGdel5}(\gamma)\big|_{\Delta=0.00001} = \frac{0.979\,\gamma^5 + 2.301e{-}05\,\gamma^4 + 1.581e{-}10\,\gamma^3 + 4.188e{-}16\,\gamma^2 + 4.719e{-}22\,\gamma\gamma + 1.909e{-}28}{1.093\,\gamma^5 + 3.777e{-}05\,\gamma^4 + 3.415e{-}10\,\gamma^3 + 1.101e{-}15\,\gamma^2 + 1.462e{-}21\,\gamma\gamma + 6.851e{-}28} \tag{35}$$
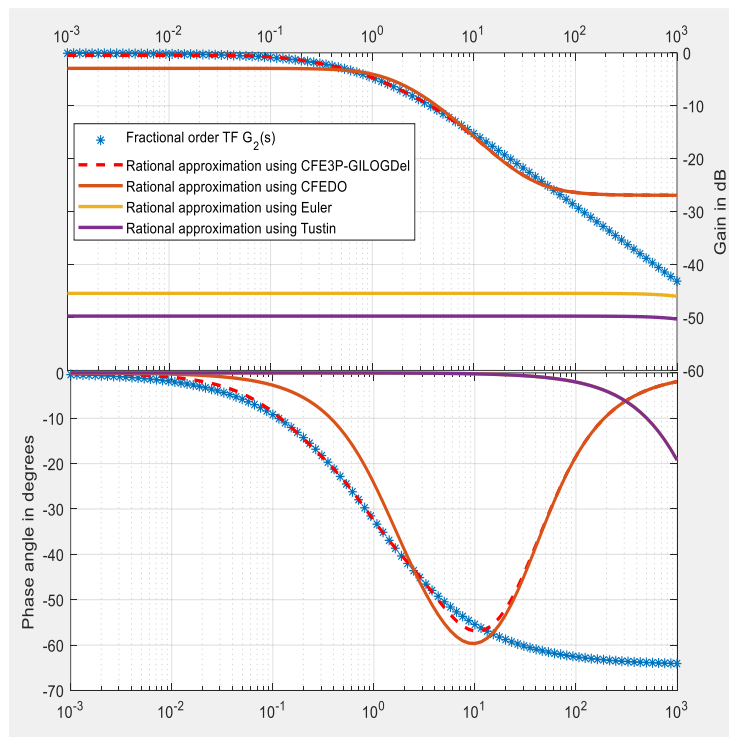
Figure 5. *Frequency response comparison after discretization of $G_2(s)$ using four methods for r=0.716 and Δ=0.00001*

Four different methods including the proposed method are used in this work to discretize the fractional order operator contained in three different continuous time fractional order systems. All systems' frequency responses (in fractional order), as well as the related discrete-time systems' frequency responses in shift as well as delta operator paramerterized domain are shown in Figure 3, Figure 4 and Figure 5 respectively. The magnitude approximation turns out to be superior over the phase approximation as can be shown from the above results. CFE-3P-GILOGDel produces the excellent frequency responses in the frequency range of (0.001 rad/s to 1000 rad/sec) for all the three cases mentioned above. The proposed method is thus more promising than the other three approaches for discretization of fractional order system or operator in discrete time domain. Additionally, the superiority of the suggested approach is demonstrated by a comparison of the results with another method created in the delta domain. From Figure 5, it can be observed that at high sampling time ($\Delta=0.00001$ sec), the frequency responses using The CFE-3P-GILOGDel method is very much closer to the frequency responses of the corresponding continuous time system. Therefore, the continuous time findings and the discrete time results with high sampling rate in delta domain are obtained in hand to hand, leading to the development of a unified framework for direct discretization o FOO in complex delta domain.

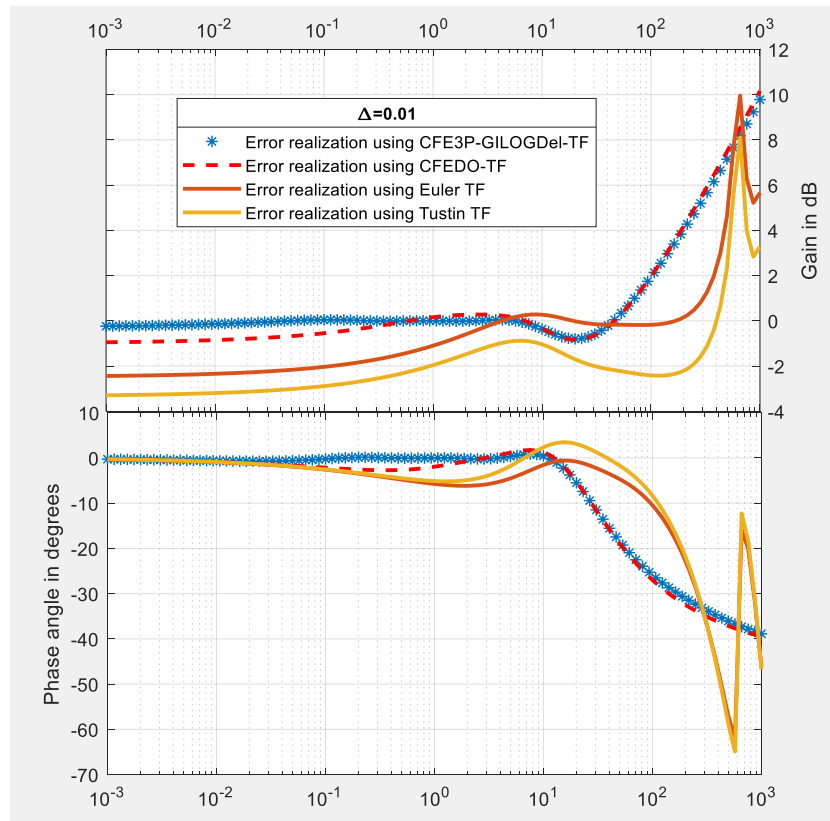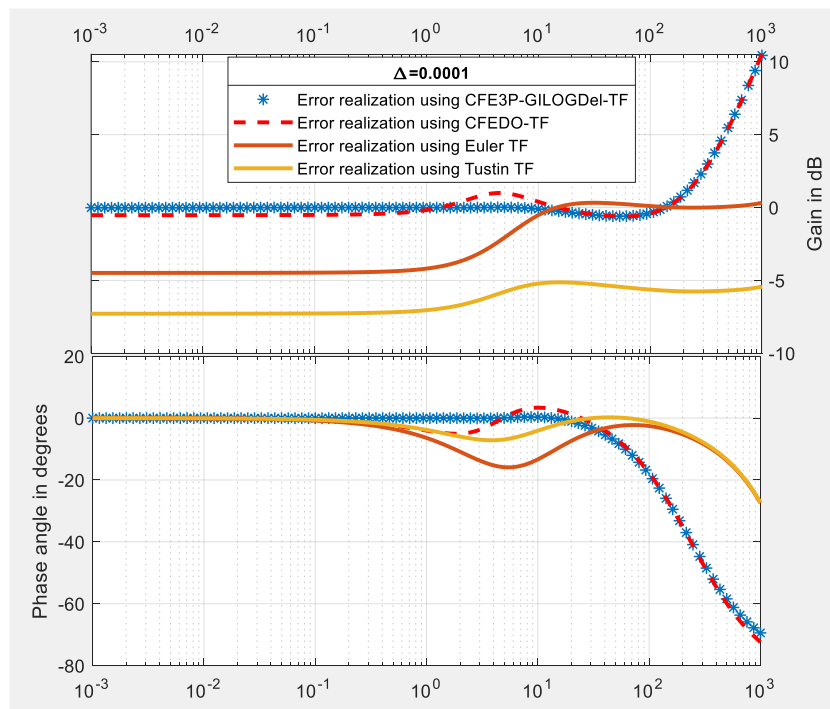**Figure 6.** *Magnitude and phase error after discretization of* $G(\mathrm{s})$ *using four methods, at r=0.5 and* Δ*=0.01*

Figure 7. *Magnitude and phase error after discretization of* $G_1(\mathrm{s})$ *using four methods at r=0.958 and* Δ*=0.0001*
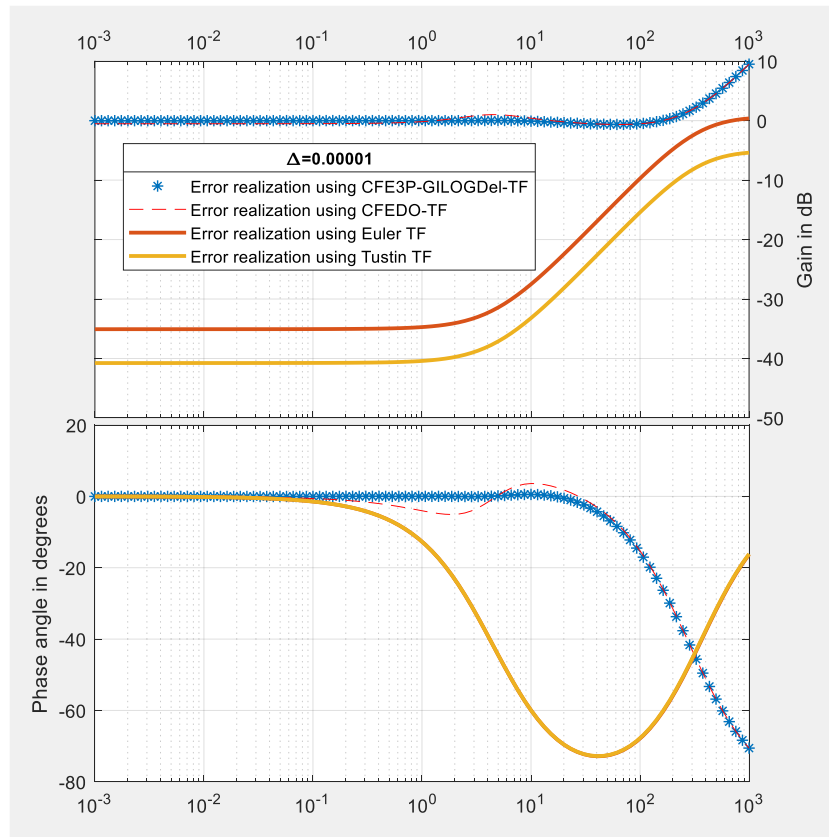
Figure 8. *Magnitude and phase error after discretization of G_2(s) using four methods at r=0.716 and Δ=0.00001*

The error in approximation of the fractional order operators using four methods are shown in Figure 6, Figure 7 and Figure 8. In each system, magnitude and phase errors are calculated through the absolute value of maximum magnitude and phase error using each of the four methods and they are tabulated in Table 4.

Table 4. *Absolute maximum magnitude error and phase error for four discretization methods for different systems*

FOS	Maximum magnitude error (dB)				Maximum phase error (degree)			
	CFE-3P GILOG Del	CFEDO	Euler	Tustin	CFE-3P GLOGD el	CFEDO	Euler	Tustin
$G(s) = s^{0.5}$	13.1065	24.3833	53.0980	56.1083	44.0834	44.9375	45	45
$G_1(s) = \dfrac{0.5863}{0.2318s^{0.958} + 1}$	9.5916	9.4648	17.0709	22.2271	47.0785	47.8811	10.7379	70.7052
$G_2(s) = \dfrac{0.979}{0.997s^{0.716} + 0.985}$	16.2447	16.2449	31.2399	35.4573	54.7988	54.8412	62.1541	62.1493

For the systems described in example 1, example 2 and example 3, the errors in magnitude and phase are less when the system is discretized using CFE3PGILOGDel method of discretization in delta domain than the other methods. At a very high limiting value of sampling rate, $\Delta = 0.00001s$, the maximum absolute magnitude error and phase error is much higher in case of discretization using Tustin and Euler method in z-domain in comparison to the discretization using delta operator parameterization. The results is visualized be visualized from Figure 8. The proposed method is proved to be superior as compared to the other methods in the literature for all three examples as stated in this paper.

The pole and zero positions of the rational transfer functions obtained using four different methods are calculated and plotted in Figure 9, Figure 10, Figure 11 and Figure 12.
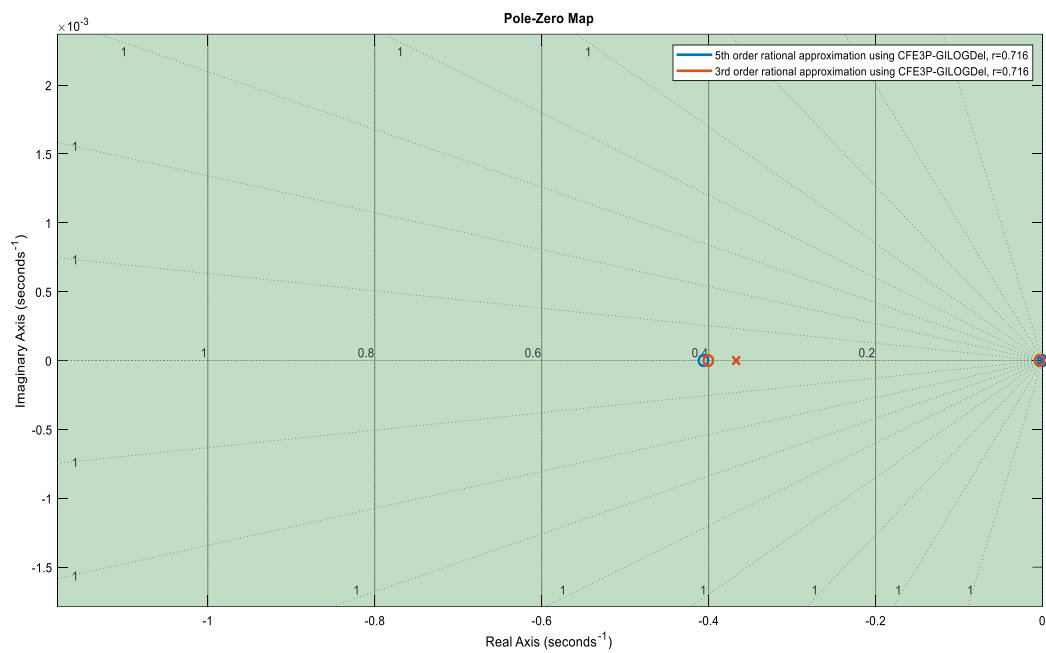
Figure 9. *The pole zero plot of third-order and fifth order approximation of $s^{0.716}$using CFE-3P-GILOGDel*

Another delta domain based discretization method (CFEDO) is adopted in this paper to discretize the fractional order operator. From Table 4, the superiority of the proposed method over CFEDO in terms of magnitude and phase error of approximation is explained. The pole–zero plot for the rational approximation of $s^{0.716}$ using CFE3GILOGDEl method and CFEDO method are shown in Figure 9 and Figure 10 respectively. It can be observed from Figure 10 that the system's rational transfer function is unstable because the system's poles are located in an unstable area, as opposed to how the poles were produced using third-order and fifth-order approximations using CFE3GILOGDEl are lying in the stable region as can be observed in Figure 9. Therefore, it is evident that the proposed method delivers preferable approximation amidst all the four discretization methods and is a viable alternative in the literature of direct discretization of fractional order operator in delta domain.

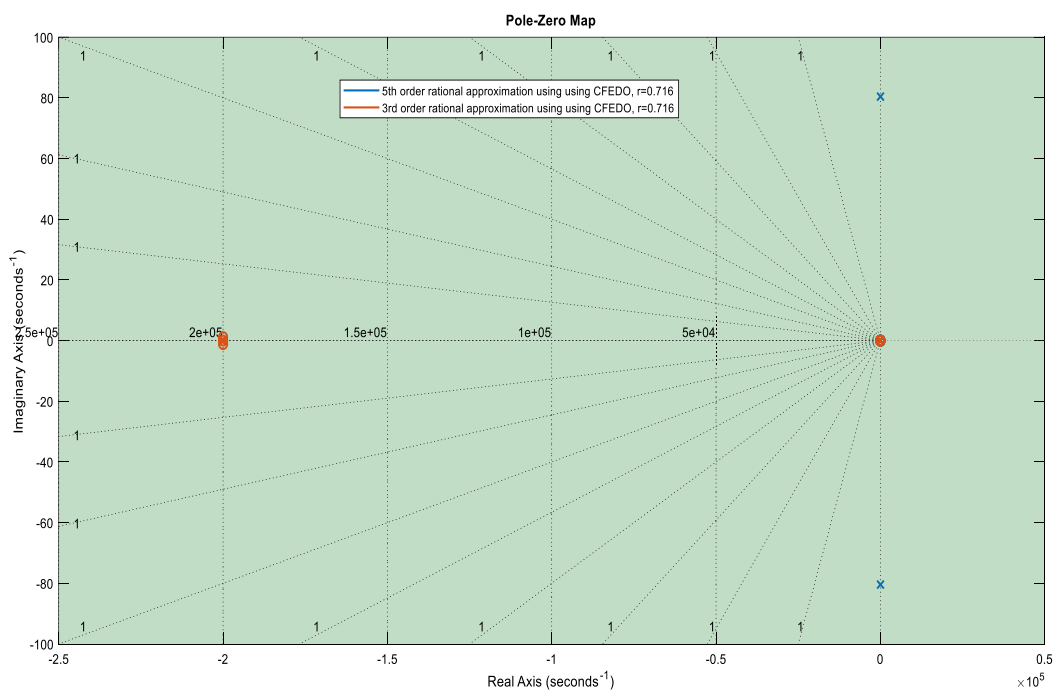***Figure 10.*** *The pole zero plot of third-order and fifth order approximation of $s^{0.716}$using CFE-DO method*
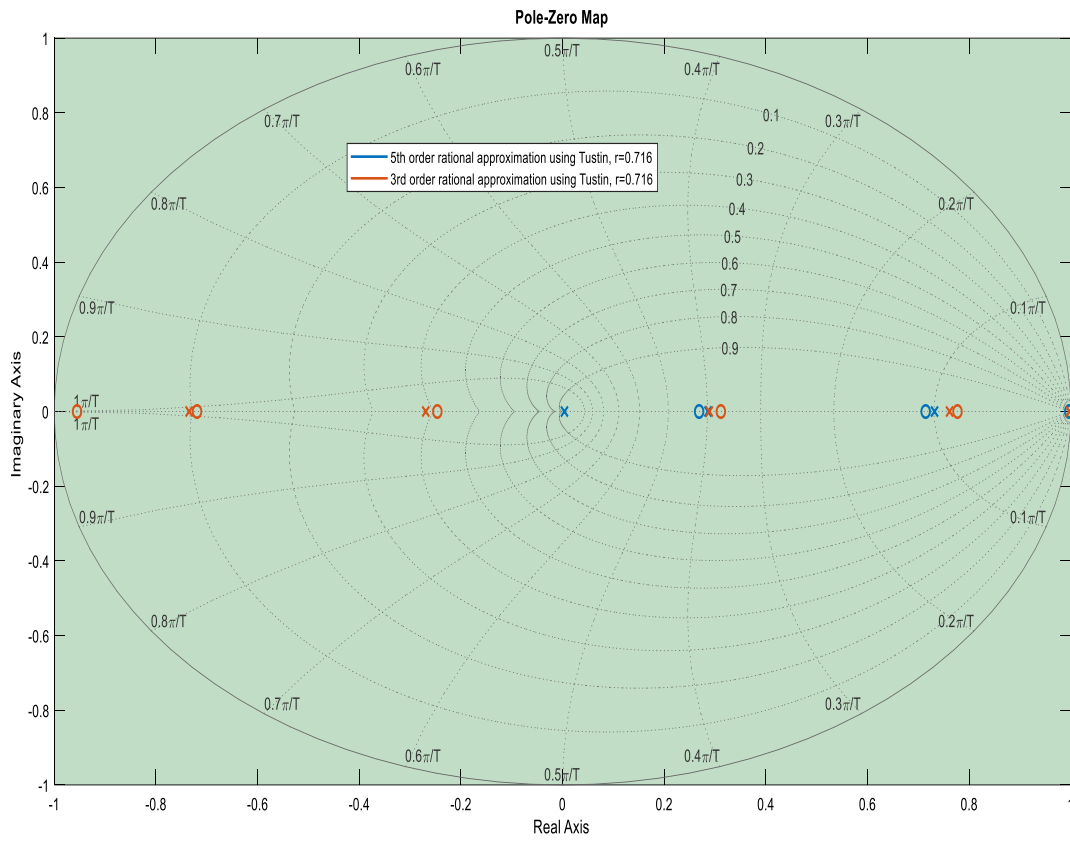
Figure 11. *The pole zero plot of third-order and fifth order approximation of $s^{0.716}$ using Tustin method*
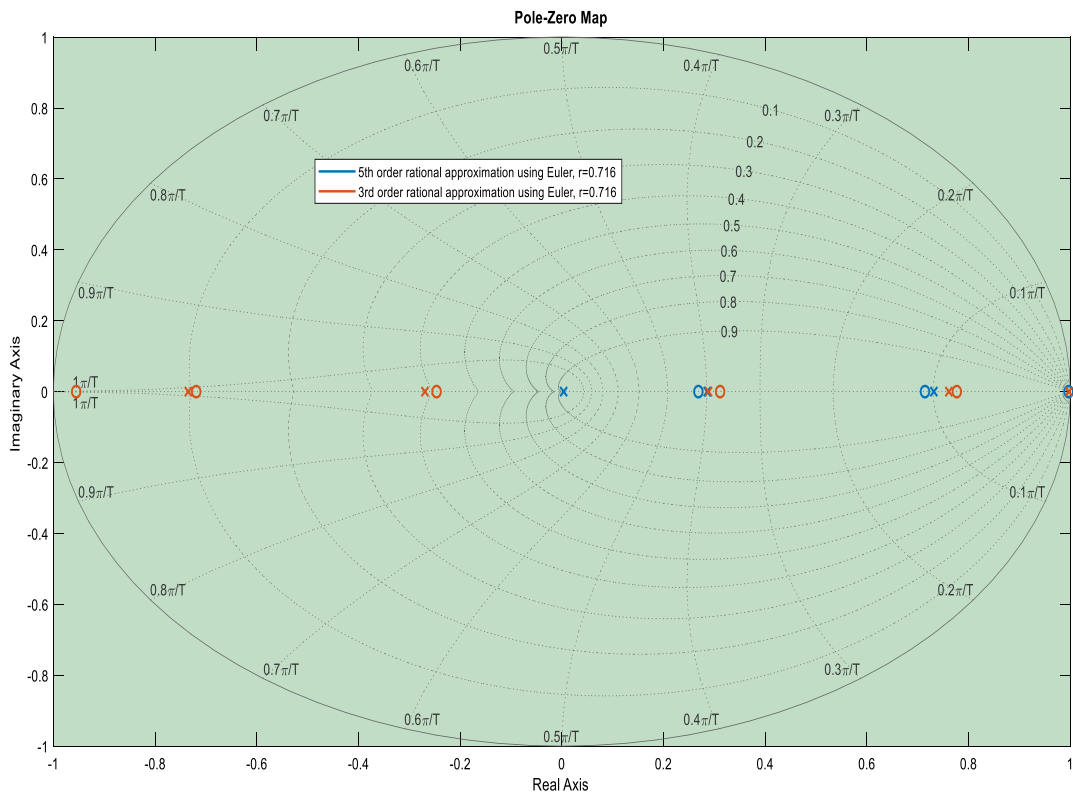

Figure 12. *The pole zero plot of third-order and fifth order approximation of $s^{0.716}$ using Euler method*

An anlaysis is made in this section to show that direct discretization of the fractional order operator is preferable ($s^{\pm\mu}, 0 < \mu < 1$) over the indirect discretization in complex delta domain. For the illustration purpose a 1/2nd order differentiator is considered for the discretization purpose. This operator is discretized using indirect discretization approach proposed by Oustaloup approximation (Baranowski et al., 2015) method as an intermediate step.

Rational approximation of $s^{0.5}$ is obtained using (Azarmi et al., 2016) as given in (36).

$$s^{0.5}\Big|_{Ous} = \frac{\begin{matrix} 10\ s^{11} + 940.9\ s^{10} + 2.674e04\ s^9 + 2.909e05\ s^8 \\ +\ 1.303e06\ s^7 + 2.473e06\ s^6 + 2.006e06\ s^5 + \\ 6.956e05\ s^4 + 1.021e05\ s^3 + 6178\ s^2 + 143\ s + 1 \end{matrix}}{\begin{matrix} s^{11} + 143\ s^{10} + 6178\ s^9 + 1.021e05\ s^8 \\ +\ 6.956e05\ s^7 + 2.006e06\ s^6 + 2.473e06\ s^5 + \\ 1.303e06\ s^4 + 2.909e05\ s^3 + 2.674e04\ s^2 + 940.9\ s + 10 \end{matrix}} \tag{36}$$

Equation. (36) is discretized in delta domain to get the rational approximation of $s^{0.5}$ with $\Delta=0.0001$ sec.

$$s^{0.5}\Big|_{ind} = \frac{1.04e004\ \gamma^5 + 1.56e005\ \gamma^4 + 4.366e005\ \gamma^3 - 2.914e032\ \gamma^2 + 4.474e004\ \gamma + 945}{947.2\ \gamma^5 + 4.477e004\ \gamma^4 + 3.125e005\ \gamma^3 + 4.366e005\ \gamma^2 + 1.559e005\ \gamma + 10395} \tag{37}$$

The rational approximation of $s^{0.5}$ in delta domain using proposed direct discretization method (CFE3GILOGDEl) is illustrated in (38) with $\Delta=0.0001$ sec.

$$s^{0.5}\Big|_{dir} = \frac{0.2495\ \gamma^5 + 0.0001962\gamma^4 + 2.198e\text{-}08\ \gamma^3 + 7.738e\text{-}13\ \gamma^2 + 1.078e\text{-}17\ \gamma + 5.195e\text{-}23}{\gamma^5 + 0.0002716\gamma^4 + 2.013e\text{-}08\ \gamma^3 + 5.587e\text{-}13\ \gamma^2 + 6.517e\text{-}18\ \gamma\gamma + 2.713e\text{-}23} \tag{38}$$
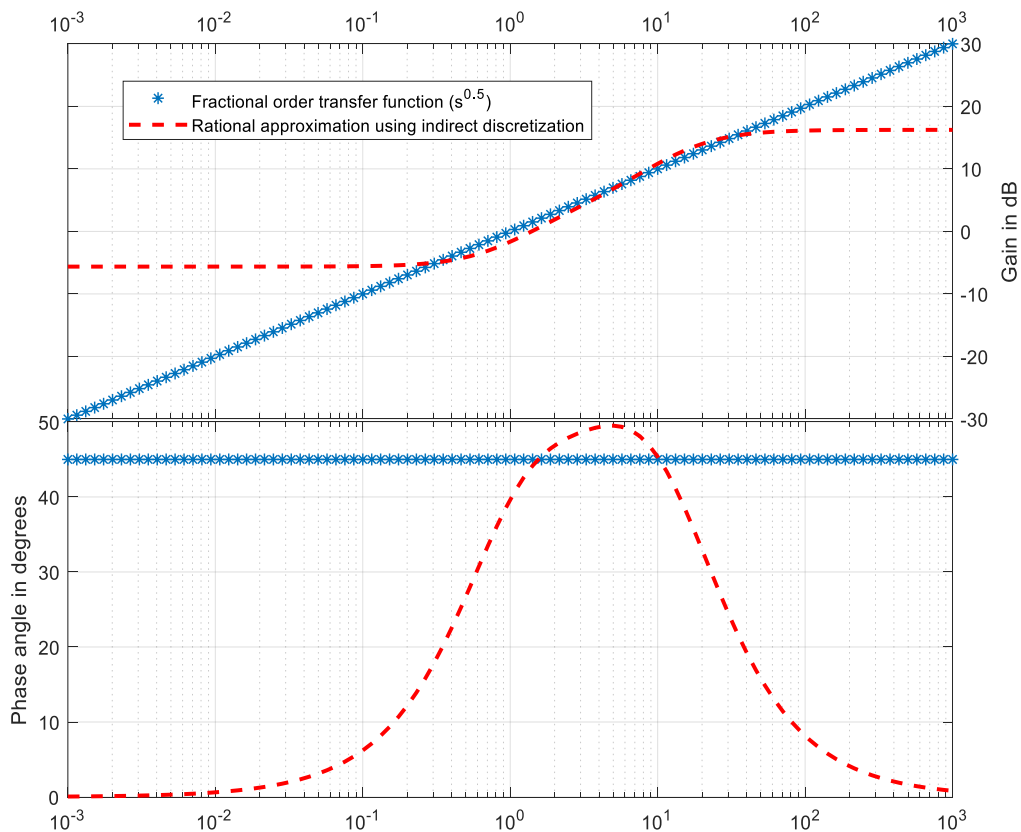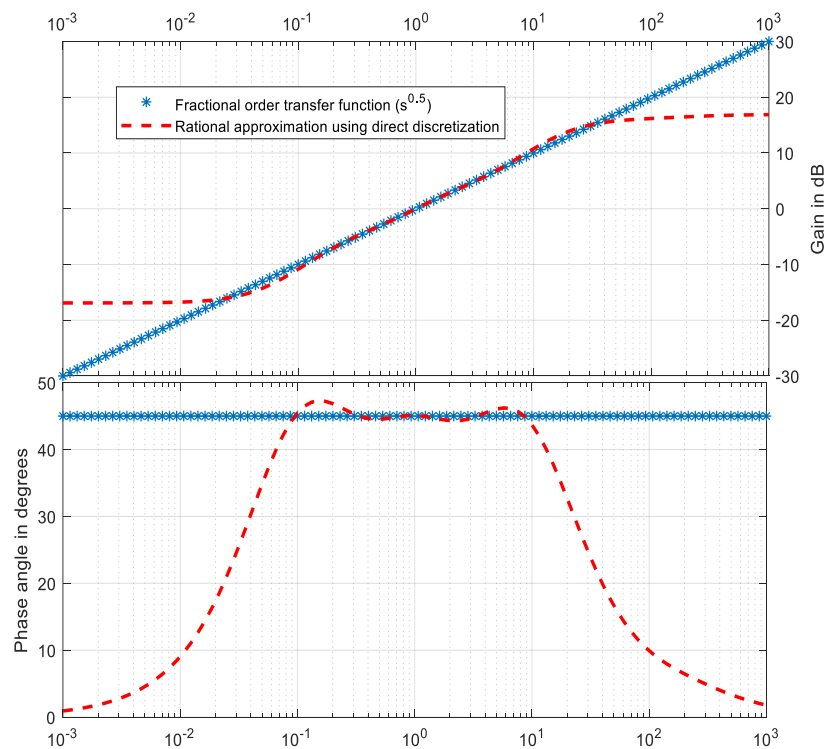

Figure 13. *Frequency response of transfer function obtained using indirect discretization of $s^{0.5}$ at Δ=0.0001 sec*

Figure 14. *Frequency response transfer function obtained using direct discretization of $s^{0.5}$ at $\Delta=0.0001$ sec*

From the Figure 13 and Figure 14, it is clearly seen that the magnitude and phase plot obtained using the direct discretization in delta domain resembles to that of the $1/2^{nd}$ order differentiator continuous time domain. In otherway, there is a notable deviation in the magnitude and phase plots of the rational transfer function obtained using indirect discretization via Oustaloup approximation technique with respect to the frequency reponse characterstics of $1/2^{nd}$ order differentiator continuous time domain. Thus, direct discretization of the fractional operator in delta domain proves to be superior over indirect discretization of fractional order operator.

4. CONCLUSION

In this paper, a new direct discretization method for fractional order operator is proposed. The discretization of the fractional order operator or system using tradional discrete z-domain can not provide meaningful information when sampled at a very fast sampling frequency. The corrsponding delta operator parameterized systems provides the continuous time results at high sampling frequency. For obtaining rational transfer function, mapping between the continuous time and delta domain variables are required. In this work, an approximation mapping between the s-domain and δ-domain is established through trapezoidal quadrature rule and traditional CFE method is used to obtain the rational transfer function corresponding to the fractional order operator in discrete delta domain.

From the simulation results, it is observed that the the proposed discretization method using delta operator is producing gratifying frequency response for the approximated transfer functions in delta domain. At fast sampling rate ($\Delta=0.00001$ sec), the delta operator parameterized system produces almost same result as that of the response obtained with original fractional order systems (Figure 5). The Table 4 illustrates the minimum errors in magnitude and phase for delta operator parameterized approximation of FOO. The superiority of the proposed method over the indirect discretization method is also verified as can be observed from Figure 13 and Figure 14. Therefore, the method proposed is said to be a viable alternate method of the direct discretization in discrete delta domain for discretizing the fractional order operator or systems available in the literature.

CONFLICT OF INTEREST

The authors declare no conflict of interest.

REFERENCES

Atangana, A., & Baleanu, D. (2016). New Fractional Derivatives with Nonlocal and Non-Singular Kernel: Theory and Application to Heat Transfer Model. *Thermal Science*, *20*(2), 763-769. doi:10.48550/arxiv.1602.03408

Azarmi, R., Tavakoli-Kakhki, M., Sedigh, A. K., & Fatehi, A. (2016). Robust Fractional Order PI Controller Tuning Based on Bode's Ideal Transfer Function. *IFAC-PapersOnLine*, *49*(9), 158-163. doi:10.1016/j.ifacol.2016.07.519

Baranowski, J., Bauer, W., Zagórowska, M., Dziwiński, T., & Piątek, P. (2015, August 24-27). *Time-domain Oustaloup approximation*. In: Proceedings of the 2015 20th international Conference on Methods and Models in Automation and Robotics (MMAR) (pp. 116-120). doi:10.1109/MMAR.2015.7283857

Boubaker, O., & Jafary, S. (Eds.) (2018) (n.d.). *Recent Advances in Chaotic Systems and Synchronization From Theory to Real World Applications*. Academic Press.

Caponetto, R., Dongola, G., Fortuna, L., & Petráš, I. (2010). *Fractional Order Systems: Modeling and Control Applications*. World Scientific. doi:10.1142/7709

Caputo, M. (1967). Linear Models of Dissipation whose Q is almost Frequency Independent—II. *Geophysical Journal International*, *13*(5), 529-539. doi:10.1111/J.1365-246X.1967.TB02303.X

Chen, Y. Q., & Moore, K. L. (2002). Discretization schemes for fractional-order differentiators and integrators. *IEEE Transactions on Circuits and Systems I: Fundamental Theory and Applications*, *49*(3), 363-367. doi:10.1109/81.989172

Chen, Y., Petras, I., & Xue, D. (2009, June 10-12). *Fractional order control - A tutorial*. In: Proceedings of the 2009 American Control Conference (pp. 1397-1411). doi:10.1109/ACC.2009.5160719

Cortés-Romero, J., Luviano-Juárez, A., & Sira-Ramírez, H. (2013). A Delta Operator Approach for the Discrete-Time Active Disturbance Rejection Control on Induction Motors. *Mathematical Problems in Engineering*, *2013*, 572026. doi:10.1155/2013/572026

Dokuyucu, M. A. (2020). Caputo and Atangana-Baleanu-Caputo Fractional Derivative Applied to Garden Equation. *Turkish Journal of Science*, *5*(1), 1-7.

Ganguli, S., Kaur, G., & Sarkar, P. (2021). Global heuristic methods for reduced-order modelling of fractional-order systems in the delta domain: a unified approach. *Ricerche di Matematica*. doi:10.1007/s11587-021-00644-7

Gao, J., Chai, S., Shuai, M., Zhang, B., & Cui, L. (2018, July 25-27). *Detecting False Data Injection Attack on Cyber-Physical System Based on Delta Operator*. In: Proceedings of the 2018 37th Chinese Control Conference (CCC) (pp. 5961-5966). doi:10.23919/ChiCC.2018.8483314

Khanra, M., Pal, J., & Biswas, K. (2010, November 29-December 01). *Rational approximation of fractional operator — A comparative study*. In: Proceedings of the 2010 International Conference on Power, Control and Embedded Systems (pp. 1-5). doi:10.1109/ICPCES.2010.5698677

Khattri, S. K. (2009). New close form approximations of ln(1 + x). *The Teaching of Mathematics*, *12*(1), 7-14.

Kothari, K., Mehta, U., & Prasad, R. (2019). Fractional-Order System Modeling and its Applications. *Journal of Engineering Science and Technology Review*, 12, 1-10. doi:10.25103/jestr.126.01

Krishna, B. T. (2011). Studies on fractional order differentiators and integrators: A survey. *Signal Processing*, *91*(3), 386-426. doi:10.1016/j.sigpro.2010.06.022

Krishna, B. T. (2015, December 18-20). *Design of Fractional order differintegrators using reduced order s to z transforms*. In: Proceedings of the 2015 IEEE 10th International Conference on Industrial and Information Systems (ICIIS) (pp. 469-473). doi:10.1109/ICIINFS.2015.7399057

Keyser, R. D., & Muresan, C. I. (2016, October 09-12). *Analysis of a new continuous-to-discrete-time operator for the approximation of fractional order systems*. In: Proceedings of the 2016 IEEE International Conference on Systems, Man, and Cybernetics (SMC) (pp. 3211-3216). doi:10.1109/SMC.2016.7844728

Lamrabet, O., Tissir, E. H., & Haoussi, F. E. (2020, June 09-11). *Controller design for delta operator time-delay systems subject to actuator saturation*. In: Proceedings of the 2020 International Conference on Intelligent Systems and Computer Vision (ISCV). doi:10.1109/ISCV49265.2020.9204303

Maione, G. (2011). High-Speed Digital Realizations of Fractional Operators in the Delta Domain. *IEEE Transactions on Automatic Control*, *56*(3), 697-702. doi:10.1109/TAC.2010.2101134

Middleton, R., & Goodwin, G. (1986). Improved finite word length characteristics in digital control using delta operators. *IEEE Transactions on Automatic Control*, *31*(11), 1015-1021. doi:10.1109/TAC.1986.1104162

Middleton, R. H. & Goodwin, G. C. (1990a). *Digital control and estimation: a unified approach*. Prentice Hall.

Middleton, R. H., & Goodwin, G. C. (1990b). *Digital Control and Estimation: A Unified Approach (Prentice Hall Information and System Sciences Series)*. Prentice Hall.

Miller, K. S., & Ross, B. (1993). *An Introduction to the Fractional Calculus and Fractional Differential Equations*. Willey Blackwell.

Nakagawa, M., & Sorimachi, K. (1992). Basic Characteristics of a Fractance Device. *IEICE Transactions on Fundamentals of Electronics, Communications and Computer Sciences*, 75, 1814-1819.

Oldham, K. B., & Spanier, J. (Eds.) (1974). *The Fractional Calculus: Theory and Applications of Differentiation and Integration to Arbitrary Order*. Elsevier.

Oustaloup, A. (1995). *La dérivation non entière: Théorie, synthèse et applications*. Hermes.

Pan, I., & Das, S. (2013). *Intelligent Fractional Order Systems and Control*. Studies in Computational Intelligence (SCI, volume 438), Springer. doi:10.1007/978-3-642-31549-7

Podlubny, I. (1999). Fractional-order systems and PI/sup /spl lambda//D/sup /spl mu//-controllers. *IEEE Transactions on Automatic Control*, *44*(1), 208-214. doi:10.1109/9.739144

Quezada-Téllez, L. A., Franco-Pérez, L., & Fernandez-Anaya, G. (2020). Controlling Chaos for a Fractional-Order Discrete System. *IEEE Open Journal of Circuits and Systems*, *1*, 263-269. doi:10.1109/OJCAS.2020.3033154

Sarkar, P., Shekh, R. R., & Iqbal, A. (2016, November 09-11). *A unified approach for reduced order modeling of fractional order system in delta domain*. In: Proceedings of the 2016 International Automatic Control Conference (CACS) (pp. 257-262). doi:10.1109/CACS.2016.7973920

Skaar, S. B., Michel, A. N., & Miller, R. K. (1988). Stability of viscoelastic control systems. *IEEE Transactions on Automatic Control*, *33*(4), 348-357. doi:10.1109/9.192189

Sun, H., Abdelwahab, A., & Onaral, B. (1984a). Linear approximation of transfer function with a pole of fractional power. *IEEE Transactions on Automatic Control*, *29*(5), 441-444. doi:10.1109/TAC.1984.1103551

Sun, H. H., Onaral, B., & Tso, Y.-Y. (1984b). Application of the Positive Reality Principle to Metal Electrode Linear Polarization Phenomena. *IEEE Transactions on Biomedical Engineering*, *BME-31*(10), 664-674. doi:10.1109/TBME.1984.325317

Swarnakar, J., Sarkar, P., Dey, M., & Singh, L. J. (2017, December 21-23). *Rational approximation of fractional order system in delta domain — A unified approach*. In: Proceedings of the 2017 IEEE Region 10 Humanitarian Technology Conference (R10-HTC) (pp. 144-150). doi:10.1109/R10-HTC.2017.8288926

Tabatadze, V., Karaçuha, K., & Veliyev, E. I. (2020). The solution of the plane wave diffraction problem by two strips with different fractional boundary conditions. *Journal of Electromagnetic Waves and Applications*, *34*(7), 881-893. doi:10.1080/09205071.2020.1759461

Vinagre, B. M., Podlubny, I., Hernández, A., & Feliu, V. (2000) Some approximations of fractional order operators used in control theory and applications. *J. Fractional Calculus Appl. Anal.*, 4, 47-66.

Vinagre, B. M., Chen, Y. Q., & Petráš, I. (2003). Two direct Tustin discretization methods for fractional-order differentiator/integrator. *Journal of the Franklin Institute*, *340*(5), 349-362. doi:10.1016/j.jfranklin.2003.08.001

Xue, D., Zhao, C., & Chen, Y. (2006, June 25-28). *A Modified Approximation Method of Fractional Order System*. In: Proceedings of the 2006 International Conference on Mechatronics and Automation (pp. 1043-1048). doi:10.1109/ICMA.2006.257769

Yumuk, E., Güzelkaya, M., & Eksin, İ. (2019). Analytical fractional PID controller design based on Bode's ideal transfer function plus time delay. *ISA Transactions*, *91*, 196-206. doi:10.1016/J.ISATRA.2019.01.034

Yumuk, E., Güzelkaya, M., & Eksin, İ. (2022). A robust fractional-order controller design with gain and phase margin specifications based on delayed Bode's ideal transfer function. *Journal of the Franklin Institute*, *359*(11), 5341-5353. doi:10.1016/J.JFRANKLIN.2022.05.033

Zhao, Y., & Zhang, D. (2017, May 24-26). *H∞ fault detection for uncertain delta operator systems with packet dropout and limited communication*. In: Proceedings of the 2017 American Control Conference (ACC) (4772-4777). doi:10.23919/ACC.2017.7963693

Microhardness and Microstructure of In-Situ Formed Fe-50%TiC Composites by Different Heating Methods

Melih KOÇYİĞİT[1] 🆔 H. Erdem ÇAMURLU[1]* 🆔

[1]*Makine Mühendisliği Bölümü, Akdeniz Üniversitesi, 07058, Kampüs, Antalya, Türkiye*

Keywords	Abstract
Volume Combustion Synthesis Fe-TiC MMCs Microhardness Microstructure	The aim of this study is to fabricate in-situ TiC particle reinforced Fe matrix composites via volume combustion synthesis (VCS) through heating by two different sources. One group of reactant pellets was ignited by heating in an induction furnace (IF). The other group was ignited via heating by using a tungsten inert gas (TIG) torch. Thus, the differences in the microhardness and microstructure of the obtained composites could be compared. Fe, C and Ti elemental powders were used to obtain composites that contained 50 vol. % TiC in the Fe matrix. In the repeated experiments, the ignition temperatures of the IF pellets were found to be in 1164-1184 ºC range. The formation of composites was verified by X-ray diffraction (XRD) analyses, where it was seen that the products were composed of TiC and Fe with trace impurity phase. Scanning electron microscope (SEM) examinations showed that the in-situ formed TiC particles were regularly distributed in matrix in both series. The TiC particles obtained by TIG heating were about 5 times larger than the particles obtained by induction heating. Microhardness values of the samples were higher in IF series as compared to TIG series. It was shown that 50 vol. % TiC particle reinforced Fe matrix composites could be obtained by both heating methods. TIG was found to be a much practical method, when compared to conducting VCS in a furnace.

1. INTRODUCTION

Materials consist of different type of constituent that have different mechanical and thermal properties, are called as composites. Metals and polymers are mostly used as the matrix of a composite. They are preferred because of their ductility. On the other hand, ceramics are commonly used as reinforcement materials in metal matrix composites due to their high hardness (Koczak et al., 1993). Moreover, in-situ production of the composites has some superiorities such as thermodynamic stability at elevated temperatures, cleanliness of the matrix-reinforcement interfaces, even distribution of the particles in the matrix when they are compared to the ex-situ methods (Tjong & Ma, 2000).

Fe has been a popular matrix material since it has advantages such as low cost and ease in accessibility. Carbides (TiC, SiC, etc.) borides (TiB_2, etc.) and oxides (Al_2O_3, etc.) are in the list of reinforcements for Fe matrix composites. Mechanical and physical properties such as high hardness, low density and good wettability with Fe, render TiC a suitable reinforcement (Emamian et al., 2011).

Combustion synthesis is a relatively simple technique that exploits the self-maintaining characteristic of the exhothermic reactions. This method may be applied in two forms. In the first one, reaction travels from one side to the other, after the ignition from one side. This sort of synthesis is called self-propagating high temperature synthesis. In the second one, as a result of even heating, as opposed to ignition from one side, a

complete reaction occurs in the total of the green pellet. Thus, this kind is called the volume combustion synthesis (Rogachev, 2017).

Combustion mechanism of Fe-Ti-C system was investigated intensively by different researchers (Fan et al., 1999; Jing & Yisan, 2007; Kocyigit & Camurlu, 2022; 2023). Choi et al. (1992) introduced the requirements of exothermic reactions in combustion synthesis in three steps. First, reaction needed to have high exothermicity. Second, there should be a liquid or vapor form for pre-reaction diffusion to occur. Third, heat loses must be less than heating rate. Accordingly, in some studies it was suggested that Fe-Ti eutectic temperatures play an important role on the reaction mechanism of the Fe-Ti-C system (Fan et al., 1999). In literature, there are studies that focus on the effect of the in-situ produced TiC particles, on the mechanical properties. It was reported that by Rahimi-Vahedi et al. (2018) that addition of TiC provided rise in hardness of the composite which was produced via combustion synthesis.

In some studies, on the formation of Fe matrix surface composites and coatings in literature, tungsten inert gas (TIG) heating method was used (Xinhong et al., 2009). The intense heat, which is created by the TIG torch, brings about the possibility of local heating on the surfaces of metals. Most studies concerning TIG heating, involve heating and melting of a powder mixture on the surface of a substrate. Thereby a surface composite is formed (Xinhong et al., 2009). Mechanical properties such as microhardness and wear resistance were reported to increase by incorporation of Fe-TiC surface composites via TIG heating (Zhao et al., 2019).

Although there are studies in literature on Fe-Ti-C system, no study was encountered on comparison of microhardness and microstructural properties of in-situ Fe-TiC composites which were produced by different heat sources such as induction furnace heating and TIG heating. In this study, in-situ formed TiC reinforced Fe matrix composites were produced by combustion synthesis from elemental fine Fe, Ti and graphite powders via both induction furnace heating and TIG heating processes. Unlike the studies in literature, in the present study TIG was not used for melting the products or formation of a coating. It was used solely for initiating the exothermic reaction in a preformed pellet of powder mixture. Effects of the two heating methods on microstructure and microhardness were compared. It was shown that 50 vol. % TiC particle reinforced Fe matrix composites could be obtained by both methods. TIG was found to be a much practical method, when compared to conducting VCS in a furnace.

2. MATERIAL AND METHOD

In-situ formed TiC-Fe composites were produced through VCS. Ignition of the samples were accomplished by two different methods. The first method involves heating in an induction furnace (IF) and in the second method the samples were heated by a tungsten inert gas (TIG) torch.

Elemental iron, titanium and carbon (as graphite) were employed to produce the in-situ Fe-50 vol.% TiC composites. In Table 1, the designation of the sample and contents of the starting materials are given. The same starting compositions were used for both induction furnace heating (IF) and tungsten inert gas (TIG) heating experiments according to Reaction (1). Prepared mixtures were pressed in a die. The green pellets were quite loose. The green pellet can be seen in Figure 1a.

$$\text{Ti} + \text{C} + x\text{Fe} \rightarrow \text{TiC} + x\text{Fe} \tag{1}$$

Table 1. *TiC contents and sample codes of the obtained composites and compositions of the starting powder mixtures*

TiC ratio of the Fe-TiC Composite (Vol. %)	Designation	Initial Mixtures		
		Fe (g)	Ti (g)	C (g)
50	IF50/TIG50	1.6689	0.8352	0.2094

2.1. Thermodynamic Calculations

Adiabatic temperatures (T_{ad}) of the systems that contained 50 vol. % TiC was calculated by HSC Chemistry 9. T_{ad} of a reaction is the maximum temperature that the products will get as a consequence of the developed exothermic energy, in the state that there is no heat loss from the yields. The Gibbs free energy (ΔG) of the Reaction (1) and of the other reactions which may occur in the system were calculated by the HSC 9.

2.2. Heating Processes

The IF50 series was heated in an induction furnace. Before the experiments, vacuum was applied to the system and then argon gas was supplied. A pyrometer was used for monitoring the temperature of the sample during heating. The exothermic reaction started by the escalation of temperature, which was taken as the ignition temperature, T_i. In induction heating, power was turned off by the time the ignition occurred. The temperature of the sample continued to increase due to the released heat and reached the combustion temperature, T_c.

The TIG50 was heated by a TIG torch (40A electrical current). In TIG heating, heating was continued for 10s since it was sometimes not possible to distinguish the ignition moment. Therefore, higher temperatures are expected to be attained by TIG heating than induction heating. The argon gas blow of the TIG torch prevented the oxidation of the reactants and the products. The argon gas blow was continued until the products were cooled to room temperature. In TIG heating, there is also an instant heating and occurrence of the reaction in the whole volume of the sample at once. Therefore, it is believed that TIG heating can be defined as VCS.

2.3. Characterization

The products were sanded with 180 - 3000 number sandpapers. Micro structures were examined by optical microscopy and scanning electron microscope which had a field emission gun (FEI). Microhardness was determined by a Micro Vickers Hardness Tester (THV-1DTe). XRD analyses were conducted on product pellets by a Rigaku Smartlab Unit by Cu-Kα cathode tube.

3. RESULTS AND DISCUSSION

3.1. T_{ad}, T_i and T_c

According to the calculations which were made in this study, the adiabatic temperature of the reaction for the formation of the composite that contained 50 vol. % TiC is 1535 ºC. This is the melting point of Fe. It was seen that the heat formed by the reaction is capable of heating the products to the melting point of iron. It can be inferred that some of the iron melts.

The combustion temperatures that were recorded during the formation of samples IF50 in different trials are presented in Table. 2. It can be seen that the measured T_c are below the calculated T_{ad} values. The difference probably arises from the loss of heat from the products through the substrate and the crucible during VCS.

Table 2. *T_i and T_c of IF50 samples*

Sample	Ignition Temperature, T_i (ºC)	Combustion Temperature, T_c (ºC)
IF50 (Trial 1)	1164	1358
IF50 (Trial 2)	1175	1358
IF50 (Trial 3)	1184	1338

The ignition temperatures of the samples were between 1164-1184 ºC. The closeness of the obtained results indicates the accuracy of the temperature measurements. In combustion synthesis, ignition mostly takes place by the formation of liquid phase in the system. In Fe-Ti there are two eutectic reactions at 1085 ºC (Ti-FeTi) and the at 1290 ºC (Fe_2Ti-Fe) (Murray, 1981). The measured combustion temperatures are slightly above the

eutectic reaction at 1085 °C. It can be suggested that after diffusion of Fe atoms into Ti particles, as a result of the eutectic reaction of Ti-FeTi, a liquid phase forms and ignition takes place. Ti and C dissolves and TiC particles precipitates in the formed liquid (Fan et al., 1999).

In this study, ignition of the reactant pellet was conducted by both induction furnace (IF) heating and TIG heating. After the combustion synthesis reactions in both systems, the product pellet remained intact and maintained its integrity (Figure 1). This observation indicated that TIG heating was utilized successfully for the ignition of the pellet.

(a)   (b)
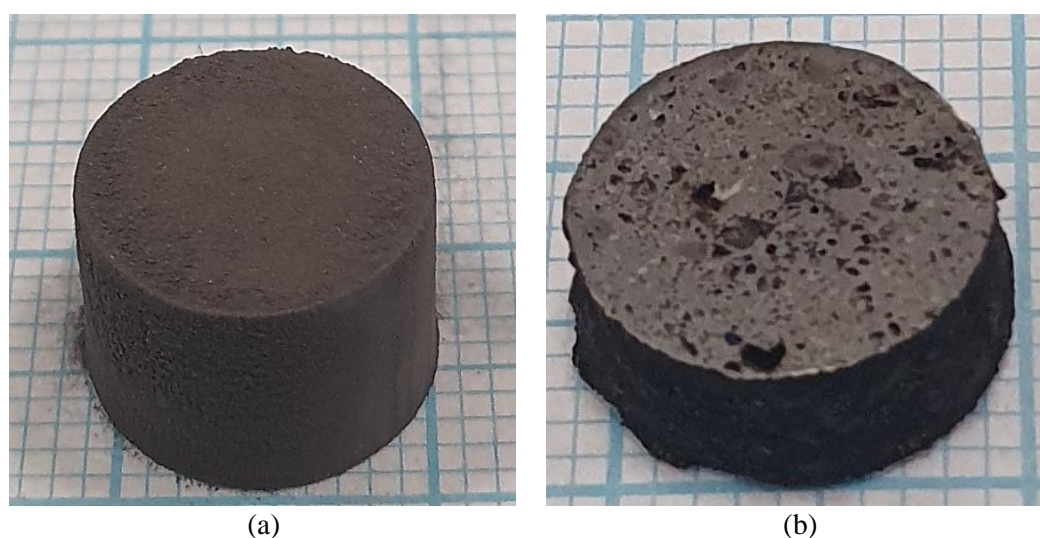
Figure 1. Images of a) IF50 green pellet, b) IF50, after VCS (Polished)

Gibbs free energy values of some of the compounds, in the Fe-Ti-C system are given in Figure 2. It can be seen that TiC is the most feasible compound in the system, with the lowest free energy values. Formation of Fe_3C is not expected due to its high free energy of formation. Fe_2Ti and FeTi are possible products, with negative Gibbs free energies. Their formation may be possible at points where C concentration is low and Reaction (1) is not complete (Kocyigit & Camurlu, 2023).
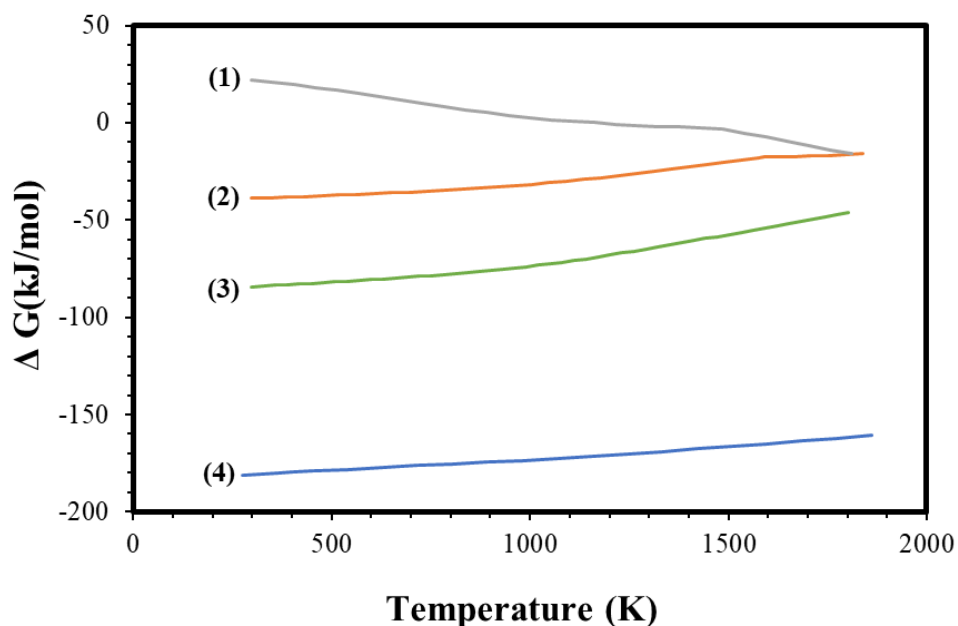
Figure 2. Gibbs free energy of some species in Fe-Ti-C reaction system;
(1) Fe₃C; (2) FeTi; (3) Fe₂Ti; (4) TiC

3.2. XRD Analyses

XRD pattern of the starting mixture of Fe-50 vol.% TiC composite is presented in Figure 3a. It can be seen that the pattern contains Fe and Ti peaks. After the VCS reaction, the Fe peaks remain, on the other hand, the peaks of the Ti phase disappear in the XRD pattern of the VCS products (Figure 3b). This indicates the consumption of the Ti phase. The Fe peaks in the XRD pattern of the products indicate that the matrix phase is composed of Fe in the composites, as intended, with trace amount of impurity phase, Fe_2Ti. According to Gibbs free energy calculations, formation of Fe_2Ti is possible, however it is not a stable product when C is present. Trace amount of this phase may have formed in regions where carbon is limited and TiC formation was not possible (Kocyigit & Camurlu, 2023). There is also the possibility of C loss from the system., which would lead to a surplus of Ti in the system. It can be seen in the XRD pattern of the products that the peaks of the TiC phase appear, indicating the formation of the TiC particles in the products.
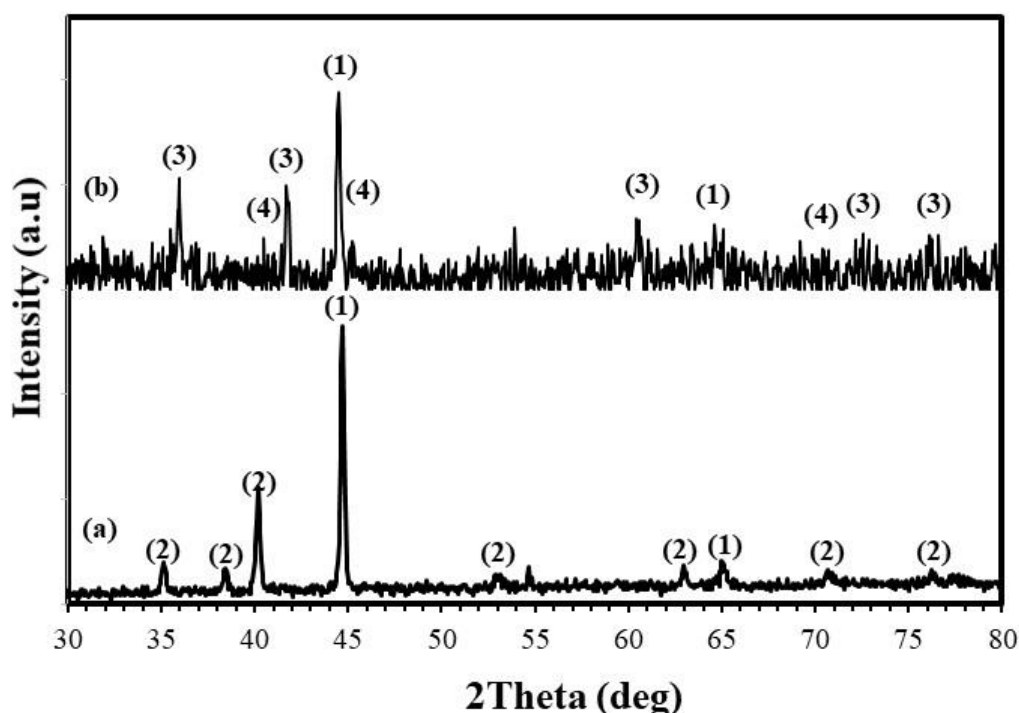
Figure 3. *XRD pattern of the **a**) IF50 initial powder mixture, **b**) IF50 composite formed after VCS by induction heating; (**1**) Fe, (**2**) Ti, (**3**) TiC, (**4**) Fe_2Ti*

3.3. Microstructure

SEM micrographs of the composites containing 50 vol. % TiC are presented in Figure 4. Product in Figure 4a was obtained by induction furnace heating and product in Figure 4b was obtained by TIG heating. In these images, the dark-colored round particles are TiC (marked as C in the Figure 4) as verified by the EDS analyses. Homogenous distribution of TiC particles was seen to take place in the composites which were obtained by both of the heating methods.

The sizes of the TiC particles were observed to be smaller in the samples which were ignited by IF heating, than the samples which were ignited by TIG heating. The sizes of the TiC particles were below 1 micrometer in the composites obtained by induction heating. On the other hand, the size of the TiC particles were 3-4 micrometers in TIG heated composite. It can be inferred that the sizes of the formed TiC particles were larger in the composites which were obtained by TIG heating. The difference may have arisen due to higher temperatures attained during TIG heating. In induction heating, power was turned off as soon as the ignition took place. On the other hand, in TIG heating, heating was continued for 10 s since it was not possible to distinguish the ignition moment. Therefore, higher temperatures are expected to be attained by TIG heating. Higher temperature attained in TIG heating may have led to higher rate of TiC grain growth caused by the Ostwald ripening.

According to the EDS analyses, regions that are marked as A (Figure 4) have 25/75 molar Ti/Fe ratio. On the other hand, regions that are marked as B has 7/93 Ti/Fe molar ratio (Table 3). The detected Ti in Fe can be taken as an indication that Reaction (1) was not complete in the system. The unconsumed Ti may have remained in the Fe matrix. Although TiC and Fe major phases were detected by the XRD analyses of the products (Figure 3), trace amount of Fe_2Ti phase was present. Therefore, the XRD results are in accord with the EDS analysis.
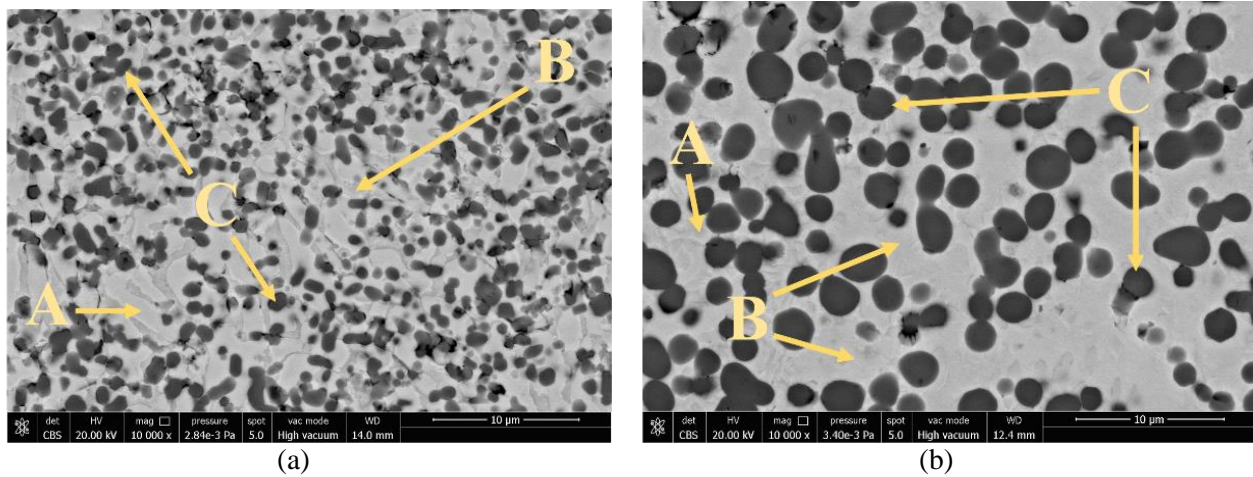
Figure 4. SEM images of the induction and TIG heated composites a) IF50, b) TIG50 (Magn. 10kX)

Table 3. Molar Ti/Fe ratios of the regions that are given in the Figure 4

Region	A	B
nTi/nFe	25/75	7/93

3.4. Microhardness

TiC was found to be effective in enhancing hardness, since the microhardness value of unreinforced Fe matrix was 29.8 $HV_{0.2}$. It can be seen in Table 4 that in general, composite that was obtained by induction heating presented slightly higher microhardness values than the composite which was obtained by TIG heating. This difference may be a result of the presence of finer TiC particles in the samples, which were obtained by induction furnace heating. The finer sizes of TiC particles were observed during microstructural examinations (Figure 4). Composites having finer reinforcement particle size generally exhibit higher hardness than the ones having coarser reinforcement (Koczak et al., 1993).

Table 4. Microhardness Values of IF50 and TIG50

Sample	Measurements					Average ($HV_{0.2}$)	Std. Dev.
	1.	2.	3.	4.	5.		
IF50	775.3	785.9	710.3	675.2	690.5	727.4	50.2
TIG50	630.9	570.1	702.9	624.4	554.8	616.6	58.5

When the two heating methods are compared, it can be suggested that the TIG heating is a much easier and faster method. TIG was found to be more practical than heating in the induction furnace.

4. CONCLUSION

In this study, the effect of different heating sources (induction furnace (IF) and tungsten inert gas (TIG) welding machine) on microstructure and microhardness of in situ TiC particle reinforced Fe matrix composites was investigated. According to microstructure examinations and XRD results, TiC particles were formed successfully in-situ in the Fe matrix via combustion synthesis by both heating techniques. Trace amount of Fe_2Ti was also detected. The TiC particles were homogeneously distributed in the structure. The TiC particles obtained by TIG heating were about 5 times larger than the particles obtained by induction heating. In general, the samples which were produced by induction furnace heating exhibited higher microhardness values than TIG produced samples. This was attributed to finer reinforcement size of the obtained composites when IF heating was used. It was shown that 50% TiC particle reinforced Fe matrix composites could be obtained by both methods. TIG was found to be a much practical method, when compared to VCS in a furnace.

ACKNOWLEDGEMENT

CONFLICT OF INTEREST

The authors declare no conflict of interest.

REFERENCES

Choi, Y., Mullins, M. E., Wijayatilleke, K., & Lee, J. K. (1992). Fabrication of metal matrix composites of TiC-Al through self-propagating synthesis reaction. *Metallurgical and Materials Transactions A*, *23*(9), 2387-2392. doi:10.1007/BF02658041

Emamian, A., Corbin, S. F., & Khajepour, A. (2011). The influence of combined laser parameters on in-situ formed TiC morphology during laser cladding. *Surface and Coatings Technology*, *206*(1), 124-131. doi:10.1016/j.surfcoat.2011.06.062

Fan, Q., Chai, H., & Jin, Z. (1999). Mechanism of combustion synthesis of TiC–Fe cermet. *Journal of Materials Science*, *34*(1), 115-122. doi:10.1023/A:1004430028260

Jing, W., & Yisan, W. (2007). In-situ production of Fe–TiC composite. *Materials Letters*, *61*(22), 4393-4395. doi:10.1016/j.matlet.2007.02.011

Koczak, M. J., Khatri, S. C., Allison, J. E., & Bader, M. G. (1993). Metal-matrix composites for ground vehicle, aerospace, and Industrial applications. In: S. Suresh, A. Mortensen, & A. Needleman (Eds.), *Fundamentals of Metal Matrix Composites* (pp. 297-326). Stoneham, USA. doi:10.1016/B978-0-08-052371-2.50020-1

Kocyigit, M., & Camurlu, H. E. (2022, June 17-19). *Comparison of microstructure and microhardness of boride and carbide reinforced iron matrix composites*. In: A. Unsal (Eds.), Proceedings of 2. International Cappadocia Scientific Research Congress, Nevşehir, Türkiye, (pp. 796-802).

Kocyigit, M., & Camurlu, H. E. (2023). Volume Combustion Synthesis in Fe–Ti–C and Fe–Ti Systems. *Metallurgical and Materials Transactions A*, *54*(1), 320-332. doi:10.1007/s11661-022-06880-2

Murray, J. L. (1981). The Fe− Ti (iron-titanium) system. *Bulletin of Alloy Phase Diagrams*, *2*(3), 320-334. doi:10.1007/BF02868286

Rahimi-Vahedi, A., Adeli, M., & Saghafian, H. (2018). Formation of Fe-TiC composite clad layers on steel using the combustion synthesis process. *Surface and Coatings Technology*, *347*, 217-224. doi:10.1016/j.surfcoat.2018.04.086

Rogachev, A. S. (2017). Fundamentals: Theory. In: I. P. Borovinskaya, A. A. Gromov, E. A. Levashov, Y. M. Maksimov, A. S. Mukasyan, & A. S. Rogachev (Eds.). *Concise Encyclopedia of Self-Propagating High-Temperature Synthesis* (pp. 140-141). Elsevier. doi:10.1016/B978-0-12-804173-4.00062-4

Tjong, S. C., & Ma, Z. Y. (2000). Microstructural and mechanical characteristics of in situ metal matrix composites. *Materials Science and Engineering: R: Reports*, *29*(3-4), 49-113. doi:10.1016/S0927-796X(00)00024-3

Xinhong, W., Lin, C., Min, Z., & Zengda, Z. (2009). Fabrication of multiple carbide particles reinforced Fe-based surface hardfacing layer produced by gas tungsten arc welding process. Surface and Coatings Technology, *203*(8), 976-980. doi:10.1016/j.surfcoat.2008.09.020

Zhao, Z., Li, J., Bai, P., Qu, H., Liang, M., Liao, H., Wu, L., Huo, P., Liu, H., & Zhang, J. (2019). Microstructure and mechanical properties of TiC-reinforced 316L stainless steel composites fabricated using selective laser melting. *Metals*, *9*(2), 267. doi:10.3390/met9020267

Effect of Diluent Amount on Properties of Porous NiAl

Gülizar SARIYER[1*] H. Erdem CAMURLU[2]

[1]Department of Space Sciences and Technologies, Akdeniz University, Türkiye
[2]Department of Mechanical Engineering, Akdeniz University, Türkiye

Keywords	Abstract
Volume Combustion Synthesis NiAl Space Holder Method Porous Intermetallic	Porous NiAl parts were formed by using Ni and Al elemental powders, preformed NiAl as diluent and NaCl particles as space holder (SH). The aim of utilizing preformed NiAl (30%-40%) as a diluent was to preserve the shape of the products. The amounts of the SH NaCl particles in NiAl were 25-50-75 vol.% and their sizes were in 300-500 μm range. Porous NiAl samples were prepared by volume combustion synthesis (VCS). The adiabatic temperatures of the Ni+Al mixtures having 30 and 40% diluent NiAl were calculated as 1638.9 and 1460.8°C, respectively. Formation of NiAl phase was verified by XRD analyses. In the green pellets, the total porosity amount was higher than the added NaCl amount. Also it was slightly higher in the product pellets than in the green pellets before VCS. Compressive strength and microhardness values of the samples which contained 30% diluent NiAl were higher than the samples which contained 40% diluent. Average compressive strength values of the products that were obtained by 25% NaCl and 30 and 40% diluent NiAl additions were 112.0±29.5 and 66.0±20.5 MPa, respectively.

1. INTRODUCTION

Porous metals are used in structural applications of various industries, including the automotive and aerospace industries, shipbuilding, sports equipment and biomedical industries (Banhart, 2001). The spacer or space holder (SH) method attracted interest because of its ability to regulate the dimensions, shape, and connection of porosity (Arifvianto & Zhou, 2014). In this method, removable particles are used for creating pores of controlled size and amount. In literature, urea and NaCl particles are most widely utilized space holders. After shaping the metal structure, they can be removed by dissolving in water or urea can also be removed by thermal decomposition (Banhart, 2001). The sintering method is one of the methods used in the production of porous materials including porous ceramics and metals. During sintering the characteristics of the pores may be regulated by physically adjusting the morphology, size and amount of the space holder among the starting powder particles (Jiang et al., 2021).

Volume combustion synthesis (VCS) is a convenient method for obtaining articles made of intermetallic compounds. It utilizes the exothermic energy of the reactions; therefore, it is an economical process. In this method, a powder mixture is ignited by heating throughout its whole volume and the reaction takes place all at once. Self-propagating high-temperature synthesis (SHS) on the other hand, involves ignition of the reactant pellet from one side, mostly by heating with a resistance wire. Systems which have higher adiabatic temperatures than 1800K were suggested to be self-propagating (Su et al., 2014). However, in VCS, sysnthesis of systems which have lower adiabatic temperature can be possible. VCS has been used for preparation of compounds such as FeAl, NiAl and NiTi, etc (Varma et al., 1998). 3 significant temperature

*Corresponding Author, e-mail: glzrysn@gmail.com

points in the combustion synthesis that affect the reaction process and properties of the end product are: 1) ignition temperature (T_i) is expressed as the stage at which the SHS initiates, 2) adiabatic temperature (T_{ad}) is the highest combustion temperature reached in adiabatic circumstances, 3) the actual combustion temperature (T_c) is the highest temperature obtained in non-adiabatic conditions (Moore & Feng, 1995).

In one of the studies in literature which employed both space holder and combustion synthesis technique, Wang et al. (2016) have produced porous TiAl-based intermetallics by VCS. They used NaCl as the space holder (SH) agent. They found that TiAl was developed as the major phase in materials sintered at 1100°C, and the open porosity increased up to 84% with the addition of 80% NaCl to Ti-50Al. Cai et al. (2021) prepared porous NiAl intermetallics by thermal explosion by using space holder NaCl. They showed that there was no cracking or deformation in the sample when the space-retaining NaCl content in NiAl reached 30% by volume. They reported that the porosity was increased to 63% when 50% NaCl was added by volume. In the study of Shu et al. (2019) porous Ni3Al, NiAl and NiAl3 were obtained by reactive sintering at 650°C for 10800 s. The products were reported to exhibit good energy absorbing characteristics. Li et al. (2019) have synthesized porous Ni_3Al, NiAl and $NiAl_3$ intermetallics by thermal explosion process. The open porosity of Ni_3Al, NiAl and $NiAl_3$ were obtained as 27.4%, 40.3% and 41.5%, respectively. They stated that especially porous NiAl showed excellent oxidation resistance. Yang et al. (2019) investigated compression fatigue properties of open-celled Al foams produced by the spacer method with different porosities. Fatigue strengths of 50%, 60% and 70% porous Al foams were obtained as 12.77 MPa, 7.61 MPa and 3.02 MPa, respectively. It was observed that there was a linear decrease with increasing porosity.

The amount of diluent is critical for the mechanical properties of the products in VCS. This is because the adiabatic temperature of the reaction decreases with the increase in the amount of diluent. When the diluent amount is too high, mechanical properties of the products becomes inferior due to inefficient sintering. On the other hand, when the diluent amount is too low, too much liquid phase may form in the product as a result of the high adiabatic temperature. This leads to partial melting, shape distortion of the product and also reduction in porosity if porous products are aimed.

In the present study, NiAl porous materials were produced using the space holder method. Pores were formed with controlled size and amount by using 25, 50 and 75 vol.% NaCl particles in NiAl as space holder. In order to control the adiabatic temperature during VCS, preformed NiAl was utilized as diluent. Therefore, the effect of 30 and 40% diluent NiAl addition on macrostructure of the formed porous articles were investigated and mechanical properties were determined.

2. EXPERIMENTAL PROCEDURE

Porous NiAl samples were produced according to Reaction (1) by using 25, 50, 75 vol.% NaCl (Merck, >99.5) as space holder particles. NaCl particles were sieved in a sieve set, in order to separate the particles in 300-500 μm range. These particles were utilized as space holder. Preformed NiAl was added to nickel (Merck, 99+%, <10 μm) and aluminum (Alfa Aesar, 99.5%, <10 μm) powders as diluent, as shown in Reaction (1).

$$(x)Ni + (x)Al + (y)NiAl = (x + y)NiAl \qquad (1)$$

2.1. Preparation of Preformed NiAl Powder

Ni, Al and MgO (Merck, 99.5%, <1 μm) were weighed and mixed. MgO was used as diluent. After the prepared powder mixture was taken into a steel mold with a diameter of 10 mm, a pressure of 100 MPa was applied. The compressed sample was removed from the mold and volume combustion synthesis was conducted in an induction furnace. The formed product was crushed in a mortar and pestle. In order to dissolve the MgO in the mixture, it was kept in HCl+pure water for about 1 hour. Then, this mixture was filtered and the residue was dried in an oven at 65°C for 1 day. As a result of these processes, diluent NiAl was obtained. XRD analyses verified that the product was single phase pure NiAl powder.

2.2. Sample Preparation

Ni, Al powders, preformed NiAl and NaCl were weighed on an analytical balance and mixed homogeneously in the mixing bowl. The sample height for each piece was calculated as 9 mm. The cylindrical samples obtained were prepared in an 8 mm diameter steel mold by applying 100 MPa pressure in a cold press. The produced part was kept in pure water for about one day in order to dissolve the NaCl particles. Afterwards, the samples were dried in an oven for about a day. After drying, the parts were subjected to combustion synthesis reaction by heating in a tube furnace up to 700°C at a rate of 10°C/min. in Ar atmosphere. Codes of the prepared samples, amount of diluent NiAl and space holder NaCl are presented in Table 1.

Prepared sample codes, amount of diluent NiAl and space holder NaCl are presented in Table 1. For example, 30DN25SN is code used for the sample that contained 30% Diluent NiAl and 25% Space holder NaCl.

Table 1. *Amount of diluent NiAl and space holder NaCl in the prepared samples and their codes*

Diluent NiAl amount (%)	NaCl Amount (vol.%)		
	25	50	75
30	30DN25SN	30DN50SN	30DN75SN
40	40DN25SN	40DN50SN	40DN75SN

Adiabatic temperatures (T_{ad}) of the reactant mixtures were calculated by the HSC Chemistry software according to Reaction (1). Adiabatic temperature is the maximum temperature that the products will reach as a result of an exothermic reaction, when there is no heat loss in the system. It can be calculated by Equation (1). ΔH_{298}, ΔH_m, Tm and C_p in Equation (1) are the reaction enthalpy, and latent heat of fusion, melting temperature and heat capacity of the product phase, respectively. T_{Ad} is the adiabatic temperature.

$$\Delta H_{298} = \int_{298}^{T_m} C_p dT + \Delta H_m + \int_{T_m}^{T_{Ad}} C_p dT \tag{2}$$

2.3. Sample Characterization

Before and after the removal of NaCl particles, the pellets were weighed, and their dimensions were measured. The density of the green pellet after NaCl removal was calculated by dividing the weight of the pellet by the volume of the pellet. The relative % density of the green pellet was calculated by dividing the density of the pellet by the theoretical density of NiAl (5.9 g/cm^3) and multiplying by 100. % total porosity was calculated by subtracting the relative % density of the pellet from 100. The amount of porosity in the cell walls of the green pellet was calculated by subtracting the NaCl amount from % total porosity of the pellet.

$$\text{Density of the green pellet } = \frac{\text{weight of the pellet}}{\text{volume of the pellet}} \tag{3}$$

$$\text{\% Relative density } = \left(\frac{\text{density of the pellet}}{\text{theoretical density of NiAl}}\right) * 100 \tag{4}$$

$$\text{\% total porosity } = 100 - \text{Relative \% density} \tag{5}$$

$$\text{Porosity in the cell walls of the green pellet} = \text{\% total porosity} - \text{ NaCl amount of the pellet} \tag{6}$$

XRD analyses were performed on selected samples. A Rigaku Smartlab unit was used with 0.02° steps and 2°/min speed. Compression test was applied to the produced samples with a Shimadzu Autograph Universal Tensile-Compression Device (50 kN) after volume combustion synthesis, in accordance with the ISO 13314 standard. The strength values of the materials were measured, and the results were presented in a stress-strain diagram. For macrostructural examinations, metallographic preparation methods were employed. Porous NiAl parts formed after volume combustion synthesis were ground on 600, 1200 and 3000 grit sandpaper and polished. After polishing, the macro structure of the samples was examined with a stereo microscope. In

addition, an optical microscope was utilized for microstructural examinations (Nikon Eclipse LV150). Microhardness measurements were conducted via a vickers microhardness tester by applying 200g load.

3. RESULTS AND DISCUSSION

3.1. Adiabatic Temperature Calculations

The adiabatic temperatures of the reactions were calculated by the HSC Chemistry (Roine, 2002) software. The calculated adiabatic temperatures of Reaction (1) is presented in Figure 1, up to 50% preformed NiAl addition. It was seen that the adiabatic temperature remains constant at 1638.9°C up to 30% preformed NiAl addition. 1638.9°C is the melting temperature of NiAl. When there is no diluent in the system, a certain fraction of NiAl in the products melts. The high amount of liquid phase that is formed in the system when there is no diluent NiAl results in distortion of the product pellet. The shape of the pellet and the pores can be preserved by the addition of diluent NiAl in VCS.

The fraction of liquid phase decreases with the increase in the diluent NiAl addition to the starting mixture, since the preformed NiAl absorbs some of the evolved heat. This continues up to 30% preformed NiAl addition. After this point, the evolved heat is not sufficient to cause melting of the products and there will be no liquid phase formation in the products. The adiabatic temperature starts to decrease with preformed NiAl addition after 30%. T_{ad} is 1460.8°C and 1253.2°C when 40 and 50% preformed NiAl was added, respectively. According to these results, 30% preformed NiAl addition was selected in order to decrease the adiabatic temperature and the amount of liquid phase in the system, for preventing the distortion of the product pellet. In VCS the reaction initiates at a higher temperature than the room temperature. Therefore, the attained temperature of the pellet may be higher than the calculated adiabatic temperature. Thus, the effect of addition of 40% diluent NiAl was also investigated.
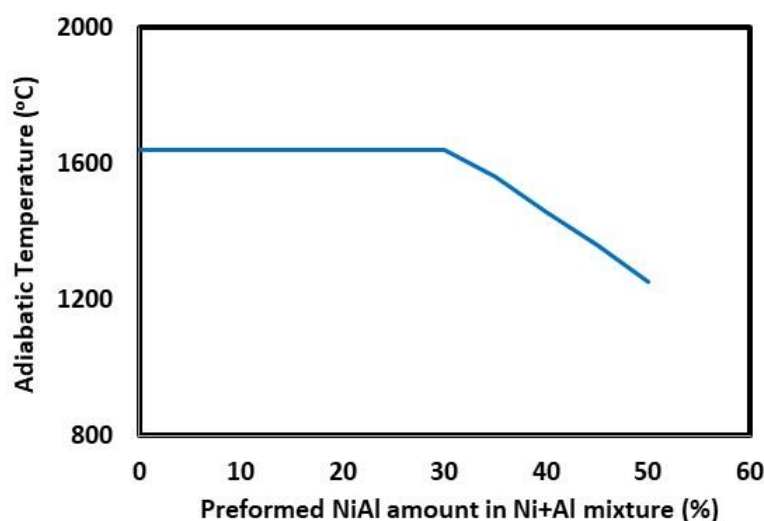
Figure 1. *Calculated adiabatic temperatures of the Ni+Al mixtures as a function of diluent preformed NiAl addition*

Selected samples in the prepared sample groups were subjected to XRD analyses. It was found that pure NiAl phase was formed in the samples by using both 30 and 40% diluent NiAl addition.

3.2. Macrostructure

Addition of both 30 and 40% diluent NiAl powder addition to the starting mixture resulted in preserving the shape of the cylindrical pellet. There was no sign of melting in the pellets. On the other hand, when no diluent NiAl was used, the shape of product pellet was distorted.

The macrostructures of the product pellets are presented in Figure 2. These images were obtained from the cross-sections of the pellets. It can be seen in these images that the created pores mostly replicated the initial

shape of the NaCl particles. The porosity increased with increasing amount of NaCl content of the initial mixture. When 75% NaCl was used, the formed pores tended to combine and unify. It can be concluded that 75% is above the limit of proper space holder content.

(a)	(b)	(c)
(d)	(e)	(f)
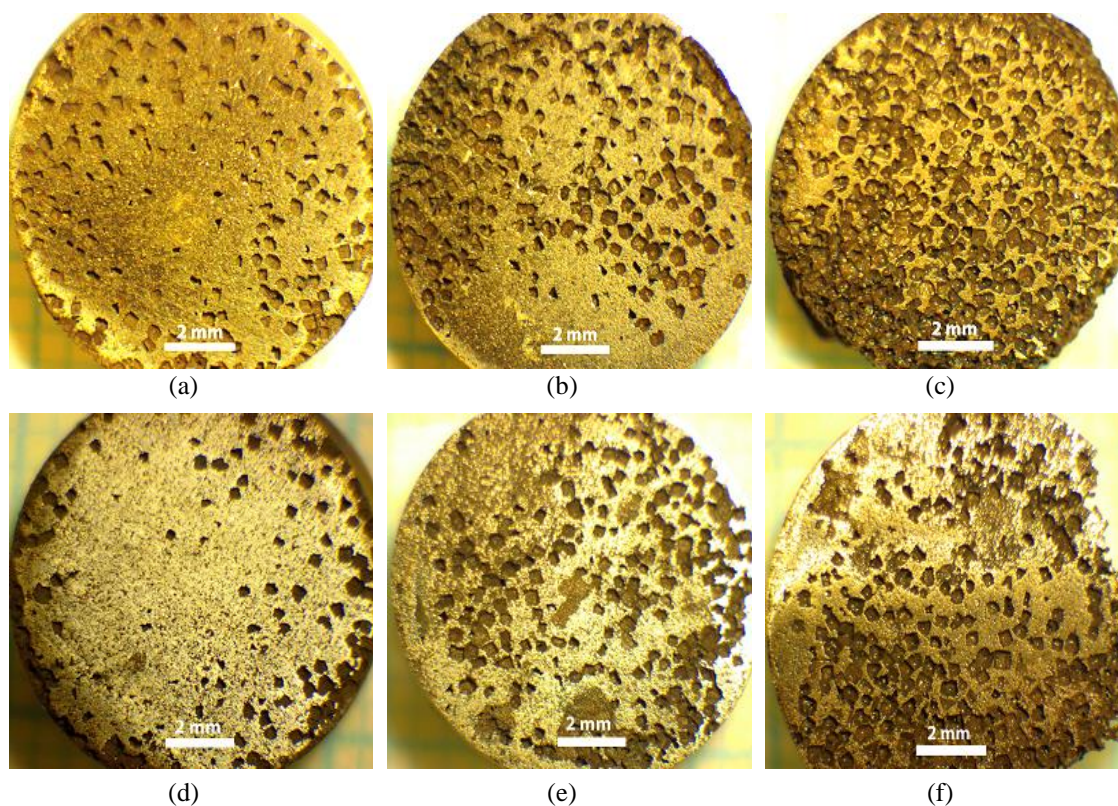
Figure 2. Macrostructures of the product pellets
a) 30DN25SN, b) 30DN50SN, c) 30DN75SN, d) 40DN25SN, e) 40DN50SN, f) 40DN75SN

Average total porosity of the green pellets having 30 and 40% diluent NiAl before VCS are presented in Table 2 and Table 3, respectively. The amount of total porosity in the green pellets before VCS was very similar in both series, as expected. It was seen that the total porosity amount was more than the added space holder NaCl amount in both series. This is due to the presence of porosity in the cell walls which contained the Ni+Al particles. This difference decreased with the increase in the NaCl content, or decrease in the amount of Ni+Al. The cells in the green pellet are the voids which were formed by the removal of the NaCl particles by dissolution in water.

The amount of porosity in the cell walls before VCS decreased with the increase in the space holder NaCl amount as shown in Table 2 and 3. It can be suggested that compressibility increased with the increase in the amount of NaCl particles.

Table 2. SH NaCl contents and average total porosity of the pellets having 30% preformed NiAl, before and after VCS

SH NaCl Content (%)	Before VCS				After VCS	
	Av. Total Porosity (%)	Standart Dev.	% Pore in Cell walls	Standart Dev.	Av. Total Porosity (%)	Standart Dev.
25	48.8	2.4	31.8	3.2	50.1	3.0
50	62.3	1.6	24.7	3.2	64.2	2.0
75	78.3	1.3	13.4	5.2	78.3	0.1

Table 3. *SH NaCl contents and average total porosity of the pellets having 40% preformed NiAl, before and after VCS*

SH NaCl Content (%)	Before VCS				After VCS	
	Av. Total Porosity (%)	Standart Dev.	% Pore in Cell walls	Standart Dev.	Av. Total Porosity (%)	Standart Dev.
25	49.1	2.3	32.1	3.1	54.3	3.1
50	62.6	1.6	25.2	3.2	65.6	1.8
75	77.9	2.3	11.4	9.2	77.9	1.2

Average pore amount in the products obtained from 30 and 40% NiAl diluent added mixtures after VCS, as a function of NaCl content are presented in Tables 2 and 3, and in Figure 3. In both series, the total porosity increased a few percent after VCS as compared to green pellets. For comparison, amount of NaCl space holder amount is indicated in Figure 2 as the gray straight line. Increase in the pore amount is expected in VCS due to gas release as a result of the temperature increase, Kirkendall effect during diffusion and density difference of the reactants and the products (Jiang et al., 2021).
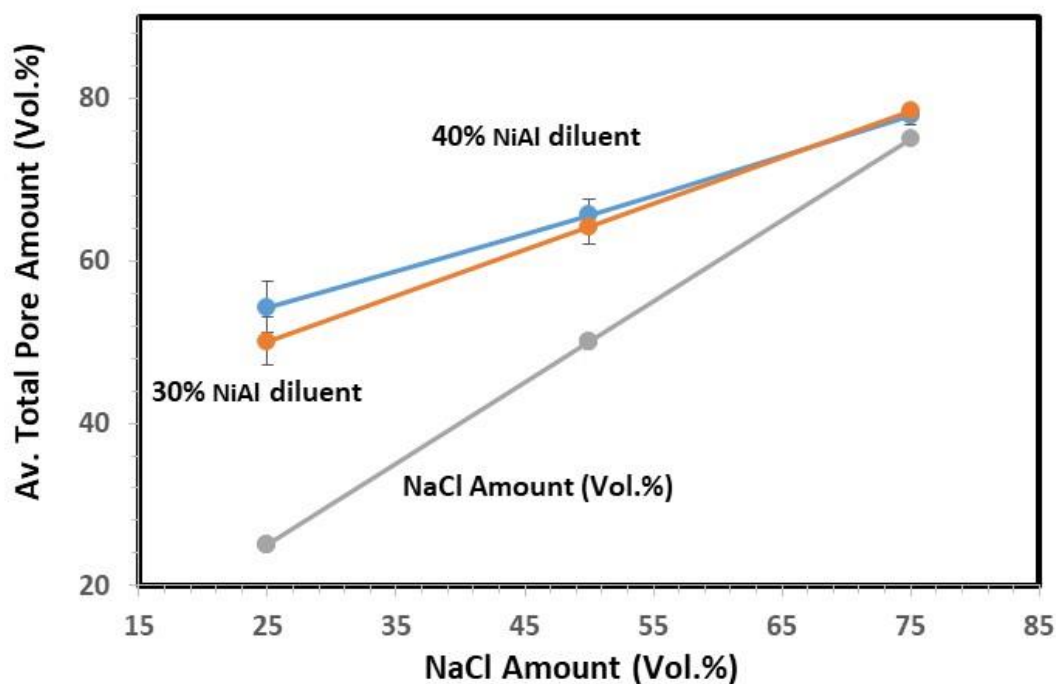
Figure 3. *Average pore amount in the products obtained from 30 and 40% NiAl diluent added mixtures after VCS, as a function of NaCl content*

3.3. Microstructure

The microstructural images of the samples are presented in Figure 4. In these images, the white regions are the cell walls and black regions are the pores. The large primary pores (cells) of about 400 μm size were formed by the space holder NaCl particles. The sizes of these large pores match well with the size of the utilized NaCl particles. It can be seen that the cell walls also contained some porosity. These secondary pores in the cell walls are believed to form due to the Kirkendall effect, porosity of the green pellet and volume difference between the reactant and product phases. It was inferred from microstructure examinations that the amount of the secondary pores in the cell walls increased with increasing diluent NiAl amount.
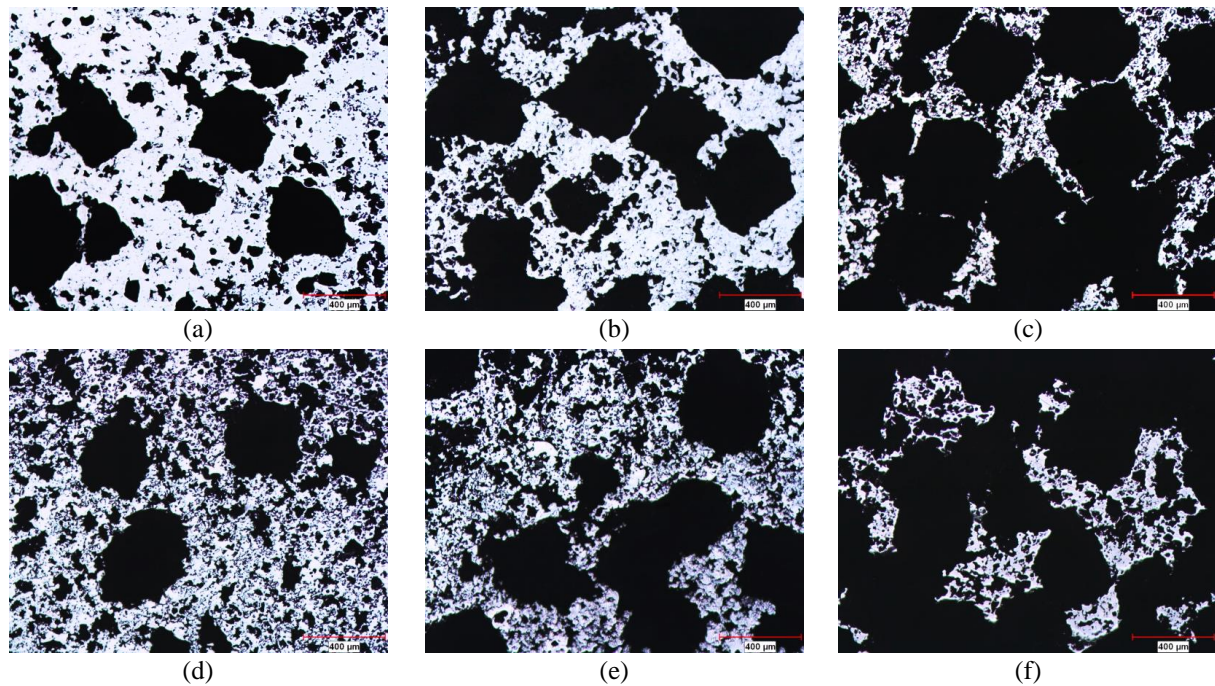
Figure 4. *Optical microscope images of the product pellets*
a) 30DN25SN, b) 30DN50SN, c) 30DN75SN, d) 40DN25SN, e) 40DN50SN, f) 40DN75SN (magn. 50X)

3.4. Mechanical Tests

Compression strength values of the samples formed by the addition of 30 and 40% diluent NiAl and 25, 50 and 75% space holder NaCl are presented in Figure 5 and Table 4. Samples with 30% NiAl diluent addition had higher compressive yield strength values than samples with 40% NiAl diluent addition. This may be a result of higher amount of liquid phase and thus better sintering of the samples that contained 30% diluent NiAl. With the increase in the amount of diluent NiAl from 30 to 40%, less amount of liquid phase is expected to form in the sample during VCS, as a result of the increased dilution effect of the higher amount of preformed NiAl.

The samples obtained from a mixture of 30 and 40% diluent NiAl and 25% spacer NaCl added showed average compressive strength values of 112.0±29.5 and 66.0±20.5 MPa, respectively. The high standard deviation may be attributed to the brittle nature of NiAl. With the increase in the amount of NaCl, there was a gradual decrease in the compressive strength of the porous NiAl samples. The compressive strength of the samples obtained from the mixtures with the addition of 30 and 40% diluent NiAl and 75% NaCl exhibited a compressive strength of 8.0±1.3 and 6.4±0.4 MPa, respectively.

Table 4. *Compressive yield strength values of the products obtained from 30 and 40% NiAl diluent added mixtures, as a function of NaCl content*

SH NaCl Content (%)	30% Diluent NiAl			40% Diluent NiAl		
	Av. Comp. Yield Str. (MPa)	Standart Dev.	Strain at max. stress (%)	Av. Comp. Yield Str. (MPa)	Standart Dev.	Strain at max. stress (%)
25	112.0	29.5	5.4	66.0	20.5	5.0
50	38.3	5.4	6.1	25.4	2.5	1.9
75	8.0	1.3	10.1	6.4	0.4	2.4
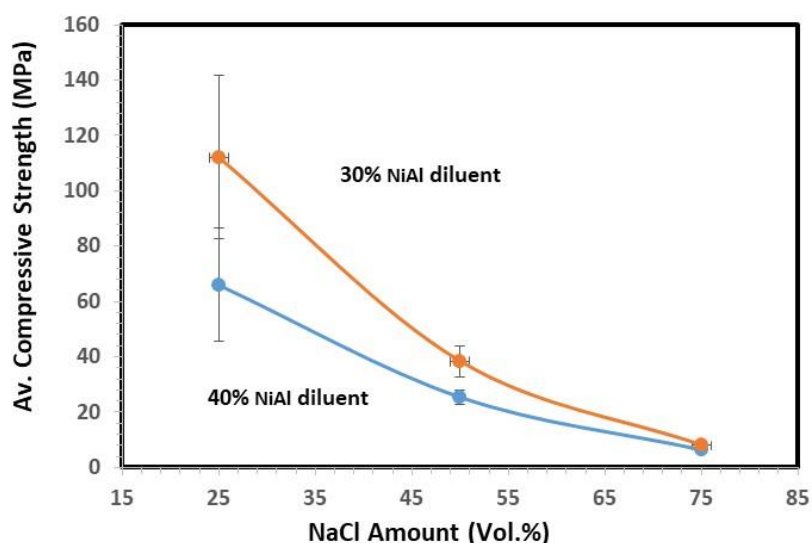
Figure 5. *Average compressive yield strength values of the products as a function of NaCl content in 30 and 40% diluent NiAl added samples*

Compressive stress-strain plots of the samples formed by the addition of 25, 50 and 75% space holder NaCl and 30 and 40% diluent NiAl are presented in Figure 6a and 6b, respectively. It can be observed that 30% diluent NiAl added samples exhibited higher compressive strength values for all NaCl amounts. There was a gradual decrease in the stress values, especially in the 50 and 75% NaCl added samples. This may be a result of the collapse of the cell walls in a sequence.

The microhardness measurements were conducted on samples which contained 25% NaCl. The thickness of the cell walls of the samples which contained higher amount of NaCl was not suitable for microhardness measurements. In addition, they contained high amount of secondary porosity in the cell walls. Microhardness of the samples which contained 30% diluent NiAl was higher than that of the samples which contained 40% diluent NiAl. This was attributed to the lower amount of secondary porosity in the samples which contained 30% diluent NiAl. The microhardness values of the samples which were produced by using 25% NaCl, and 30 and 40 diluent NiAl were 243 ± 34, 188 ± 25 $HV_{0.2}$, respectively. The microhardness of non-porous NiAl was previously reported as 394 ± 37 $HV_{0.2}$, (Camurlu & Maglia, 2009) which is in accordance with the microhardness values obtained in the present study for porous samples.

(a)   (b)
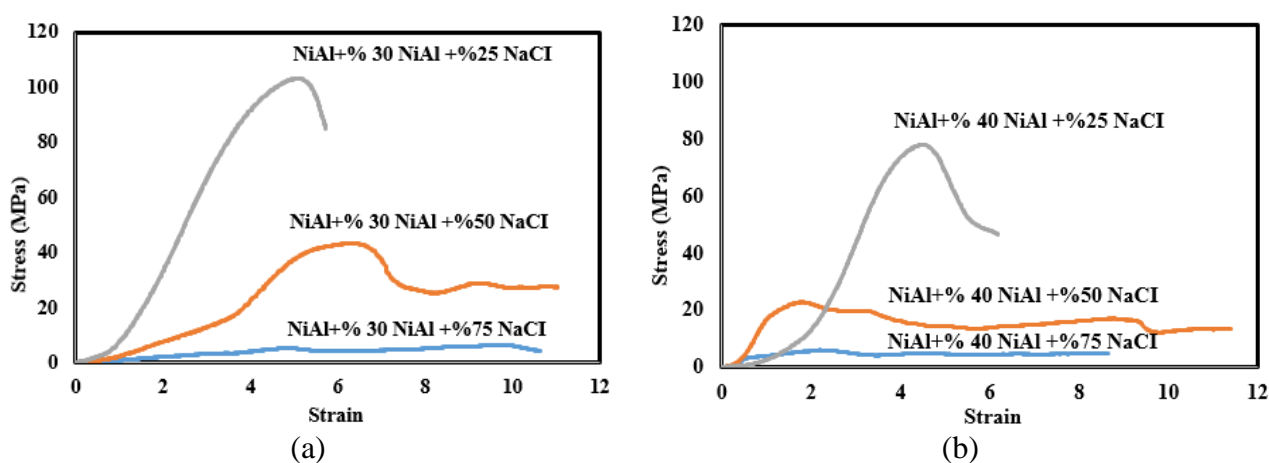
Figure 6. *Compressive stress-strain plots of samples which were formed by **a)** 30% and **b)** 40% diluent NiAl and 25, 50 and 75% space holder NaCl addition*

4. CONCLUSION

Porous NiAl parts were prepared by using NaCl space holder particles and via volume combustion synthesis technique, from Ni and Al powders. Addition of both 30 and 40% diluent preformed NiAl powder to the starting mixture resulted in preserving the shape of the cylindrical pellet. The adiabatic temperatures of the mixtures having 30 and 40% diluent NiAl were calculated as 1638.9 and 1460.8°C, respectively. The total porosity amount was seen to be more than the added space holder NaCl amount in both series. There was slight increase in total porosity amount in both series as a result of VCS reaction. This was attributed to the density difference of reactants and products, initial porosity in the reactants and Kirkendall effect during diffusion. Secondary porosity in the cell walls increased with increasing amount of diluent NiAl. Compressive strength and microhardness values were higher when 30% diluent NiAl was utilized. This was attributed to better sintering of the samples. Strength values decreased as a result of increase in the pore amount.

CONFLICT OF INTEREST

The authors declare no conflict of interest.

REFERENCES

Arifvianto, B., & Zhou, J. (2014). Fabrication of metallic biomedical scaffolds with the space holder method: a review. *Materials*, *7*(5), 3588-3622. doi:10.3390/ma7053588

Banhart, J. (2001). Manufacture, characterisation and application of cellular metals and metal foams. *Progress in Materials Science*, *46*(6), 559-632. doi:10.1016/S0079-6425(00)00002-5

Cai, X., Li, Z., Jiao, X., Wang, J., Kang, X., Feng, P., Akhtar, F., & Wang, X. (2021). Preparation of porous NiAl intermetallic with controllable shape and pore structure by rapid thermal explosion with space holder. *Metals and Materials International*, *27*(10), 4216-4224. doi:10.1007/s12540-020-00904-5

Camurlu, H. E., & Maglia, F. (2009). Self-propagating high-temperature synthesis of ZrB_2 or TiB_2 reinforced Ni–Al composite powder. *Journal of Alloys and Compounds*, *478*(1-2), 721-725. doi:10.1016/j.jallcom.2008.11.139

Jiang, Y., He, Y., & Gao, H. (2021). Recent progress in porous intermetallics: Synthesis mechanism, pore structure, and material properties. *Journal of Materials Science & Technology*, *74*, 89-104. doi:10.1016/j.jmst.2020.10.007

Li, Z., Cai, X., Ren, X., Kang, X., Wang, X., Jiao, X., & Feng, P. (2019). Rapid preparation of porous Ni–Al intermetallics by thermal explosion. *Combustion Science and Technology*, *192*(3), 486-492 doi:10.1080/00102202.2019.1576652

Moore, J. J., & Feng, H. J. (1995). Combustion synthesis of advanced materials: Part I. Reaction parameters. *Progress in Materials Science*, *39*(4-5), 243-273. doi:10.1016/0079-6425(94)00011-5

Roine, A. (2002). *Outokumpu HSC chemistry for windows. Chemical Reaction and Equilibrium Software with Extensive Ther-Mochemical Database*. PDF

Shu, Y., Suziki, A., Takata, N., & Kobashi, M. (2019). Microstructure and mechanical property of porous nickel aluminides Fabricated by Reactive Synthesis with Space Holder Powder. *MRS Advances*, *4*, 1515-1521. doi:10.1557/adv.2019.153

Su, X., Fu, F., Yan, Y., Zheng, G., Liang, T., Zhang, Q., Cheng, X., Yang, D., Chi, H., Tang, X., Zhang, Q., & Uher, C. (2014). Self-propagating high-temperature synthesis for compound thermoelectrics and new criterion for combustion processing. *Nature Communications*, *5*, 4908. doi:10.1038/ncomms5908

Varma, A., Rogachev, A. S., Mukasyan, A. S., & Hwang, S. (1998). Combustion synthesis of advanced materials: principles and applications. *Advances in Chemical Engineering*, 24, 79-226. doi:10.1016/S0065-2377(08)60093-9

Wang, Z., Jiao, X., Feng, P., Wang, X., Liu, Z., & Akhtar, F. (2016). Highly porous open cellular TiAl-based intermetallics fabricated by thermal explosion with space holder process. *Intermetallics, 68*, 95-100. doi:10.1016/j.intermet.2015.09.010

Yang, X., Hu, Q., Du, J., Song, H., Zou, T., Sha, J., He, C. & Zhao, N. (2019). Compression fatigue properties of open-cell aluminum foams fabricated by space-holder method. *International Journal of Fatigue*, 121, 272-280. doi:10.1016/j.ijfatigue.2018.11.008

Influence of the Hot Water Parameter on the Structural and Optical Properties of SILAR-Deposited ZnO Samples

Salih AKYÜREKLİ[1] [iD] Tuğba ÇORLU[1] [iD] Irmak KARADUMAN ER[2*] [iD] Selim ACAR[3] [iD]

[1]Innovative Technologies Application and Research Center, Suleyman Demirel University, Isparta, Türkiye
[2]Department of Medical Services and Techniques, Eldivan Medical Services Vocational School, Çankırı Karatekin University, Çankırı, Türkiye
[3]Department of Physics, Faculty of Science, Gazi University, Ankara, Türkiye

Keywords	Abstract
ZnO SILAR Morphological Characterization The Temperature of the Hot Water	In this study, ZnO thin films were grown by the Successive Ionic Layer Adsorption and Reaction (SILAR) method. The SILAR method is a chemical solution-based method consisting of 4 steps: solution, hot water, air and deionized water. Our main goal is to examine the changes in SILAR method production by changing the hot water parameter from these steps. It is widely known that chemical synthesis methods and their relative parameters have a crucial effect on the size of the produced thin films, surface area/volume ratio, porosity as well as defects in the film which in turn affect the morphology. All parameters were kept the same and changes were made in the hot water step, in addition to the classic 90°C hot water step, constant temperature ultrasonic cleaner at 40 ºC, an ultrasonic cleaner at room temperature, and an ultrasonic breaker at room temperature are used instead of the hot water step. For this purpose, alternative devices such as ultrasonic cleaner and ultrasonic breaker were used to break the unwanted weak bonds at lower temperatures during production. The structural, morphological, optical and electrical properties were characterized and the results were investigated in detail.

1. INTRODUCTION

Zinc oxide (ZnO) material is one of the most promising candidates due to its inexpensive, abundance, chemical and mechanical stability, and optical and electrical properties among metal oxide materials (Irani et al., 2016; Vaizoğullar, 2018). One of the most significant reasons for the wide application area of ZnO material is that the direct band gap of ZnO is 3.37 eV and the excitation binding energy value is 60 meV (Şahin et al., 2022). Due to these properties, ZnO has lots of applications. Some of these are rubber, ceramic, pharmaceutical and electronic industry, medical applications, and many others. Great interest in ZnO nanoparticles is used by biological sciences such as an antibacterial, antifungal, and antifouling agent. The safeness of ZnO molecules and their compatible nature with the human body made them appropriate materials for biological applications. ZnO nanoparticles have diameters less than 100 nanometers.

The effect of defects on the performance of optoelectronic devices is a well-known issue. Defects can act as non-namely recombination centers in optoelectronic circuit devices such as light-emitting diode and Iazer. Thus, it can reduce the efficiency of the circuit device and even make light production impossible. In this case, the defects can act as centers that reduce carrier mobility and that prevent the circuit device from operating at high frequencies. Particle size and crystal morphology play an important role in making better circuits. For this reason, many thin-film growth methods have been developed. These are physical vapor deposition, ion sputtering, solvothermal method, hydrothermal methods, sol-gel methods, spray pyrolysis, chemical bath

deposition, and SILAR (Successive Ionic Layer Adsorption and Reaction), etc. Among these methods, SILAR is one of the fast and most affordable methods because it does not require any sophisticated substrate (Çorlu et al., 2018). Parameters can be controlled and changeable according to the main purpose. SILAR method is based on sequential ionic layer adsorption and reaction (Çorlu et al., 2018). The originality in this method is the adsorption (deposition) of one substance onto another substance on the substrate (Şahin et al, 2022). Changing the molarity of the solution used in the SILAR cycle, increasing or decreasing the hot water temperature, changing the thickness, differences in the waiting time in the solution, etc. parameters lead to different structural, optical and electrical properties in samples grown with SILAR (Karaduman Er et al., 2021).

The spooling operation can be performed in a single row or with multiple consecutive repetitions (Radhi Devi et al., 2020). The removal of unwanted substances that may occur on the surface is achieved by rinsing with the step of deionized water. In general, the quality of the films can be changed by changing the structural, optical and electrical properties of the films produced by changing one or more parameters from these steps. Şahin et al. (2022) have studied the effect of thymus syriacus plant extract on the physical properties of ZnO nanoparticles synthesized by SILAR method and studied their properties with this changing process. Gahramanli et al. (2021) have investigated role of temperature in the growth and formation of $CdxZn1-xS/PVA$ nanocomposites through SILAR method. The main purpose of this study is to discuss the results obtained by changing the hot water parameter from SILAR parameters and also the effect of the vibration on this parameter. Structural, optical and electrical changes will be shown on the effect of changing this step on production and its difference from the traditional production method. For this purpose, the structural, morphological, optical and electrical properties of the produced ZnO thin films were investigated and The most suitable parameter for advanced industrial or technological applications was determined.

2. MATERIAL AND METHOD

($[Zn(NH_3)_4]^{2+}$) zinc-ammonia mixture was used for the production of ZnO on the cleaned glass substrates. In order to prepare the zinc-ammonia mixture, firstly, 1,363 g of $ZnCl_2$ (99% Sigma Aldrich) material was weighed on a precision balance. The weighed material was placed in a flask and 100 mL of distilled water was placed on it and mixed in a magnetic stirrer for 30 minutes. Thus, 0.1 M $ZnCl_2$ (pH≈5.5) solution was obtained. The prepared solution was mixed with 25-28% (2 mL) NH_3 at [18:2] ratios to make it ready for growth.

A SILAR cycle of the produced ZnO thin films is given in Figure 1. Each glass substrate was cleaned individually in propanol for 10 minutes. Solutions were prepared during the substrate cleaning process. The cleaned and prepared glass substrates were subjected to the classical SILAR cycle as the first growth method. The glass substrate was kept in the ($[Zn(NH_3)_4]^{2+}$) solution, which was prepared before, for 15 seconds, respectively. The substrate, which was removed from the solution, was kept in distilled water at 90°C for 7s. The substrates, which were kept in air for 60 s after hot water, were then immersed in distilled water at room temperature and kept there for 30 s. Thus, a cycle is completed. After the first growing process, ultrasonic cleaner was chosen as the hot water parameter in the second growing method. The cleaned substrate was first immersed in the prepared solution and then in an ultrasonic cleaner containing water at 40°C temperature, and the subsequent stages were kept the same as the first growth process. In another growth process, the prepared glass substrate was immersed in an ultrasonic cleaner filled with room-temperature water as an alternative to the hot water parameter. Finally, the cleaned glass substrate was used in the magnification process at room temperature using an ultrasonic breaker. Thus, ZnO material was grown on glass substrates by using different methods as an alternative to the hot water parameter. This cycle was repeated forty times.

Each sample was named according to the production parameter. The sample grown using the 90°C hot water parameter was named ZnO1, the growth using the ultrasonic cleaner with 40°C water was named ZnO2, the growth made with an ultrasonic cleaner with room temperature water was named ZnO3, and the growth with a 1 pulse vibration ultrasonic breaker with room temperature water was named ZnO4, as given in Table 1.

XRD analysis were measured in the Bruker D8 Advance Twin-Twin XRD system using the Bragg-Brentano method in the angle range of 20°-80° (2Θ). The surface morphological characterization using FEI QUANTA FEG 250 SEM device of ZnO thin films were observed. Elemental components were obtained by using energy dispersive X-ray spectrometry (EDAX) together with SEM analysis. Optical analyzes such as absorbance and

transmittance were performed using the UV-1800 SHIMADZU device. The surface morphology of all the thin films were investigated with using the ez-AFM Nanomagnetics device in 2×2 μm^2 area. The electrical characterization was taken with a Keithley 2400 source meter by a computer.

The thickness was estimated by the weight difference method using this relation;

$$d = \frac{m}{\rho A} \tag{1}$$

with m is the film mass deposited on the substrate, ρ is the density of the ZnO material in the bulk form (ZnO; ρ=5.61 g/cm^3). The thickness of the ZnO thin films were found 375 nm, 390 nm, 400 nm and 415 nm for ZnO1, ZnO2, ZnO3 and ZnO4, respectively It is thought that the molecules in the solution cannot sufficiently adhere to the surface due to the vibration effect and as a result, the thickness of the samples decreases. Even if samples are grown in the same cycles, changes in parameters can lead to changes in thickness (Abdulrahman et al., 2021).
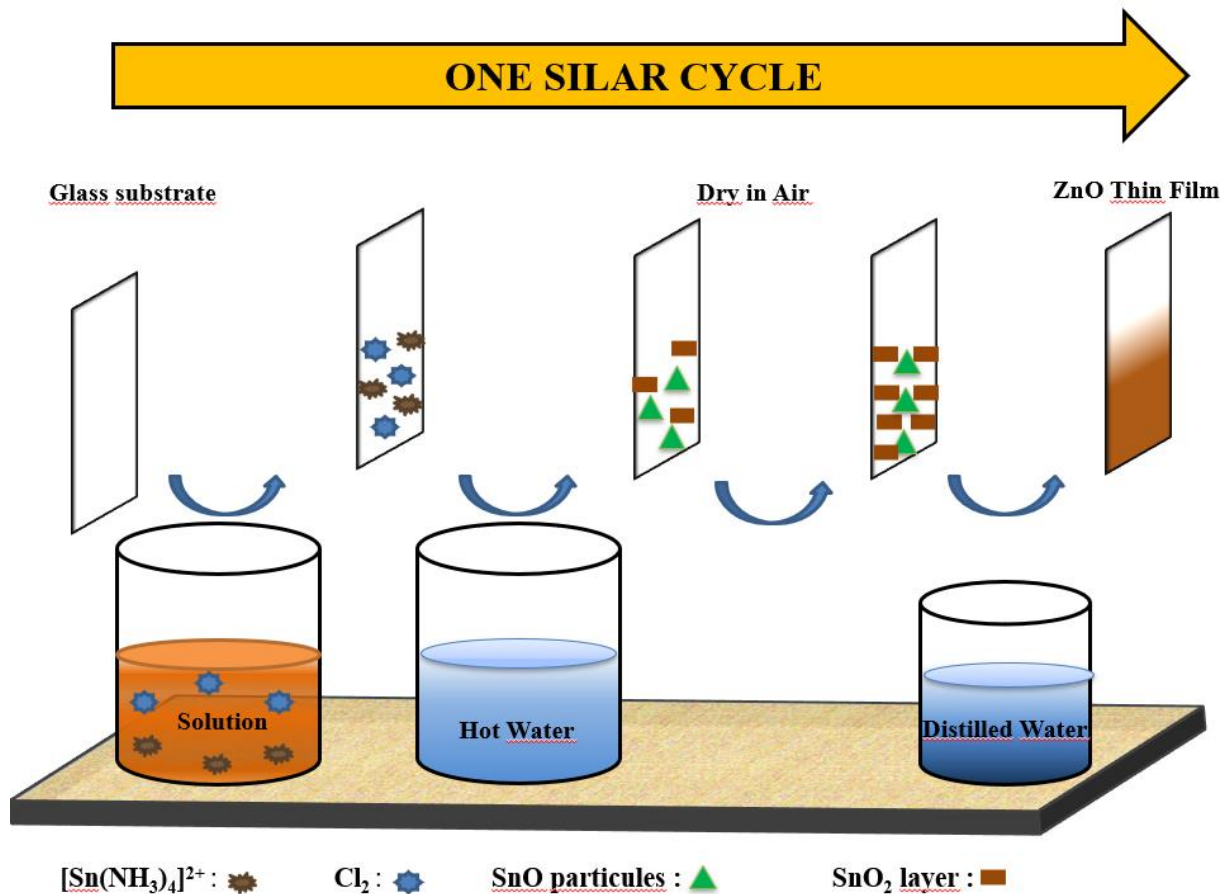
Figure 1. *The schematic diagram of SILAR cycle*

Table 1. *Renaming of each sample according to the production parameter*

Producing Parameter	Sample Code
the 90°C hot water	ZnO1
the ultrasonic cleaner with 40°C water	ZnO2
with an ultrasonic cleaner with room temperature water	ZnO3
with a 1 pulse vibration ultrasonic breaker with room temperature water	ZnO4

3. RESULTS AND DISCUSSION

Figure 2 shows the pattern of XRD analysis of all samples. It was observed that (100), (002) and (101) zinc peaks were dominant in ZnO1 and ZnO2 thin films and the peaks overlapped with a wurtzite structure (JPDS Card No: 01-079-0208) (Gujar et.al., 2008; Yıldırım & Ateş, 2010). The water parameter was utilized to deposit nanoparticles on the substrate. Each alternative parameter affected the thickness and crystallinity of the produced films and therefore the peak intensities in the XRD patterns changed. Since the ZnO material is very thinly coated in ZnO3 and ZnO4 thin films, no peak is observed in the XRD pattern (Raidou et al., 2014). Raidou et al. (2014) have changed the rinsing period of ZnO films to 20 s, 30 s and 40 s. They looked at the changes in the XRD peaks with the change of time and seen that the crystallinity of the XRD peaks increased with increasing time. The enhancement of the rinsing period was provided more thermal energy (Raidou et al., 2014). There are several factors that increase the reaction rate during thin film production. High temperature causes situations such as increasing chemical reactivity and changing the reaction path in production. This is why good quality films are produced using the temperature parameter. The transition phase from the prepared solution to the thin film form consists of two processes; nucleation and growth. Thin film thickness occurs when small molecules come together to form larger particles during the nucleation stage. In this research, the use of an ultrasonic breaker formed an obstacle for the molecules to come together, so that the desired thickness of the sample did not occur (Rayathulhan et al., 2017).
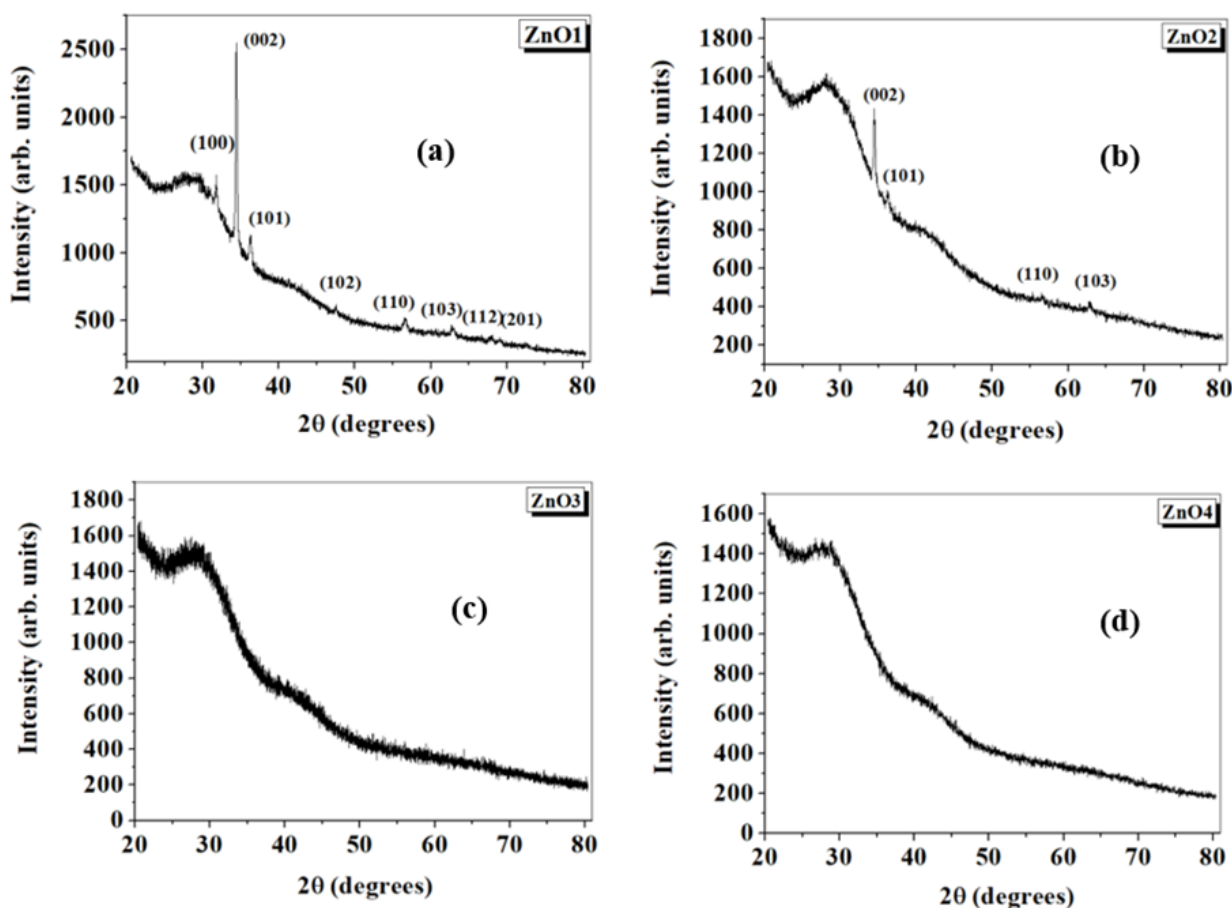
Figure 2. *The pattern of XRD analysis of ZnO thin films;* ***a)*** *ZnO1,* ***b)*** *ZnO2,* ***c)*** *ZnO3 and* ***d)*** *ZnO4*

Figure 3 depicts the SEM analysis of ZnO thin films. It was observed that the ZnO1 material coated on the glass was thicker and more homogeneous than the other magnifications Although similar homogeneity was seen in the ZnO2 thin film, the material grew thinner on the surface than the ZnO1 thin film. The surface homogeneity and adhesion of the material on the surface decreased gradually in ZnO3 and ZnO4 thin films, respectively.
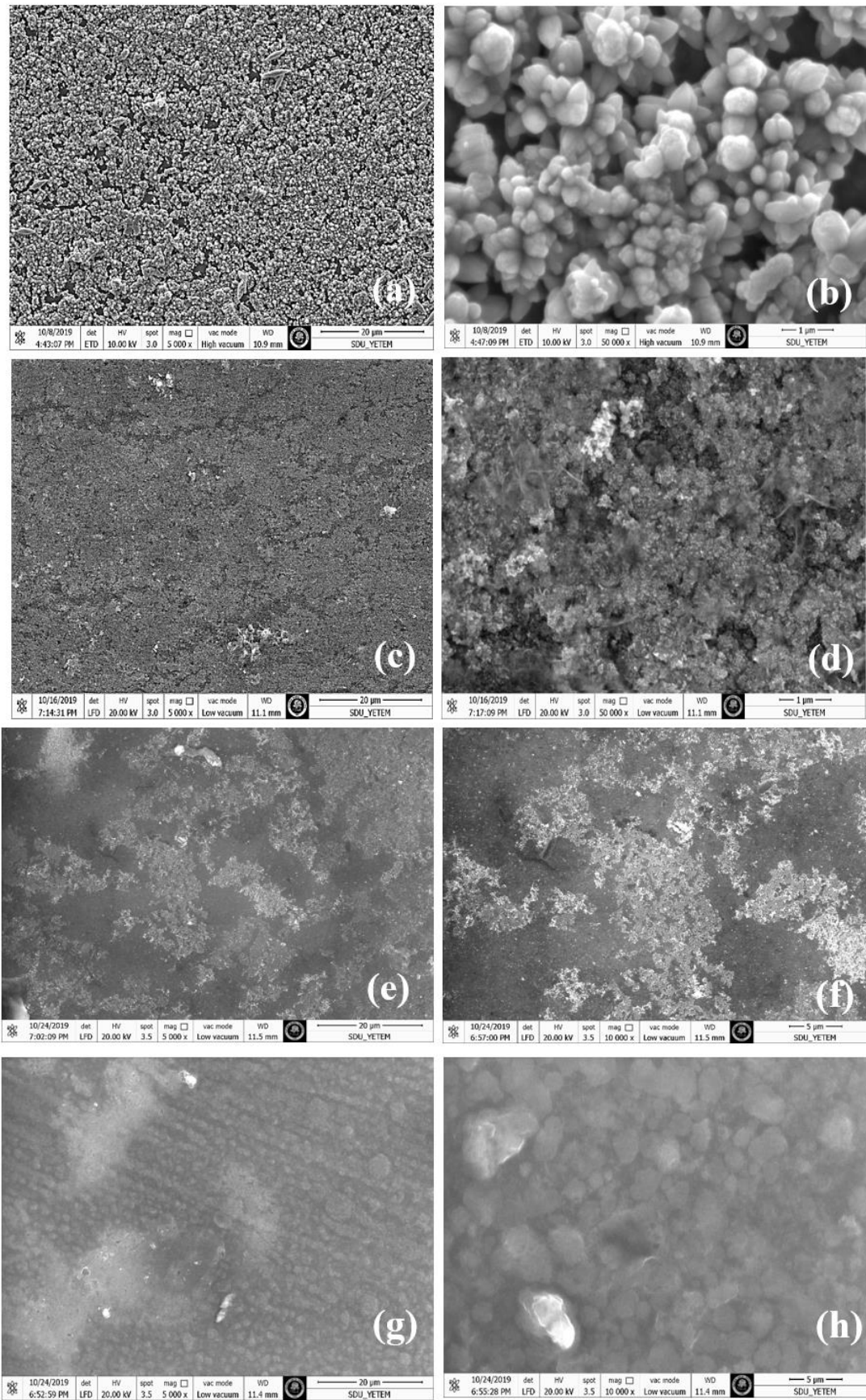
Figure 3. *SEM analysis ZnO thin films;* ***a) b)*** *ZnO1,* ***c) d)*** *ZnO2,* ***e) f)*** *ZnO3 and* ***g) h)*** *ZnO4*

EDAX analysis was taken to confirm the existence of desired elements in the thin films produced. EDAX spectra of all the synthesized samples are provided in Figure 4. It is important to note that all expected elements (Zn and O in samples) were detected along with the other impurities (Si and C). Changes were observed in the amount of elements depending on the differences used in the hot water parameter. Also, it is thought that the molecules in the solution cannot sufficiently adhere to the surface due to the vibration effect and as a result, the atomic ratio is decreased. Consequently, looking at the article as a whole, it is seen that the results compatible with the classical method are obtained in the sample produced with the help of an ultrasonic cleaner by changing the temperature parameter. It is understood from this that the Zn atoms of the samples produced at room temperature cannot sufficiently adhere to the sample. There are problems in the entry of atoms into the structure due to the low kinetic energy due to the low temperature of the water.
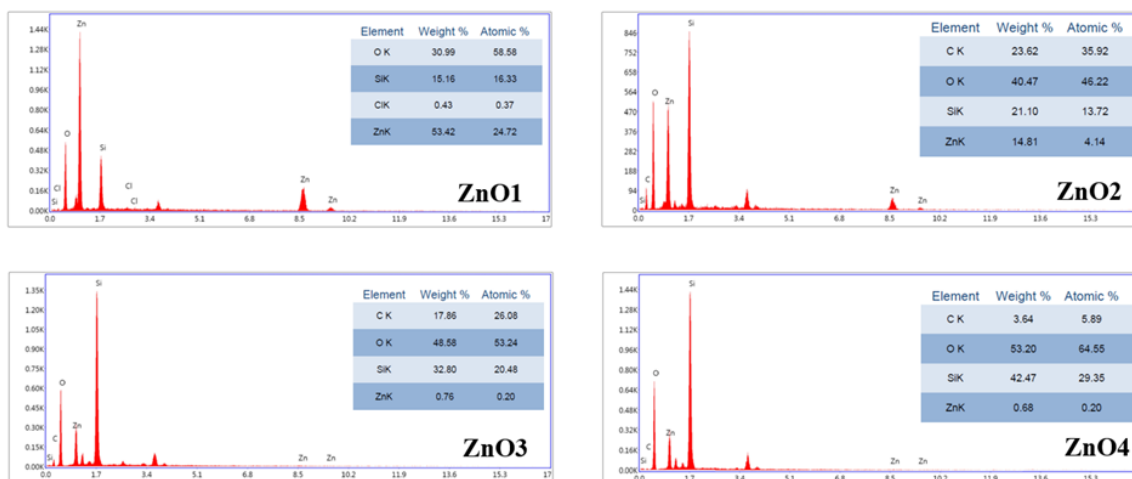
Figure 4. *EDAX analysis of ZnO thin films; **a)** ZnO1, **b)** ZnO2, **c)** ZnO3 and **d)** ZnO4*

Figure 5 shows the AFM AFM images of ZnO1 (a), ZnO2 (b), ZnO3 (c) and ZnO4 (d). All samples were investigated with using the ez-AFM Nanomagnetics device in 2×2 μm^2 area. It was observed that the films, which were given AFM images, respectively, had rough surfaces. With the change of the hot water parameter in the production step, some changes in the surface roughness of the films were observed (Méndez-Vilas et al., 2007). The surface roughness values of each thin film are given in Table 2. These values were found to be compatible with the results of SEM, EDAX and XRD analysis.

Although no clear growth was observed in the SEM and XRD analyses, it can be seen from the AFM results that the samples were formed very thin and the surface was completely amorphous. However, roughness values were obtained from the AFM results, which may indicate some growth in the samples. One pulse vibration will be so strong that the coating has not grown in the desired thickness and homogeneity. It can be attributed that the bonds of the chemicals are broken and there are difficulties in adhering to the surface. When the ZnO2 and ZnO3 samples are compared, the effect of temperature is clearly seen. Desired growth was not observed at room temperature. As the temperature increases, better adhesion to the surface is provided. The best example is ZnO1.

In optoelectronic systems, ZnO lasers are used distance and height measurement systems, medical communication and communication systems. The spectrum of light emitted in semiconductor lasers depends on the material used. They have a very high working speed. Therefore, ZnO is preferred more than other semiconductor types. Also, the electrical properties, atomic structure, and electronic band structure of semiconductors can be associated with the optical properties. Figure 6 shows the absorbance measurements of SILAR-deposited ZnO thin films. ZnO exhibits strong UV absorption spectra with the absorption peak ranging from 360 to 375 nm due to their excitonic transition (Kumar et al., 2014). This is in harmony with the semiconductor behavior (Kumar et al., 2014). ZnO film exhibits high transmittance (~75%) in the visible region, as given in Figure 7. Transmission is inversely proportional to absorbance. As you explained above, the film thickness increases, which means more light is absorbed in the thick film. Therefore, the permeability is reduced.
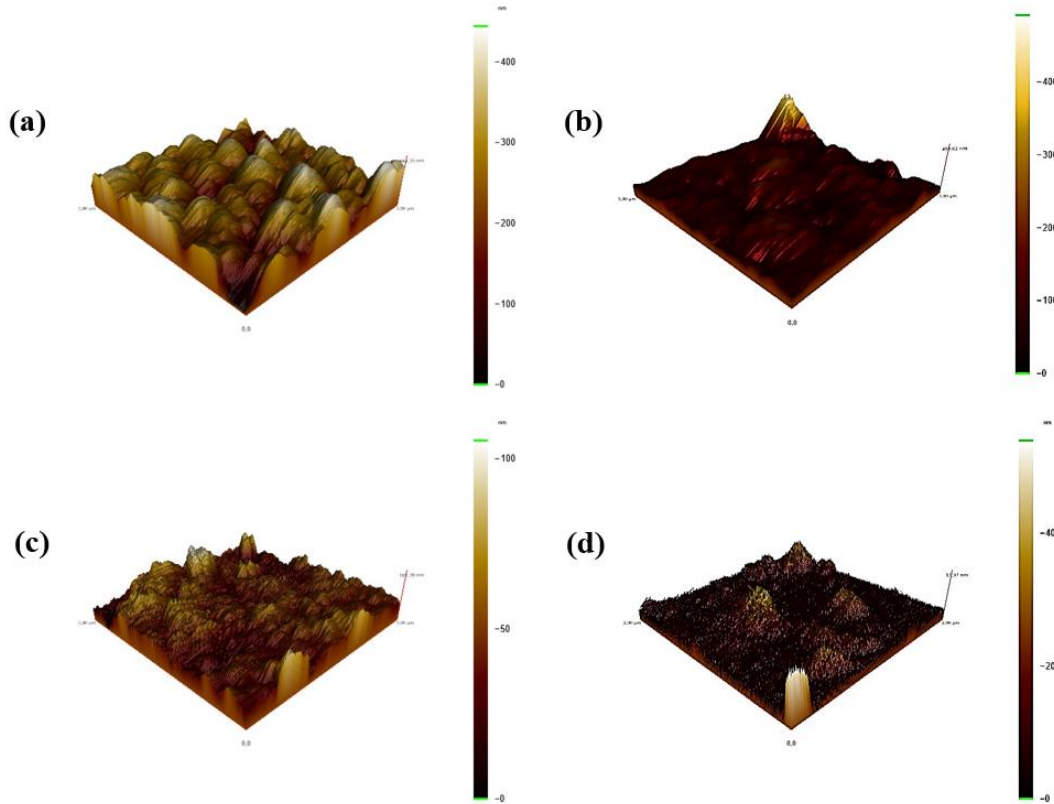
Figure 5. *AFM images of a) ZnO1, b) ZnO2, c) ZnO3 and d) ZnO4*

Table 2. *Surface roughness values of each thin film*

	ZnO1	**ZnO2**	**ZnO3**	**ZnO4**
Surface Roughness	46.58 nm	39.84 nm	20.32 nm	19.73 nm
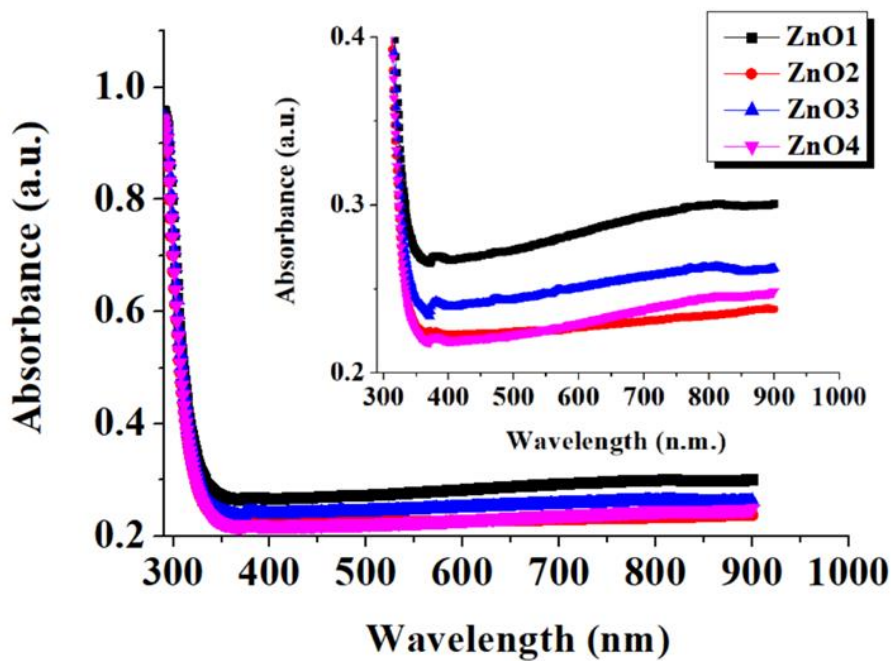
Figure 6. *Absorbance spectrum of deposited films*
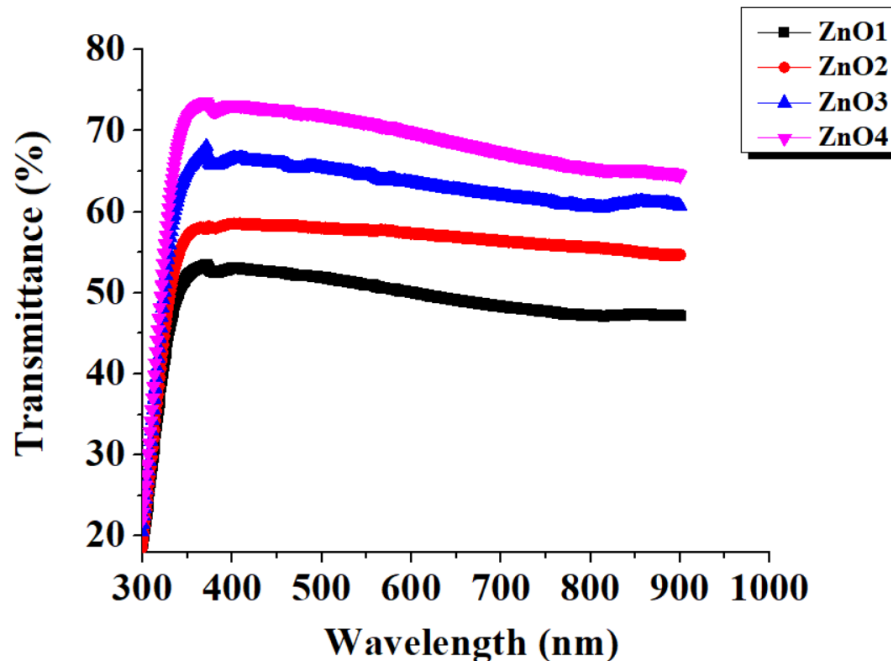
***Figure 7.** Transmittance spectrum of deposited films*

Reflectance can be calculated from the below equation (Komaraiah et. al., 2016);

$$\text{Absorbance} + \text{Transmittance} + \text{Reflectance} = 1 \tag{2}$$

Figure 8 gives the Reflectance spectra of ZnO thin films. When the reflectance values are examined, it is seen that the samples are compatible with each other. As can be seen, there is a reflectance graph for the ZnO2 sample, but it is very low compared to other samples. The peak at 380 nm corresponds to the intrinsic transition of exciton from the ZnO conduction band to valence band. The electron transition from the localized level slightly below conduction band to valence band is associated with the peak at 392 nm, which has been reported by several authors (Fu et al., 1998; Komaraiah et. al., 2016).

The variation of absorption coefficient (α) is showed in Figure 9 and the following equation is being used to compute this parameter (Komaraiah et. al., 2016);

$$\alpha = \frac{2.303}{d} . A \tag{3}$$

Where A is absorbance and d is film thickness. Extinction coefficient (k) analyse is some of the very important parameter in optical-based device design. The following equation is being used to compute this parameter (Tekin and Karaduman Er, 2022);

$$k = \frac{\alpha \lambda}{4\pi} \tag{4}$$

Figure 9 and Figure 10 show the absorption and extinction coefficient of thin films. It is believed that the absorption coefficient has exponential behavior due to random fluctuations of the interior fields in structural disorders.
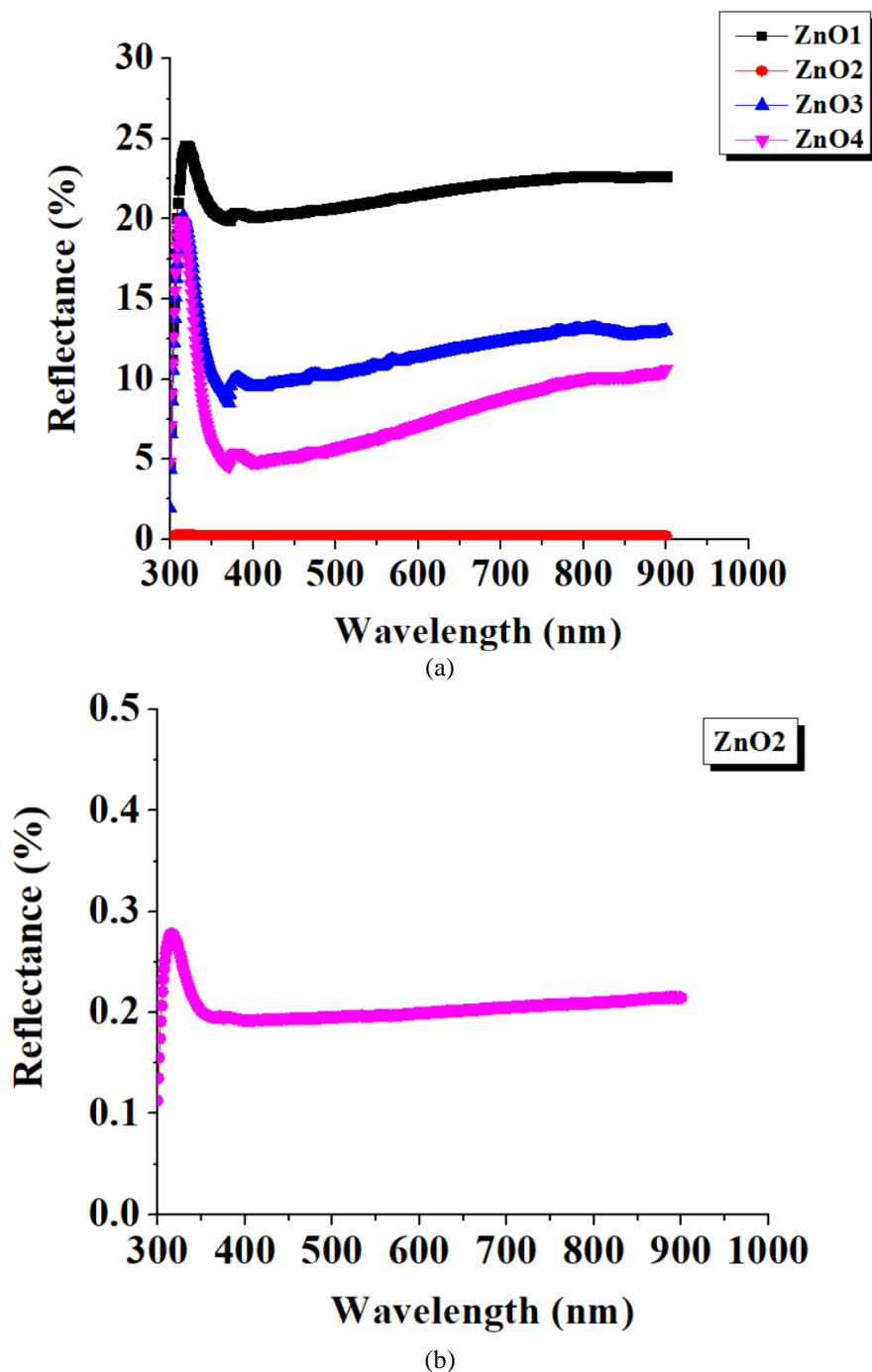
Figure 8. a) Reflectance spectrum of ZnO thin films b) Reflectance spectrum of ZnO2 thin films

Since band gap change is an important issue in optoelectronic applications, band gap change of thin films has been investigated. Figure 11 shows the plot of $(\alpha h v)^2$ against hv. The nature of the transition was determined by using this relation, Tauc plot (Hammad et al, 2018);

$$\alpha = \frac{A(h\vartheta - E_g)^n}{h\vartheta} \tag{5}$$

where the symbols have their usual meanings. The optical band gap energy values of 3.39 eV, 3.40 eV, 3.43 eV and 3.45 eV were estimated ZnO1, ZnO2, ZnO3 and ZnO4, respectively. Variation is observed depending on the thickness and producing hot water parameters, affecting the optical band gap. When examined in the literature, an increase and decrease can be observed depending on the thickness, which is given by Zheng et al. (2022) and Hammad et al. (2018), respectively. Also, Shaba et al. (2021) have reported that synthesis

parameters affecting the properties of zinc oxide and its applications. Habibi et al. (2009) have reported that SILAR-deposited ZnO thin films were investigated by tuning the synthesis parameters and as a result of this, changes in the formation of structures were seen. Also, the quality of ZnO with the reaction time was enhanced in their study.
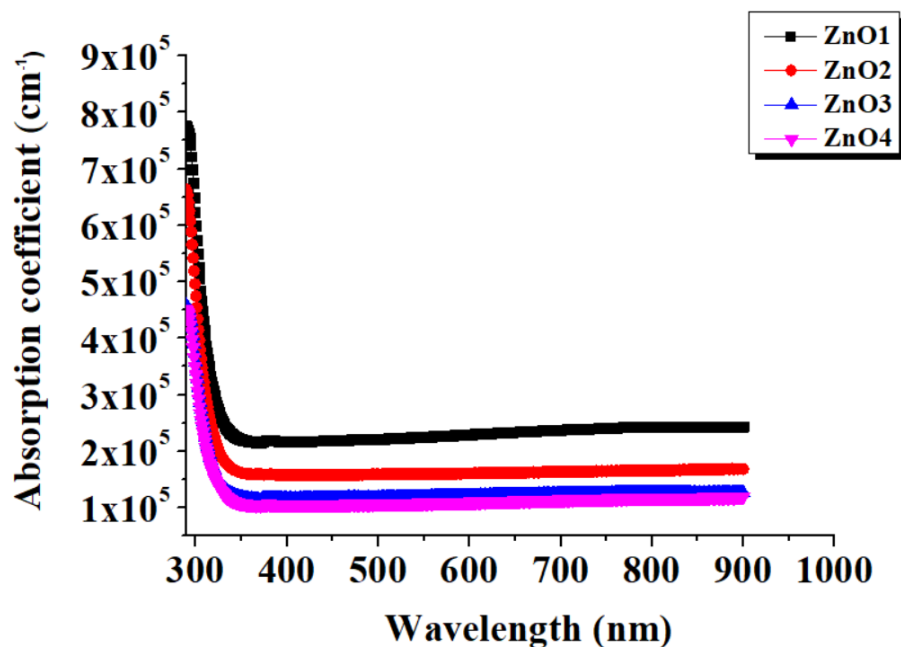
Figure 9. Absorption Coefficient of ZnO thin films
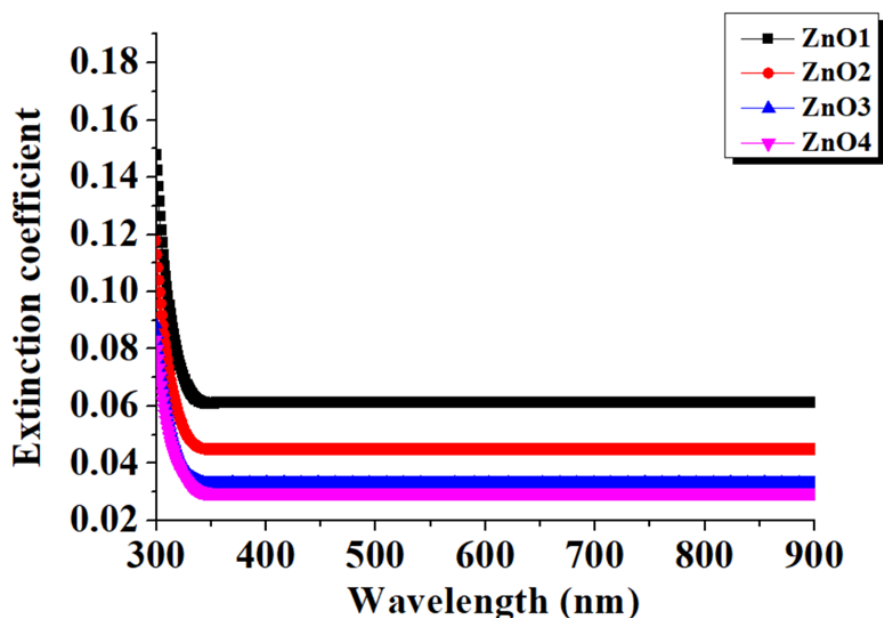
Figure 10. Extinction Coefficient of ZnO thin films

Figure 12 shows the current-voltage characteristics of SILAR-deposited ZnO thin films. All plots in Figure 12 indicate the ohmic behavior which is the nature of semiconductor ZnO thin films. ZnO4 is formed in a more amorphous structure, its electrical resistance is quite high compared to ZnO1, ZnO2 and ZnO3 samples. The resistance of growth samples was calculated as $1.21 \times 10^5 \, \Omega$, $1.33 \times 10^5 \, \Omega$, $9.14 \times 10^5 \, \Omega$ and $2.48 \times 10^9 \, \Omega$ for ZnO1, ZnO2, ZnO3 and ZnO4, respectively. The obtained resistance values are in good agreement with the previously

reported results (Gurav et al., 2010; Jambure et al., 2014). Table 3 shows the parameters of each thin film with morphological, optical and electrical results.
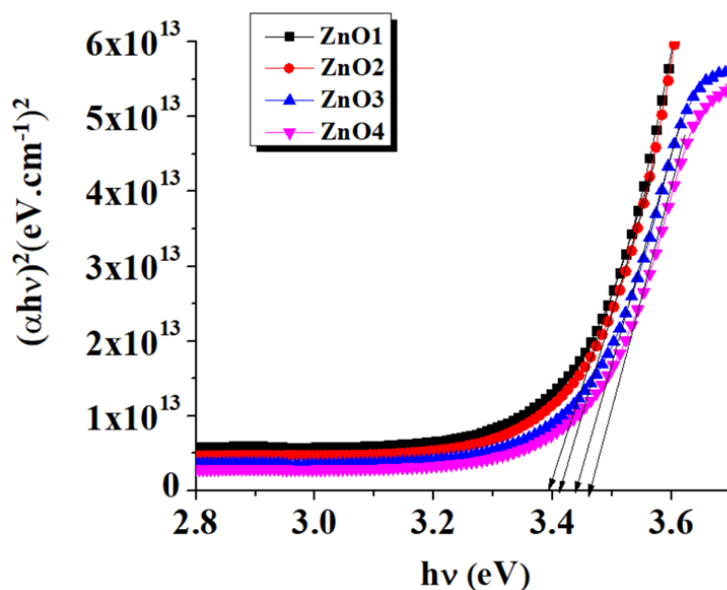
Figure 11. The plot of (αhν)² against hν of ZnO thin films
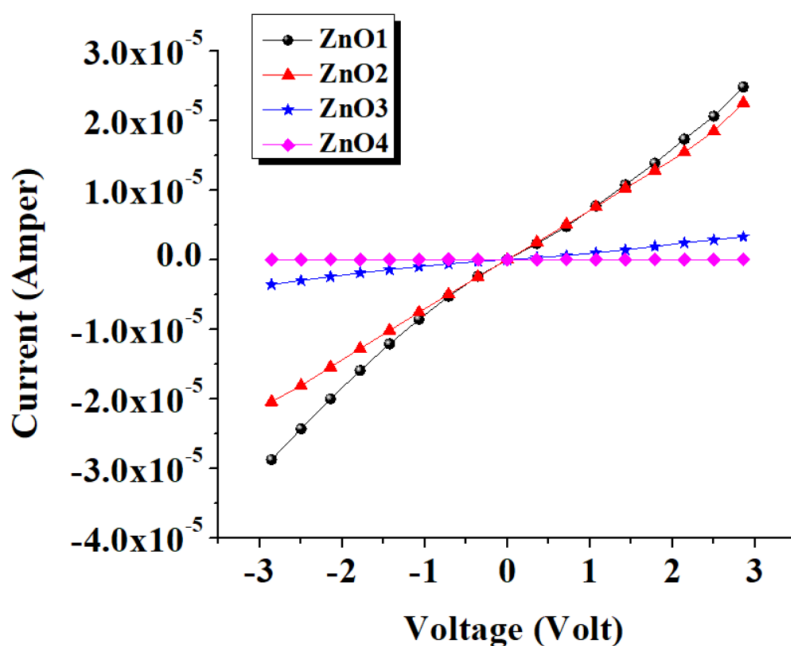
Figure 12. The I-V plots of ZnO thin films

Table 3. The parameters of each thin film with morphological, optical, electrical results

	ZnO1	ZnO2	ZnO3	ZnO4
Thickness (nm)	375	390	400	415
Optical Band Gap (eV)	3.39	3.40	3.43	3.45
Electrical Resistance (Ω)	1.21×10^5	1.33×10^5	9.14×10^5	2.48×10^9

4. CONCLUSION

In this work, ZnO material was grown by changing the second parameter of the classical SILAR method on glass substrates and the structural characterizations of the grown thin films were investigated. Adhesion effects of the material to be coated on the substrates were investigated by using hot water, ultrasonic cleaner and ultrasonic breaker, respectively, during magnification. It was observed that the dominant peak intensities also changed with the changed SILAR parameter in the thin films whose XRD patterns were examined. While the crystal phase orientation intensities were the highest in the ZnO1 thin film, the orientation intensity decreased in the ZnO2 thin film, and no peak was observed in the ZnO3 and ZnO4 thin films. Each value was found to be compatible. Optical analysis shows that thin films have high transmittance values, compared to absorbance and reflectance. Despite the fact that alternative devices such as ultrasonic cleaner and ultrasonic breaker were used to remove unwanted weak bonds at lower temperatures during production, The desired results could not be obtained and the samples could not adhere to the surface. It is thought that these vibrations cause excessive breakage and prevent the adhesion of Zn and O molecules. Different from the classical SILAR method production method, when the samples produced at 40 °C with the help of an ultrasonic cleaner are examined in detail, structural, optical and electrical results compatible with the literature have been obtained and a new approach has been brought to the SILAR method production.

CONFLICT OF INTEREST

The authors declare no conflict of interest.

REFERENCES

Abdulrahman, A. F., Abd-Alghafour, N. M., & Ahmed, S. M. (2021). Optimization and characterization of SILAR synthesized ZnO nanorods for UV photodetector sensor. *Sensors and Actuators A: Physical*, *323*, 112656. doi:10.1016/j.sna.2021.112656

Çorlu, T., Karaduman, I., Galioglu, S., Akata, B., Yıldırım, M. A., Ates, A., & Acar, S. (2018). Low level NO gas sensing properties of Cu doped ZnO thin films prepared by SILAR method. *Materials Letters*, *212*, 292-295. doi:10.1016/j.matlet.2017.10.121

Fu, Z.-x., Guo, C.-x., Lin, B.-x., & Liao, G.-h. (1998). Cathodoluminescence of ZnO Films. *Chinese Physics Letters*, *15*(6), 457. doi:10.1088/0256-307X/15/6/025

Gahramanli, L. R., Muradov, M. B., Balayeva, O. O., Eyvazova, G. M., & Mirsultanova, R. M. (2021). Role of temperature in the growth and formation of $Cd_xZn_{1-x}S$/PVA nanocomposites through SILAR method. *Materials Research Bulletin*, *137*, 111162. doi:10.1016/j.materresbull.2020.111162

Gujar, T. P., Shinde, V. R., Kim, W.-Y., Jung, K.-D., Lokhande, C. D., & Joo, O.-S. (2008) Formation of CdO films from chemically deposited $Cd(OH)_2$ films as a precursor. *Applied Surface Science*, *254*(13), 3813-3818. doi:10.1016/j.apsusc.2007.12.015

Gurav, K. V., Fulari, V. J., Patil, U. M., Lokhande, C. D., & Joo, O.-S. (2010) Room temperature soft chemical route for nanofibrous wurtzite ZnO thin film synthesis. *Applied Surface Science, 256*(9), 2680-2685. doi:10.1016/j.apsusc.2009.09.080

Habibi, R., Towfighi Daryan, J., & Rashidi, A. M. (2009). Shape and size-controlled fabrication of ZnO nanostructures using novel templates. *Journal of Experimental Nanoscience*, *4*(1), 35-45 doi:10.1080/17458080802680796

Hammad, A. H., Abdel-wahab, M. Sh., Vattamkandathil, S., &Ansari, A. R. (2018) Structural and optical properties of ZnO thin films prepared by RF sputtering at different thicknesses. *Physica B: Condensed Matter*, *540*, 1-8 doi:10.1016/j.physb.2018.04.017

Irani, M., Mohammadi, T., & Mohebbi, S. (2016). Photocatalytic Degradation of Methylene Blue with ZnO Nanoparticles; a Joint Experimental and Theoretical Study. *Journal of The Mexican Chemical Society*, *60*(4), 218-225. doi:10.29356/jmcs.v60i4.115

Jambure, S. B., Patil, S. J., Deshpande, A. R., & Lokhande, C. D. (2014). A comparative study of physico-chemical properties of CBD and SILAR grown ZnO thin films. *Materials Research Bulletin*, *49*, 420-425. doi:10.1016/j.materresbull.2013.09.007

Karaduman Er, I., Yıldırım, M. A., Örkçü, H. H., Ateş, A. & Acar, S. (2021). Structural, morphological and gas sensing properties of $Zn_{1-x}Sn_xO$ thin films by SILAR method. *Applied Physics A*, *127*, 230 doi:10.1007/s00339-021-04354-7

Komaraiah, D., Radha, E., Vijayakumar, Y., Sivakumar, J., Reddy, M. V. R., & Sayanna, R. (2016) Optical, Structural and Morphological Properties of Photocatalytic ZnO Thin Films Deposited by Pray Pyrolysis Technique. *Modern Research in Catalysis*, *5*(4), 130-146. doi:10.4236/mrc.2016.54011

Kumar, B., Smita, K., Cumbal, L., & Debut, A. (2014). Green Approach for Fabrication and Applications of Zinc Oxide Nanoparticles. *Bioinorganic Chemistry and Applications*, 523869. doi:10.1155/2014/523869

Méndez-Vilas, A., Bruque, J. M., & González-Martín, M. L. (2007). Sensitivity of surface roughness parameters to changes in the density of scanning points in multi-scale AFM studies. Application to a biomaterial surface. *Ultramicroscopy*, *107*(8), 617-625. doi:10.1016/j.ultramic.2006.12.002

Radhi Devi, K., Selvan, G., Karunakaran, M., Kasirajan, K., Shkir, M., & AlFaify, S. (2020). A SILAR fabrication of nanostructured ZnO thin films and their characterizations for gas sensing applications: An effect of Ag concentration. *Superlattices Microstructure*, *143*, 106547. doi:10.1016/j.spmi.2020.106547

Raidou, A., Benmalek, F., Sall, T., Aggour, M., Qachaou, A., Laanab, L., & Fahoume, M. (2014). The influence of rinsing period on the structural and optical properties of ZnO thin films. *Optical and Quantum Electronics*, *46*, 171-178. doi:10.1007/s11082-013-9737-6

Rayathulhan, R., Kayode Sodipo, B., & Abdul Aziz, A. (2017). Nucleation and growth of zinc oxide nanorods directly on metal wire by sonochemical method. *Ultrasonics Sonochemistry*, *35*(Part A), 270-275. doi:10.1016/j.ultsonch.2016.10.002

Shaba, E. Y., Jacob, J. O., Tijani, J. O., & Suleiman, M. A. T. (2021). A critical review of synthesis parameters affecting the properties of zinc oxide nanoparticle and its application in wastewater treatment. *Applied Water Science*, *11*, 48. doi:10.1007/s13201-021-01370-z

Şahin, B., Aydin, R., Soylu, S., Türkmen, M., Kara, M., Akkaya, A., Çetin, H., & Ayyıldız, E. (2022). The effect of thymus syriacus plant extract on the main physical and antibacterial activities of ZnO nanoparticles synthesized by SILAR method. *Inorganic Chemistry Communications*, *135*, 109088. doi:10.1016/j.inoche.2021.109088

Vaizoğullar, A. İ. (2018). Comparing Photocatalytic Activity of ZnO and Nanospherical ZnO/Bentonite Catalyst: Preparation, Structural Characterization and their Photocatalytic Performances using Oxytetracycline Antibiotic in Aqueous Solution. *Journal of The Mexican Chemical Society*, *62*(1), 1-17. doi:10.29356/jmcs.v62i1.578

Yıldırım, M. A., & Ates, A. (2010). Influence of films thickness and structure on the photo-response of ZnO films. *Optics Communications*, *283*(7), 1370-1377. doi:10.1016/j.optcom.2009.12.009

Zheng, Z., Peng, Z., Yu, Z., Lan, H., Wang, S., Zhang, M., Li, L., Liang, H., & Su, H. (2022) Thickness-dependent optical response and ultrafast carrier dynamics of $PtSe_2$ films. *Results in Physics*, *42*, 106012. doi:10.1016/j.rinp.2022.106012

Comparison of Electronic and Magnetic Properties of 4d Transition Metals Based NbAl₂F₄ and TcAl₂F₄ Spinels

Evren Görkem ÖZDEMİR[1*] iD

[1]Gazi University, Faculty of Science, Department of Physics, 06560 Teknikokullar Ankara, Türkiye

Keywords	Abstract
Spinel NbAl₂F₄ GGA+mBJ Half-metallic TcAl₂F₄	Half-metallic properties of NbAl₂F₄ spinel and semiconductor characteristics of TcAl₂F₄ spinel were investigated with the help of the WIEN2k program. NbAl₂F₄ spinel shows a metallic character in the up-electron states, while it has a semiconductor nature in the down-electron states. In NbAl₂F₄ spinel, the E_g bandgaps were calculated in GGA and GGA+mBJ 1.551 eV and 1.622 eV, respectively. The E_{HM} half-metallic bandgaps were obtained 0.410 eV and 0.422 eV, respectively. In the up-spin states of TcAl₂F₄ spinel, E_g values were obtained 1.199 eV and 1.447 eV for the GGA and GGA+mBJ methods, respectively, while they were obtained 1.281 eV and 1.519 eV in the down-spin states, respectively. When GGA+mBJ is used, it is easily observed that the semiconductor characters increase. Total magnetic moments of NbAl₂F₄ and TcAl₂F₄ spinels were calculated 6.00 μ_B/cell and 10.0 μ_B/cell, respectively. When both electronic and magnetic moment values are carefully examined, NbAl₂F₄ and TcAl₂F₄ spinels can be used as alternative compounds in spintronic applications.

1. INTRODUCTION

In recent years, the characteristics of magnetic materials, especially with the effect of their spin orientation, have begun to be used in many areas of technological applications. This branch of science, which forms the basis of spin orientations, is called spintronics. In short, spintronics is the science that examines the technological properties of nano-sized devices depending on their spin orientation. Hirohata et al. (2020) have recently carried out a very detailed study involving spintronic applications. They showed similar and different properties of magnetic and semiconductor devices. Since spin generation and spin-polarized electrons form the basis of spintronic applications, they mentioned the methods by which spins can be polarized even in non-magnetic materials. These methods are spin injection from a magnetic field, an electric field or a ferromagnetic material. Magnetic random-access memories (MRAM) are one of the application products of spintronic technology. Shin et al. (2006) investigated the effects of Cl₂ and O₂ gases with varying density on the Co₂MnSi magnetic film, which was thought to be used for MRAM devices. They experimentally proved that the etch rate of the Co₂MnSi magnetic film decreased with increasing Cl₂ and O₂ gas densities. Quiroz et al. (2020) investigated the properties of Co/TiO₂ bilayer and TiO₂:Co thin films. It was observed that these materials, obtained experimentally at 293 K and 473 K temperatures, had low energy consumption and expanding storage capacities in the applied magnetic field. Just like MRAM, magnetic sensors (MS) are one of the products obtained as a result of spintronic applications. Zhang et al. (2020) investigated the magnetic sensor properties of boron-doped FeGa film. As a result of their experimental measurements, the magnetic sensitivity of the FeGaB magnetic sensor was obtained as 152.1 Hz/mT. This value was found to be almost four times the FeGa film obtained without boron doping. The sensitivity characteristics of the BaTiO₃-Fe-Ga&PDMS magnetic

sensor were reported by Xu et al. (2022). The best value of the sensitivity of the magnetic sensor was experimentally obtained as 3.4 V/T when the $BaTiO_3$ concentration was 20%. In addition, experimental investigations of silicon-based Bi_2FeNiO_6 double perovskite-based and $MgAl_2O_4$ barrier magnetic tunnel junctions (MTJ) were performed by Ravi (2020) and Khanal et al. (2022), respectively. When Bi_2FeNiO_6 double perovskite was used, tunnelling magnetoresistance varying from 0.2% to 1.8% was obtained at different temperatures. While the magnetic anisotropy energy density of the $MgAl_2O_4$ barrier magnetic tunnel joint annealed at 400 ^{0}C degree was obtained as 2.25 mJ/m^2, 60% success was achieved in the magnetoresistance. As can be seen from the examples, there are many technological devices that spintronic applications are transformed into.

When de Groot et al. (1983) discovered the half-metallic (HM) features of NiMnSb ferromagnetic material, half-metallic materials have also been widely used in spintronic applications. Half-metallic materials attract attention with their 100% spin polarization and different electronic properties under magnetic fields. One of the spin orientations of HM materials shows metallic character around the Fermi energy level, while the other shows semiconductor character. The spin orientation, which shows semiconductor character, adds 100% spin polarization to the materials. Therefore, these materials are true half-metallic. In cases where the Fermi energy level is cut by electrons and still has a band gap, the spin polarization ratio decreases. In such cases, materials are called nearly half-metallic. Birsan and Kuncser (2022) and Patel et al. (2022) investigated the half-metallic character of Zr_2CrAl and Mn_2SiRh Heusler compounds. The HM band gap (E_{HM}) and total magnetic moment of Zr_2CrAl ferrimagnetic compound were calculated as 0.35 eV and 1.00 μ_B/f.u., respectively. In Mn_2SiRh compound, the E_{HM} value was obtained as 0.36 eV. The half-metallic characters of the $Cd_{1-x}Zn_xCr_2Se_4$, $GeGa_2O_4$ and $MnTi_2O_4$ spinels were studied by Bouhbou et al. (2019), Rafiq et al. (2022) and Nadeem et al. (2022), respectively. Differences in half-metallic band gaps were observed according to varying x-amounts of $Cd_{1-x}Zn_xCr_2Se_4$ (x = 0, 0.125, 0.375 and 0.5) compounds. In x=0, the theoretical band gap values were obtained as 0.43 eV and 1.11 eV by GGA and GGA+mBJ methods, respectively. Here, an experimental band gap of 1.3 eV was obtained and the closest theoretical calculation to this value was with GGA+mBJ. It was observed that the theoretical band gaps obtained with increasing x values decreased. $GeGa_2O_4$ oxide spinel showed semiconductor character with band gaps of 1.605 eV in the spin-up state and 1.578 eV in the spin-down state. The $MnTi_2O_{4-x}$ compound was obtained with a direct band gap of about 5 eV in the spin-up states. Here x represents the vanadium concentration. The band gap rises above 5 eV when the compound is changed to $MnTi_{2-x}O_4$. As can be seen from the examples given, spintronic application areas involved different types of materials. One of the most widely used among these types is half-metallic characters. The main purpose of this study is to examine in detail the electronic, magnetic and HM characters of 4d-transition metal-based $NbAl_2F_4$ and $TcAl_2F_4$ spinels. The magnetic moments of $NbAl_2F_4$ and $TcAl_2F_4$ spinels were calculated as 6.00 μ_B/cell and 10.0 μ_B/cell, respectively. $NbAl_2F_4$ spinel has a half-metallic ferromagnetic structure while $TcAl_2F_4$ spinel has a semiconductor nature. Therefore, two different compounds $NbAl_2F_4$ and $TcAl_2F_4$ spinels will be alternative compounds for spintronics applications.

2. MATERIAL AND METHOD

Electronic and magnetic properties of $NbAl_2F_4$ and $TcAl_2F_4$ spinels were performed using WIEN2k developed by Blaha et al. (2020, 2022). Both GGA-PBE (Perdew et al., 1996) and GGA+mBJ (Tran & Blaha, 2009) methods were used with the help of WIEN2k, which is based on Density Functional Theory. Some research on Density Functional Theory and its methods was carried out by Singh (1994). While forming $NbAl_2F_4$ and $TcAl_2F_4$ spinels, 227-space number and Fd-3m symmetry group were chosen.

Here, the transition metals (Nb, Tc), Al and F atoms are placed at the space coordinates of 0.125/0.125/0.125, 0.50/0.50/0.50 and 0.25/0.25/0.25, respectively. The cubic structures obtained with the help of all these space numbers, symmetry groups and atomic coordinates were given in Figure 1. For the initial state calculations, the spin cutoff values ($R_{MT}K_{max}$) were set to 7 giving the minimum energy values. While performing the potential calculations of the atoms using the GGA method, all atoms of the formed structure are examined separately. Therefore, potential calculations of Nb, Tc, Al, and F atoms examined in this study are performed in Muffin-Tin spheres, an imaginary sphere surrounding these atoms. The radii of these Muffin-Tin spheres must be larger than the radii of the atoms they surround. If they are small, potential leaks from atoms can occur. Therefore, inaccurate results may occur in the calculations performed. In this study, the radii of Muffin-Tin

spheres surrounding Nb, Tc, Al, and F atoms were selected as 2.00 a.u., 1.88 a.u., 2.22 a.u., and 2.02 a.u., respectively. Electron convergence values were chosen as 0.0001 e within 1728 special k-points in the first Brillouin zone.
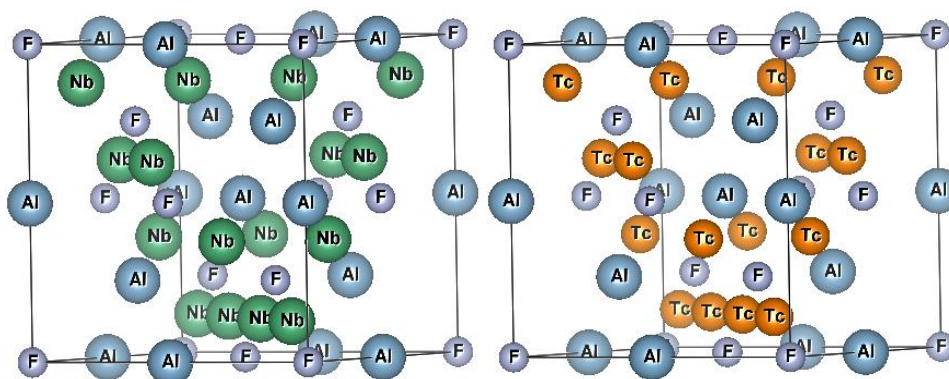
Figure 1. *The molecular schematic representations of NbAl₂F₄ and TcAl₂F₄ spinels*

3. RESULTS AND DISCUSSION

The energies obtained around the values corresponding to -10%, 8%, 6%, 4%, 2%, 0%, 2%, 4%, 6%, 8% and 10% changes of the lattice parameters, and volume-energy curves of NbAl₂F₄ and TcAl₂F₄ spinels were obtained. According to these curves, ferromagnetic phases were obtained as more stable for both spinels. Since Murnaghan's equation of state (1944) fit these energy values, the initial state values were calculated, and optimization curves were given in Figure 2.
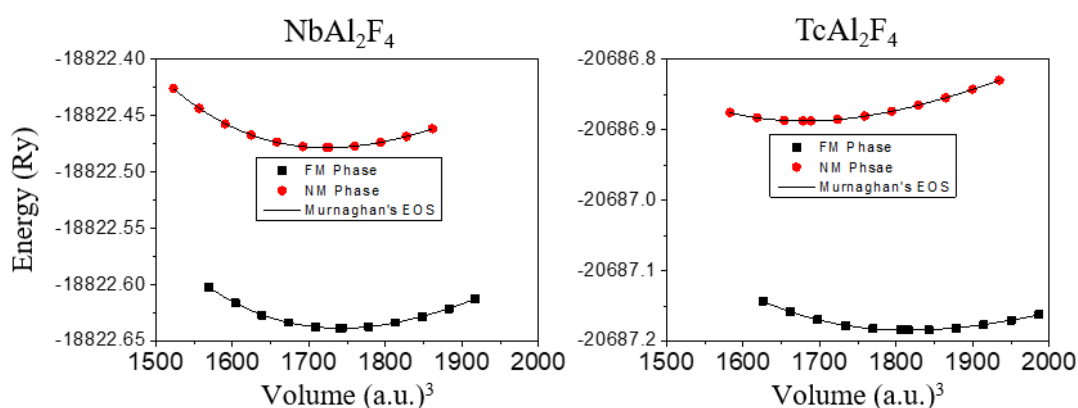
Figure 2. *The calculated energy-volume curves of NbAl₂F₄ and TcAl₂F₄ spinels*

Equilibrium lattice parameters, bulk modulus and the first derivative of bulk modulus, equilibrium volume and energy values of NbAl₂F₄ and TcAl₂F₄ spinels were given in Table 1. The lattice parameter of NbAl₂F₄ spinel was calculated as 10.11 Å, while it was calculated as 10.25 Å for TcAl₂F₄ spinel. The lattice parameter obtained at the equilibrium point of the TcAl₂F₄ spinel formed by using the Tc element, whose atomic radius is smaller than the Nb element, is larger. Therefore, the equilibrium lattice parameters of the compounds may need to be evaluated independently of the atomic radii of the elements. Similar studies were obtained by Mahmood et al. (2022). The equilibrium lattice parameters of CaTi₂S₄, CaV₂S₄, CaCr₂S₄, and CaFe₂S₄ spinels obtained as 10.73 Å, 10.75 Å, 10.91 Å, and 10.88 Å when Ti, V, Cr, and Fe elements were used, respectively. Although the atomic radii of the transition metals are used to decrease, the equilibrium lattice parameters and thus the volumes of the compounds obtained tend to increase. However, it may not be right to talk about the fact that this increase or decrease can occur at certain rates. As can be seen, there was a decrease in the lattice parameter when the transition metal Fe was used. The bulk modulus of NbAl₂F₄ and TcAl₂F₄ spinels were obtained as 51.25 GPa and 48.44 GPa, respectively. Therefore, the resistance of NbAl₂F₄ spinel to volume change was higher than that of TcAl₂F₄ spinel. The B' value, which shows the value of the bulk modulus against pressure change, was obtained as 4.90 in NbAl₂F₄ spinel, while it was obtained as 5.26 in TcAl₂F₄ spinel. This is the

expected result. Since the value of the bulk modulus is lower in $TcAl_2F_4$ compound, it indicates that there is a possibility of undergoing more volume changes with the applied pressure. Comparison of decreasing bulk modulus with increasing lattice parameter can be done with $CaTi_2S_4$, CaV_2S_4, $CaCr_2S_4$, and $CaFe_2S_4$ spinels. When Ti, V, Cr, and Fe transition metals were used, the ballast modulus of the structure obtained was 65.38 GPa, 62.10 GPa, 50.00 GPa, and 54.71 GPa, respectively. As can be seen, when Ti, V, and Cr transition metals are used, decreases in bulk modulus were observed inversely with increasing lattice parameters.

Table 1. *The initial state values of $NbAl_2F_4$ and $TcAl_2F_4$ spinels*

Compounds	a (Å)	B (GPa)	B'	V_0 (a.u.)^3	E_0 (Ry)
$NbAl_2F_4$	10.11	51.25	4.90	1740.807	-18822.638
$TcAl_2F_4$	10.25	48.44	5.26	1815.716	-20687.184

After the obtained initial state values, the electronic properties of $NbAl_2F_4$ and $TcAl_2F_4$ spinels were investigated. First, the total densities of states (TDOS) were plotted for the -10 eV and +8 eV energy regions and were given in Figure 3.
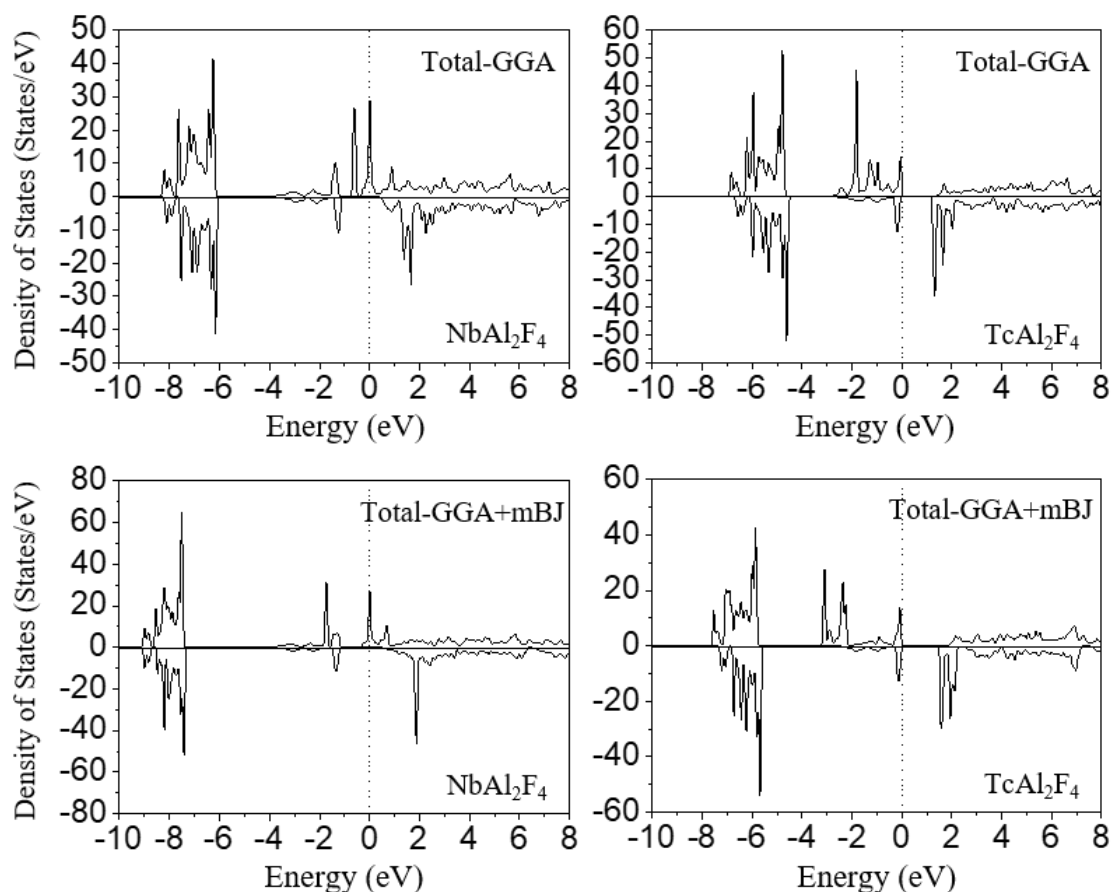
Figure 3. *TDOS of $NbAl_2F_4$ and $TcAl_2F_4$ spinels*

Positive values of the total densities of states represented up-spins (majority), while negative values represent down-spins (minority). In the far negative energy densities of $NbAl_2F_4$ spinel, sharp peaks were observed at the GGA method. The 100% symmetry between the up and down spins indicated that electrons were bounded in these energy regions. These conditions were the same both in the value obtained by the GGA+mBJ of $NbAl_2F_4$ spinel and in the calculation results of $TcAl_2F_4$ spinel. The vertical dotted lines at total densities of states indicated Fermi energy levels. As the Fermi energy levels were approached, there were separations in the electron densities. At each method, the up-spin electrons of $NbAl_2F_4$ spinel contacted Fermi energy levels. This showed that the valence electrons can pass to the conduction band, that is, the metallic character revealed.

In down-spins, band gaps existed. In down-spin states, $NbAl_2F_4$ spinel had a semiconductor character. Therefore, $NbAl_2F_4$ spinel was a half-metallic ferromagnetic material. It is possible to see band gaps in both the up and down spins of $TcAl_2F_4$ spinel when using the GGA and GGA+mBJ. In this case, $TcAl_2F_4$ spinel had a semiconducting nature. The differences in the symmetry between the up and down spins of $NbAl_2F_4$ spinel around the Fermi energy level allow for the formation of a net magnetic character. Likewise, the presence of these asymmetric electron distributions in energy ranges near the Fermi energy level of $TcAl_2F_4$ spinel made the magnetic characters appear. It is possible to talk about studies similar to the electronic structure of spinels in this study. Nazar et al. (2022) investigated the magnetic and electronic calculations of Gd_2MgS_4 and Tm_2MgS_4 spinel sulfides using the first principles method. The band gaps of the up and down electrons of the Gd_2MgS_4 spinel were obtained as 1.44 eV and 1.65 eV, respectively. Thus, Gd_2MgS_4 spinel showed a semiconductor character. While the up spins of the Tm_2MgS_4 spinel showed a metallic character, the down spins showed a semiconductor character. Therefore, Tm_2MgS_4 spinel was obtained as half-metallic ferromagnetic by Nazar et al. (2022). The electronic properties of the semiconductor and half-metallic spinels Gd_2MgS_4 and Tm_2MgS_4 obtained by Nazar et al. (2022) show similar characteristics to the electronic properties of $TcAl_2F_4$ and $NbAl_2F_4$ spinels obtained in this study.

The atomic contributions of $NbAl_2F_4$ and $TcAl_2F_4$ spinels were shown in Figure 4 and Figure 5 to investigate the partial electron densities to the total electron distributions. The electron contributions of the 4d transition metals Nb and Tc atoms were shown in the energy range of -6 eV to +6 eV. Their changes clearly and unequivocally come from these transition metals. Nb atoms have band gaps in their down-spins while their up-spin cuts the Fermi energy levels. This supports TDOS. Most electron contributions come from d-orbitals in transition metals. In the -9 eV and -6 eV energy regions, contributions belong to the p-orbitals of fluorine atoms, while the main contributions come from the s-orbitals of aluminum atoms. This is the expected result because Nb atom has 5 electrons in 4d orbital, Tc atom has 4 electrons in 4d orbital and 1 electron in 5s orbital. The main electron contributions of 4d orbitals of Nb and Tc atoms have also been shown by Saberi et al. (2014) in transition metals doped to GaN nanotubes, Zhang et al. (2022) in Tc, Ru, Rh, and Cd doped to the blue P monolayer, Ali et al. (2021) in K_2NbCl_6 and Rb_2NbCl_6 variant perovskite compounds. In short, the electronic properties obtained in this study gave similar results with many studies in the literature.

It can be said that the electron distributions of aluminum and fluorine atoms of both $NbAl_2F_4$ and $TcAl_2F_4$ spinels have almost 100% symmetry. That is, the electrons of the aluminum and fluorine atoms are almost completely bounded. Both total and partial electron (PDOS) states show that $NbAl_2F_4$ spinel shows a half-metallic character, while $TcAl_2F_4$ spinel shows a semiconductor character.
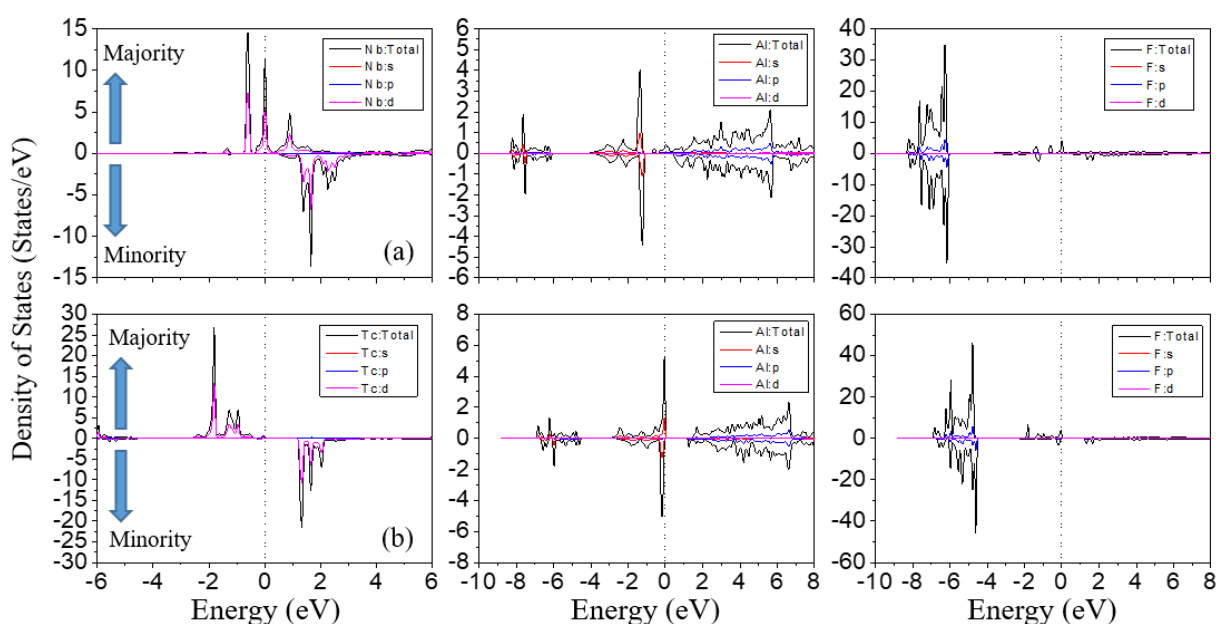

Figure 4. *The obtained PDOS of (a) $NbAl_2F_4$ and (b) $TcAl_2F_4$ spinels in GGA method*
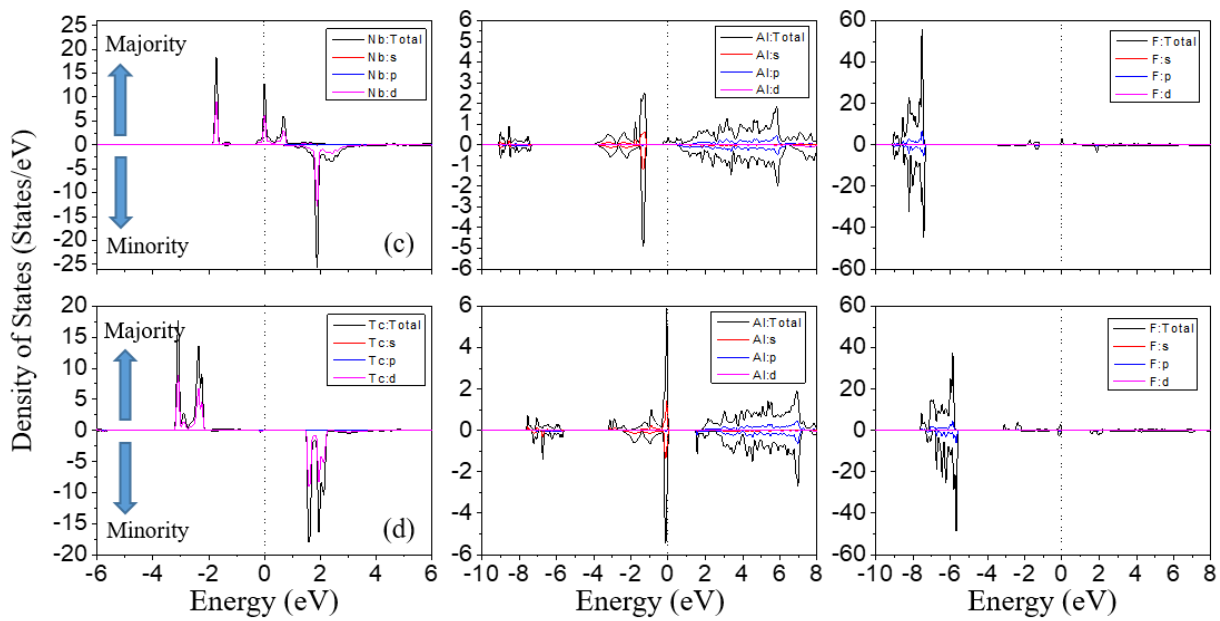
Figure 5. *The obtained PDOS of (c)NbAl$_2$F$_4$ and (d) TcAl$_2$F$_4$ spinels in GGA+mBJ method*

In order to support all these densities of states, the band structures were obtained and given in Figure 6 for the up and down spins of NbAl$_2$F$_4$ and TcAl$_2$F$_4$ spinels. It can be clearly seen in Figure 6 that the up-spins of NbAl$_2$F$_4$ spinel show metallic character by cutting the Fermi energy levels in each method. In the GGA, electron densities are available in the -0.5 eV energy region. However, in the GGA+mBJ, all the electrons are destroyed in the range of 0 to -1 eV. Electron densities obtained in the GGA shifted to the range of -2 eV in the GGA+mBJ. In other words, the GGA+mBJ directly affected the energy gaps of the valence electrons.
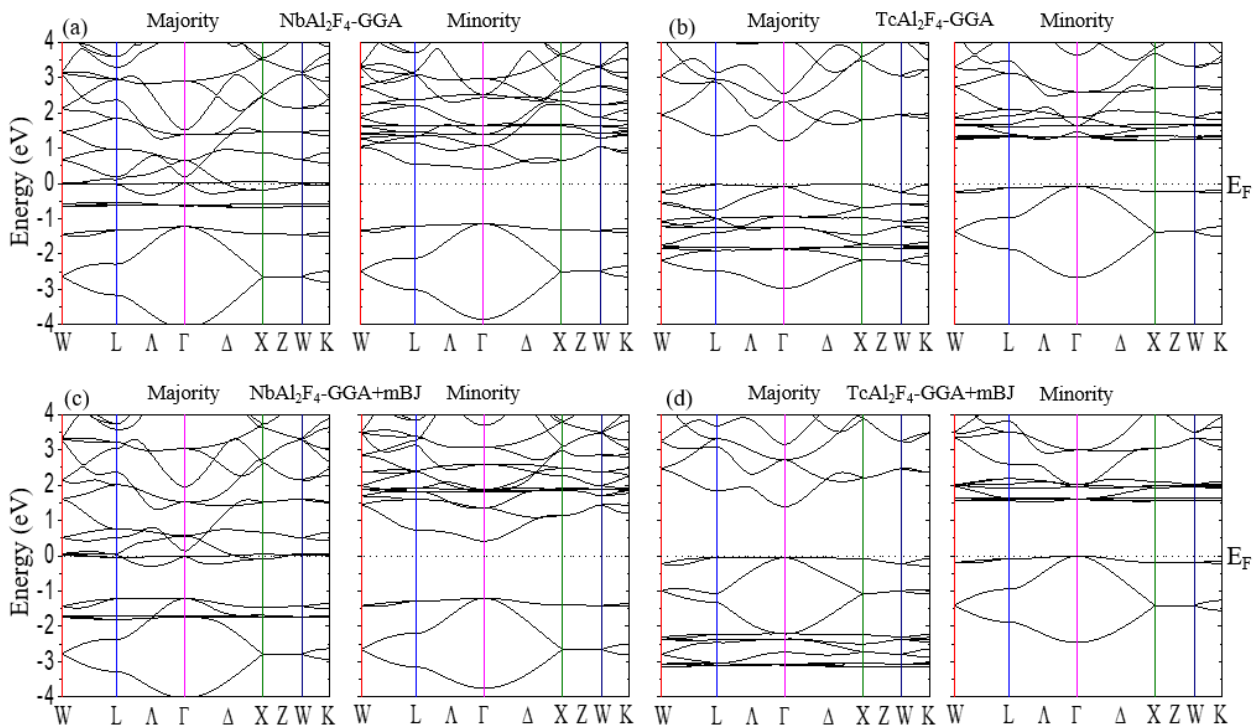
Figure 6. *The calculated majority (up-spin) and minority (down-spin) band structures of NbAl$_2$F$_4$ and TcAl$_2$F$_4$ spinels*

In down-spin states, there are direct band gaps in each method. Valence band maximum (VBM) and conduction band minimum (CBM) values were at Γ-points. VBM, CBM, band gap (E_g) and HM band gap (E_{HM}) values of $NbAl_2F_4$ and $TcAl_2F_4$ spinels were given in Table 2 and Table 3 for each method.

***Table 2.** The calculated VBM, CBM, E_g and E_{HM} of down-spin of $NbAl_2F_4$ spinel*

Compounds	VBM (eV)	CBM (eV)	E_g (eV)	E_{HM} (eV)
$NbAl_2F_4{}^{GGA}$	-1.141	0.410	1.551	0.410
$NbAl_2F_4{}^{GGA+mBJ}$	-1.200	0.422	1.622	0.422

***Table 3.** The calculated VBM, CBM, and E_g of both up and down-spins of $TcAl_2F_4$ spinel*

Compounds	$VBM^{Majority}$ (eV)	$CBM^{Majority}$ (eV)	$VBM^{Minority}$ (eV)	$CBM^{Minority}$ (eV)	$E_g^{Majority}$ (eV)	$E_g^{Minority}$ (eV)
$TcAl_2F_4{}^{GGA}$	0	1.199	-0.067	1.214	1.199	1.281
$TcAl_2F_4{}^{GGA+mBJ}$	-0.047	1.400	0	1.519	1.447	1.519

In GGA calculations, the VBM and CBM values were calculated as -1.414 eV and 0.410 eV, respectively. In the GGA+mBJ, the VBM and CBM values were -1.200 eV and 0.422 eV, respectively. According to these results, the band gap values were obtained 1.551 eV and 1.622 eV in GGA and GGA+mBJ, respectively. The band gap values in the down spins of $NbAl_2F_4$ spinel, a HM ferromagnetic material, can be calculated as different values in different applied methods. The band gaps of both the up and down spins of $TcAl_2F_4$ spinel with semiconductor character can be clearly seen. There are direct band gaps in each method. In Figure 6, the band gaps increase when the GGA+mBJ is used. In addition, the VBM values in the up-spins are 0 and -0.047 eV in the GGA and GGA+mBJ, respectively, while the CBM values are 1.199 eV and 1.400 eV, respectively. Therefore, band gaps in the up-spin of $TcAl_2F_4$ spinel were obtained as 1.199 eV and 1.447 eV in GGA and GGA+mBJ, respectively. When using the GGA method in down-spin conditions, the VBM value was calculated as -0.067 eV, while the CBM value was obtained as 1.214 eV. The band gap in the down-spin of the $NbAl_2F_4$ spinel using the GGA method was 1.281 eV. When the GGA+mBJ was used, it was observed that the valence band electrons approached the Fermi energy level. The CBM value was 1.519 eV while the VBM value was 0. In other words, the E_g was obtained as 1.519 eV in the GGA+mBJ. The E_g values obtained in GGA+mBJ methods increased in both spinels. In short, while $NbAl_2F_4$ spinel is a HM ferromagnetic material with its semiconductor character in its down-spins, $TcAl_2F_4$ spinel was obtained as a semiconductor ferromagnetic material with its semiconductor character in both up and down spins.

Total magnetic moment values of $NbAl_2F_4$ and $TcAl_2F_4$ spinels were obtained as 6.00 μ_B/cell and 10.0 μ_B/cell, respectively. Most contributions to the total magnetic moments came from the Nb and Tc transition metals. The partial magnetic moments of the $NbAl_2F_4$ spinel are 1.561 μ_B/f.u., 0.003 μ_B/f.u. and 0.031 μ_B/f.u. for Nb, Al and F, respectively. The partial magnetic moments of $TcAl_2F_4$ spinel are 3.149 μ_B/f.u., 0.003 μ_B/f.u. and 0.092 μ_B/f.u. for Tc, Al and F, respectively. It was mentioned that the unbounded electrons at the total state densities are the 4d transition metals Nb and Tc. Therefore, these unbounded electrons did not create magnetic moments. It is clearly seen how much these electron contributions in Fermi energy levels affect the magnetic moments. As a result, $NbAl_2F_4$ spinel is a HM ferromagnetic material with 6.00 μ_B/cell magnetic moment, while $TcAl_2F_4$ spinel is a semiconductor ferromagnetic material with 10.0 μ_B/cell magnetic moment.

4. CONCLUSION

In this study, the electronic and magnetic properties of $NbAl_2F_4$ and $TcAl_2F_4$ spinels were investigated. Ferromagnetic phases of spinels were found to be more stable at ground state values. $NbAl_2F_4$ spinel was obtained as a true half-metallic ferromagnetic in each method. In the down-spins of $NbAl_2F_4$ spinel, the E_g=1.551 eV and E_g=1.622 eV values were found for the GGA and GGA+mBJ, respectively. However, since the value of electron densities closest to the Fermi energy level was CBM, the half-metallic band gaps were obtained as E_{HM}=0.410 eV and E_{HM}=0.422 eV in each method. $TcAl_2F_4$ spinel showed semiconductor character

in both methods. The band gaps in the up-spins were obtained as E_g=1.199 eV and E_g=1.447 eV, respectively, while the band gaps in the down-spins were obtained as E_g=1.281 eV and E_g=1.519 eV, respectively. $NbAl_2F_4$ and $TcAl_2F_4$ spinels have high magnetic moment values. The magnetic moment of $NbAl_2F_4$ spinel was obtained as 6.00 μ_B/cell, while it is 10.0 μ_B/cell in $TcAl_2F_4$ spinel. In both spinels, the most contributions belonged to the 4d transition metals Nb and Tc. As a result, $NbAl_2F_4$ spinel is a true half-metallic ferromagnetic and $TcAl_2F_4$ spinel is obtained as a semiconductor ferromagnetic material, and they are good alternative materials in spintronic applications for experimental works.

CONFLICT OF INTEREST

The author declares no conflict of interest.

REFERENCES

Ali, M. A., Ullah, R., Abdullah, S., Khan, M. A., Murtaza, G., Laref, A., & Kattan, N. A. (2021). An investigation of half-metallic variant perovskites A_2NbCl_6 (A= K, Rb) for spintronic based applications. *Journal of Solid State Chemistry*, *293*, 121823. doi:10.1016/j.jssc.2020.121823

Birsan, A., & Kuncser, V. (2022). Half-metallic properties of Zr_2CrAl ferrimagnetic full-Heusler compound, investigated in tetragonal, orthorhombic and rhombohedral crystal structures. *Journal of Alloys and Compounds*, *900*, 163491. doi:10.1016/j.jallcom.2021.163491

Blaha, P., Schwarz, K., Tran, F., Laskowski, R., Madsen, G. H. K., & Marks, L. D. (2020). WIEN2k: an APW+lo program for calculating the properties of solids. *The Journal of Chemical Physics*, *152*, 074101. doi:10.1063/1.5143061

Blaha, P., Schwarz, K., Madsen, G. K. H., Kvasnicka, D., Luitz, J., Laskowski, R., Tran, F., & Marks, L. D. (2022) *WIEN2k An Augmented Plane Wave Local Orbitals Program for Calculating Crystal Properties*. Vienna University of Technology Institute of Materials Chemistry, Vienna, Austria. ISBN 3-9501031-1-2 PDF

Bouhbou, M., Moubah, R., Bakkari, K., Zaari, H., Sabrallah, A., Khelfaoui, F., Mliki, N., Abid, M., Belayachi, A., & Lassri, H. (2019). Magnetic, half-metallicity and electronic studies of $Cd_{1-x}Zn_xCr_2Se_4$ chromium selenospinels. *Journal of Magnetism and Magnetic Materials*, *476*, 86-91. doi:10.1016/j.jmmm.2018.12.063

de Groot, R. A., Mueller, F. M., van Engen, P. G., & Buschow, K. H. J. (1983). New class of materials: half-metallic ferromagnets. *Physical Review Letters*, *50*(25), 2024-2027. doi:10.1103/PhysRevLett.50.2024

Hirohata, A., Yamada, K., Nakatani, Y., Prejbeanu, I.-L., Diény, B., Pirro, P., & Hillebrands, B. (2020). Review on spintronics: Principles and device applications. *Journal of Magnetism and Magnetic Materials*, *509*, 166711. doi:10.1016/j.jmmm.2020.166711

Khanal, P., Zhou, B., Andrade, M., Mastrangelo, C., Habiboglu, A., Enriquez, A., Fox, D., Warrilow, K., & Wang, W.-G. (2022). Enhanced magnetoresistance in perpendicular magnetic tunneling junctions with $MgAl_2O_4$ barrier. *Journal of Magnetism and Magnetic Materials*, *563*, 169914. doi:10.1016/j.jmmm.2022.169914

Mahmood, Q., Nazir, G., Alzahrani, J., Kattan, N. A., Al-Qaisi, S., Albalawi, H., Mera, A., Mersal, G. A. M., Ibrahim, M. M., & Amin, M. A. (2022). Room temperature ferromagnetism and thermoelectric behavior of calcium based spinel chalcogenides CaZ_2S_4 (Z= Ti, V, Cr, Fe) for spintronic applications. *Journal of Physics and Chemistry of Solids*, *167*, 110742. doi:10.1016/j.jpcs.2022.110742

Murnaghan, F. D. (1944). The Compressibility of Media under Extreme Pressure. *Proceedings of the National Academy of Sciences*, *30*(9) 244-247. doi:10.1073/pnas.30.9.244

Nadeem, A., Bashir, A. I, Azam, S., Rahman, A. U., & Iqbal, M. A. (2022). First-principles quantum analysis on the role of V-doping on the tuning of electronic and optical properties of spinel oxides $MnTi_2O_4$. *Materials Science & Engineering B*, *278*, 115643. doi:10.1016/j.mseb.2022.115643

Nazar, M., Nasarullah, Aldaghfag, S. A., Yaseen, M., Ishfaq, M., Khera, R. A., Noreen, S., & Abdellattif, M. H. (2022). First-principles calculations to investigate structural, magnetic, optical, electronic and

thermoelectric properties of X_2MgS_4 (X= Gd, Tm) spinel sulfides. *Journal of Physics and Chemistry of Solids*, *166*, 110719. doi:10.1016/j.jpcs.2022.110719

Patel, P. D., Pandya, J., Shinde, S., Gupta, S. D., & Jha, P. K. (2022). Robust half metallic ferrimagnetic behavior and thermoelectric response of newly discovered Full-Heusler compound Mn_2SiRh: DFT study. *Materials Today: Proceedings*, *67*(6), 939-942. doi:10.1016/j.matpr.2022.07.468

Perdew, J. P., Burke, K., & Ernzerhof, M. (1996). Generalized Gradient Approximation Made Simple. *Physical Review Letters*, *77*, 3865. doi:10.1103/PhysRevLett.77.3865

Quiroz, H. P., Calderón, J. A., & Dussan, A. (2020). Magnetic switching control in Co/TiO_2 bilayer and TiO_2:Co thin films for Magnetic-Resistive Random Access Memories (M-RRAM). *Journal of Alloys and Compounds*, *840*, 155674. doi:10.1016/j.jallcom.2020.155674

Rafiq, M. A., Javed, A., Rasul, M. N., Nadeem, M., Iqbal, F., & Hussain, A. (2022). Structural, electronic, magnetic and optical properties of AB_2O_4 (A = Ge, Co and B = Ga, Co) spinel oxides. *Materials Chemistry and Physic*s, *257*, 123794. doi:10.1016/j.matchemphys.2020.123794

Ravi, S. (2020). Spin transport through silicon using a double perovskite-based magnetic tunnel junction. *Superlattices and Microstructures*, *147*, 106688. doi:10.1016/j.spmi.2020.106688

Saberi, S. H., Baizaee, S. M., & Kahnouji, H. (2014). Electronic structure and magnetic properties of transition-metal (Y, Zr, Nb, Mo, Tc, Ru, Rh, Pd, Ag and Cd) doped in GaN nanotubes. *Superlattices and Microstructures*, *74*, 52-60. doi:10.1016/j.spmi.2014.05.013

Shin, B., Park, I. H., & Chung, C. W. (2006). Inductively coupled plasma reactive ion etching of Co_2MnSi magnetic films for magnetic random access memory. *Studies in Surface Science and Catalysis*, *159*, 377-380. doi:10.1016/S0167-2991(06)81612-5

Singh, D. J. (1994). *Planewaves, Pseudopotentials and the LAPW Method*. Kluwer Academic, Boston. doi:10.1007/978-1-4757-2312-0

Tran, F., & Blaha, P. (2009). Accurate band gaps of semiconductors and insulators with a semi-local exchange-correlation potential. *Physical Review Letters*, *102*(22), 226401. doi:10.1103/PhysRevLett.102.226401

Xu, M., Zhang, Q., Tan, Q., Zhang, W., Sang, S., Yang, K., & Ge, Y. (2022). A magnetostrictive $BaTiO_3$-Fe-Ga&PDMS magnetic field sensor: Research on magnetic detection performance. *Sensors and Actuators: A. Physical*, *335*, 113383. doi:10.1016/j.sna.2022.113383

Zhang, J.-M., Duan, J.-P., Huang, Y.-H., & Wei, X.-M. (2022). Effects of the Tc, Ru, Rh and Cd substitution doping on the structural, electronic, magnetic and optical properties of blue P monolayer. *Thin Solid Films*, *756*, 139386. doi:10.1016/j.tsf.2022.139386

Zhang, Z., Sang, L., Huang, J., Chen, W., Wang, L., Takahashi, Y., Mitani, S., Koide, Y., Koizumi, S., & Liao, M. (2020). Enhanced magnetic sensing performance of diamond MEMS magnetic sensor with boron-doped FeGa film. *Carbon*, *170*, 294-301. doi:10.1016/j.carbon.2020.08.049

Characterization of Hot Extruded Hybrid Composites Al 2024 Metal Matrix Reinforced with TiO₂ and ZrO₂

Ayşenur PEKTAŞ[1,2]* [iD] Okan Can EBETÜRK[3] [iD] Uğur GÖKMEN[3] [iD]

[1]Gazi University, Institute of Science and Technology, Department of Advanced Technologies, Ankara, Türkiye
[2]KTO Karatay University, School of Applied Sciences, Department of Flight Training, Konya, Türkiye
[3]Gazi University, Institute of Science and Technology, Department of Metallurgical and Materials Engineering, Ankara, Türkiye

Keywords	Abstract
Hybrid Composites Powder Metallurgy Hot Press Method Radiation Shielding	In this study, the microstructure and mechanical properties of Al 2024 powder, the prominent type of Al 2XXX series aluminum alloys widely used in the aerospace industry, and TiO₂ and ZrO₂ reinforcement elements used to improve material properties were investigated. Each reinforcement element is included in the material at the rate of 10%. For hybrid composite sample production, 10% hybrid composite material was procured by adding each reinforcing element equally. For each sample, powders were mixed in a 3D mixer to ensure an equal distribution of matrix powder and reinforcement elements in the samples. The samples were churned out by subjecting the two-stage them to a one-way hot press process. The furnace temperature was kept at 600 ^{o}C to preserve samples. Density and microstructure analyses were performed on the formed samples, and the results were evaluated. After all, the Archimedean density measurement method was used to obtain final densities, these samples were taken to bakelite for optical images, then scanning electron microscope (SEM) and Brinell hardness of the samples was measured. The cross-fracture strength test was completed to analyze each sample's microstructural behavior. Finally, the theoretical radiation shielding properties of each sample were investigated. The Phy-X/PSD program was used to examine the radiation permeability properties. According to the test and analysis results, the effect of reinforcement elements on the material was determined. As a result, the highest hardness value measured was 97.5 HB at the 10% ZrO₂-reinforced MMCs. However, the relative density of the hybrid composite is better than ZrO₂-reinforced MMCs. Thus, the best cross-fracture strength measured was 635 MPa in 10% hybrid MMCs. The radiation shielding parameters showed that the 10% ZrO₂-reinforced MMCs are best for shielding. Therefore, the second reasonable material for radiation shielding is hybrid reinforced materials. In the final decision, hybrid composite materials became prominent because the distinctive features of each material enhanced the samples.

1. INTRODUCTION

Composites, which are widely used in aviation, are preferred in the industry because they improve the physical and mechanical properties of the structure. However, composites reinforced with various reinforcing elements, such as ceramics, have become the materials sought in the aerospace industry by providing good wear resistance, high hardness, strength, and improvements in corrosion resistance (Naito et al., 2021). The widely preferred aluminum matrix composites combine critical lightness and high-strength properties. Features such as high wear, low density, and flexible production ability play an essential role in the aerospace industry's preference for aluminum matrix composites (Naito et al., 2021). 2XXX series aluminum alloys are distinguished from other series due to their superior machinability and are frequently preferred in aircraft structures and the automotive industry. ZrO₂ and TiO₂ materials have higher densities, according to aluminum compounds. Though, they are used as reinforcement elements in MMCs, they improve the properties of

*Corresponding Author, e-mail: ayse.nur.pektas@karatay.edu.tr

materials. The zirconia particles are expected to increase the strength and toughness of the composite due to their ability to undergo the stress-induced transformation from a tetragonal to a monoclinic phase (Eckner et al., 2016). Titanium dioxide has properties like chemical stability, good optical transparency, wear resistance, and mechanical and good thermal properties (Joshua et al., 2018).

This research examines the mechanical properties of Al 2024 metal matrix composites enriched with TiO_2 and ZrO_2 reinforcing elements to evaluate their use in aerospace. TiO_2 and ZrO_2 can be examples of ceramic materials added to the aluminum matrix to form composite materials. At the same time, hybrid composites containing TiO_2 and ZrO_2 ceramic particles offer better properties by taking advantage of the mechanical properties of two different reinforcement elements. Composite material production can be achieved in different ways. In this study, three different metal matrix composite samples were produced using the powder metallurgy method. The powder metallurgy method provides distinct advantages, such as homogeneous reinforcing element distribution and reasonable microstructure control (Gökmen, 2016; Alekhya, 2022). The samples produced as 10% TiO_2, 10% ZrO_2, and 10% hybrid by weight were produced by powder metallurgy method at Gazi University laboratories and formed by applying the hot-pressing method. After the hot-pressing method, the effect of reinforcement ratio on the microstructure and mechanical properties of the composite material was determined by obtaining optical images, scanning electron microscope, cross-fracture tests, and radiation permeability analysis.

Most known and common radiation shielding materials are generally lead-based and polymeric structures (McAlister, 2018). TiO_2 is a good choice because it is a chemically stable material, and it is known for its mechanical properties to improve the flexural and compressive strength of the composite (Nikbin et al., 2019; Park et al., 2019). The ZrO_2 envelopes the TiO_2 with its decent hardness value to become a suitable shielding material. As far as is known, there is no available data about the radiation shielding properties of TiO_2 and ZrO_2-based aluminum matrix hybrid composites. Hence, this study enlightens the microstructural properties of selected materials and investigates radiation shielding parameters to widen the literature.

2. MATERIAL AND METHOD

2.1. Material

In this research, metal matrix composite samples were produced by Powder Metallurgy (PM) and hot-pressing methods. The matrix material is pre-alloyed Al 2024, and TiO_2 and ZrO_2 powders are used as reinforcement elements. The powder's SEM images do not exist. Though, the SEM images are taken after the production of each sample. The matrix alloy's chemical composition and the powders' physical properties are given in Table 1 and 2, respectively.

Table 1. Chemical Composition of the Matrix Alloy

Element	Cu	Mn	Mg	Fe	Al
Rate (Weight %)	4,4	1,8	0,25	0,5	Other

Table 2. Physical Properties of Powders Used

Material	Physical Properties		
	Density (g/cm³)	Melting Temperature (°C)	Powder Size (μm)
Al 2024	2,74	502-638	20 μm
TiO₂	4,26	1843	1 μm
ZrO₂	5,68	2370	20 μm

2.2. Method

Pre-alloyed Al 2024 powder was mixed separately in a three-dimensional mixer as separate samples, containing 10% TiO_2 and 10% ZrO_2 by weight. Afterward, 10% hybrid composite powder was mixed in which 5% TiO_2 and 5% ZrO_2 were included simultaneously. The turbulent mixer was run for 30 minutes for each sample to homogenize. Next, the mixed powders were exposed to a pressure of 400 MPa on a one-way press machine and sintered for 1 hour by being thrown into the vacuumed furnace at 600 °C. At the end of the period, the mold removed from the furnace was again subjected to 800 MPa pressure on a one-way pressure machine, and then the sample was left to cool. The sample dimensions obtained are 31.2*12.6*6.35 mm. After the cooling process, the samples removed from the mold were cut by wire erosion to become cross-fracture test products by powder metal sample standards (MPFI-41, 1998).

In the present study, three metal matrix composite samples containing 10% reinforcement elements were obtained using a hot press with the PM method. Three samples were produced from each reinforcement material matrix composite, and nine samples were used in the experiments. For sample production, each reinforcement element and Al 2024 were added to the mixing bowl in the determined proportions and mixed with a turbular mixer for 30 minutes until they became homogeneous. The powder mixtures obtained were taken into the lubricated mold and first pressed with a uniaxial hydraulic press under a load of 10 tons and made compact. After pressing, the samples were kept in the oven at 600 °C for 1 hour and pressed again under 20 tons of load. Materials whose sample production was completed were subjected to a 3-point bending test. Then, bakelite was taken from the broken samples to obtain optical images, and the surface roughness was removed. After all, the SEM images were obtained. The gamma behaviors of a novel shielding material of Al 2024 Metal Matrix Reinforced with TiO_2 and ZrO_2 were also investigated. The shielding effectiveness of these materials for gamma-ray has not been studied until now. In this work, for the first time, the LAC, MAC, TVL, HVL, and MFP of Al 2024 Metal Matrix Reinforced with TiO_2 and ZrO_2 using the Phy-X platform were theoretically calculated considering the radiation shielding. Furthermore, all the values calculated for these composite materials by running the Phy-X platform were compared.

2.3. Characterization

Densities of the samples produced by applying a hot press with powder metallurgy method were determined according to Archimedes principle by using Sartorius brand balance with 0.0001 g precision and density kit. The composite samples obtained were sanded under water with 240-400-800-1200 grit sandpapers for characterization and then polished using 1 and 3 μm diamond paste on the polishing felts. The interfaces of ZrO_2 and TiO_2 particles dispersed in the produced hybrid composites with the matrix material were examined with the help of a Leica brand optical microscope and JEOL JSM 6060LV Scanning Electron Microscope (SEM), and EDS analyzes were made. Fractured surfaces were characterized with the help of SEM. The hardness measurements of the composite samples were measured as Brinell using the Emco test duravision 2000 brand hardness measuring device. The hardness values were determined by taking the average measurements from 5 regions for each sample. Cross-fracture tests of sintered and extruded samples were performed using Instron 3369 model test device. Cross-fracture tests were performed by taking the average of 3 samples for each composite. MPIF Standard 41 and previous studies were taken as references in preparing the test samples and executing the tests (Gökmen, 2016).

3. RESULTS AND DISCUSSION

### 3.1. Density and Microstructure Analysis

The densities are calculated for manufactured composites, and the microstructure of the samples is characterized. As the density of Al 2024 is 2.78 g/cm^3, the reinforcement materials, which are TiO_2's density is 4.26 g/cm^3, and ZrO_2's density is 5.68 g/cm^3. Thus, the content ratio of each sample is 10% mixed with 90% Al 2024. In the beginning, theoretical densities are calculated, as shown below.

$$d_{10\% \, TiO_2} = \frac{90\% \, (Al2024) + 10\% \, (TiO_2)}{100} \qquad d_{10\% \, TiO_2} = \frac{250.2 + 42.6}{100} = 2.928 \, \frac{g}{cm^3}$$

$$d_{10\% \, ZrO_2} = \frac{90\% \, (Al2024) + 10\% \, (ZrO_2)}{100} \qquad d_{10\% \, ZrO_2} = \frac{250.2 + 56.8}{100} = 3.07 \, \frac{g}{cm^3}$$

$$d_{10\% \, Hybrid} = \frac{90\% \, (Al2024) + 5\% \, (TiO_2) + 5\% \, (ZrO_2)}{100} \qquad d_{10\% \, Hybrid} = \frac{250.2 + 28.4 + 21.3}{100} = 2.998 \, \frac{g}{cm^3}$$

The theoretical density of 10% TiO_2 reinforced Al 2024 is 2.93 g/cm^3, 10% ZrO_2 reinforced Al 2024 is 3.07 g/cm^3, and finally, the 10% hybrid (5% both TiO_2 and ZrO_2) reinforced Al 2024 metal matrix composite is calculated as 2.99 g/cm^3. After the sample production, the density of each sample is calculated according to the principles of Archimedes. In Figure 1, the comparison of the theoretical and actual densities is graphed. The Archimedes density results are lower than the theoretical densities of the samples. The closer results are obtained in Al 2024 without reinforcement element, and the most distant results are observed in 10% ZrO_2 reinforced MMCs. In the metal matrix composite prepared by using both reinforcement elements, changes in the density values were determined after the sintering and pressing processes. Even if the reinforcement element percentage is the same for every sample, we are getting different densities because the particle size used is different for each element powder. It is known that as the particle size increases, the powder metal material's density will decrease (Rahimian et al., 2009).
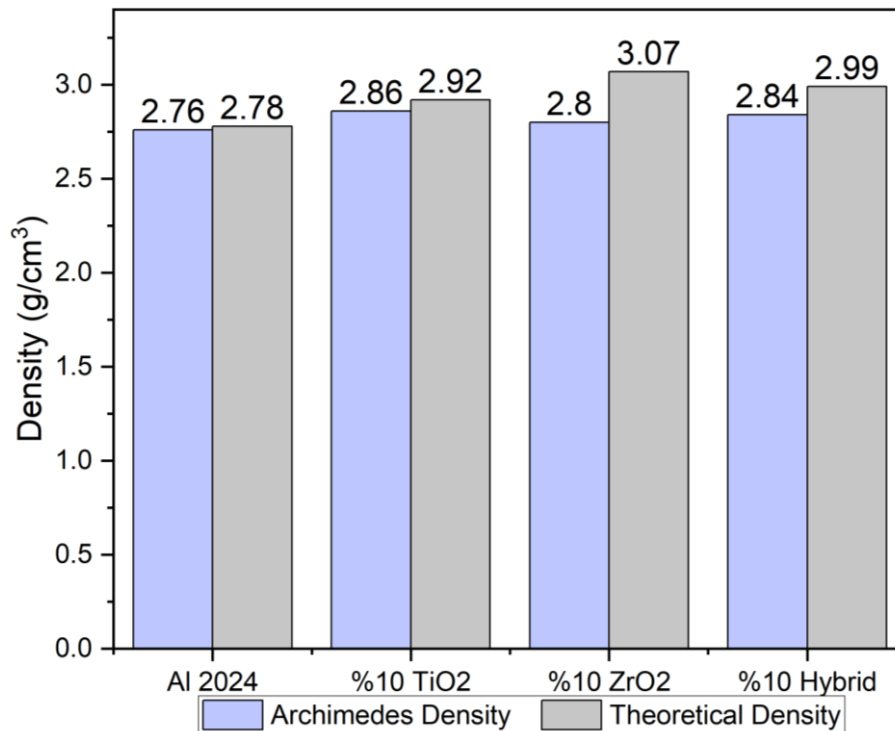
*Figure 1. Comparison between the theoretical and the Archimedes density for each sample*

Figure 2 shows the optical microscope images of 10% TiO_2, 10% ZrO_2, and 10% Hybrid composite samples. Figure 2 includes the maximized microstructural images showing the relation between the particle and matrix material interface. It is observed that particles are dispersed equally in the Al 2024 matrix with the guidance of these figures. Also, the micropores are independent of each other and when these images are analyzed there are partial flocculation occurs in material samples.
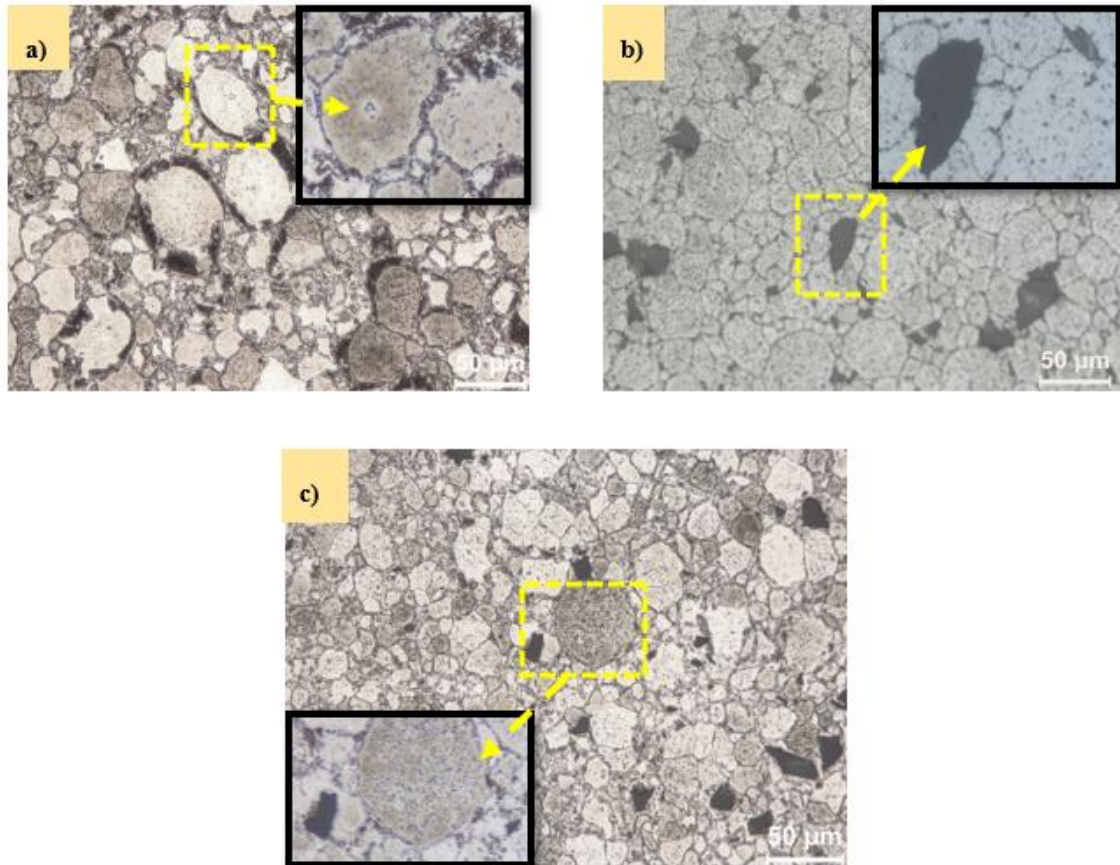
Figure 2. a) *Optical image of 10% TiO$_2$ reinforced Al 2024,* ***b)*** *Optical image of 10% ZrO$_2$ reinforced Al 2024,* ***c)*** *Optical image of 10% Hybrid reinforced Al 2024*

After the optical microscope images are taken, the EDS analysis is done to analyze the elemental distribution of each sample.

Figure 3 and 4 show the selected point's elemental distribution of TiO$_2$ and ZrO$_2$ separately. At point number 2 for Figure 3a, it can be seen that TiO$_2$ and Al 2024 materials are mixed, and the intermediate phase is comprised. For Figure 3b and 4b, The ZrO$_2$ is clearly observed in point 1.
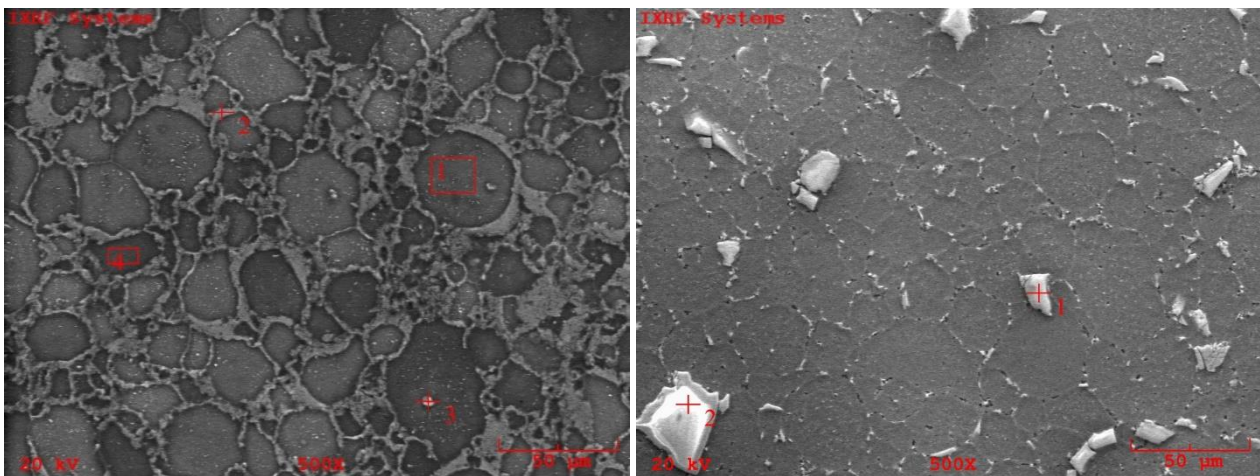
Figure 3. a) *EDS image of 10% TiO$_2$ reinforced Al 2024,* ***b)*** *EDS image of 10% ZrO$_2$ reinforced Al 2024*
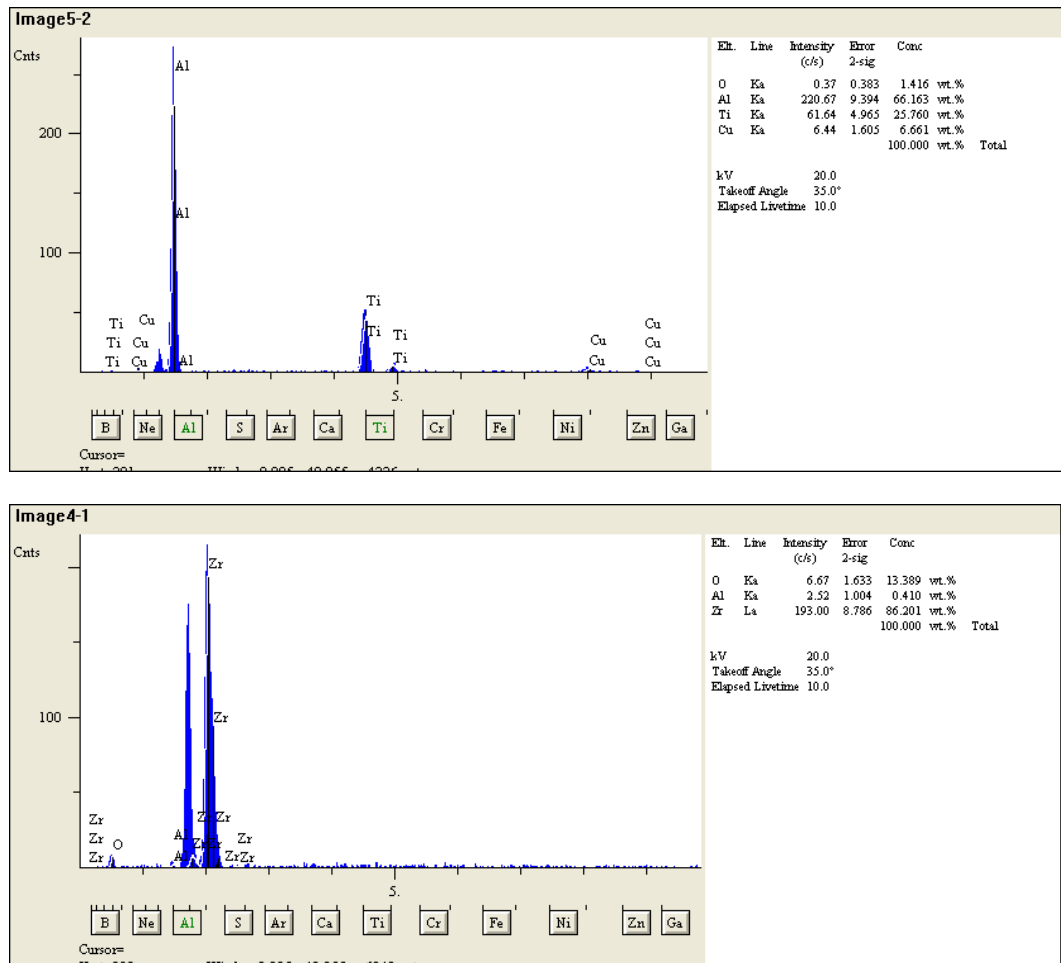
Figure 4. a) Elemental analysis for obtained points in 10% TiO_2 reinforced Al 2024 image, b) Elemental analysis for obtained points in 10% ZrO_2 reinforced Al 2024 image

The hybrid composite sample's EDS analysis resulted in Figures 5 and 6. The obtained points 2 and 4 are investigated in figures. As a result, the ZrO_2, TiO_2, and the compounds of Al 2024 were observed from EDS analysis.
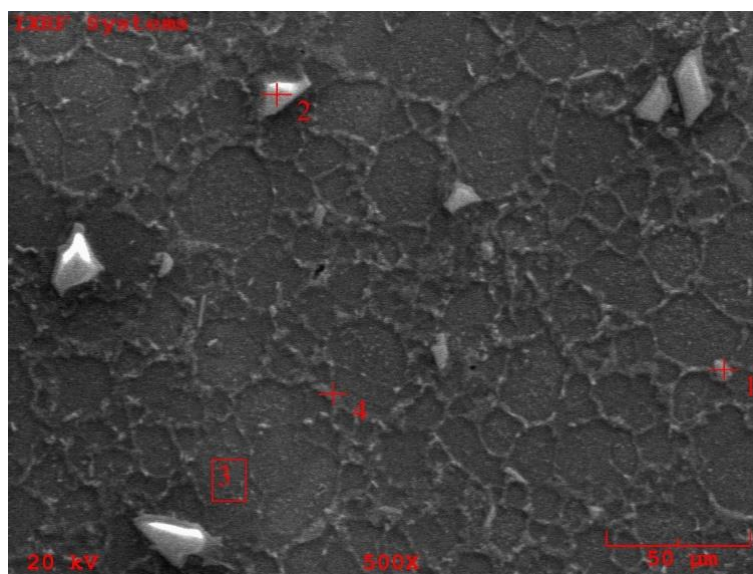
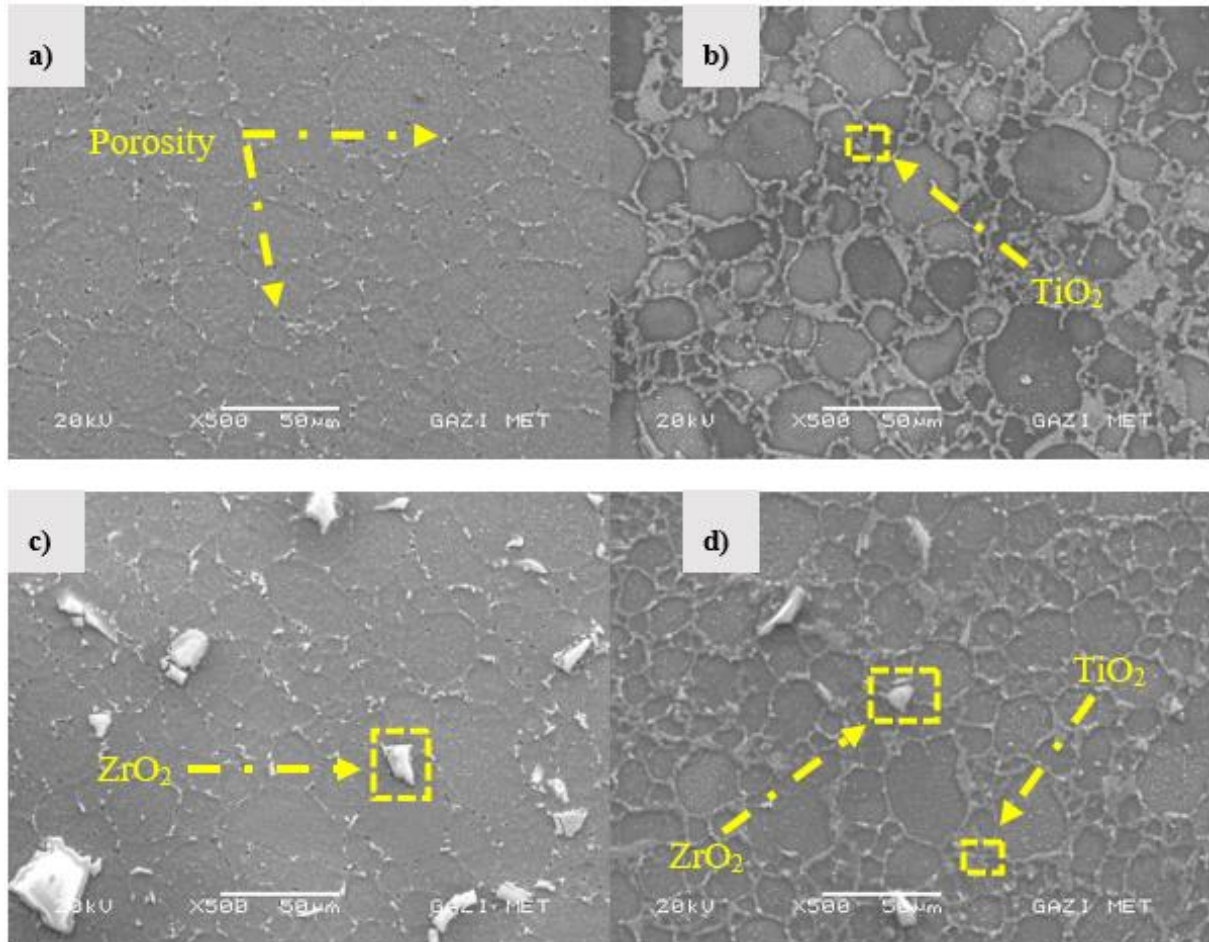*Figure 5. EDS image of 10% hybrid reinforced Al 2024*
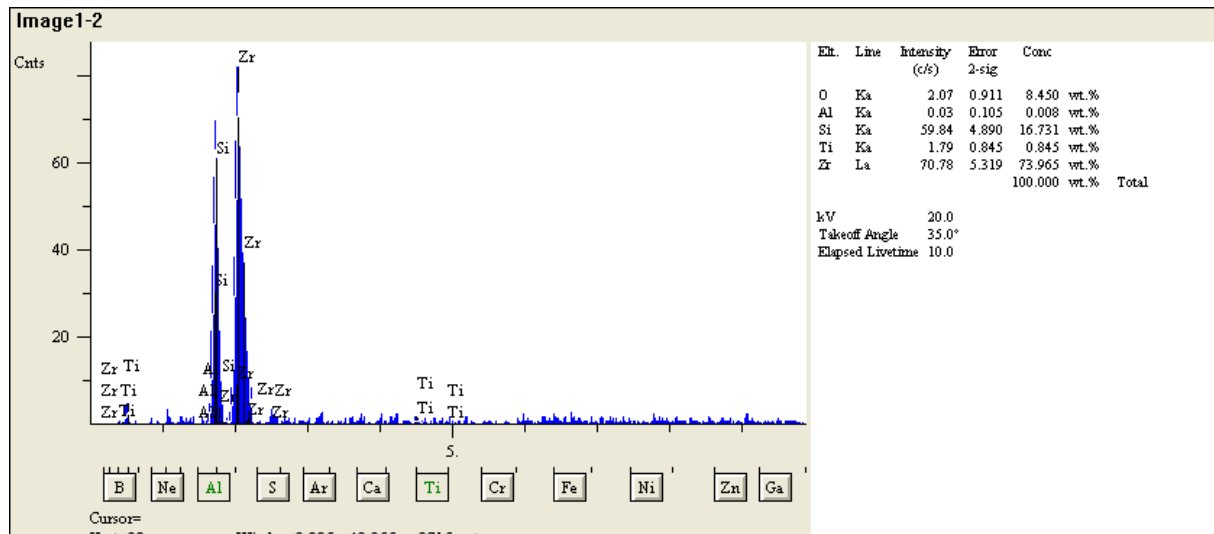
(a)
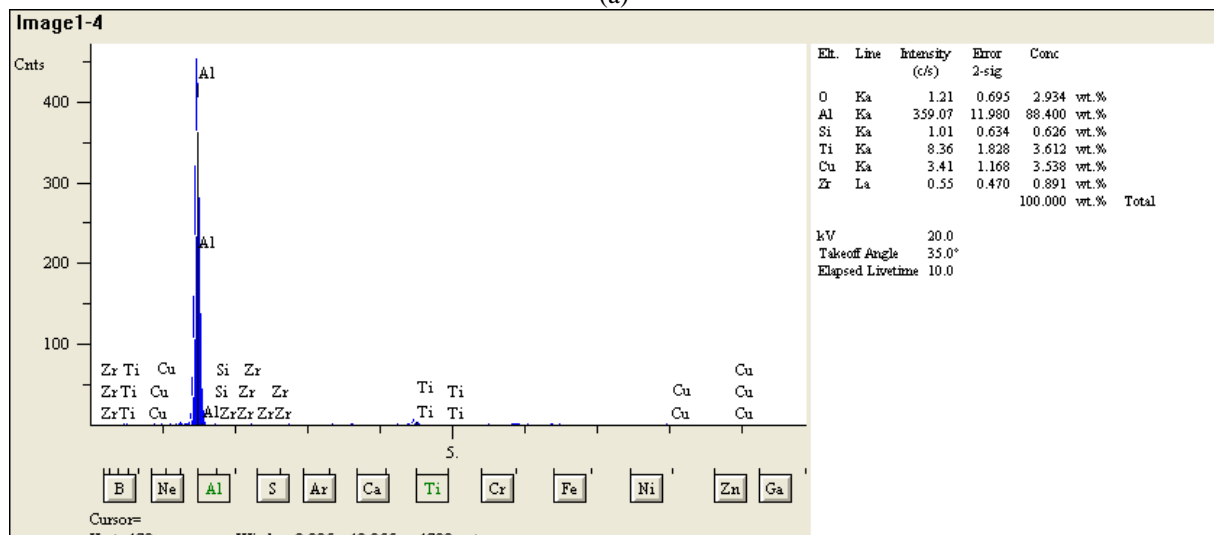
(b)

Figure 6. a) *Elemental analysis for point 2 in 10% hybrid reinforced Al 2024 image,* ***b)*** *Elemental analysis for point 4 in 10% hybrid reinforced Al 2024 image*

The SEM images after the hot press given in Figure 7 supports the partial aggregation detected between the Al 2024 matrix and the particles. It is known that in powdered metal composite materials, particles cause agglomeration and pores, and this affects the material's performance (Dobrzański et al., 2005). In the examinations, it was observed that the agglomeration caused by the reinforcement particles in the structure before the extrusion process occurred more, the agglomerations were distributed after the extrusion process, and a more homogeneous structure was formed.

SEM images showing the distribution of TiO_2 and ZrO_2 particles in the Al 2024 matrix are given in Figure 3. According to the images given in Figure 3, it can be said that the particles existing in the composite are homogeneously distributed. Partial voids were observed between the matrix surface and TiO_2 and ZrO_2 particles, as well as partial particle aggregation in some regions according to the SEM images given in Figure 7, at 7b and 7c. However, it has been determined that these particle aggregations do not exist in the entire composite structure. It is thought that the hot extrusion process disperses the particle aggregations and supports the homogeneity of the ceramic particle distribution in the matrix. Gaps were observed between the Al 2024 matrix and the ceramic particles. When the SEM image of the hybrid composite given in Figure 7, at 7d is examined, it is seen that the ZrO_2 particles are partially clustered around the TiO_2 particles.

Figure 7. a) *SEM image of Al 2024, **b)** SEM image of 10% TiO$_2$ reinforced Al 2024, **c)** SEM image of 10% ZrO$_2$ reinforced Al 2024, **d)** SEM image of 10% Hybrid reinforced Al 2024*

3.2. Mechanical Properties

In Figure 8, each TiO$_2$ and ZrO$_2$ reinforced Al 2024 hot-pressed metal matrix composite's Brinell hardness values can be reviewed. It is normal to observe that as the particle amount increases in the Al 2024 matrix, the hardness increases (Leyi et al., 2011). The lowest hardness value is measured at 80.52 HB in 10% TiO2-reinforced Al 2024 elements. Also, the highest hardness value is observed in 10% ZrO2-reinforced Al 2024 material. That makes sense to get a hybrid metal matrix composite's hardness is 83.74 HB, an average for overall observation. The highest hardness value is measured as 97.5 HB in the Al 2024 sample containing 10% by weight of ZrO$_2$. When the hardness values of samples containing the same amount of TiO$_2$ and ZrO$_2$ in the Al 2024 matrix are compared, it is observed that the hardness values of the composites containing ZrO$_2$ are significantly higher.

In the literature, it is known that ZrO$_2$ particles have higher hardness values according to the TiO$_2$ particle (Kumar et al., 2019; Paul & Islam, 2021). It was determined that the hardness value of the Al 2024 matrix with the TiO$_2$ and ZrO$_2$ reinforced hybrid composite was higher than the composite sample containing 10% TiO2reinforced Al 2024 matrix composite. It is thought that the 5% ZrO$_2$, which is one-half of the 10% reinforcement elements in the hybrid composite, together with the high density obtained after the pressing process caused an increase in hardness value.

In Figure 9, the strength and elongation values obtained after the cross-fracture test applied to Al 2024 MMCs are given. Ceramic-based composites have high hardness values, and they need to be produced in smaller dimensions. Thus, the TRS method is optimum for ceramic-based MMCs. Tensile stress is the most common and one of the most accurate tests to measure the elastic deformation of the sample. Nevertheless, this research focused on the effect of porosity ratios on the sample's rupture strength. Porosity is an important problem in

parts produced with powder metallurgy. This test method is interesting because the transverse rupture strength test is very sensitive to porosity levels (Fang, 2005). The highest cross-fracture strength was obtained in the composite sample reinforced with 10% Hybrid with 635 MPa. The cross-fracture value obtained in the composite samples containing ZrO_2 was higher than the samples reinforced with TiO_2. The highest elongation amount reached in the produced MMCs was determined in Al 2024 samples without reinforcement elements, and the lowest elongation value was determined in composites containing 10% TiO_2. The change observed in the elongation values is parallel with the hardness of the MMCs. It is thought that the change observed in the cross fracture and elongation amounts of 10% hybrid composite materials is due to the increase in density in parallel with this situation, where the TiO_2 and ZrO_2 particles gather around each other and improve the particle/matrix interface with the extrusion process. The cross-fracture strength relates to the hardness values of the material. It is expected that materials with high hardness also have high cross-fracture strength (Kim et al., 2005; Qian et al., 2005). Thus, the materials containing ZrO_2 particles showed better cross-fracture strength than the TiO_2-reinforced MMCs in Figure 9. The hybrid composite sample has the best strength because the relative density results of the hybrid composite are better than the ZrO_2-reinforced MMCs. As the relative density increases, the porosity amount decreases. In addition to this, the material's strength against dislocation formation increases (Bin et al., 2006; Kim et al., 2016). Figure 9 shows that the hybrid MMC sample resulted from better cross-fracture strength than the ZrO_2-reinforced MMCs.
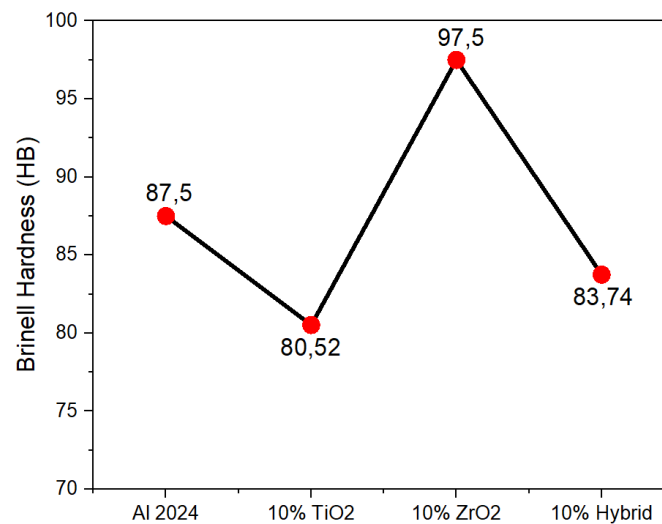
**Figure 8.** *Brinnel Hardness Test Results of Samples*
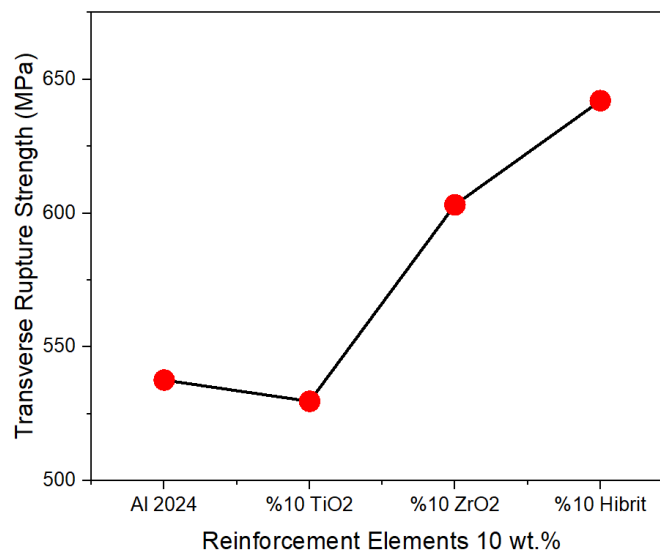
Figure 9. *Transverse Rupture Strength Results of 10 wt. % Reinforcement Elements with Al 2024*

3.3. Radiation Shielding

Radiation can be defined as the energy traveling in the medium. The source of radiation can be investigated as natural and artificial. (Gökmen et al., 2022) Natural radiation sources are radiation that occurs without human contribution. Also, the radiation can be examined in two subtopics which are ionizing and non-ionizing radiation. The alpha, beta, and neutron particles are particle-based ionizing radiations, and the X and gamma rays are electromagnetic radiations (Sürücü & Subaşı, 2021; Gökmen et al., 2022). The situation that distinguishes ionizing radiation from non-ionizing radiation is that the charge balance in the atom is disrupted as a result of ionizing radiation removing electrons from the atom or binding electrons to the atom (Sürücü & Subaşı, 2021).

As seen in Figure 10a, the lowest LAC value among the samples was calculated as Al 2024 without reinforcement. The LAC values of the other samples are pretty close to each other. However, when evaluated among them, the highest LAC value was measured as 10% doped ZrO_2. The samples following this value are hybrid-doped Al 2024 and 10% doped TiO_2, respectively. The LAC value generally decreases and increases inversely with the energy. The MAC value is procured by dividing the LAC values by the sample densities. Accordingly, Figure 10b shows that the lowest MAC value was calculated for Al 2024 without reinforcement material, while the highest MAC value was assessed as 10% doped TiO_2. In general, HVL and TVL values were examined in Figure 11 to determine the material that gives the best shielding properties among the four composite materials. The material thickness values required for material radiation shielding increased in direct proportion to the increase in energy. The sample Al 2024 without reinforcement that required the most material thickness for shielding was approximately 10 cm for HVL, while it was 40 cm for TVL. The half-value layer of the 10% ZrO_2 reinforced MMCs are measured at ~9 cm, and the tenth-value layer is measured at ~32 cm. The material requiring the lowest thickness was determined as 10% doped ZrO_2. In this case, the best shielding properties were determined as 10% doped ZrO_2, 10% doped hybrid, 10% doped TiO_2, and undoped Al 2024, respectively. Figure 12 shows that the distance required for photon collision is less in low-energy regions, but the distance increases gradually in higher energy ranges where pair production and Compton scattering can occur. The lowest distance is measured at ~13 cm in 10% ZrO_2-reinforced MMCs. Figure 13 shows the effective atomic mass number and the number of electrons of each sample. Results showed that 10% ZrO_2-reinforced MMCs are significantly higher than others.
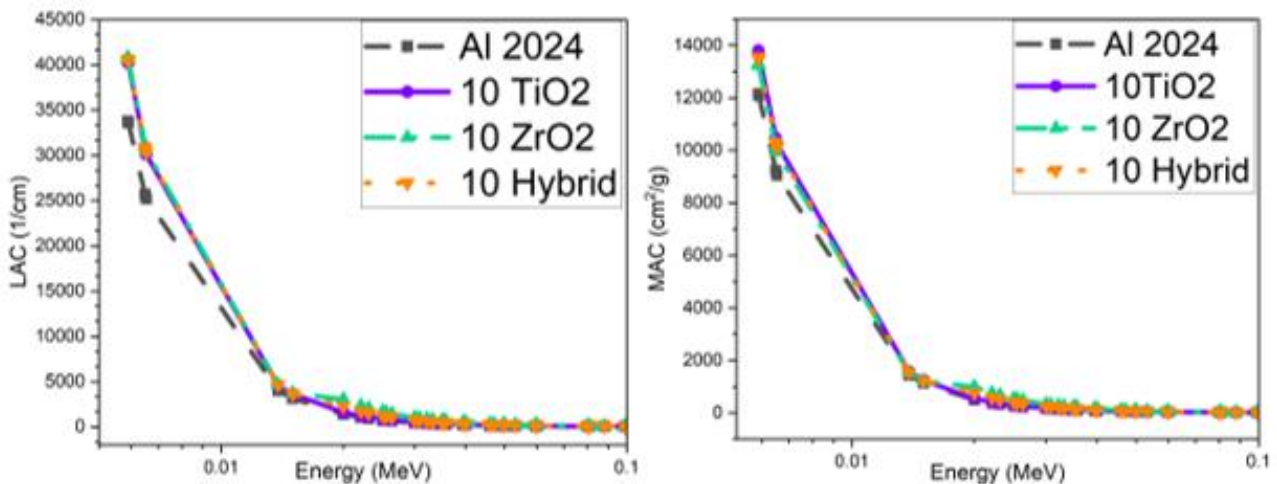
Figure 10. a) *The linear attenuation coefficient of each sample versus Energy,* ***b)*** *The mass attenuation coefficient of each sample versus Energy*
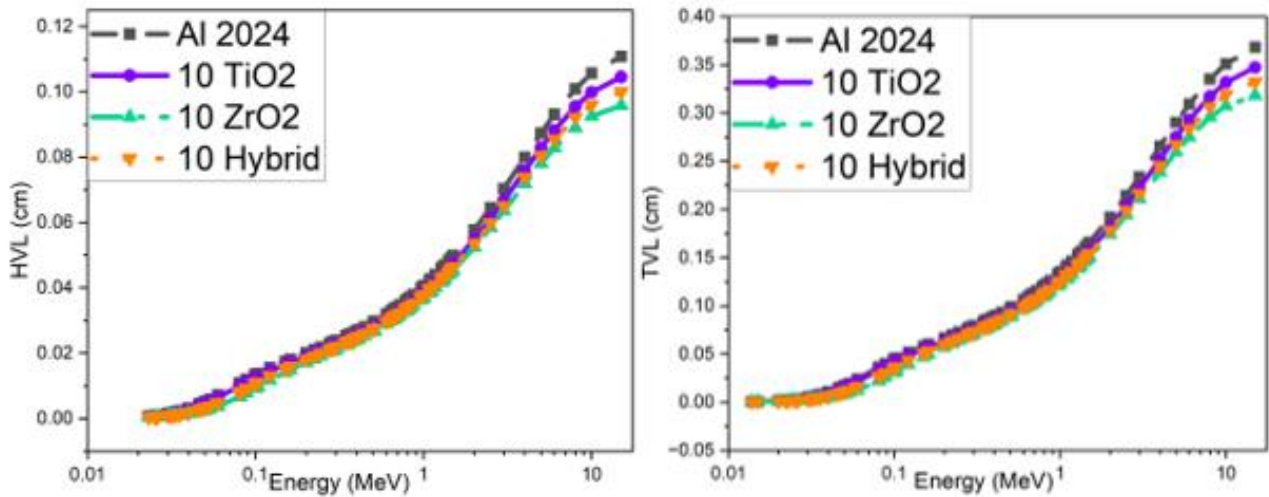
***Figure 11. a)** The half-value layer alteration of each sample versus Energy, **b)** The tenth-value layer alteration of each sample versus Energy*
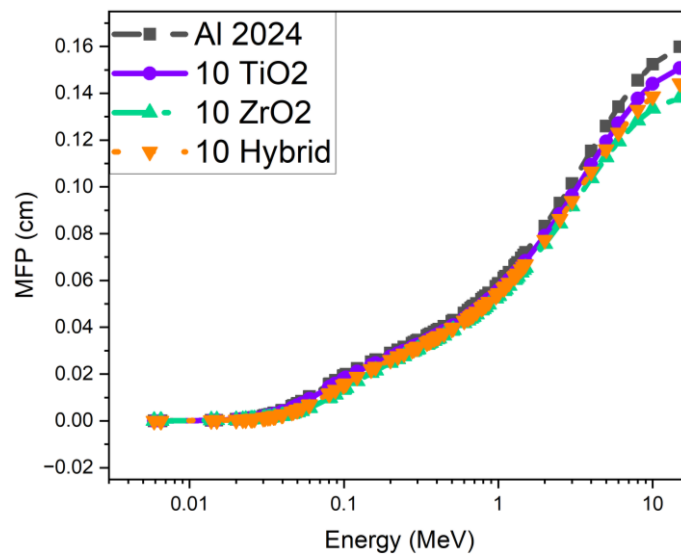

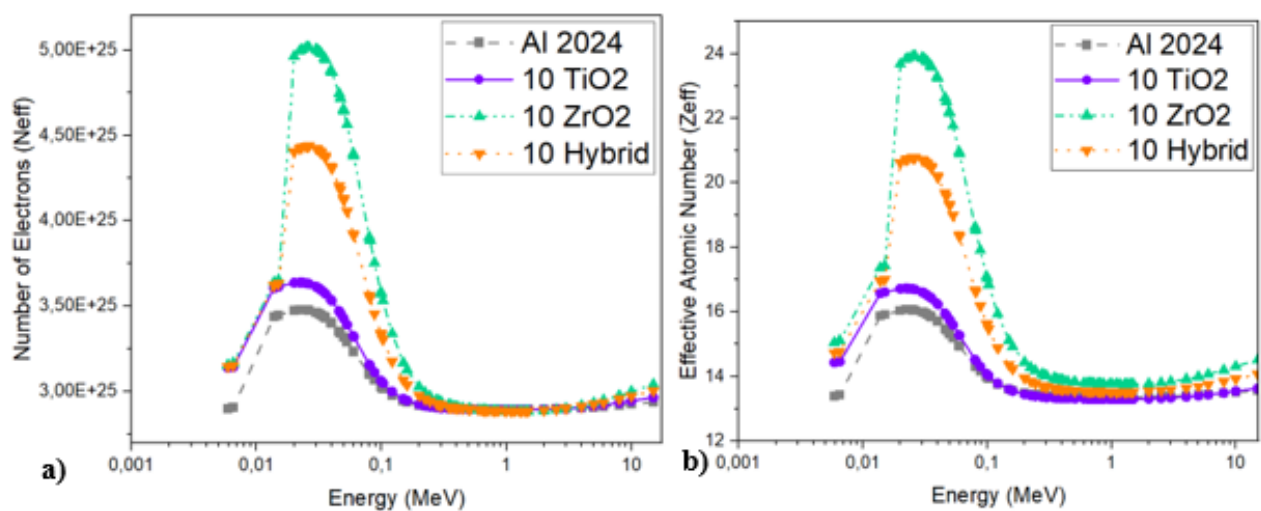***Figure 12.** The mean free path alteration of each sample versus Energy*

***Figure 13. a)** The effective atomic mass number alteration of each sample versus Energy, **b)** The number of electrons of each sample versus Energy*

4. CONCLUSION

The samples are produced by the powder metallurgy method. For each sample, the production method, which is a hot-pressed powder metallurgy method, is done to strengthen the samples. After all, optical images of these samples are taken from bakelite. The optical images show that the materials mixed homogeneously and the porosity distribution over the sample. The highest hardness value among the samples taken from Brinell hardness values was observed as 97.5 HB in 10% ZrO2-added samples. After that, a 3-point bending test was done to investigate the relationship between the maximum load applied to the sample and the elastic deformation. The TRS test was the best option due to the sample size. Results show that the maximum load is read in a 10% hybrid reinforced Al 2024 sample. The maximum applied load at the breaking point is calculated as 9180.713 N. The maximum flexural stress at break is also read in the 10% Hybrid reinforced Al 2024 sample. In conclusion, the Radiation shielding test results, the MAC, LAC, HVL, TVL, and MFP values are calculated. When the radiation shielding values of the samples are examined, LAC and MAC values show the absorption capacity of the material. High values indicate a good absorption capacity. The HVL, TVL, and MFP values determine the shielding properties. Low values indicate that the material has a good shielding capacity. According to the logarithmic increase in energy, the most absorptive sample is observed as a 10% ZrO_2-reinforced Al 2024 sample. The hybrid composite sample has close results with the 10% ZrO_2. The most vulnerable material from all of the samples is decided as Al 2024 sample without reinforcement. This leads us to understand that each material and reinforcement element have different advantages, and they provide improvement for the material's shielding properties.

ACKNOWLEDGEMENT

CONFLICT OF INTEREST

The authors declare no conflict of interest.

REFERENCES

Alekhya, Ch., Prajoshna, A., Baig, M. A., Chandrika, Ch., Devaraju, A., & Gadakary, S. (2022). Preperation and characterization of Al-TiO$_2$-Mg composites through powder metallurgy. *Materials Today: Proceedings*, *66*(2), 489-495. doi:10.1016/j.matpr.2022.03.725

Bin, J., Zejun, W., & Naiqin, Z. (2006). Effect of pore size and relative density on the mechanical properties of open cell aluminum foams. *Scripta Materialia*, *56*(2), 169-172. doi:10.1016/j.scriptamat.2006.08.070

Dobrzański, L. A., Wlodarczyk, A., & Adamiak, M. (2005). Structure, properties and corrosion resistance of PM composite materials based on EN AW-2124 aluminum alloy reinforced with the Al$_2$O$_3$ ceramic particles. *Journal of Materials Processing Technology*, *162-163*, 27-32. doi:10.1016/j.jmatprotec.2005.02.006

Eckner, R., Krampf, M., Segel, C., & Krüger, L. (2016). Strength and fracture behaviour of a particle-reinforced transformation-thoughened trip steel/ZrO2 composite. *Mechanics of Composite Materials*, *51*(6), 707-720. doi:10.1007/s11029-016-9541-z

Fang, Z. Z. (2005). Correlation of transverse rupture strength of WC-Co with hardness. *International Journal of Refractory Metals & Hard Materials*, *23*(2), 119-127. doi:10.1016/j.ijrmhm.2004.11.005

Gökmen, U. (2016). Sıcak Ekstrüze Edilmiş Al 2024 Matrisli B4C/Al2O3 Takviyeli Hibrit Kompozitlerin Üretimi ve Karakterizasyonu. *Journal of Polytechnic*, *19*(4), 445-453.

Gökmen, U., Özkan, Z., Taşçı, U., & Ocak, S. B. (2022) Investigation of radiation shielding by adding Al$_2$O$_3$ and SiO$_2$ into the high-speed steel composites: comparative study. *Physica Scripta*, *97*(5), 055307. doi:10.1088/1402-4896/ac65be

Joshua, K. J., Vijay, S. J., & Selvaraj, D. P. (2018). Effects of Nano TiO2 particles on microhardness and microstructural behaviour of AA7068 metal matrix composites. *Ceramics International*, *44*(17), 20774-20781. doi:10.1016/j.ceramint.2018.08.077

Kim, C. K., Kim, Y. C., Park, J. I., Lee, S., Kim, N. J., & Yang, J. S. (2005). Effects of alloying elements on microstructure, hardness, and fracture toughness of centrifugally cast high-speed steel rolls. *Metallugical and Materials Transactioans A*, *36*, 87-97. doi:10.1007/s11661-005-0141-0

Kim, Y., Jo, H., Allen, J. L., Choe, H., Wolfenstine, J., & Sakamoto, J. (2016). The effect of relative density on the mechanical properties of hot pressed cubic $Li_7La_3Zr_2O_{12}$. *Journal of the American Ceramic Society*, *99*(4), 1367-1374. doi:10.1111/jace.14084

Kumar, G. B. V., Pramod, R., Sekhar, Ch. G., Kumar, G. P., & Bhanumurthy, T. (2019). Investigation of physical, mechanical and tribological properties of Al6061–ZrO2 nano-composites. *Heliyon, 5*(11), 02858. doi:10.1016/j.heliyon.2019.e02858

Leyi, G., Wei, Z., Jing, Z., & Songling, H. (2011). Mechanics analysis and simulation of material Brinell hardness measurement. *Measurement*, *44*(10), 2129-2137. doi:10.1016/j.measurement.2011.07.024

McAlister, D. R. (2018). *Gamma Ray Attenuation Properties of Common Shielding Materials.* PG Research Foundation, Inc. 1955 University Lane Lisle, IL 60532. PDF

Naito, M., Kitamura, H., Koike, M., Kusano, H., Kusumoto, T., Uchihori, Y., Endo, T., Hagiwara, Y., Kiyono, N., Kodama, H., Matsuo, S., Mikoshiba, R., Takami, Y., Yamanaka, M., Akiyama, H., Nishimura, W., & Kodaira, S. (2021). Applicability of composite materials for space radiation shielding of spacecraft. *Life Sciences in Space Research*, *31*(1), 71-79. doi:10.1016/j.lssr.2021.08.004

Nikbin, I. M., Mohebbi, R., Dezhampanah, S., Mehdipour, S., Mohammadi, R., & Nejat, T. (2019). Gamma ray shielding properties of heavy-weight concrete containning Nano-TiO₂. *Radiation Physics and Chemistry*, *162*, 157-167. doi:10.1016/j.radphyschem.2019.05.008

Park, J., Suh, H., Woo, S. M., Jeong, K., Seok, S., & Bae, S. (2019). Assesment of neutron shielding performance of nano-TiO2-incorporated cement paste by Monte Carlo simulation. *Progress in Nuclear Energy*, *117*, 103043. doi:10.1016/j.pnucene.2019.103043

Paul, S., & Islam, M. M. (2021, December 12-14). *Fabrication of Aluminum Metal Matrix Composites Reinforced with TiO₂ by Powder Metallurgy Techniques*. Proceedings of the International Conference on Mechanical Engineering and Renewable Energy (ICMERE 2021), Chattogram, Bangladesh.

Qian, J., Daemen, L. L., & Zhao, Y. (2005). Hardness and fracture toughness of moissanite. *Diamond and Related Materials*, *14*(10), 1669-1672. doi:10.1016/j.diamond.2005.06.007

Rahimian, M., Ehsani, N., Parvin, N., & Baharvandi, H. R. (2009). The effect of particle size, sintering temperature and sintering time on the properties of Al–Al₂O₃ composites, made by powder metallurgy. *Journal of Materials Processing Technology*. *209*(14), 5387-5393. doi:10.1016/j.jmatprotec.2009.04.007

Sürücü, A. M., & Subaşı, S. (2021). Nanomateryallerin Kompozit Malzemelerin Radyasyon Zırhlama Özelliklerine Etkisinin İncelenmesi. *El-Cezeri*, *8*(1), 182-194 . doi:10.31202/ecjse.812372

Investigation and Development of Polarographic Method for Pb (II) and Cd (II) Analyses in Oils

Şükrü KALAYCI[1]* (iD) Sinan Mithat MUHAMMET[1] (iD) Bekir Sıtkı ÇEVRİMLİ[1] (iD)

[1]Department of Chemistry, Vocational School of Technical Sciences, Gazi University, 06500, Ankara, Türkiye

Keywords	Abstract
Olive Oil Analysis Pb (II) Cd (II) Differential Pulse Polarography	In this study, Differential Pulse Polarography (DPP) method was preferred of Cd (II) and Pb (II) levels, which have toxic effects. This method was applied to determine Cd and Pb levels in cold-pressed olive oil brought from 5 different provinces of Turkey. The samples were dissolved in microwave digestion using concentrated HNO_3 and H_2O_2. Analyses were carried out in acetate buffer (pH 4) to which EDTA was added. The LOD for Cd and Pb was found as 0.74, 0.52 µg L^{-1} and the LOQ was 0.96, 0.82 µg L^{-1}. Additions were made from standard Cd and Pb solutions and the % recovery values were measured as 98 and 99. The relative standard deviation (RSD, %) was found < 5. This method was found to be sensitive to the analyses of two toxic elements in cold pressed olive oil.

1. INTRODUCTION

Fats play an important role among the essential nutrients necessary for people to carry out their life activities. People meet about 25-30% of their daily energy needs from fats. Vegetable oils are obtained from many plant species (Nash et al., 1983). In Turkey, it is produced from olives, sunflowers and hazelnuts. Recently, the tendency of people to consume oil has been increasing. Cold pressed oils are preferred more because of their unique smell, aroma and not using chemicals.

As a result of direct or indirect pollution of air, water and soil, heavy metal contents increase. Excess amounts of heavy metals cause many vital problems and poisonings in living things. Pb, Hg and Cd determinations were made in hair samples taken from various age groups and their effects on child health were investigated (Orun et al., 2011). Therefore, the determination of heavy metals becomes extremely important.

Spectroscopic, chromatographic and electroanalytical methods are used in heavy metal analyses. Metals were determined by using the EAAS method with some organic solvents and appropriate test conditions were investigated (Karadjova et al., 1998; Schiavo et al., 2008). The elements in oils were measured using the GF-AAS method with a THFA atomizer (Canário & Kaskov, 2005). The copper in the samples was enriched with the micro-extraction method. In the naturel sample was carried out with the FAAS method (Menghwar et al., 2019). Other spectroscopic methods (Jiménez et al., 2003; Frazolli et al., 2007) were used for metal analyses in oil. In addition, ion chromatography method of heavy metal determinations in oils was also used (Ramos et al., 2020).

*Corresponding Author, e-mail: skalayci@gazi.edu.tr

It has been used in electroanalytical methods in metal analyses (Kalayci & Somer, 2020; Kalayci, 2021; Kalayci & Muhammet, 2021). It is preferred in the determination of metal levels due to its high sensitivity, absence of interference effects and pre-concentration processes (Somer et al., 2019). The amounts of some metals in oils were determined at the ng level. Toxic elements in various oils were analyzed after the samples were dissolved with a microwave digestion (Kucukkolbasi et al., 2014). Recently, electroanalytical methods with a modified electrode have also been used (Devnani & Satsangee, 2015; Wang & Yue, 2017; Silah et al., 2021).

In this study, some cold-pressed olive oils were dissolved in Pb and Cd by microwave digestion method. Samples were analyzed using DPP with a dripping mercury electrode with high reproducibility and sensitivity. Our method determined for the analyses in this study is summarized in Figure 1 below.
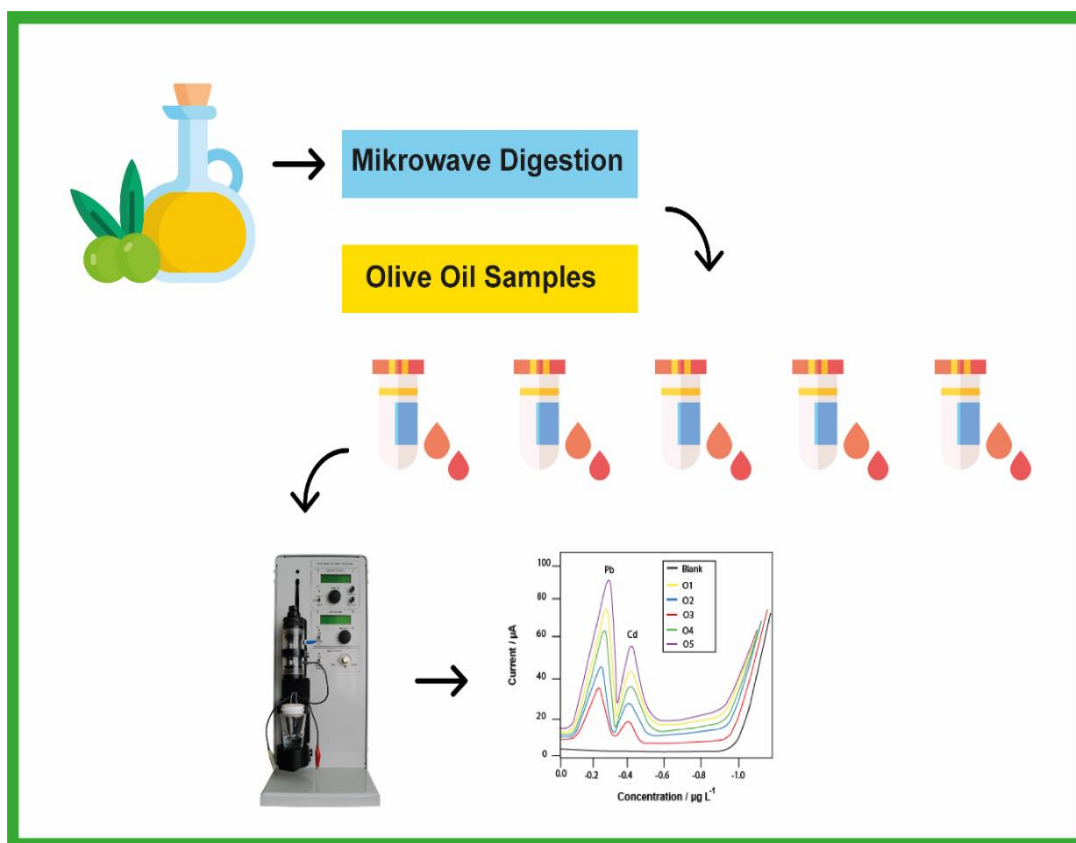
Figure 1. *Summary of method used for Pb and Cd determination in oil*

2. MATERIALS

2.1. Instruments

These measurements (Figure 2) were made with the Entek brand polarography analyzer with a dripping mercury electrode, Ag/AgCl with Pt electrode and C4 cell. In addition, pure nitrogen gas was used to eliminate the effect of dissolved oxygen in the solution. Milestone microwave digestion device was used to dissolve the oil samples.

2.2. Reagents

Deionized water system was used as solvent in solutions and samples (Heal Force, Smart RO30, Chinese), the resistivity measured after this treatment was not less than 10 MΩ cm. Certain volumes of nitric acid (63%, w/w) and hydrogen peroxide (35%, w/w) were used for sample dissolution. For element determination, 1 mol L^{-1} solution was prepared from acetic acid (100%, w/w) and ammonia (17%, w/w) as electrolytes. As the working electrode, metallic mercury and the salts of the elements to be used in the analyses (Merck) have analytical purity.

2.3. Solubilization of Oil Samples

Cold pressed oil samples brought from 5 different parts of Turkey were named O1 (Bursa), O2 (Manisa), O3 (Muğla), O4 (Denizli) and O5 (Kilis), respectively. The samples weighed about 0.500 g. In the process of solubilization of the samples, it was carried out with a microwave digestion device by applying high heat and pressure. The solubilization of oils was done with a microwave digestion device. The samples were placed in Teflon containers and to them, a mixture of acid was added according to the procedure. These were resolved by applying the parameters for 15 minutes at 200 psi and 10 minutes at 170 °C. This oil samples were cooled at 25°Cm, filtered and diluted to 25 ml in volume.

A

B

Figure 2. A) Polarography and B) microwave digestion device used during analyses

3. RESULTS AND DISCUSSION

3.1. Polarographic Behavior of Elements

Qualitative analyses of elements are carried out according to their potential. The potentials of the elements differ according to the electrolytes. (Locatelli & Melucci, 2013). Electrolyte medium with high sensitivity should be chosen in elemental analyses. The polarograms of Pb and Cd in olive oils were examined in various electrolytes. These peak potentials are given in Table 1. From this, electrolytes suitable for the quantitation of each element were determined. EDTA added acetate buffer was used for the measurements of the elements.

Table 1. Peak potentials of elements in oil samples

Analyte	pH 4 (1M AcOH + 0.1 M EDTA)	pH 7 (1M AcOH + 0.1 M EDTA)	pH 10 (1M NH$_3$)
Pb	-0.20	-0.30	-0.40
Cd	-0.40	-0.41	-0.55

3.2. Method Evaluation

The analytical parameters of the applied method were examined. For this, the sensitivity, linear range, LOD and LOQ of the method were measured (Kalayci, 2022). These parameters are shown in Table 2.

Table 2. Performance values of the applied method

Analyte	LOD, µgL⁻¹	LOQ, µgL⁻¹	R^2	Linear range, µgL⁻¹
Pb	0.52	1.82	0.9975	5-50
Cd	0.74	2.36	0.9956	5-50

3.3. Samples Analyses

Olive oil is produced from olives in the early harvest period. Olive oil is a healthy oil on its own. However, especially cold-pressed olive oil is a very healthy type of oil. Olive oils are produced by cold press method in two-phase systems under 22°C. With this production method, the values of vitamin E, phenolic components and antioxidant substances that are beneficial for health are at high levels (Matthäus & Brühl, 2003).

Differential pulse polarography method, which can determine high and low concentrations with sensitivity, reproducibility, has been used in metal analyses in many samples. Standard addition method was preferred for content of Cd and Pb in olive oils. This type of calibration was chosen to minimize the error rate in metal analyses in oil types. The polarograms of the samples are given in Figure 3 and calibration graphics obtained by adding standard solutions are given in Figure 4. Analyses of Pb and Cd levels in 5 olive oils are shown in Table 3.
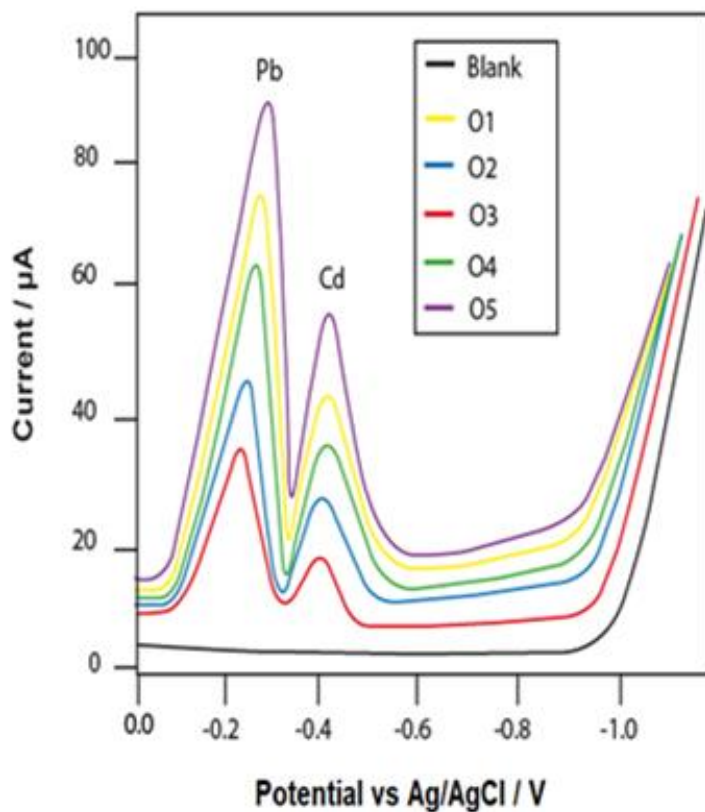
Figure 3. Polarograms obtained from analytical curves of standard solutions Pb and Cd.
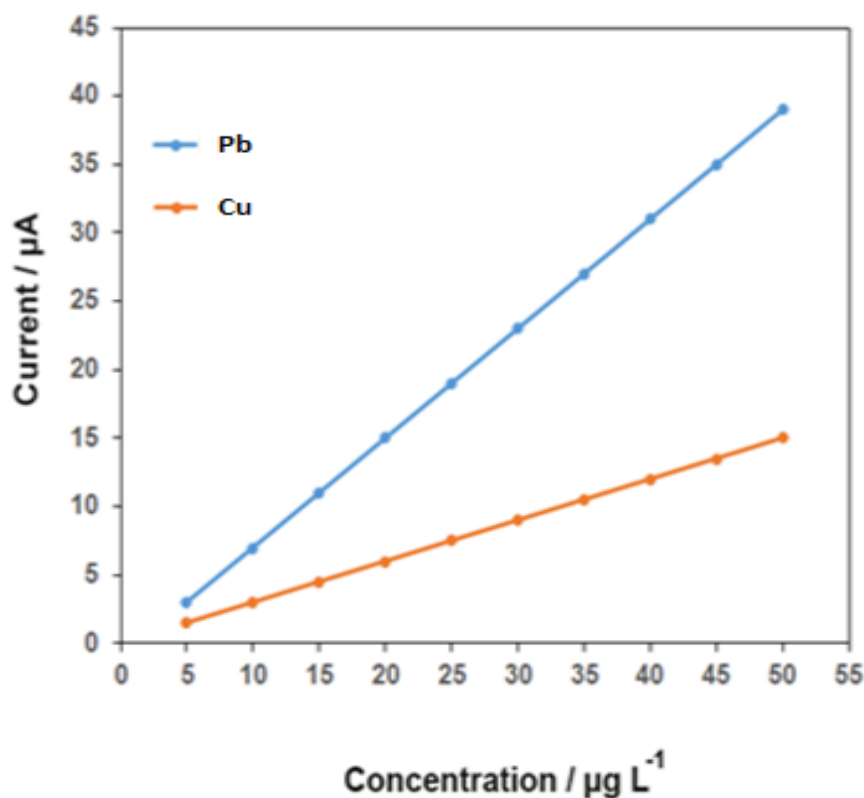
Figure 4. Analytical signals versus Pb and Cu concentrations

Table 3. Pb and Cd amounts in 5 different cold pressed oil samples (CL 95%, N=4)

Sample	Concentration, µg L^{-1} (x ± $\frac{txS}{\sqrt{N}}$)	
	Pb	Cd
O1	18.23 ± 2.74	4.52 ± 0.27
O2	16.85 ± 1.95	3.23 ± 0.22
O3	14.46 ± 1.37	2.89 ± 0.18
O4	17.23 ± 2.22	4.05 ± 0.24
O5	19.23 ± 3.12	4.86 ± 0.33

In addition, the amount and recovery values found against the amount of analyte added to the cell were examined and these parameters are given in Table 4.

Table 4. The recovery versus standard additions in O1(Bursa) sample

Sample	Analyte	Added µg L^{-1}	Found µg L^{-1}	Recovery, %
O1	Pb	0	ULQ	---
		1.50	1.48 ± 0.15	99
		3.25	3.23 ± 0.26	99
	Cd	0	ULQ	---
		1.00	0.97 ± 0.04	97
		2.00	1.96 ± 0.13	98
ULQ: Under the limit of quantification				

3.4. Comparation of Electroanalytical and Other Methods

The comparison of Pb and Cd values in oil samples with electroanalytical methods given in the literature is shown in Table 5. The name of each method was given the detection limit. In Pb and Cd analyses, it was determined that the most suitable method among the compared methods was electroanalytical methods.

***Table 5.** The comparation of methods for Pb and Cd contents in oils samples in literature*

Analytes	Sample	Methods	Detection limits	Reference
Cd, Pb	Edible oil	ASV	Cd:0.3; Pb:0.5 ng g^{-1}	Kucukkolbasi et al., 2014
Cd, Pb	Vegetable oil	SWASV	Cd:0.006; Pb: 0.01 µg kg^{-1}	Shishov et al., 2022
Cd, Pb	Olive oil	DPP	Cd: 0.96; Pb:0.82 µg L^{-1}	This work

The O1 (Bursa) oil sample was analyzed by atomic absorption spectroscopy and ICP-OES, respectively, and the results were compared with the results obtained by differential pulse polarography. The t-test was applied to the obtained results. These values are given in Table 6. The results were found to be compatible with each other.

***Table 6.** Comparison of Pb and Cd amounts of AAS, ICP-OES and Differential pulse polarography, (CL 95%, N=4)*

Methods	Pb (II): µg L^{-1}	Cd (II): µg L^{-1}
AAS	20.11 ± 3.54	4.79 ± 0.315
ICP-OES	18.41 ± 2.89	4.55 ± 0.285
Differential pulse polarography	18.23 ± 2.74	4.52 ± 0.268
t-test (t $_{Critical}$=3.18)	2.03	2.61

4. CONCLUSION

For Cd and Pb analyses in cold pressed olive oil brought from 5 different regions of Turkey, measurements were made by differential pulse polarography method. The detection limits were between 0.82-0.92 µg L^{-1} and allowed the determination of two toxic metal levels in 5 samples. The recovery values obtained against the added Pb and Cd amounts show that this method is suitable for analyses in the samples. Differential pulse polarography method was found to be suitable because of its high reproducibility, no need for pre-concentration processes, no interference effects, and low detection limit. It was also determined that the measured Pb and Cd values were not in the range to cause toxic effects.

ACKNOWLEDGEMENT

CONFLICT OF INTEREST

The authors declare that they have no competing interests.

REFERENCES

Canário, C. M., & Kaskov, D. A. (2005). Direct determination of Cd and Pb in edible oils by atomic absorption spectrometry with transverse heated filter atomizer. *Journal of Analytical Atomic Spectrometry*, *20*(12), 1386-1388. doi:10.1039/B506627C

Devnani, H., & Satsangee, S. P. (2015). Green gold nanoparticle modified anthocyanin-based carbon paste electrode for voltammetric determination of heavy metals. *International Journal Environmental Science Technology*, *12*(4), 1269-1282. doi:10.1007/s13762-014-0497-z

Frazolli, C., D`llio, S., & Bocca, B. (2007). Determination cadmium and lead in honey by SF-ICP-MS: validation figures and uncertainly of results. *Analytical Letters*, *40*(10), 1992-2004. doi:10.1080/00032710701484525

Jiménez, M. S., Velarte, R., & Castillo, J. R. (2003). On-line emulsions of olive oil samples and ICP-MS multi-elemental determination. *Journal of Analytical Atomic Spectrometry*, *18*(9), 1154-1162. doi:10.1039/B303131D

Kalayci, S. (2021). High Sensitivity Sulphite Membrane Selective Electrode and its Application. *Journal of the Chemical Society of Pakistan*, *43*(4), 451-455. doi:10.52568/000590/JCSP/43.04.2021

Kalayci, S. (2022). Investigation of Arsenic Content in Field Pesticides using inductively coupled plasma optical emission spectroscopy (ICP-OES). *GU. J Sci, Part A*, *9(2)*, 96-103. doi:10.54287/gujsa.1100870

Kalayci, S., & Muhammet, S. (2021). Analysis of trace elements in Turkish raki by differential pulse polarography. *International Journal of Electrochemical Science*, *16*, 210932. doi:10.20964/2021.09.43

Kalayci, S., & Somer, G. (2020). Differential Pulse Polarography Method for the Determination of Trace Fe, Ni, Pb, Zn, Se and Cu in Black Tea Leaves. *Chemical Science International Journal*, *29*(4), 15-23. doi:10.9734/CSJI/2020/v29i430171

Karadjova, I., Zachariadis, G., Boskou, G., & Stratis, J. (1998). Electrothermal atomic absorption spectrometric determination of aluminum, cadmium, chromium, copper, iron, manganese, nickel and lead in olive oil. *Journal of Analytical Atomic Spectrometry*, *13*(3), 201-204. doi:10.1039/A707256B

Kucukkolbasi, S., Temur, O., Kara, H., & Khaskheli, A. R. (2014). Monitoring of Zn (II), Cd (II), Pb (II) and Cu (II) during refining of some vegetable oils using differential pulse anodic stripping voltammetry. *Food Analytical Methods*, *7*(4), 872-878. doi:10.1007/s12161-013-9694-5

Locatelli, C., & Melucci, D. (2013). Voltammetric method for ultra-trace determination of total mercury and toxic metals in vegetables. Comparison with spectroscopy. *Open Chemistry*, *11*(5), 790-800. doi:10.2478/s11532-013-0221-8

Matthäus, B., & Brühl, L. (2003). Quality of cold-pressed edible rapeseed oil in Germany. *Nahrung/Food*, *47*(6), 413-419. doi:10.1002/food.200390092

Menghwar, P., Yilmaz, E., Sherazi, S. T. H., & Soylak, M. (2019). A sensitive and selective deep eutectic solvent-based ultrasound-assisted liquid phase microextraction procedure for separation preconcentration and determination of copper in olive oil and water samples. *Separation Science and Technology*, *54*(15), 2431-2439. doi:10.1080/01496395.2018.1547317

Nash, A. M., Mounts, T. L., & Kwolek, W. F. (1983). Determination of ultratrace metals in hydrogenated, vegetable oils and fats. *Journal of American Oil Chemists' Society*, *60*(4), 811-814. doi:10.1007/BF02787433

Orun, E., Yalcin, S. S., Aykut, O., Orhan, G., Morgil, G. K., Yurdakok, K., & Uzun, R. (2011). Breast milk lead and cadmium levels from suburban areas of Ankara. *Science of the Total Environment*, *409*(13), 2467-2472. doi:10.1016/j.scitotenv.2011.02.035

Ramos, A. C. O. P., Caldeira, G. R. F., Nunes, C. R. O., Terra, W. S., & Souza, M. O. (2020). Optimization of extraction induced by emulsion breaking variables for subsequent determination of crude oil salinity by ion chromatography. *Brazilian Journal of Analytical Chemistry*, *7*(27), 31-39. doi:10.30744/brjac.2179-3425.AR-15-2020

Schiavo, D., Neira, J. Y., Nóbrega, J. A. (2008). Direct determination of cadmium, copper and lead in wines and grape juices by thermo spray flame furnace atomic absorption spectrometry. *Talanta*, *76*(5), 1113-1118. doi:10.1016/j.talanta.2008.05.010

Shishov, A., Volodina, N., Semenova, E., Navolotskaya, D., Ermakov, S., & Bulatov, A. (2022). Reversed-phase dispersive liquid-liquid microextraction based on decomposition of deep eutectic solvent for the determination of lead and cadmium in vegetable oil. *Food Chemistry*, *373*(Part B), 131456. doi:10.1016/j.foodchem.2021.131456

Silah, H., Erkmen, C., Demir, E., & Uslu, B. (2021). Modified indium tin oxide electrodes: Electrochemical applications in pharmaceutical, biological, environmental and food analysis. *TrAC Trends in Analytical Chemistry*, *141*, 116289. doi:10.1016/j.trac.2021.116289

Somer, G., Kalayci, S., & Yılmaz, U. (2019). Determination of Sulfite in Wine Using Differential Pulse Polarography. *Russian Journal of Electrochemistry*, *55*(12), 1360-1365. doi:10.1134/S1023193519020101

Wang, T., & Yue, W. (2017). Carbon nanotubes heavy metal detection with stripping voltammetry: a review paper. *Electroanalysis, 29*(10), 2178-2189. doi:10.1002/elan.201700276

Attenuation Effect of Sample Container in Radioactivity Measurement by Gamma-ray Spectroscopy

Esra UYAR[1*] (iD)

[1]*Gazi University, Faculty of Sciences, Department of Physics, Ankara, Türkiye*

Keywords	Abstract
Gamma-Ray Spectroscopy Efficiency Self-Attenuation Effect Sample Container PHITS GESPECOR	The measurement of radioactivity in environmental samples containing natural radionuclides such as ^{238}U, ^{232}Th, and ^{40}K in gamma-ray spectrometry is the most common application. One of the most widely used sample containers for environmental radioactivity measurements is volumetric sample containers of certain sizes in cylindrical geometry. These cylindrical containers can be made of materials with different densities and thicknesses. In this intention, in this study, the effect of the sample container, which is one of the many parameters affecting the detector efficiency, was investigated. For this purpose, acrylic and polypropylene materials with of different densities were examined. IAEA RGU-1, IAEA-RGTh-1 and IAEA-RGK-1 standards containing uranium, thorium and potassium environmental radionuclides analyzed in gamma-ray spectrometric measurements were used as samples for these sample containers with different densities. Additionally, since the spectra in cylindrical geometry are taken by placing them on the detector endcap, the effect of the bottom thickness was investigated by changing the bottom thickness of these materials. Different material and bottom thickness evaluations were made using PHITS and GESPECOR Monte Carlo simulation programs. Compatible results were obtained with a difference of <5% between the PHITS and GESPECOR programs. From the outcome of this study, it can be concluded that when choosing the container material, the density should be as low as possible and especially the bottom thickness should be thin.

1. INTRODUCTION

γ-ray spectrometry is a rapid and non-destructive method used to determine the radioactivity of gamma-ray emitting radionuclides in a sample. Due to their high-energy resolution, high-purity germanium (HPGe) detectors can be used in gamma-ray spectrometry to measure the activity of natural and artificial radionuclides in environmental, geological and biological samples (Azbouche et al., 2015). There are many parameters in the calculation of activity in gamma-ray spectrometry. For an accurate calculation, we must minimize the uncertainties that may come from these parameters such as efficiency, count rate, decay, random summing and self-absorption correction, mass, sample height and homogeneity (Gilmore, 2008). This is the uncertainty that can come from the efficiency calculation, which is directly related to the sources of uncertainty. Because there are similar uncertainties when calculating the efficiency. The efficiency value, which shows the performance of HPGe detectors, must be determined accurately and precisely, no matter what the detector is used for (Modarresi et al., 2017). It has been shown by many studies in the literature that the Monte Carlo simulation method can be successfully applied in gamma-ray spectrometry, especially in the efficiency calculation (Abd El Gawad et al., 2020; Trang et al., 2021; Stríbrnský et al., 2022). Two types of Monte Carlo simulation software are used in gamma-ray spectroscopy: these are either general-purpose codes such as GEANT,

PENELOPE, EGS4, FLUKA, PHITS, or GESPECOR, DETEFF, ETNA, EFFTRAN, etc. as dedicated-purpose codes (Lépy et al., 2019; Sima et al., 2020).

In this study, the effect of the sample container on the efficiency, which has not been examined in the literature, was investigated using PHITS and GESPECOR Monte carlo programs. The attenuation effect of the sample container material type and thickness on the radioactivity measurement of volumetric samples in cylindrical geometry was examined. For this purpose, acrylic and polypropylene, which are mostly used sample container materials in gamma-ray spectroscopy laboratories, were chosen (Knoll, 2010; Guerra et al., 2018). Such samples are usually prepared in cylindrical sample containers of different sizes according to the sample amount, and the volume source is obtained. Self-absorption and true coincidence summing corrections, which are the correction factors that need to be made in the radioactivity calculation, are also effective in the volume source geometry counted on the detector endcap. Self-absorption correction is a factor that is effective especially in high-density matrices containing elements with high atomic number, which occurs as a because of the absorption of gamma rays passing through the sample due to the sample matrix and density, causing losses in the photopeak count (Yücel et al., 2010). Therefore, this loss depends not only on the sample, but also on the sample container, as it depends on a process until it reaches the detector. The more high-density or thicker sided sample containers are used, the more absorption there will be, which will affect the count. The sample container to be used should have the appropriate size, shape and density (Knoll, 2010).

2. MATERIAL AND METHOD

Two Monte Carlo programs were used in this study. The first is the general-purpose Monte Carlo program, PHITS, and the other is the dedicated-purpose program, the GESPECOR Monte Carlo program. It has been shown that both programs can be used reliably in gamma-ray spectrometric studies (Sima et al., 2001; Lépy et al., 2019; Uyar & Bölükdemir, 2022). While Monte Carlo programs have similar algorithms, it is expected that there will be differences between their results because they use different cross-sections, databases and libraries. With the EGS5 (Electron Gamma Shower) library in the PHITS Monte Carlo program, the atomic interactions of electrons and photons in a wide energy range ranging from 1 keV to 1 TeV (depending on the atomic numbers of the target materials) are simulated in the desired geometry. EGS code system started with EGS1 written in FORTRAN-IV language and consists of EGS5, which is the last version developed and improved continuously as EGS2, EGS3, EGS4. The data library in EGS5 is PHOTX (Photon Interaction Cross Section Library). The PHOTX data library provides results for elements with atomic numbers between 1 and 100 and photon energies between 1 keV and 100 MeV. It provides cross sections for coherent and non-coherent scattering, photoelectric absorption and pair production (Hirayama et al., 2006). In GESPECOR, the photon interaction cross sections are evaluated for each material of interest before starting the simulations, in the step of preparing and saving the material file. The basic cross sections are computed using the XCOM program which can be dowloaded from the NIST website (Berger et al., 2010). These basic cross sections are used for evaluating the interaction coefficients in a grid of 100 energy points equally spaced in logarithmic scale between 2 keV and 4 MeV.

PHITS (version 3.28) is a multi-application, general-purpose Monte Carlo simulation program that deals with the transport of all particles from thermal energies to 1 TeV using various nuclear data libraries and nuclear reaction models (Sato et al., 2018). In PHITS, full-energy peak efficiency values are obtained using the [t-deposit] tally, a function of calculating the energy deposited in the volumes specified by the users. IAEA RGU-1, RGTh-1 and RGK-1 materials with cylindrical geometry were modeled in PHITS using s-type=1. When the s-type parameter is set to 1, the source constructs a sphere with the center coordinates (x, y, and z) and radius r in an inward direction. The HPGe detector, whose geometric parameters were given in our previous study, was modeled (Bölükdemir et al., 2021).

GESPECOR is a user-friendly code commonly used in gamma-ray spectrometry to obtain true coincidence summing and self-absorption correction factors and to calculate the full energy peak efficiency (Sima & Arnold, 2002). Similarly, the detector is modeled in GESPECOR by entering dimension information into the parts defined in the program. Then, the sample containers were modeled in cylindrical geometry. The geometric dimensions of the modeled cylinder are; the inner height is 6 cm, the inner radius is 2.5 cm, and the side wall thickness is 0.15 cm. These sizes are chosen because they are generally the most commonly used

cylinder container sizes. Since it was aimed to examine the effect of the sample container, materials with different densities, polypropylene and polymethyl methacrylate (acrylic), which are widely preferred in gamma-ray spectroscopy laboratories, were used as container materials. Density and chemical composition data of polypropylene and acrylic from NIST are given in Table 1 (NIST, 2022).

Table 1. *Densities and chemical compositions of the acrylic and polypropylene*

		Chemical composition (Fraction by weight)		
	Density (g/cm³)	H	C	O
Acrylic	1.19	0.080538	0.599848	0.319614
Polypropylene	0.9	0.143711	0.856289	-

Additionally, the bottom thickness of the sample containers was increased from 1 mm to 5 mm at 1 mm intervals, and the effect of thickness was investigated (Figure 1). IAEA RGU-1, RGTh-1 and RGK-1 materials containing radionuclides with different energies were used as samples inside the containers. To examine the change in a wide energy range, 46.5 keV, 63.3 keV, 143.8 keV, 185.7 keV, and 1001 keV peaks in RGU-1 material, 129.1 keV, 209.2 keV, 583.2 keV, 860.5 keV, and 2614.5 keV peaks in RGTh-1 material and 1460.8 keV peak, which is the only energy found in RGK-1 material, were investigated. As can be seen, the energy range of the peaks used in the radioactive analysis results in the gamma spectrometer, in the range of 46.5 keV – 2614.5 keV, has been examined.

All simulations used 10 million particles as the number of histories. The statistical error of the simulated efficiency values obtained is less than 0.1% with this particle history number.

(a)   (b)
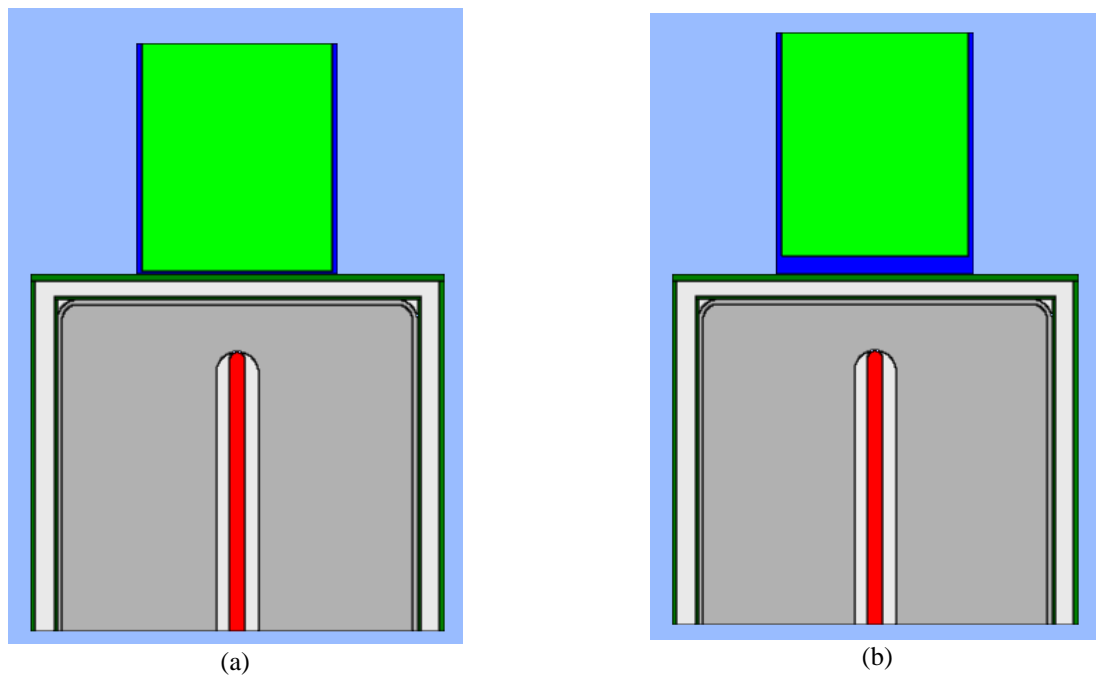
Figure 1. *Schematic representation of the sample container modeled in PHITS with*
a) *bottom thickness of 1 mm,* ***b)*** *bottom thickness of 5 mm*

3. RESULTS AND DISCUSSION

In this study, the effect of the sample container on the efficiency was focused using IAEA-RGU-1, IAEA-RGTh-1 and IAEA-RGK-1 samples with different densities and chemical compositions. This effect was investigated in detail according to the efficiency values obtained from PHITS and GESPECOR by changing the bottom thickness of the sample container materials of different densities.

The efficiency values obtained with the PHITS Monte Carlo program are given in Table 2 and 3. Since PHITS is a general-purpose Monte Carlo program, the detector and sample container are modeled as desired. Since GESPECOR is a ready-made package program, it limits the user. For example, since there is no parameter in GESPECOR to model the front edge of the germanium crystal with rounded edges as it should be, the detector is modeled as sharp-edged and the copper contact pin in the middle of the Ge crystal cannot be included in the modeling. Therefore, there may be differences between the results obtained from the two programs due to both the modeling differences and the differences in the libraries and databases they use in the background. For this reason, the results from PHITS are given in more detail.

In Table 2, the acrylic is chosen as the container materials and the efficiency change depending on the bottom thickness of the container is seen. In Table 3, polypropylene is selected as the container materials and the efficiency change depending on the bottom thickness is given similarly. When Table 2 and 3 are examined, it is seen that the efficiency values obtained with the low density (0.9 g/cm^3) polypropylene container are higher than those with the acrylic material (1.19 g/cm^3) and the acrylic material decreases the detector efficiency.

Table 2. *Effect of change in thickness of sample container material on full-energy peak efficiency (for acrylic)*

Reference material	Gamma-ray energy	Acrylic					
		1 mm	2 mm	3 mm	4 mm	5 mm	% Diff.*
RGU-1	46.5 keV	0.001564	0.001519	0.001474	0.001431	0.001386	11.4
RGU-1	63.3 keV	0.015780	0.015241	0.014724	0.014219	0.013743	12.9
RGTh-1	129.1 keV	0.062174	0.059630	0.057171	0.054845	0.052622	15.4
RGU-1	143.8 keV	0.068012	0.065165	0.062491	0.059925	0.057507	15.4
RGU-1	185.7 keV	0.068684	0.065817	0.063102	0.060509	0.058039	15.5
RGTh-1	209.3 keV	0.066299	0.063528	0.060910	0.058425	0.056053	15.4
RGTh-1	583.2 keV	0.043226	0.014570	0.039972	0.038483	0.037060	14.3
RGTh-1	860.5 keV	0.036096	0.034754	0.033507	0.032299	0.031186	13.6
RGU-1	1001.0 keV	0.033573	0.032357	0.031198	0.030087	0.029039	13.5
RGK-1	1460.8 keV	0.027147	0.026190	0.025295	0.024444	0.023640	12.9
RGTh-1	2614.5 keV	0.019522	0.018875	0.018261	0.017676	0.017109	12.4

*****% Differences between 1 mm and 5 mm thickness.

Table 3. *Effect of change in thickness of sample container material on full-energy peak efficiency (for polypropylene)*

| Reference material	Gamma-ray energy	Polypropylene					
		1 mm	**2 mm**	**3 mm**	**4 mm**	**5 mm**	**% Diff.**[*]
RGU-1	46.5 keV	0.001584	0.001547	0.001509	0.001473	0.001440	9.1
RGU-1	63.3 keV	0.015941	0.015476	0.015013	0.014571	0.014141	11.3
RGTh-1	129.1 keV	0.062684	0.060357	0.058120	0.055970	0.053924	14.0
RGU-1	143.8 keV	0.068535	0.065953	0.063493	0.061129	0.058872	14.1
RGU-1	185.7 keV	0.069155	0.066526	0.064007	0.061623	0.059326	14.2
RGTh-1	209.3 keV	0.066733	0.064188	0.061756	0.059458	0.057249	14.2
RGTh-1	583.2 keV	0.043405	0.041842	0.040341	0.038924	0.037576	13.4
RGTh-1	860.5 keV	0.036223	0.034946	0.033761	0.032622	0.031539	12.9
RGU-1	1001.0 keV	0.033682	0.032524	0.031431	0.030364	0.029355	12.8
RGK-1	1460.8 keV	0.027225	0.026302	0.025445	0.024639	0.023859	12.4
RGTh-1	2614.5 keV	0.019564	0.018931	0.018330	0.017774	0.017226	12.0

[*]**%** Differences between 1 mm and 5 mm thickness.

As the bottom thickness increases, it is seen that there is a decrease of up to 15.5% in the acrylic material and 14.2% in the polypropylene material, independently of energy.
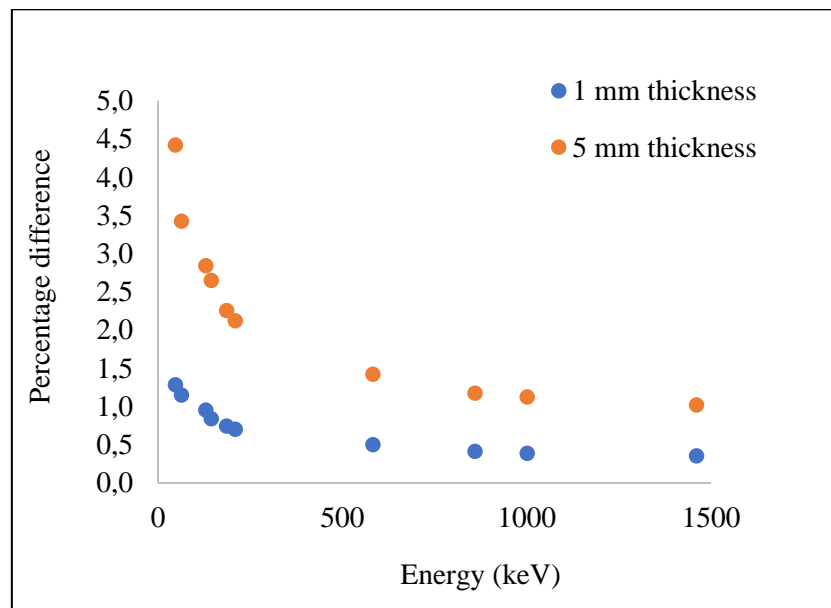
Figure 2 shows the percentage difference between acrylic and polypropylene materials at 1 mm and 5 mm bottom thickness obtained with PHITS. When polypropylene is used instead of acrylic, there is an increase of up to 0.3% - 1.2% in efficiency at 1 mm bottom thickness and up to 0.9% - 3.8% at 5 mm bottom thickness (Figure 2). While this increase is more effective, especially at low energies (46.5 keV and 63.3 keV), the material difference does not have a significant effect (<1%) on the efficiency at energies >1000 keV as the energy increases.

Similarly, in Figure 3, the percentage difference between acrylic and polypropylene materials in 1 mm and 5 mm base thicknesses obtained with GESPECOR is seen. When polypropylene is used instead of acrylic, there is an increase of up to 0.3% - 1.3% in efficiency at 1 mm bottom thickness and up to 0.8% - 4.4% at 5 mm bottom thickness (Figure 3).

It is used in some laboratories in containers made of polyethylene with a density of 1.05 g (Lépy et al., 2010). Since it has a density between the acrylic and polypropylene used in this material, it will cause a similar change. In other words, the yield values to be obtained will be between acrylic and poly, and the change depending on the thickness will be approximately 10% - 15% as in the others.
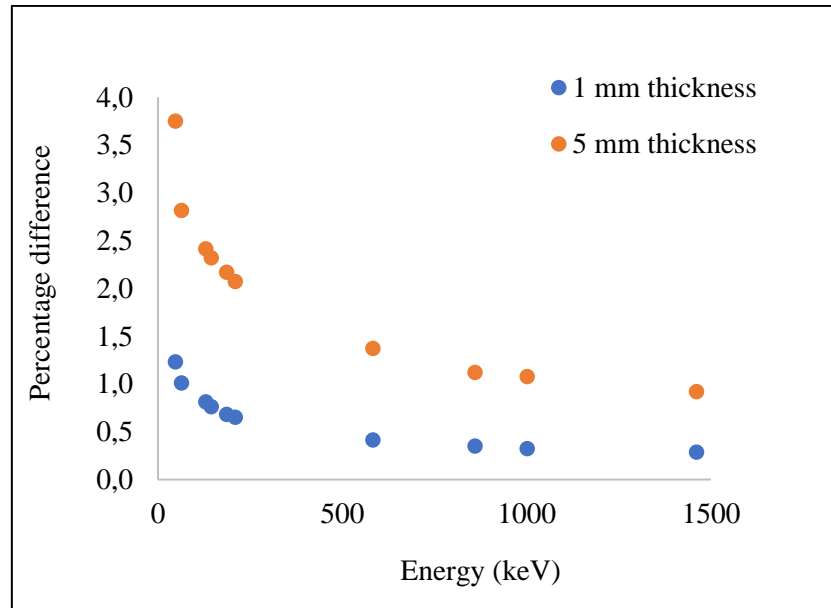
Figure 2. *Percentage difference between acrylic and polypropylene materials at 1 mm and 5 mm bottom thickness (with PHITS)*

Figure 3. *Percentage difference between acrylic and polypropylene materials at 1 mm and 5 mm bottom thickness (with GESPECOR)*

4. CONCLUSION

In this study, we examined the effect of the sample container material on the efficiency value, which is one of the most important parameters determined by the user and shows the performance of the detector. For this purpose, IAEA-RGU-1, RGTh-1 and RGK-1, which contain the most commonly used material types as container materials, acrylic and propylene, and the most radioactively analyzed uranium, thorium and potassium environmental radionuclides as samples, were modeled. The difference of <5% between the PHITS and GESPECOR programs used to obtain the efficiency values is also within acceptable limits.

According to the results obtained from both programs, it was observed that the efficiency values calculated using the sample container made of polypropylene material, which has a lower density in all energy values,

increased compared with the results obtained using the acrylic sample container under the same conditions. Additionally, as the bottom thickness of the sample container increased, the efficiency decreased.

The sample container, which is easily available in the market and preferred by gamma-ray spectroscopy laboratories, is acrylic containers with a bottom thickness of 1-3 mm. Therefore, with this study, it is seen that it would be more appropriate to choose low-density materials instead of this material and the bottom should be chosen as thin as possible. In this way, while there are many parameters that reduce and affect the efficiency, there is no extra reduction from the selected sample container material provided by the user.

CONFLICT OF INTEREST

The author declare no conflict of interest.

REFERENCES

Abd El Gawad, K., Zhijian, Z., & Hazzaa, M. H. (2020). Improving the analysis performance of gamma spectrometer using the Monte Carlo code for accurate measurements of uranium samples. *Results in Physics*, *17*, 103145. doi:10.1016/j.rinp.2020.103145

Azbouche, A., Belgaid, M., & Mazrou, H. (2015). Monte Carlo calculations of the HPGe detector efficiency for radioactivity measurement of large volume environmental samples. *Journal of Environmental Radioactivity*, *146*, 119-124. doi:10.1016/j.jenvrad.2015.04.015

Berger, M. J., Hubbell, J. H., Seltzer, S. M., Chang, J., Coursey, J. S., Sukumar, R., Zucker, D. S., & Olsen, K. (2010). XCOM: Photon Cross Section Database. Gaithersburg, MD. doi:10.18434/T48G6X

Bölükdemir, M. H., Uyar, E., Aksoy, G., Ünlü, H., Dikmen, H., & Özgür, M. (2021). Investigation of shape effects and dead layer thicknesses of a coaxial HPGe crystal on detector efficiency by using PHITS Monte Carlo simulation. *Radiation Physics and Chemistry*, *189,* 109746. doi:10.1016/j.radphyschem.2021.109746

Gilmore, G. (2008). *Practical Gamma-Ray Spectrometry.* John Wiley and Sons.

Guerra, J. G., Rubiano, J. G., Winter, G., Guerra, A. G., Alonso, H., Arnedo, M. A., Tejera, A., Martel, P., & Bolivar, J. P. (2018). Modeling of a HPGe well detector using PENELOPE for the calculation of full energy peak efficiencies for environmental samples. *Nuclear Instruments and Methods in Physics Research Section A: Accelerators, Spectrometers, Detectors and Associated Equipment*, *908*, 206-214. doi:10.1016/j.nima.2018.08.048

Hirayama, H., Namito, Y., Bielajew, A. F., Wilderman, S. J., & Nelson, W. R. (2006). The EGS5 Code System. Technical Report (SLAC-R-730) (KEK 2005-8), Stanford Linear Accelerator Center, Menlo Park, California.

Knoll, G. F. (2010). *Radiation Detection and Measurement.* John Wiley and Sons.

Lépy, M.-C., Altzitzoglou, T., Anagnostakis, M. J., Arnold, D., Capogni, M., Ceccatelli, A., De Felice, P., Dersch, R., Dryak, P., Fazio, A., Ferreux, L., Guardati, M., Han, J. B., Hurtado, S., Karfopoulos, K. L., Klemola, S., Kovar, P., Lee, K. B., Ocone, R., … Vidmar, T. (2010). Intercomparison of methods for coincidence summing corrections in gamma-ray spectrometry. *Applied Radiation and Isotopes*, *68*(7-8), 1407-1412. doi:10.1016/j.apradiso.2010.01.012

Lépy, M. C., Thiam, C., Anagnostakis, M., Galea, R., Gurau, D., Hurtado, S., Karfopoulos, K., Liang, J., Liu, H., Luca, A., Mitsios, I., Potiriadis, C., Savva, M. I., Thanh, T. T., Thomas, V., Townson, R. W., Vasilopoulou, T., & Zhang, M. (2019). A benchmark for Monte Carlo simulation in gamma-ray spectrometry. *Applied Radiation and Isotopes*, *154*, 108850. doi:10.1016/j.apradiso.2019.108850

Modarresi, S. M., Masoudi, S. F., & Karimi, M. (2017). A method for considering the spatial variations of dead layer thickness in HPGe detectors to improve the FEPE calculation of bulky samples. *Radiation Physics and Chemistry, 130,* 291-296. doi: 10.1016/j.radphyschem.2016.08.020

NIST, (2022). Composition of material. (Accessed: 01/10/2022) URL

Sato, T., Iwamoto, Y., Hashimoto, S., Ogawa, T., Furuta, T., Abe, S.-I., Kai, T., Tsai, P.-E., Matsuda, N., Iwase, H., Shigyo, N., Sihver, L., & Niita, K. (2018). Features of Particle and Heavy Ion Transport code System

(PHITS) version 3.02. *Journal of Nuclear Science and Technology*, *55*(6), 684-690. doi:10.1080/00223131.2017.1419890

Sima, O., De Vismes Ott, A., Dias, M. S., Dryak, P., Ferreux, L., Gurau, D., Hurtado, S., Jodlowski, P., Karfopoulos, K., Koskinas, M. F., Laubenstein, M., Lee, Y. K., Lépy, M. C., Luca, A., Menezes, M. O., Moreira, D. S., Nikolič, J., Peyres, V., Saganowski, P., … Yucel, H. (2020). Consistency test of coincidence-summing calculation methods for extended sources. *Applied Radiation and Isotopes*, *155*, 108921. doi:10.1016/j.apradiso.2019.108921

Sima, O., & Arnold, D. (2002). Transfer of the efficiency calibration of Germanium gamma-ray detectors using the GESPECOR software. *Applied Radiation and Isotopes*, *56*(1-2), 71-75. doi:10.1016/S0969-8043(01)00169-5

Sima, O., Arnold, D., & Dovlete, C. (2001). GESPECOR: a versatile tool in gamma-ray spectrometry. *Journal of Radioanalytical and Nuclear Chemistry*, *248*(2), 359-364. doi:10.1023/a:1010619806898

Stríbrnský, B., Hinca, R., Farkas, G., Petriska, M., & Slugeň, V. (2022). Modeling and Optimization of HPGe Detector GC0518 Using MCNP5 Code. *Radiation Protection Dosimetry*, *198*(9-11), 704-711. doi:10.1093/rpd/ncac123

Trang, L. T. N., Chuong, H. D., & Thanh, T. T. (2021). Optimization of p-type HPGe detector model using Monte Carlo simulation. *Journal of Radioanalytical and Nuclear Chemistry*, *327*(1), 287-297. doi:10.1007/s10967-020-07473-2

Uyar, E., & Bölükdemir, M. H. (2022). The effect of front edge on efficiency for point and volume source geometries in p-type HPGe detectors. *Nuclear Engineering and Technology*, *54*(11), 4220-4225. doi:10.1016/j.net.2022.06.009

Yücel, H., Solmaz, A. N., Köse, E., & Bor, D. (2010). Methods for spectral interference corrections for direct measurements of ^{234}U and ^{230}Th in materials by gamma-ray spectrometry. *Radiation Protection Dosimetry*, *138*(3), 264-277. doi:10.1093/rpd/ncp239

Engineering Properties of Lightweight Mortars Containing Wood Waste Particles

Niyazi Uğur KOÇKAL[1*] (ID) H. Erdem ÇAMURLU[2] (ID)

[1]Civil Engineering Department, Akdeniz University, Antalya, Türkiye
[2]Mechanical Engineering Department, Akdeniz University, Antalya, Türkiye

Keywords	Abstract
Lightweight Mortar Lightweight Aggregate Wood Waste Particle	Utilization of wood waste particles (WWP) is important for environmental and economic concern. This study focuses on the behavior of mortars having WWP with various amounts. Incorporation of WWP brings about the advantages such as decrease in the mass and cost of the mortar. In the present study, the proportions of the wood waste particles replacing the crushed sand in the mortars by volume were 0, 10, 20, 30 and 40 %. Physical, mechanical and capillary absorption properties have been investigated. In addition, microstructure of the mortars has been examined with optical microscope. As compared to control specimen, dry bulk density decreased from 2.2 to 1.5 kg/m^3, apparent porosity increased about 2 folds, and water absorption increased about 4 folds, for sample in which 40 % of crushed sand was replaced with WWP. Mechanical values reduced with increasing WWP amount. On the other hand, during compressive and flexural strength tests, samples containing WWP presented a gradual decrease in strength, thus they exhibited a more ductile behavior.

1. INTRODUCTION

Some wastes emerging from industrial applications remain unutilized and cause storage problems, or they are used inefficiently in some fields such as filling material, etc. There are attempts that seek alternative ways to exploit these materials effectively (Akhavan Kazemi et al., 2015; Gupta et al., 2015; Nazmul Huda et al., 2016; Mostonejad et al., 2017; Dhinakaran & Sreekanth, 2018; Gulmez & Kockal, 2021). However, most of them require energy and cost due to many additional operations such as burning at high temperatures or penetrating into alkali solutions to improve binding abilities. Some of these industrial wastes are used in the construction sector, which brings about solutions for environmental and economic problems. Wood waste is one of the industrial wastes which can be used as a component of construction materials especially for energy efficiency. The huge quantity of wastes formed as a result of the wood treating processes in numerous countries causes difficulties for their handling. This may actually be an opportunity for the utilization of these wood wastes as a construction material (Udoeyo et al., 2006).

Manufacturers of wood products and furniture produce chips and sawdust. They are generated as a result of furniture machining operations in which the wood is cut, drilled or milled for obtaining the final article. The wood dust particles are accumulated by filtering. The wood waste is mainly utilized in the form of ash that is formed by combusting the waste sawdust or wood shavings.

There are many investigations conducting experimental studies on concrete containing wood waste ash (Udoeyo et al., 2006; Sashidhar & Rao, 2010). In the study of Udoeyo et al. (2006) wood waste ash (WWA),

which was obtained from sawdust and wood shaving, was added into concrete at ratios of 0, 5, 10, 15, 20, 25, and 30% by weight of cement. The mechanical and physical properties of the matrix were examined. Sashidhar and Rao (2010) performed durability studies on concrete with wood ash additive. It was found that 28 day cube compressive strength decreases with increasing WWA content from 0 to 30%.

However, production of ash requires high energy for combustion, and therefore it is highly expensive process. Thus, attempts have been made to recycle wood waste as aggregate in concrete in recent years (Taoukil et al., 2013; Gloria & Filho, 2016; Thandavamoorthy, 2016; Akkaoui et al., 2017;). In the study of Thandavamoorthy (2016), concretes, having wood aggregate 0, 15, 20 and 25 % instead of crushed stone, were prepared. The mix proportion was 1:1.26:2.76 and water/binder was 0.45. Addition of wood aggregate generally resulted in a reduction in compressive strength, however, there was a slight increase in compressive and indirect tensile strength values when 15% wood particle was used. The increase in wood aggregate was seen to increase acid and alkali attack and water absorption rates. In a comprehensive review by Momoh and Osofero (2020), utilization of oil palm trunk fibers was stated to increase the strength of cement composites. This was attributed to the high intrinsic strength of the fibers.

Some of the studies in the literature on utilization of wood waste aggregate focus on the thermal properties of the obtained concretes. In the study of Gloria and Filho (2016), wood shaving/cement ratio was changed in 1:0.5 and 1:3.0 ratio. Thermal conductivity was seen to decrease down to 0.06 from 0.535 W/mK, with the increase in the wood shaving/cement to 1:0.5 from 1:3.0. On the other hand, compressive strength values for the respective samples were 0.44 and 15.97 MPa. In the study of Taoukil et al. (2013), wood shavings and sawdust were utilized in order to lighten the concrete and to alter thermal properties. It was seen that with 10 % addition of sawdust or shavings, thermal conductivity value was about half of that observed in control sample. On the other hand, porosity increased and bulk density decreased.

In the present study, mortar samples were produced by adding wood waste particles (WWP) in order to reduce the amount of crushed sand in mortar. This composite material can be used in panels that function as partitions and in applications where lightness should be at the forefront. The advantages are believed to be three-fold. First, a waste product is utilized and its negative effects on storage and cost of its elimination are decreased. Secondly, the substitution of WWP with crushed sand reduces the weight of the mortar, which brings about a structural advantage. Thirdly, by this means, the cost of the mortar decreases. This is expected to decrease the density of the mortar, resulting in improvement of thermal insulation properties. The properties of WWP containing mortar samples were compared with those of the control samples which had only crushed sand as aggregate.

2. MATERIAL AND METHOD

Binding material used in mortar was CEM I 42.5R. Specific gravity and Blaine specific surface of cement are 3.13 and 3610 cm^2/g, respectively. Table 1 represents the constituents of the cement. Fine aggregate was calcareous sand provided from Burdur region, Turkey. Wood waste particles were shavings collected from a local manufacturer of wood products and furniture. Gradation curves of calcareous sand and wood waste particles are shown in (Figure 1) SSD state specific gravity and fineness modulus of waste particle were 1.1 and 3.43, respectively. The fine aggregate was crushed sand with a specific gravity, absorption, and fineness modulus of 2.71, 1.7% and 2.80, respectively. Some properties of wood waste and crushed sand are given in Table 2.

The proportions of the waste particles replacing with the crushed sand by volume were 0%, 10%, 20%, 30%, 40% and the notations for those specimens were CS, WWP10, WWP20, WWP30, WWP40, respectively. All aggregates were introduced into the mix in saturated surface dry (SSD) state. The water/cement and total cement values were maintained the same, as 0.60 and 300 kg/m^3, respectively.

Table 1. *Chemical composition of the cement*

Oxides	CaO	SiO$_2$	Al$_2$O$_3$	Fe$_2$O$_3$	MgO	SO$_3$	Loss on Ignition
Percentages	63.80	21.10	4.07	3.61	1.08	2.40	2.74
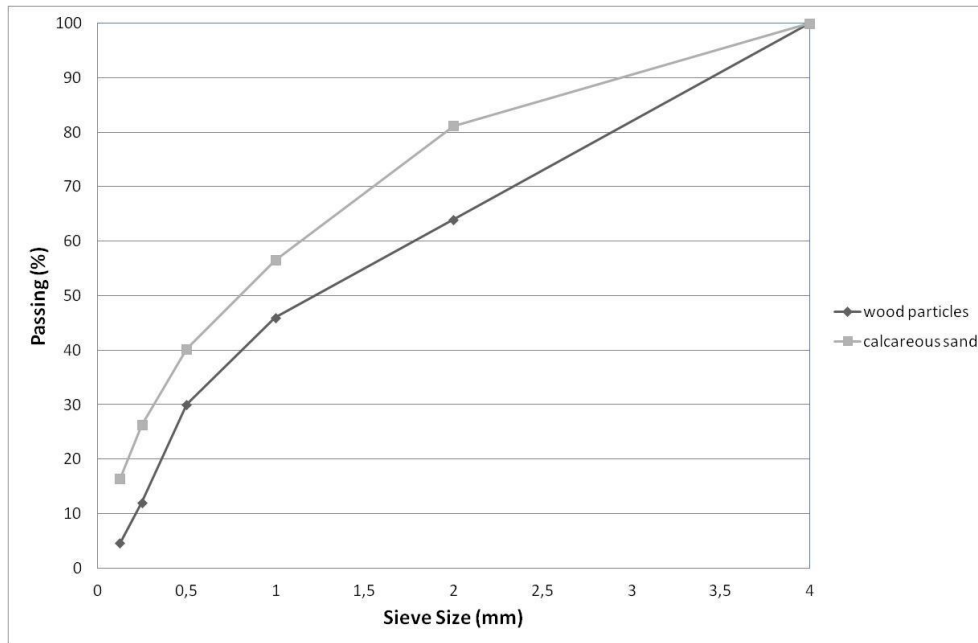
Figure 1*. Gradation of calcareous sand and wood particle aggregates*

Table 2. *Some properties of aggregates used in the study*

Aggregates	Specific Gravity (g/cm^3)	Rodded Bulk Density (g/dm^3)	Loose Bulk Density (g/dm^3)	Rodded Void Ratio (%)	Loose Void Ratio (%)
CS	2,71	1746	1611	35,4	40,4
WWP	1,1	113	93	89,7	91,6

Prismatic specimens 40x40x160 mm in size were cast according to ASTM C192. Mixtures were cast in layers. The specimens were demoulded after 1 day and all mortars were kept in a tank to be cured for 7 and 28 days before testing.

Consistency, bulk density, water absorption, porosity, compressive strength, flexural strength, capillary absorption coefficient were determined. Compressive and flexural strength values of the control sample and samples containing WWP were determined by a Shimadzu Autograph 50kN universal tester, with a rate of 0.5 mm/s. The porosity values were determined on 40x40x160 mm^3 prismatic specimens according to the procedure described in ASTM C 642 by the equation given below:

$$P = [(W2 - W1)/(W2 - W3)] \times 100 \tag{1}$$

P is the porosity (%); W1 is the mass of oven-dried sample in air (g), W2 is the mass of surface-dry sample in air (g) and W3 is the mass of surface-dry sample in water (g).

3. RESULTS AND DISCUSSION

Produced samples were characterized in terms of density and porosity, water absorption and capillarity, microstructure; split tensile, compressive and flexural strength.

3.1. Density and Porosity

Fresh unit weight values of the obtained specimens are presented in (Figure 2) Fresh unit weight values of the samples were found to decrease with the increase in the WWP content. It can be seen that fresh unit weight of control specimen was 2250 kg/m^3, on the other hand fresh unit weight of the WWP40 specimen was 1750 kg/m^3.

Dry bulk density values presented a similar trend with that of fresh unit weight data, as shown in (Figure 3) It was decreasing with increasing WWP content of the samples. Dry bulk density of control sample was 2.1 kg/m^3 whereas that of the WWP40 sample was 1.5 kg/m^3. Dry bulk density values of the samples were similar after 7 days and 28 days. SSD bulk density values of the samples presented a similar trend with that of dry bulk density data, as shown in (Figure 4) They were about 15 % higher than dry bulk density values. Gloria and Filho (2016) used wood shavings in cement and they also observed a decrease in the density, as a result of the increase in the amount of wood shavings in cement. Sadiku (2015) also revealed that wood particles decreased the density of wood-cement composites.

Apparent porosity values of the samples exhibited an opposite trend to that was observed for fresh unit weight and dry bulk density. Apparent porosity was found to increase with the increase in WWP content, as shown in (Figure 5) Apparent porosity was 15 % in the control sample and it was slightly over 35 % in the WWP40 sample. In all the samples, apparent porosity values after 7 days were slightly higher than that after 28 days.

3.2. Water Absorption and Capillarity

Water absorption and coefficient of capillarity values are presented in Figure 6 and Figure 7, respectively. Water absorption and coefficient of capillarity values of the samples exhibited a similar trend to that was observed apparent porosity values. Differences in porosity of mortars can be due to the ingredients selected for recipe also affecting quality of interfacial transition zone (Kockal 2013; 2015; 2016). Water absorption and capillarity coefficient was found to increase with the increase in WWP content. They were 7 % and 0.0007 cm/s$^{1/2}$, respectively, for the control sample and they were about 25 % and 0.0045 cm/s$^{1/2}$, respectively, for the WWP40 sample. In all the samples, water absorption and coefficient of capillarity values after 7 days were higher than those after 28 days. This can be attributed to the fact that water penetrable voids and capillary pores decreased due to the enhancement of microstructural properties of cement paste matrix resulting from continuing hydration. However, in contrast to water absorption of WWP40 sample, which is observed to decrease by time (Figure 6), capillarity of these samples did not change within time (Figure 7).
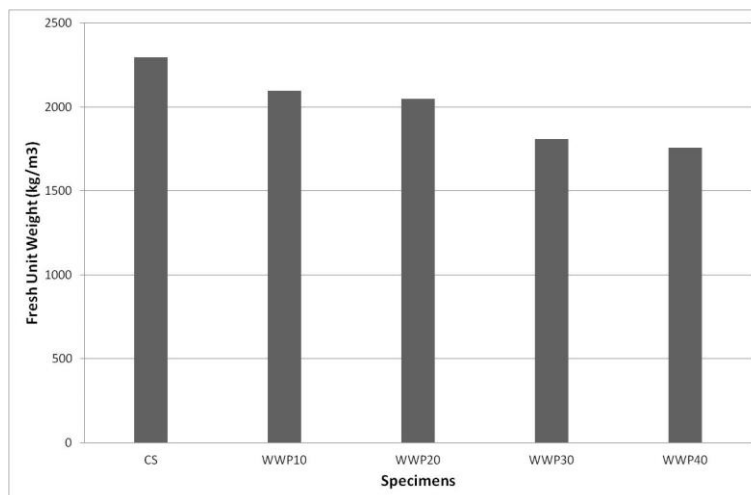
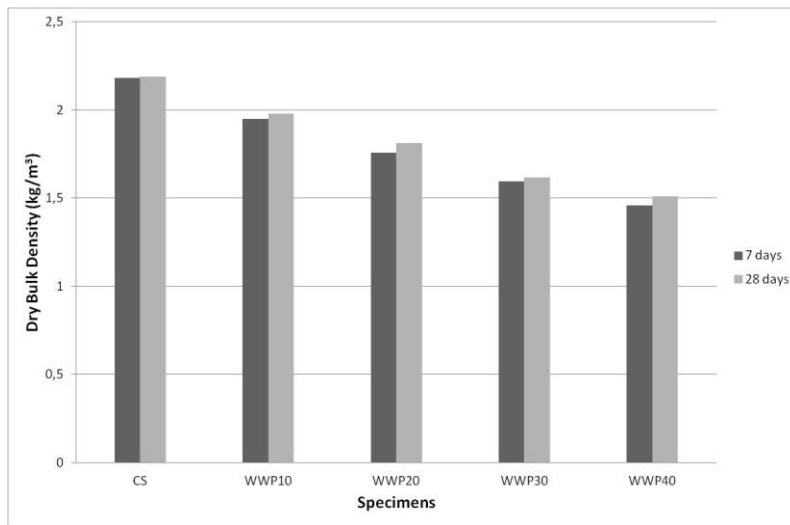***Figure 2.*** *Fresh unit weight values of the specimens*

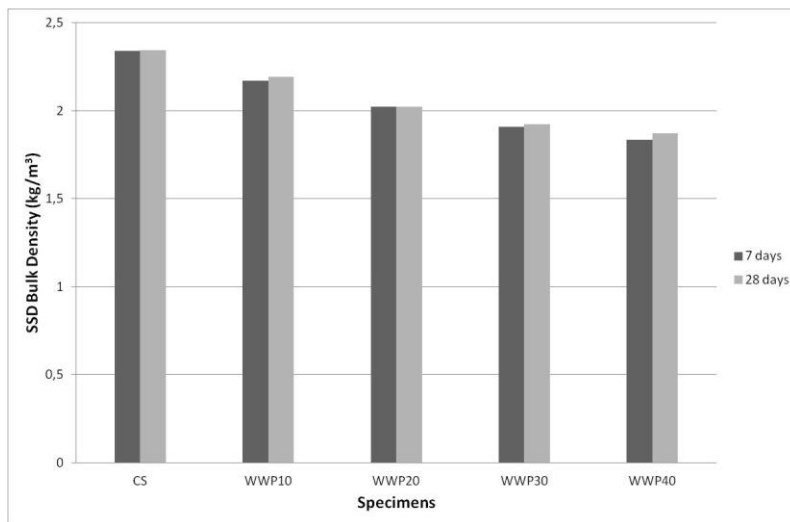***Figure 3.*** *Dry bulk density values of the specimens*

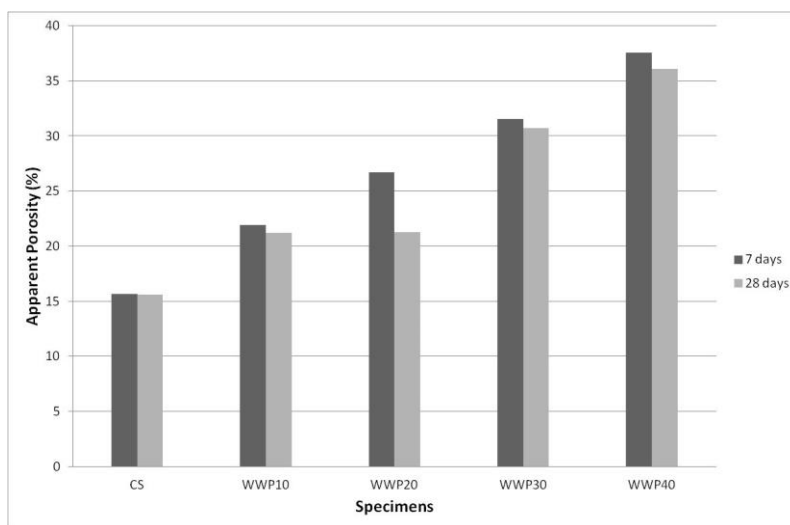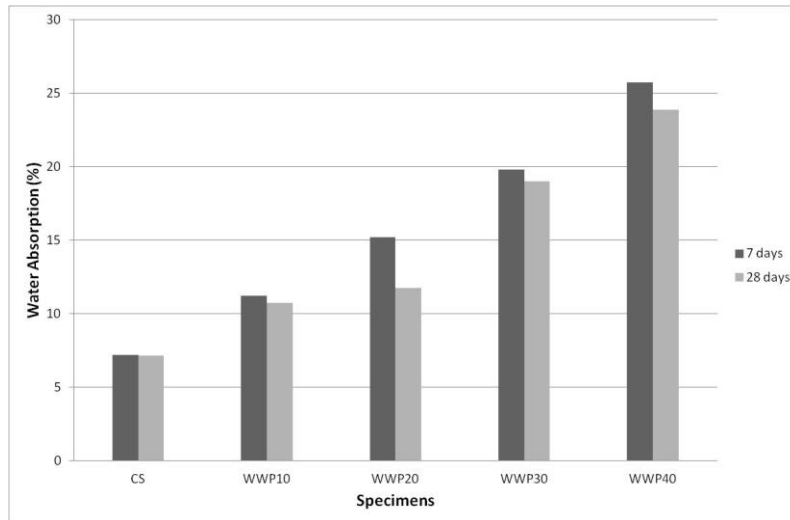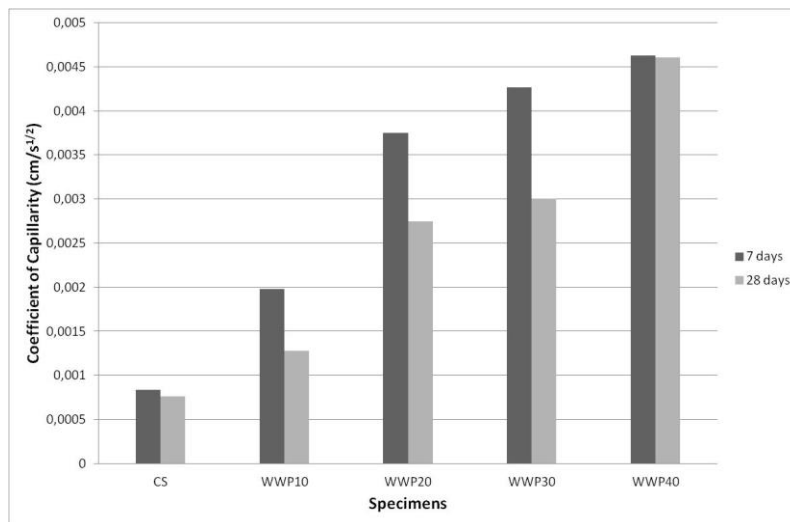***Figure 4****. SSD bulk density of the specimens*

***Figure 5.*** *Apparent porosity values of the specimens*

Figure 6. *Water absorption values of the specimens*

Figure 7. *Coefficient of capillarity values of the specimens*

3.3. Microstructure

Microstructural illustrations of the specimens are presented in (Figure 8) It can be observed that the aggregates are homogenously distributed in the microstructure of control sample and there is small amount of porosity (Figure 8a). Samples containing 20 % and 40 % WWP are presented in (Figure 8b, 8c), respectively. The yellowish-brown fractions in these images are WWP. The amount of these particles can be seen to increase with the increase in the WWP amount in the mortar. The size of the WWPs is similar to the size of the calcareous sand aggregates. They are 1-3 mm in length and about 0.5 mm in thickness. They are seen to have acicular morphology and mostly needle-like shape. Sizes pronounced here satisfy the data given in (Figure 1) which illustrates the particle size distribution of aggregates. It can be inferred from the cross-sectional images of entire body (representative typical images are given in (Figure 8) that porosity in cement paste matrix among the aggregate particles increases with the increase in the WWP amount. This finding is in accordance with the results of the porosity and capillarity test, which were given in the previous sections; and they are also in accordance with the results of the mechanical tests, which will be presented in the following sections. The reason of increasing porosity with increase in WWP amount may be the seepage of water from WWP in saturated surface dry condition into the cement paste, leading to the rise in water-cement ratio.
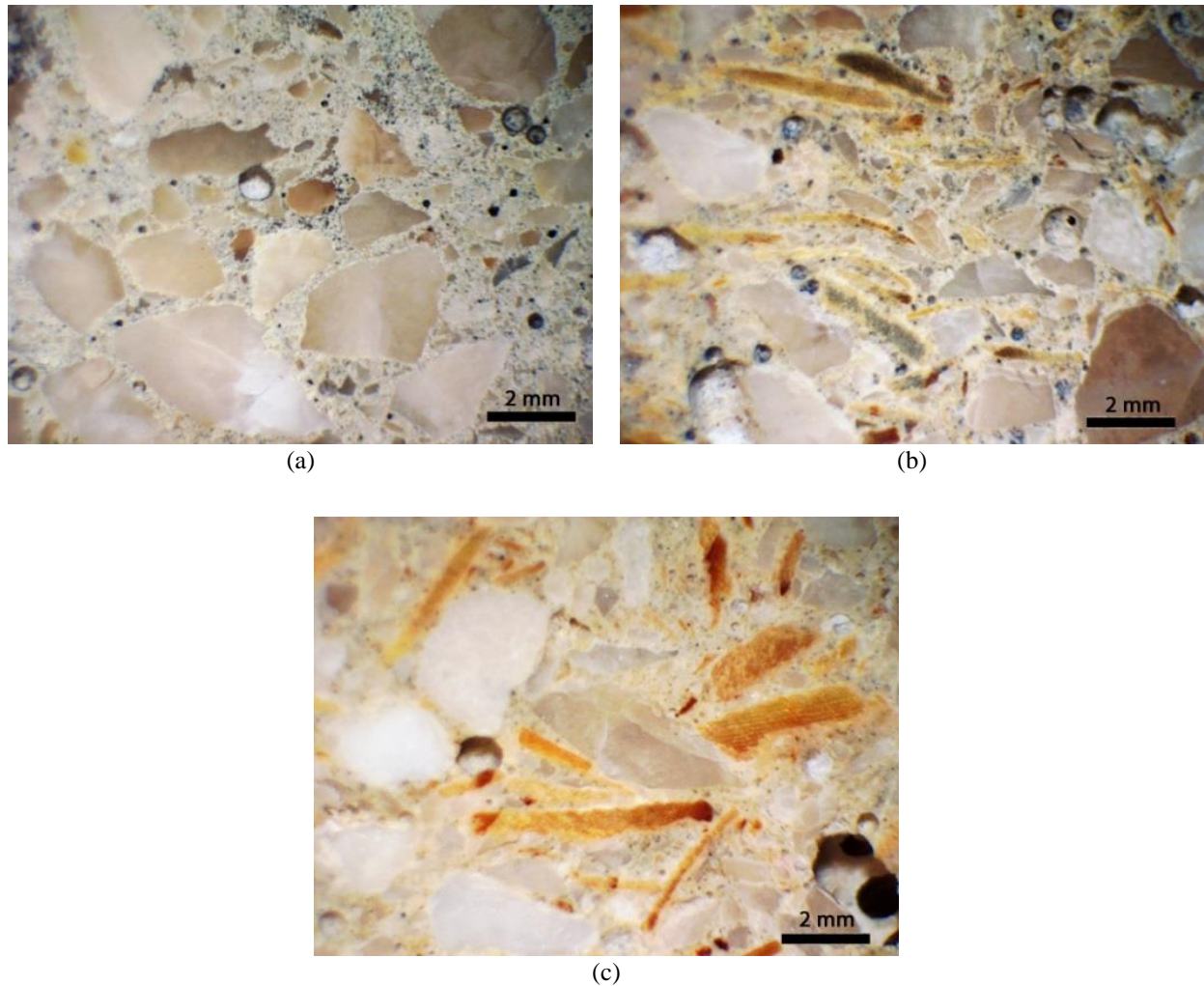
Figure 8. Optical micrographs of the a) control sample, and samples containing b) 20 % and c) 40 % WWP

3.4. Compressive Strength

The compressive strength values of the control specimen and specimens containing WWP are presented in Figure 9. The control specimen had 27 MPa after 7 days and 38-40 MPa after 28 days. The compressive strength values of WWP mortars were smaller than that of the CS mortar and they showed a reduction in compressive strength with the rise in the WWP amount. WWP 40 sample had a compressive strength of 5 MPa after 7 days and 6 MPa after 28 days. The stress-strain graphs of the control sample, WWP20 and WWP40, which were obtained after 28 days, are given in Figure 10. It can be seen that there was a sharp decrease of stress in the control sample after fracture. On the other hand, samples containing WWP present a gradual decrease in stress and therefore they exhibit a tougher behavior. In the studies of some other researchers (Bdeir, 2012; Mohammed et al., 2014; Thandavamoorthy, 2016), compressive strength values were also seen to decrease with the increase in the wood aggregate addition. They observed a slight increase in the compressive strength when 15 % wood waste was used. Gloria and Filho (2016) used wood shavings in cement and they reported a reduction in the compressive strength with the rise in the amount of wood shavings. If the wood in the mortar is exposed to moisture and water for a long time, it may rot. On the contrary, there is no decay in the short term. If the mortar samples are maintained in dry condition and/or insulated, wood rot is not observed. Considering that the wood in the mortar does not contribute positively to the strength, additional strength reductions are not expected after rotting.

3.5. Flexural Strength

Flexural strength values of the control sample and samples containing WWP, which were determined after 7 days and 28 days, are presented in Figure 11. The flexural strength values of the control sample were 5.5 and

7 MPa after 7 and 28 days, respectively. The flexural strength values were seen to decrease with the increase in the WWP contents in the concretes. The flexural strength of WWP40 sample was 2 MPa. The reduction in the flexural strength with the rise in the WWP amount is an expected result. Since the WWP act as voids in the structure of the concrete, in which crack initiation is possible.

The flexural stress vs. strain graphs of the control sample and of the WWP20 and WWP40 samples are presented in Figure 12. It can be seen that after fracture, stress decreased abruptly in the control sample. However, stress decreased gradually after fracture of the WWP20 and WWP40 samples. This can be taken as an indication the toughness and ductility of the WWP samples was higher than the control sample. In the study of Thandavmoorthy (2016), flexural strength values were also seen to decrease with the increase in the wood aggregate addition. In their study, shredded wood waste was utilized. They observed a similar compressive strength when 15 % wood waste was used, as compared to control sample. Corinaldesi et al. (2016) reported that the replacement of sawdust with wood shavings at a similar ratio resulted in a decrease in mechanical strengths of about 30%. The reason could also be the geometry of wood particles which were flat and thin.
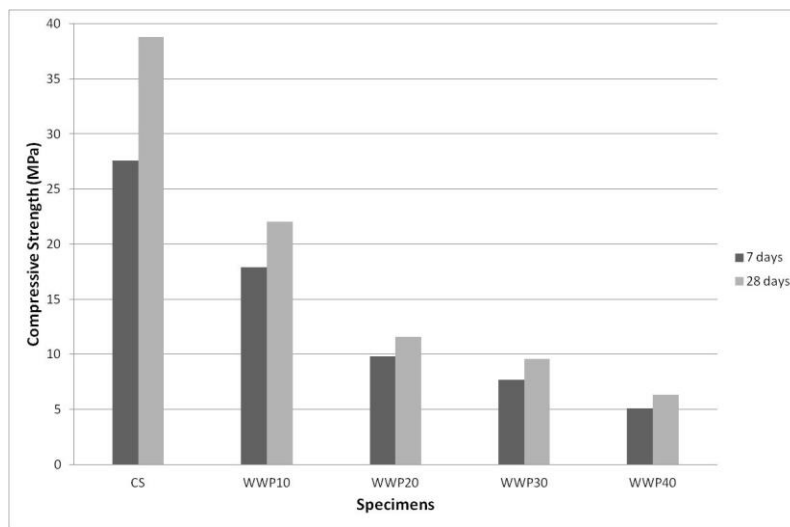

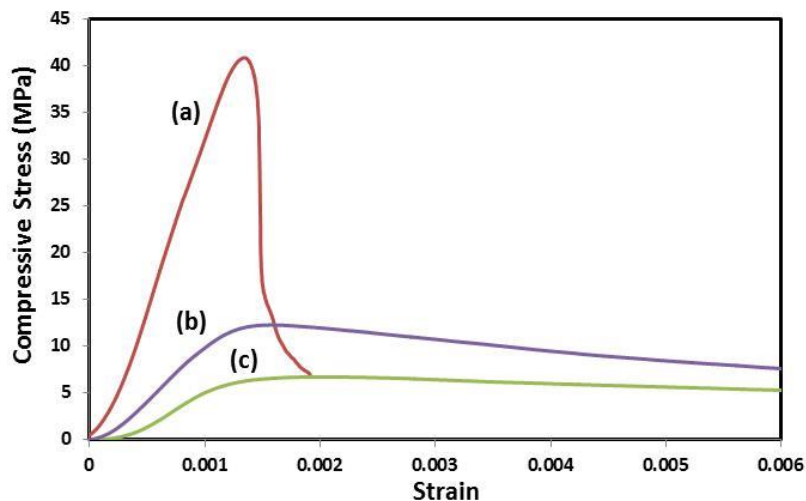***Figure 9.*** *Compressive strength values of the specimens*

Figure 10. *Compressive stress-strain plots of **a)** control sample, **b)** WWP20, **c)** WWP40*
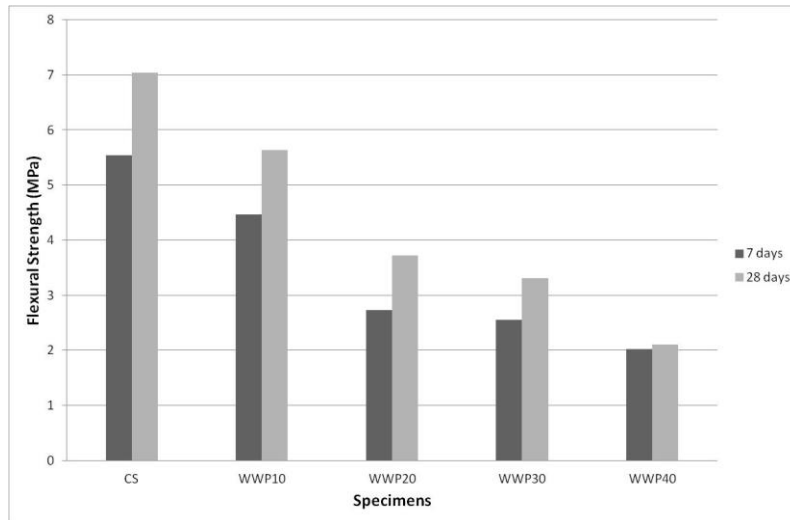
Figure 11. *Flexural strength values of the specimens*
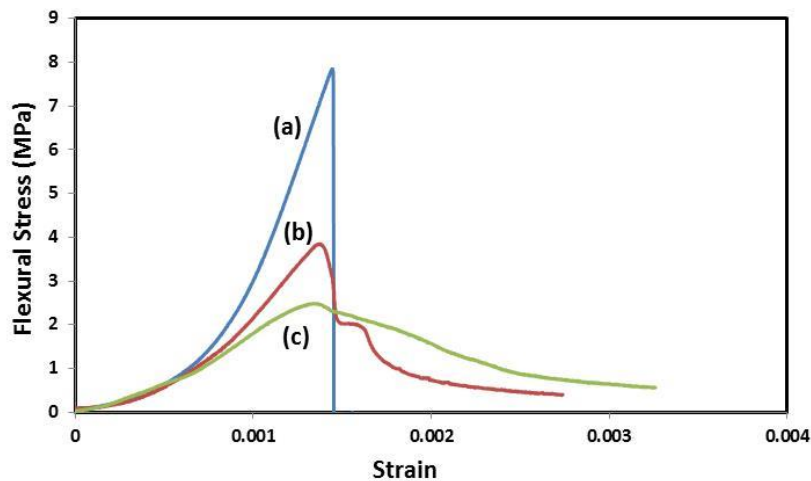

Figure 12. *Flexural stress-strain plots of **a)** control sample, and samples containing*
***b)** 20 % WWP, **c)** 40 % WWP*

4. CONCLUSION

Mortars having lower weight and lower cost were successfully produced by utilizing a wood waste in place of crushed sand. Dry bulk density decreased about 30%, whereas apparent porosity and water absorption increased significantly as a result of 40% replacement of crushed sand with WWP the mortar. Compressive and flexural strength values decreased with increasing WWP amount. However, during compressive tests, samples containing WWP presented a gradual decrease in strength, indicating their higher ductility.

ACKNOWLEDGEMENTS

CONFLICT OF INTEREST

The authors declare no conflict of interest.

REFERENCES

Akhavan Kazemi, K., Eren, O., & Rezaei, A. R. (2015). Some mechanical properties of normal and recycled aggregate concretes. *Sci Iran A*, *22*(6), 1972-1980.

Akkaoui, A., Caré, S., & Vandamme, M. (2017). Experimental and micromechanical analysis of the elastic properties of wood-aggregate concrete *Construction and Building Materials*, *134*, 346-357. doi:10.1016/j.conbuildmat.2016.12.084

Bdeir, L. M. H. (2012). Study Some Mechanical Properties of Mortar with Sawdust as a Partially Replacement of Sand. *Anbar J Eng S.*, *5*(1), 22-30.

Corinaldesi, V., Mazzoli, A., & Siddique, R. (2016). Characterization of lightweight mortars containing wood processing by-products waste. *Construction and Building Materials*, *123*, 281-289. doi:10.1016/j.conbuildmat.2016.07.011

Dhinakaran, G., & Sreekanth, B. (2018). Physical, mechanical, and durability properties of ternary blend concrete. *Sci Iran A*, *25*(5), 2440-2450. doi:10.24200/sci.2017.4210

Gloria, M. Y. R., & Filho, R. D. T. (2016, April 27-29). *Influence of the Wood Shavings/Cement Ratio on Lightweight Wood Shavings-Cement Based Composites*. In: Proceedings of the 6th Amazon & Pacific Green Materials Congress and Sustainable Construction Materials LAT-RILEM Conference (pp. 365-374), Colombia.

Gulmez, N., & Kockal, N. U. (2021). Effects of iron powder on properties of geopolymers subjected to different curing regimes. *Indian J Eng Mater S.*, *28*(4), 393-408.

Gupta, T., Sharma, R. K., & Chaudhary, S. (2015). Influence of waste tyre rubbers on strength and carbonation of concrete. *Sci Iran A*, *22*(4), 1481-1489.

Kockal, N. U. (2013). Effects of elevated temperature and re-curing on the properties of mortars containing industrial waste materials. *Iran J Sci Technol.*, *37*(C1), 67-76.

Kockal, N. U. (2015). Behavior of mortars produced with construction wastes exposed to different treatments. *Indian J Eng Mater S.*, *22*(2), 203-214.

Kockal, N. U. (2016). Investigation about the effect of different fine aggregates on physical properties of mortars. *Construction and Building Materials*, *124*, 816-825 doi:10.1016/j.conbuildmat.2016.08.008

Mohammed, B. S., Abdullahi, M., & Hoong, C.K. (2014). Statistical models for concrete containing wood chipping as partial replacement to fine aggregate. *Construction and Building Materials*, *55*, 13-19. doi:10.1016/j.conbuildmat.2014.01.021

Momoh, E. O., & Osofero, A. I. (2020). Recent developments in the application of oil palm fibers in cement composites. *Front. Struct. Civ. Eng.*, *14*(1), 94-108. doi:10.1007/s11709-019-0576-9

Mostonejad, D., Noorpour, S., Noorpour, M., Karbati Asl, R., Sadeghi Balkanlouc, V., & Karbati Asl, A. (2017). Effects of petrochemical wastes on the properties of concrete. *Sci Iran A*, *24*(3), 1017-1026. doi:10.24200/sci.2017.4085

Nazmul Huda, Md., Bin Jumat, M. Z., Saiful Islam, A. B. M., & Rahman Soeb, M. (2016). Influence of palm oil factory wastes for green lightweight concrete. *Revista de la Construcción (Journal of Construction)*, *15*(3), 133-139. doi:10.4067/S0718-915X2016000300013

Sashidhar, C., & Rao, H. S. (2010, August 25-27). *Durability Studies on Concrete with Wood Ash Additive*. In: Proceedings of the 35th Conference on Our World in Concrete & Structures (pp 1-6), Singapore.

Sadiku, N. A. (2015). Utilizing wood wastes as reinforcement in wood cement composite bricks. *J Fac Forestry Istanbul University*, *65*(2), 31-37. doi:10.17099/jffiu.80051

Taoukil, D., El Bouardi, A., Sick, F., Mimet, A., Ezbakhe, H., & Ajzoul, T. (2013). Moisture content influence on the thermal conductivity of wood–concrete composite. *Construction and Building* Materials, 48, 104-115. doi:10.1016/j.conbuildmat.2013.06.067

Thandavamoorthy, T. S. (2016). Wood Waste as Coarse Aggregate in the Production of Concrete. *Eur J Environ Civ Eng.*, *20*(2), 125-141. doi:10.1080/19648189.2015.1016631

Udoeyo, F. F., Inyang, H., Young, D. T., & Oparadu, E. E. (2006). Potential of Wood Waste Ash as an Additive in Concrete. *J Mater Civil Eng.*, *18*(4), 605-611. doi:10.1061/(ASCE)0899-1561(2006)18:4(605)

Effects of Different Culture Media Compositions on *In Vitro* Micropropagation from Paradox Walnut Rootstock Nodes

Cem DİRLİK[1] (ID) Hacer KANDEMİR[2] (ID) Nurberat ÇETİN[2] (ID) Senem ŞEN[2] (ID) Begüm GÜLER[3*] (ID) Aynur GÜREL[4] (ID)

[1]Department of Biotechnology, Ege University Graduate School of Natural and Applied Sciences, İzmir, Türkiye
[2]Department of Bioengineering, Ege University Graduate School of Natural and Applied Sciences, İzmir, Türkiye
[3]Genetic and Bioengineering Department, Kırşehir Ahi Evran University Faculty of Engineering and Architecture, Kırşehir, Türkiye
[4]Department of Bioengineering, Ege University Faculty of Engineering, İzmir, Türkiye

Keywords	Abstract
Micropropagation Walnut *Juglans regia* L. Paradox *In vitro*	The aim of this study is to establish an effective protocol for *in vitro* micropropagation from node explants of the 'Paradox' (*Juglans regia* x *J. hindsii*) rootstock. In the first stage of the study, the node explants were cultured in semi-solid media after being exposed to different sterilization methods. The most effective sterilization method was observed as ST2 with the lowest darkening rate (4 %). According to the results, SP4 medium provided the highest number of shoots per unit explant (1.05 shoots/explant) and 100 % shoot formation, SP2 medium provided the best mean shoot length (1.6 cm) and the mean number of nodes per unit explant (7.95 nodes/explant). Best root induction was provided from ½ Modified MS medium containing 4 mg/L IBA with 30 g/L sucrose. For root induction explants were retained under dark conditions for 7 days at 24±2ºC. In order to ensure root formation and elongation, shoot explants with root induction cultured in a 16-hour photoperiod (3500 lux) for 21 days in different nutrient media containing 2.4 mg/L Gelrite, hormone-free and mixed with vermiculite (1:1 v/v) and was rooting rate is 45.45 % in ¼DFe medium.

1. INTRODUCTION

Systematically, walnut is included in Juglandales (Walnuts) order, Juglandaceae (Walnuts) family, and Juglans (Walnut) genus. Walnut has 2n=32 chromosomes and 25 species, and the most important and first thing that comes to mind is *Juglans regia* L.. This species is known in the world as "Anatolian walnut", "Persian walnut" and "English walnut" and is widely cultivated especially for its fruit (Şen, 2011). Walnuts are consumed a lot, especially in the form of dried fruit. The bark, fruit peel, green fruit peel and leaf parts of the walnut plant are widely used in the pharmaceutical and cosmetic industry, and as a dyestuff in the carpet and textile industry (Yiğit et al., 2009).

The important walnut producing countries in the world are China, the United States of America, Iran and Turkey. All walnut production in the USA is obtained from closed walnut orchards established with standard varieties (Açıksöz, 2020). While our country was at the forefront of walnut production in the world in the 1970s, it fell to the second place in the 1980s, the third in the 1990s, and the fourth in the 2000s, and even the amount of walnuts we produce has become unable to meet the needs of our country (Aslansoy, 2012). The biggest obstacles to walnut production in our country are; high pH of the soil, walnut anthracnose disease and

*Corresponding Author, e-mail: begüm.guler@ahievran.edu.tr

indoor worm. Therefore, it is necessary to expand the production and plantations of materials resistant to these stress factors in Turkey (Budak, 2010).

As with other fruit species, propagation by seed in walnuts is not a preferred propagation method due to genetic expansion, except for rootstock or seedlings and breeding studies. For this reason, the most frequently used reproduction method is grafting (Budak, 2010). However, grafting processes are dependent on many factors, which reduces the chance of success and alternative methods are sought (Er et al., 2017). Plant tissue culture allows intensive production of desired clones with its advantages. Therefore, it becomes an important option against traditional propagation methods such as seed, cutting, branching and grafting in various plant species. However, micropropagation of fruit species and especially nut species is more difficult than micropropagation of herbaceous plants. For this reason, it is extremely important to choose the appropriate physiological period and explant, to overcome the harmful effects of tannin and other toxic compounds in cultures, to provide an acceptable shoot reproduction rate, to obtain rooted shoots in the micropropagation of selected hard-shelled fruit clones (Şirin, 2014).

Plant tissue culture is a proven method that has long been used to establish and maintain a variety of different plant species. Plant tissue culture techniques cover the methods used to obtain the new plant product aimed the study from cell, tissues and organs transferred to a sterile nutrient medium (Gürel et al., 2013). Plant tissue culture consists of cutting plant tissues and their growth on a nutrient medium (Kumar & Loh, 2012). For this reason, the most important step in plant tissue cultures is the sterilization process (Kyte, 1987). Contaminations may originate from exogenous and endogenous microorganisms. Plant cultures can be contaminated by a wide variety of bacterial, fungal and viral organisms, many of which are species-specific (Varghese & Joy, 2016). These contaminants may show themselves immediately, or they may not show their effects in any way for a long time (Ray & Ali, 2016). Approximately 20-55 % of contamination losses in *in vitro* plant cultures are due to bacteria (Tekielska et al., 2019). It is aimed to remove invading microorganisms from the environment with the sterilization process applied during tissue culture studies. In studies carried out with plant tissue collected from the field or with the possibility of microbial contamination, surface sterilization with additional surfactant is required in addition to ethyl alcohol and/or bleach. Concentration and exposure time are determined experimentally depending on the type of explant used (Leelavathy & Sankar, 2016). Fu et al. (2003) in their study on *Carya illinoensis* (pecan) plant, the most appropriate sterilization method is to first soak it in 70 % EtOH and mix it in 0.2 % $HgCl_2$ (with the addition of a few drops of Tween 20) for 15 minutes and then rinsing with sterile distilled water 10 times. They also found that adding penicillin and streptomycin to the nutrient medium prevented contamination (Fu et al., 2003). Leal et al. (2007) stated that internal contamination is an important problem in micropropagation experiments with explants taken from mature walnut trees. In addition, they stated that darkening as a result of oxidation in the tissues during the surface sterilization stage caused a great reduction in shoot formation and this problem could be overcome by using young shoot explants that are more resistant to disinfection but are semi-woody (Leal et al., 2007).

Vahdati et al. (2009) stated that the success of tissue culture depends on the chemical composition of the culture medium and the micropropagation of the walnut is partially limited by the lack of a suitable culture medium. It was thought that the minerals present in similar proportions to those found in walnut seeds may provide an optimum environment for shoot micropropagation. The mineral composition of the seeds of five walnut cultivars 'Serr', 'Pedro', 'Lara', 'Hartley' and 'Ron de Montignac' was analyzed by Inductively Coupled Plasma-Optical Emission Spectroscopy (ICPOES). In addition, the effect of Cu and myo-inositol on shoot length and rooting rate of explants was determined. Mineral concentrations in walnut seeds were reported to be 2 to 26 times higher than in Driver and Kuniyuki Walnut (DKW) medium. Based on the minimum mineral concentration determined in the seeds, two new media containing DKW macro and micronutrients at strengths of 1.5 and 2 were formulated. It has been reported that explants cultured in DKW nutrient medium at 2 and 1.5 power form shoots with green leaves, but they produce callus similar to those cultured in DKW nutrient medium. The researchers, who stated that a better growth was observed in DKW medium at 1.5 power, found the growth rates different in all the cultivars they used. They stated that the maximum shoot length and the number of lateral buds were obtained in "Vina" variety at 1.5 DKW. It has been shown that the number of lateral buds per shoot and shoot length is increased with higher Cu and myo-inositol concentrations. It was stated that better rooting (up to 70 %) was obtained when the shoots were placed in media containing 10x Cu and 2x concentrations of myoinositol in nutrient medium. As a result, the researchers stated that some walnut

cultivars should be grown in environments with higher mineral concentrations than DKW nutrient media, and that higher Cu and myo-inositol levels may be effective in increasing the growth rate and rooting rate of walnut explants (Vahdati et al., 2009). In another study conducted by Kepenek and Kolağası (2016) in *J. regia* L., it was determined that the multiplication rate increased depending on the TDZ and IBA concentrations. It was also stated that the highest multiplication number (5.33 shoots) was obtained in NGE medium containing 2.5 mg/L TDZ and 2.5 mg/L IBA (Kepenek & Kolağası, 2016).

One of the main problems with tissue culture techniques in walnut micropropagation is the low propagation rate. It has been reported that the reason for this low rate is the slow growth of the regenerated shoots, the long culture times and the hidden contamination in the culture (Revilla et al., 1989). On the other hand, Fidancı (2005) stated that the most important problem in the culture initiation phase in micropropagation studies carried out in walnuts is contamination and darkening (Fidancı, 2005). They also reported that the propagation of *J. regia* L. varies widely according to the genotype, and slow *in vitro* growth causes low reproduction rates and difficulties encountered when traditional rooting methods are used (Tuan et al., 2017). In countries where walnut cultivation is developed, many studies have been carried out on the reproduction of walnuts by tissue culture and significant knowledge has been obtained. Most of these studies focused on the appropriate growth regulator concentration to be added to the culture medium. Some researchers have stated that one of the most important problems encountered in the reproduction of walnuts by tissue culture is the darkening caused by phenolic substances. It has also been reported that there are significant differences between genotypes in terms of shoot formation rate and shoot length (Şirin, 2014). In micropropagation studies carried out in walnut species, the desired success has not been achieved yet. The main reason for this is that almost all species of walnut plant are resistant to micropropagation. There are some limitations encountered in the micropropagation of walnut and still waiting to be resolved. Factors such as explant-induced internal contamination, darkening, low reproduction and rooting rate limit the micropropagation success of the walnut, and these limitations are thought to arise depending on the genotype. For this reason, there is a need for more detailed research and development of *in vitro* studies, especially in walnut species (Licea-Moreno et al., 2020).

Paradox rootstock is a first generation hybrid (F1) obtained from pollination of *J. hindsii* and *J. regia*. The apical and lateral meristems of the Paradox were discussed by Driver and Kuniyuki to examine the *in vitro* propagation of this rootstock. It has been stated that DKW, a walnut-specific medium, provides optimum multi-shoot growth with the addition of 4.5 µM benzyladenine (BA) and 5 nM indolebutyric acid (IBA), and the multiplication coefficient can be up to five (Driver & Kuniyuki, 1984). On the other hand, Bosela and Michler (2008) observed a lower rate of vitrification in black walnut (*Juglans nigra* L.) environments in high salt environments (DKW and MS) than in low salt environments (WPM and ½ DKW). Shoot regeneration occurred in node explants in all media containing Zeatin, BAP and TDZ, however, the highest shoot length was obtained in nutrient media containing combinations of BAP and Zeatin as a result of the eight-week culture period (Bosela & Michler, 2008).

One of the most important limitations in micropropagation of walnut species is the low rooting rate. Researchers have tried various methods to overcome this problem (Scaltsoyiannes et al., 1997). Jay-Allemand et al. (1992) determined that the use of ¼ strength DKW and vermiculite (250/200 h/h) promoted root elongation and secondary root development in two-week cultures. In the study, it was also determined that rooting increased by 15-50 % and the number of primary roots was 2-6 times higher than the control group. Researchers; also reported that root penetration and aeration of vermiculite were higher than gelrite and weak rooting was observed in the trials in which only distilled water was added to vermiculite (Jay-Allemand et al., 1992). In another study by Caboni and Damiano (2006), the critical factors to obtain a good rooting response are; ½ strength DKW medium containing 10µM IBA and a 10-12 day dark treatment (induction phase) has been reported. It has been stated that it is also important to transfer the microshoots to a hormone-free environment after the induction phase (Caboni & Damiano, 2006). Tuan et al. (2017) used liquid and semi-solid nutrient media prepared with Rugini and DKW media containing different concentrations of IBA and BAP in their study on walnut. As a result of 21 days of culture, while a higher percentage of fresh weight was obtained in Rugini medium, it was determined that solid medium was more suitable for shoot propagation and the best plant growth regulator and concentration was 2.2 µM BA. It was determined that 5 days of darkness was required for rooting in semi-solid media containing 12 µM IBA and there was no significant difference between ¼ DKW + Vermiculite and ¼ MS + Vermiculite media (Tuan et al., 2017). Steven and Pijut achieved

shoot regenerations in semi-solid DKW medium supplemented with 8.9 µM BAP, 0.005 µM IBA, 200 mg/L casein hydrolyzate, 50 mg/L adenine hemisulphate, 2 mL/L PPM™, and 4.1 µM MT. Micropropagation of shoots was achieved when cultured in a 3L polycarbonate Fernbach-style flask in liquid initiator medium on a rotary shaker at 25°C under a 16 hour photoperiod (100 rpm). For rooting, 5-week cultures were carried out in DKW medium containing 0.11 % Phytagel, 50 µM IBA and vermiculite (2:1 v/v) (Stevens & Pijut, 2018).

In this study, it was aimed to establish an effective micropropagation protocol by providing complete plant regeneration in Paradox variety, which is one of the important walnut rootstocks. In addition, it is aimed to apply different sterilization methods in order to prevent darkening and contamination problems that cause difficulties in micropropagation of walnut species. After determining the most suitable sterilization method, experiments were carried out under semi-solid culture conditions in order to ensure shoot induction and determine the maximum multiplication coefficient. It is based on the establishment of a suitable micropropagation protocol in this walnut variety, which is generally known to be resistant to *in vitro* culture by transferring the obtained shoots to rooting media.

2. MATERIAL AND METHOD

2.1. Material

As the material, node explants of "Paradox" walnut rootstock obtained from the greenhouse in Menemen/Yahseller region by ULU CEVİZ Tarım Ürünleri Sanayi ve Ticaret Anonim Şirketi were used.

2.2. Method

Semi-solid media composition

In the study, DKW (Driver & Kuniyuki, 1984), Rugini (Rugini, 1984) and MS (Murashige & Skoog, 1962) nutrient media were prepared to be used in different micropropagation stages, with full power, half power, modified form and different doses of plant growth regulators (Table 1, Table 2).

Sterilization

The fresh shoots of Paradox walnut rootstocks taken from the greenhouse were brought to the laboratory in a humid environment immediately after they were cut from the tops in spring and summer. The explants separated from their leaves were cut with one or two nodes in each piece. The cut explants were rinsed with detergent water for 10 minutes. It was then kept under running water for 10 min. After the pre-sterilization process, the explants were subjected to 4 different sterilization processes in a laminar flow cabinet (Table 3). After deciding on the best nutrient medium and sterilization process, attempts were made to establish node cultures.

Shoot induction

In the sterilization trials, it was decided that the most successful sterilization method determined by statistical analysis was ST2. Node explants sterilized by the ST2 method continued to be cultured. For shoot induction experiments, node explants were cultured in three replications with 10 explants in each replication in glass tubes containing DKW and Rugini-based nutrient media, whose contents were given in Table 2, at 1/2 strength, as well as modified and/or plant growth regulator added versions of these media.

In vitro rooting

Rooting experiments were carried out with propagated shoots. The media and contents used for rooting experiments are given in Table 4. Rooting experiments were carried out in 2 stages (Caboni & Damiano, 2006; Peixe et al., 2015). In the first stage, 2-3 cm long micro-sprouts transferred to different medium (Table 4) were kept under dark conditions for a period of 7 days to ensure root induction. After root induction was achieved, it was transferred to different rooting media (Table 5) in a 21-day period. Attempt; randomized plots were established according to the experimental design with 3 replications and 10 explants in each replication. Culture dishes were stored in a photoperiod of 16 hours light/8 hours dark, at 24±2°C and 3500 lux light intensity with white LED illumination.

Table 1. *The main nutrient media ingredients used in the research (pH:5.8)*

Compounds (mg/L)	DKW (Driver & Kuniyiki, 1984)	Modified DKW (MDKW) (Fidancı, 2005)	Rugini (Rugini, 1984)	MS (Murashige & Skoog, 1962)	Modified MS medium
NH_4NO_3	1416.00	708	412.00	1650	1650
H_3BO_3	4.80	4.8	12.40	6.2	6.2
$CaCl_2.2H_2O$	147.00	74.5	440.00	440	440
$Ca(NO_3)_2.4H_2O$	1960.00	984	600.00	-	-
KNO_3	-	1100.00		1900	1900
KCl	-	500.00		-	-
KI	-	-	-	0.83	0.83
$CuSO_4.5H_2O$	0.25	0.25	0.25	0.025	0.025
$MgSO_4.7H_2O$	740	335	1500.00	370	720
$MnSO_4.H_2O$	33.50	33.5	16.90	16.9	16.9
KH_2PO_4	259.00	132.5	340.00	170	265
K_2SO_4	1560.00	779.5	-	-	-
$Na_2MoO_4.2H_2O$	0.39	0.39	0.25	0.25	0.25
$ZnSO_4.7H_2O$	17.00	17.00	14.30	8.6	17
$CoCl_2.6H_2O$	-	-	-	0.025	0.025
$FeSO_4.7H_2O$	33.40	16.9	27.80	27.8	27.8
Na_2EDTA	44.70	22.7	37.30	37.3	37.3
Myo-inositol	1000.00	100	100.00	100	100
Tiamin-HCL	2.0	2.0	0.50	0.1	0.1
Nicotinic acid	2.0	1.0	5.0	0.5	0.5
Pyridoxine-HCl	-	-	0.50	0.5	0.5
Glycine	2.0	2	2.0	2.0	2
Biotin	-	-	-	-	
Folic acid	-	-	-	-	
Glutamine	-	-	2190	-	
Sucrose	30000	30000-40000	30000	30000	30000-40000

Statistical analysis

In vitro applications within the scope of the project were carried out in three replications according to the randomized plot design. The data obtained from the applications were evaluated using the Minitab® 17 statistical program.

Table 2. Media composition

	Basal medium	Plant growth regulators (mg/L)	Other added chemicals (mg/L)
DKW	DKW	-	-
D1B	DKW	1 BAP	-
D2B	DKW	2 BAP	-
D4B	DKW	4 BAP	-
SP	DKW	-	200 casein hydrolyzate + 50 adenine hemisulphate
SP1	DKW	1 BAP + 0.001 IBA	200 casein hydrolyzate + 50 adenine hemisulphate
SP2	DKW	2 BAP + 0.001 IBA	200 casein hydrolyzate + 50 adenine hemisulphate
SP4	DKW	4 BAP + 0.001 IBA	200 casein hydrolyzate + 50 adenine hemisulphate
Ru	Rugini	-	-
Ru1	Rugini	1 BAP	-
Ru2	Rugini	2 BAP	-
MRu0,5	Modified Rugini	0.001 IBA	200 casein hydrolyzate + 50 adenine hemisulphate
MRu1	Modified Rugini	0.001 IBA	200 casein hydrolyzate + 50 adenine hemisulphate

Table 3. Sterilization process

Sterilization code	Sterilization process	Medium
ST1	1 min 70 % EtOH + 5 min 0.1 % $HgCl_2$	DKW
ST2	5 min 70 % EtOH + 5 min 0.2 % $HgCl_2$ (Tween 20 added)	DKW
ST3	5 min 70 % EtOH+3 min 20 % bleach	D1B
ST4	1 min 70 % EtOH + 5 min 0.1 % $HgCl_2$ +5 min 12 % bleach	DKW

Table 4. Medium composition for in vitro root induction*

Code	Basal medium	Plant growth regulators	Carbon sourse
1I30	MMS	4 mg/L IBA	30 g/L sucrose
1I40	MMS	4 mg/L IBA	40 g/L sucrose
½I30	½ MMS	4 mg/L IBA	30 g/L sucrose
½ 30	½ MMS	-	30 g/L sucrose
½ I40	½ MMS	4 mg/L IBA	40 g/L sucrose
MD304	MDKW	4 mg/L IBA	30 g/L sucrose
MD404	MDKW	4 mg/L IBA	40 g/L sucrose
MDFI	MDKW	4 mg/L IBA+119 mg/L FeEDDHA	30 g/L sucrose

*Gelrite: 2.4 g/L

Table 5. *Medium compositions for in vitro root growth (Carbon source: 30 g/L sucrose; Gelrite: 2.4 g/L)*

Code	Basal medium	Medium composition
MDFe	MDKW	119 mg/L FeEDDHA
¼ DFe	¼ DKW	119 mg/L FeEDDHA
MDV	MDKW	1:1 vermiculite
¼ DV	¼ DKW	1:1 vermiculite

3. RESULTS AND DISCUSSION

3.1. Result

Sterilization

The effects of the sterilization experiments on the observation parameters were examined and the data were recorded. Values were calculated as percentages. (Table 6 and Figure 1). According to its effect on contamination, the most successful method was determined as ST1. Contaminations seen in cultured explants were of bacterial or yeast origin. Generally, contaminations were observed 7 to 15 days after the culture period (Figure 2). When considered in terms of darkening effects, the ST4 method was found to be the most unsuccessful with 46.7 % on darkening. No darkening was observed in the explants cultured in the ST1 method. ST1 method was determined to be more successful than other methods in terms of darkening. Darkening problem usually emerged within the first week of node explants. According to the effect on vitrification, no vitrification problem was encountered when ST1 and ST2 methods were used and they were accepted as successful methods. The highest vitrification was recorded in the ST3 method with 33.3 %. The emergence of vitrification in the shoots occurred on the 7th day after the explants were cultured. According to the necrosis effect, ST3 was determined as the most unsuccessful sterilization method with 33.3 % necrosis formation percentage, no necrosis was observed in the ST1 and ST4 sterilization methods and they were considered successful. The emergence of necrosis in the shoots occurred on the 7th day after the explants were cultured. When these data were examined, ST1 was evaluated as a more successful sterilization method. However, due to increased contamination and darkening in the advancing processes of the culture, studies were continued with ST2, a mercuric chloride-based sterilization method containing Tween20®. In all trials after the sterilization trial, the explants were sterilized and cultured using the ST2 method.

***Table 6.*** *Effects of different sterilization methods on darkening, contamination, vitrification and necrosis*

Sterilization code	Darkening (%)	Contamination (%)	Vitrification (%)	Necrosis (%)
ST1	0	13.3	0	0
ST2	12.5	37.5	0	8.3
ST3	4.17	37.5	33.3	33.3
ST4	46.7	20	3	0

Shoot Induction

In the trials where the effects of the medium in which the explants were transferred after sterilization on shoot initiation, the highest darkening was observed in the Ru medium with 72 %, while no darkening was observed in the MRu1 medium. While no vitrification was observed in most of the media (D4B, SP1, SP2, Ru2, MRu0,5 and MRu1), 33.3 % vitrification was detected in the D1B medium. While necrosis was not observed in DKW, D4B, SP, SP1, SP4, Ru1, Ru2, MRu0,5 and MRu1 nutrient media, necrosis occurred at a rate of 33.3 % in D1B media (Table 7 and Figure 3).
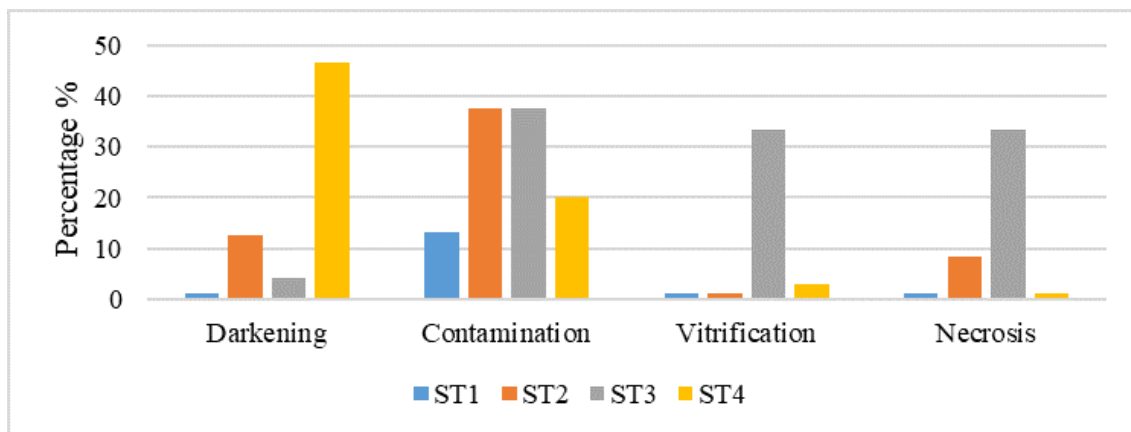
Figure 1. *Evaluation of different sterilization methods according to four observation parameters (darkening (%), contamination (%), vitrification (%), necrosis (%))*
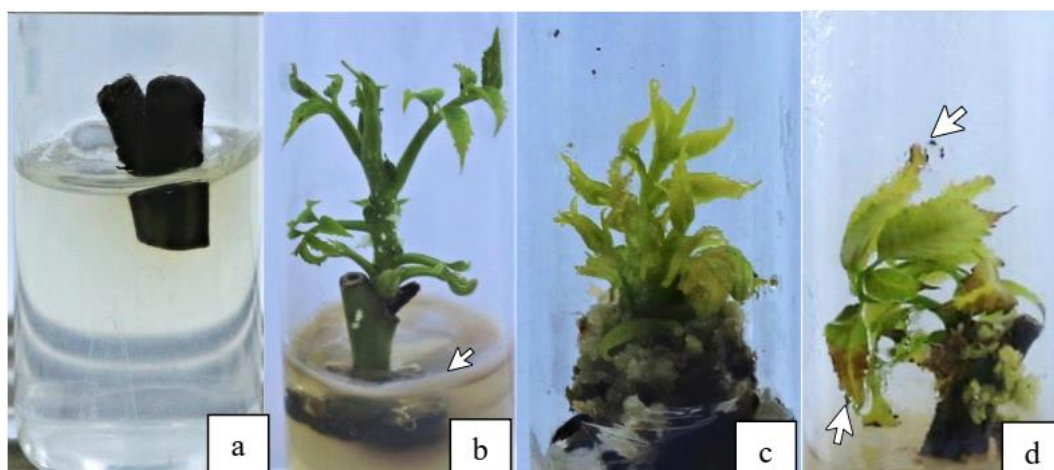

Figure 2. *Examples of problems encountered in walnut culture are **a**) darkening, **b**) contamination, **c**) vitrification, **d**) necrosis*

Table 7. *The effect of different medium composition on the percentages of darkening. vitrification and necrosis*

Code	Darkening (%)	Vitrification (%)	Necrosis (%)
DKW	46.7	3	0
D1B	4.17	33.3	33.3
D2B	8.3	12.5	4.17
D4B	5.6	0	0
SP	3.3	3.3	0
SP1	23	0	0
SP2	3	0	0
SP4	14	4.6	0
Ru	72	25	50
Ru1	47.3	9.3	0
Ru2	28	0	0
MRu0.5	4.67	0	0
MRu1	0	0	0
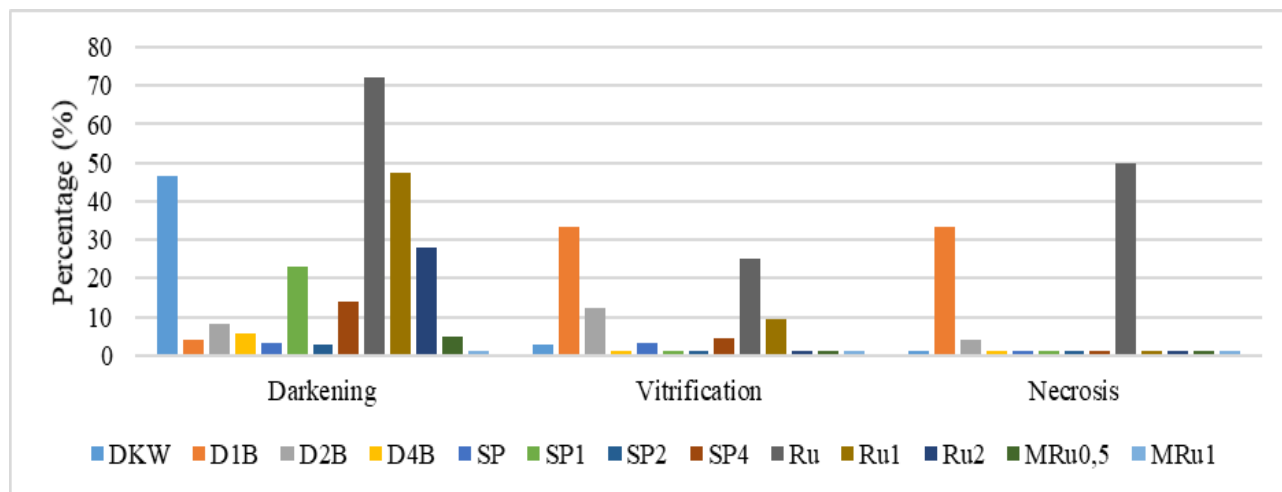
Figure 3. *The effect of different medium composition on the percentages of darkening, vitrification and necrosis*

As a result of the analysis of variance, the effect of the nutrient medium on the number of shoots and the percentage of shoot formation was found to be significant ($p < 0.05$) (Table 8). The most successful nutrient medium was SP4 with 1.05 units/explant and 100 % shoot formation. According to these parameters, the least successful nutrient medium was Ru nutrient medium with 0.57 units/explant and 57 % shoot formation (Table 8, Figure 4 and Figure 5).

Table 8. *Data from shoot initiation experiments**

Code	Average number of shoots obtained per explant (Mean ± S.E.)	Mean shoot length (cm) obtained per explant (Mean ± S.E.)	Percentage of shoot-forming explants (Mean ± S.E.)	Mean number of nodes obtained per explant (Mean ± S.E.)
DKW	0.90 ± 0.07 ab	1.04 ± 0.13 ab	80.00 ± 17.3 abc	4.33 ± 0.66 b
D1B	1.00 ± 0.07 ab	0.68 ± 0.12 bc	93.33 ± 5.77 ab	4.67 ± 0.64 b
D2B	0.90 ± 0.17 ab	0.43 ± 0.08 c	67.00 ± 6.93 abc	1.62 ± 0.34 c
D4B	1.00 ± 0.14 ab	0.41 ± 0.06 c	71.00 ± 6.93 abc	2.69 ± 0.44 bc
SP	0.71 ± 0.10 ab	0.37 ± 0.07 c	63.30 ± 30.6 bc	2.91 ± 0.49 bc
SP1	0.80 ± 0.09 ab	0.37 ± 0.07 c	81.00 ± 8.66 abc	3.95 ± 0.75 bc
SP2	0.95 ± 0.05 ab	1.60 ± 0.19 a	96.67 ± 5.77 ab	7.95 ± 0.69 a
SP4	1.05 ± 0.05 a	0.36 ± 0.09 c	100.0 ± 0.00 a	3.57 ± 0.50 bc
Ru	0.57 ± 0.11 b	0.23 ± 0.10 c	57.00 ± 14.0 c	1.57 ± 0.48 c
Ru1	0.67 ± 0.13 ab	0.63 ± 0.17 bc	61.67 ± 8.08 bc	2.76 ± 0.58 bc
Ru2	0.76 ± 0.10 ab	1.15 ± 0.20 ab	76.00 ± 8.66 abc	3.62 ± 0.58 bc
MRu0.5	0.90 ± 0.07 ab	1.04 ± 0.12 ab	90.67 ± 8.08 abc	3.71 ± 0.40 bc
MRu1	1.00 ± 0.07 ab	1.04 ± 0.12 ab	90.67 ± 8.08 abc	4.10 ± 0.23 bc
p value	0,009	0,000	0,001	0,000

*Applications were made in triplicate and 10 explants were used for each replication. The differences between the mean values shown with different letters in the same column are significant at the $P \leq 0.01$ level according to the Tukey multiple comparison test. SE: Standard Error
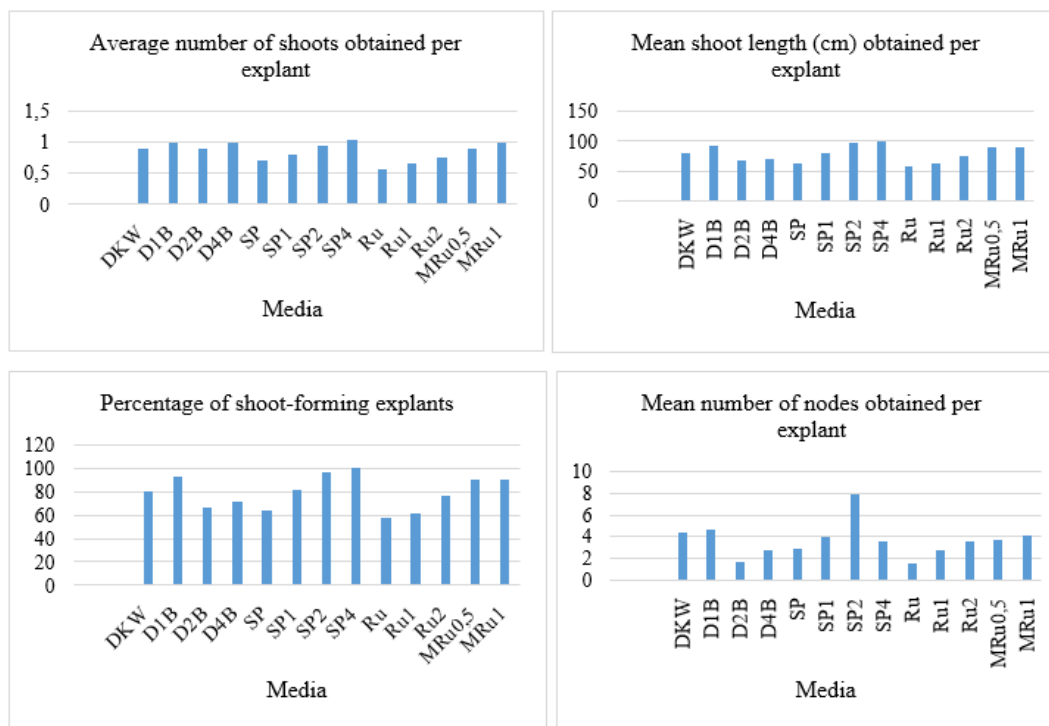
509

Cem DİRLİK, Hacer KANDEMİR, Nurberat ÇETİN, Senem ŞEN, Begüm GÜLER, Aynur GÜREL
GU J Sci, Part A, 9(4): 500-515 (2022)

Figure 4. *Graphics from shoot initiation experiments*

Figure 5. *Shoot regeneration from each medium **a**) DKW **b**) D1B **c**) D4B **d**) SP1 **e**) SP2 **f**) SP4 **g**) Ru **h**) Ru1*
***i**) Ru2 **j**) MRu0,5 **k**) MRu1*

In vitro rooting

Rooting was achieved in two stages in the study. Root induction was performed in the first stage, and the development of these roots was ensured in the second stage of the study. In the light of these data, the nutrient media that initiate the most effective induction process in rooting were determined as ½ I30, ½ I40, 1I30, MD304, ½ 30 and MDFI. The most successful root induction medium was determined as ½ I30 medium (33.3%) containing 4 mg/L IBA (Figures 6 and 7).
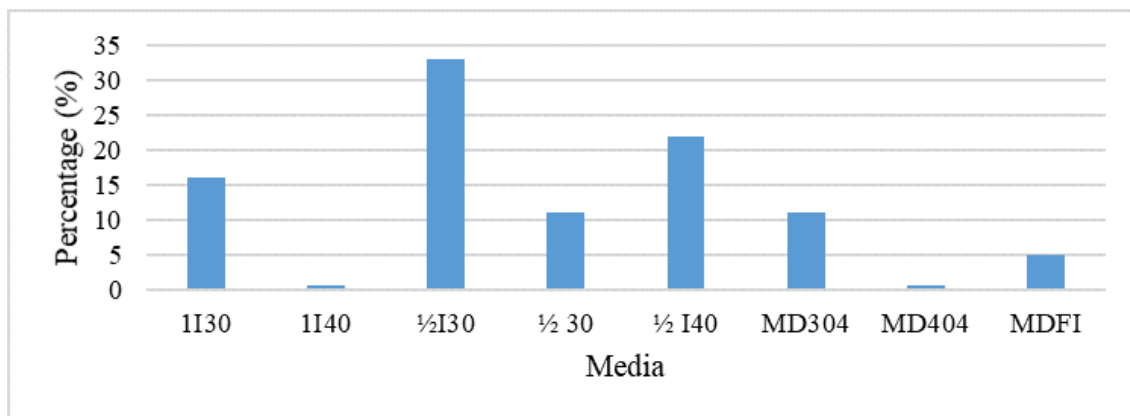
Figure 6. *Effect rates of root induction media on the initiation of root formation (%)*
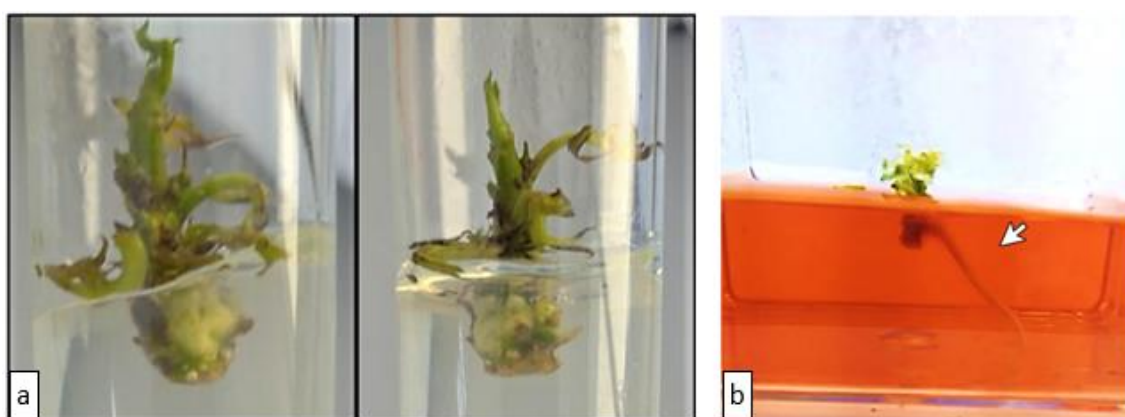
Figure 7. *In vitro rooting with two steps a) Root induction in MD304 medium, b) Root regeneration in ¼ DFe medium*

Root-induced shoots were cultures in different medium composition in Table 4 for root development during 21 days, 16 hours light/8 hours dark photoperiod, 24±2°C and 3500 lux light intensity with white LED illumination. The effects of the medium composition used in the experiments on the average root length (cm) and root number (number) were recorded. Observation data gave statistically insignificant differences (Table 9). It was determined that the most successful rooting medium was ¼ DFe. According to the results obtained from the study, the most successful rooting rate was recorded as 45.45 %. Depending on the nutrient media used, callus formations occurred at rates ranging from 0 to 77.7 % on the shoot bases (Figure 7). In root development experiments, callus formation occurred at the leaf tip of the growing shoot in the culture dish containing ¼ DFe medium. It has been determined that the adventitious root formation also consists of this callus tissue (Figure 8).

Table 9. *The effect of medium compositions on parameters in rooting experiments*

Rooting medium	Rooting regeneration ratio (%)	Longest root lenght (cm)	Average root lenght (cm)	Average root number (number)	Callus regeneration ratio (%)
MDFe	33.3	1	0.34	1	77.7
¼ DFe	45.45	2.5	1.22	2.4	54.5
MDV	11.1	2	2	1	11.1
¼ DV	0	0	0	0	0
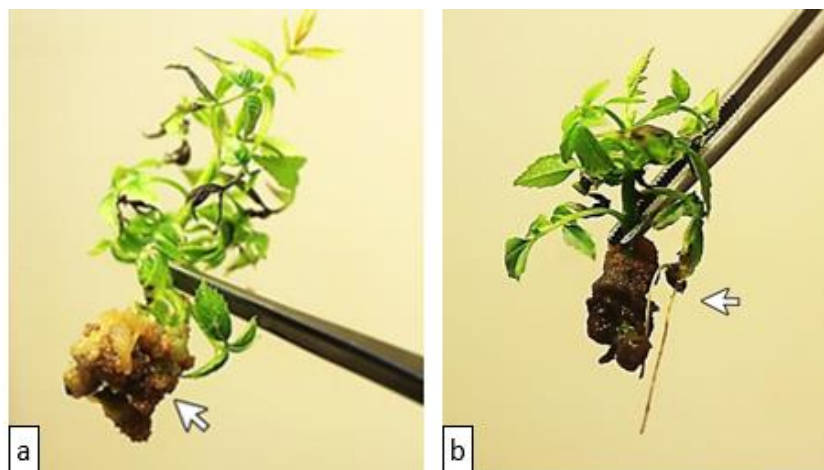
Figure 8. *Callus regeneration on explants **a)** Callus and root structure formed in MDFe medium **b)** Callus and root formed at the leaf tip of the shoot developed in ¼ DFe medium*

3.2. Discussion

The first stage carried out within the scope of this study is the surface sterilization of the node explants. Elimination of internal contamination sources from walnut plant explants is the most important step in micropropagation studies. Because the darkening and contamination problem encountered in micropropagation studies with walnut varieties and the results of which cannot be clarified yet, should be eliminated. In tissue culture studies performed on all species of Juglans plant, it has been determined that they are quite stubborn against micropropagation. Darkening due to oxidation of the phenolic component in explants, internal contamination sources in explants, difficulties in adaptation to the culture medium, rooting and transfer to the soil are the most important problems of walnut micropropagation. Many scientific studies on walnut micropropagation have been published since the 1980s, but there is still not enough information to establish an accurate micropropagation protocol depending on the species (Kepenek & Kolağası, 2016; Licea-Moreno et al., 2020). Fidancı (2005) stated in his research using Şebin and KR-2 walnut varieties that the most important problem encountered during the cultivation phase of micropropagation is contamination and darkening.

In our study, it was thought that the most important problem to be solved was contamination and darkening, and studies were carried out in this direction. In the different sterilization trials, the highest contamination rate (37.5 %) was recorded in ST2 and ST3 trials, while the lowest contamination rate (13.3 %) was recorded in ST1. Similarly, while the highest darkening (46.7 %) was recorded in ST4, the lowest darkening (0 %) was recorded in the ST1 sterilization method. As a result of the trials carried out by applying different sterilization protocols, the sterilization method in which darkening (4 %) and contamination were minimized was determined as ST2 (5 min. 70 % EtOH + 5 min. 0.2 % HgCl$_2$-Tween 20 added). Dong et al. (2007) reported that for successful sterilization in regeneration experiments of walnut explants, the explants were kept in 70 % EtOH for a while, followed by sterilization with 0.1 % HgCl$_2$, and then rinsed with sterile distilled water. Şirin (2014), in order to develop a sterilization protocol in the axillary buds of Kaman-1 and Kaman-5 walnut varieties, exposed the explants to 70 % ethyl alcohol for 1 minute and then sterilized them in 0.2 % HgCl2 for 5 minutes. In order to prevent the intense darkening in walnut regeneration studies, it was tried to be prevented by adding 100 mg/L ascorbic acid and 100 mg/L citric acid, and it was reported that the study was continued by subculture at 3, 24 and 48 hour intervals.

In the study carried out by Scaltsoyiannes et al. (1997), to sterilize the embryos, the fruits were cracked and kept in 70 % EtOH for 5 minutes and then in 0.1 % NaOCl for 5 minutes, rinsed three times with sterile distilled water and the embryos were cultured. Sterilization success was determined as 0-59 % in the study. When compared with the study carried out by us, it is observed that the results show suitability.

In a study by Tarinejad (2013) on the sterilization of node planes in walnuts, it was determined that 70 % EtOH for 2 minutes, 5 % NaOCl for 10 minutes, followed by 0.7 % HgCl$_2$ for 3 minutes are required for sterilization.

In addition, it was determined that internal contaminations were revealed in the cultures that progressed in the trials in which antibiotics were not used. On top of that, it was determined that the sterilized explants should be cultured in media containing 12.5 mg/L gentamicin and 100 mg/L vancomycin to prevent this. The sterilization method was recommended by us is a more usable method because it includes the use of fewer sterilization agents and the application is shorter and more practical. In addition, a cheaper and commercially preferable method has been proposed due to the use of sterilization without the use of antibiotics.

One of the problems encountered in the studies carried out on walnut has been stated as the low reproduction rate. The reason for this was thought to be the long culture period and latent contaminations as a result of the slow growth of regenerated shoots (Revilla et al., 1989). Lone (2017) stated that woody species had a weaker *in vitro* micropropagation response than herbaceous plants, and this was due to darkening and explant necrosis. Necrosis can occur when plants do not have enough nutrients. Extremely low amounts of phosphorus initially cause the leaves of the plant to appear bright green, but older leaves become necrotic. Other nutrients that cause necrosis are potassium, nitrogen, boron, iron and nickel (Schader, 2019). In our study, the rate of necrosis and especially darkening was observed to be higher in Rugini environments in general. On the other hand, it was observed that the darkening decreased in the modified Rugini media created by adding casein hydrolyzate and adenine hemisulphate based on Rugini. It can be thought that the low salt concentration of Rugini media compared to MS and DKW media may cause darkening and necrosis, and the casein hydrolyzate and adenine hemisuflate explants added to the medium protect from this condition. In the light of this information, it can be stated that the sterilization method we carried out in the 'Paradox' walnut rootstock species is compatible with the literature and can help prevent darkening and contamination problems in walnut species.

In the study carried out by Tetsumura et al. (2002) on different walnut varieties, the highest shoot number was obtained as 1.7, while the highest shoot length was determined as 1.97 cm. In another study carried out by Kepenek and Kolağası (2016), the highest number of shoots obtained per explant was found to be 5.32, while the shoot length was 3.88 cm. In our study node explants with surface sterilization were transferred to the specified media for shoot induction. According to the results obtained at the end of 21 days; the highest number of shoots per explant (1.05 shoots/explant) was obtained in semi-solid SP4 (DKW containing 4 mg/L BAP + 0.001 mg/L IBA + 200 mg/L casein hydrolysate + 50 mg/L adenine hemisulphate) nutrient medium. In addition, the most successful medium was semi-solid SP2 (DKW containing 2 mg/L BAP + 0.001 mg/L IBA + 200 mg/L casein hydrolyzate+50 mg/L adenine hemisulphate) in terms of the highest number of nodes (7.95 nodes/explant) and shoot length (1,6 cm) per explant.

Scaltsoyiannes et al. (1997) in their regeneration study on *Juglans regia* L., it was found that the best axillary shoots were in DKW nutrient medium containing 4.44 μM BAP and 0.005 μM IBA, and the shoot length was maximum in culture medium containing 2.22 μM BAP. Saadat and Hennerty (2002), was stated that it gave better results in DKW medium than MS and WPM environments, and the use of Phytagel as a gelling agent was recommended. Tetsumura et al. (2002) obtained successful results in DKW nutrient medium with 5 μM BAP and 0.05 μM IBA. Fidancı (2005) tested MS, DKW, WPM media in Şebin and KR-2 walnut cultivars and the best growth was observed in DKW medium containing 1.0 mg/L BAP and 0.01 mg/L IBA. In our study, successful results were obtained in the formation of shoots in the presence of BAP from the node explants cultured in semi-solid DKW medium.

In their study, Meier-Dinkel and Wenzlitschke (2015) cultured nodal segments in DKW and ROM media containing BAP and IBA, and higher reproduction rate (7.59) and shoot length (2.1 cm) were achieved in ½ ROM media. In our study, Rugini and DKW media and their modifications were tested. DKW, which we tried at full strenght, gave higher shoot number than Rugini medium. In their study by Bosela and Michler (2008), vitrification of black walnut explants was observed at frequencies of 60-100 % in WPM and ½ DKW environments, compared to frequencies of 10-40% in high-salt environments (DKW and MS). In our study, more vitrification was found in DKW media than in Rugini media.

After the shoot induction and propagation stages, the shoots reaching 3-5 cm in length were taken and transferred to the specified rooting media. Rooting experiments were carried out in two stages. In the first stage, shoot explants taken into nutrient media for root induction were kept in dark conditions for 7 days. In this induction stage, the most successful medium (33 %) was ½I30 nutrient medium, whereas root induction

did not occur or explants died in nutrient media with the codes 1I40, ½30, MD404. In the next stage, shoot explants taken from dark conditions were transferred to rooting media containing different nutrient compositions in order to achieve root formation, and they were maintained in a light 16 hours light/8 hours dark photoperiod in a 21-day period. At the end of this period, the explants in ¼ DFe coded medium were most successfully rooted (2.4 cm root length, 1.22 root number). After root induction is achieved in shoots kept in dark conditions for a while, there is a lot of literature information about promoting root elongation under light conditions (Kamali et al., 2001; Fu et al., 2003; Caboni & Damiano, 2006; Tuan et al., 2017). Same as our study, in their study, Caboni and Damiano (2006), determined that the dark application was effective on adventitious rooting, which not only increased IBA uptake but also affected the concentration of endogenous auxin in free and conjugated forms. In Caboni and Lauri (1995) and Ripetti et al. (1994) studies, they stated that for the initiation of rooting in walnuts, the explants should be taken into an environment containing IBA first, and then the subculture should be made in a fresh hormone-free medium for the elongation of the roots.

4. CONCLUSION

The problems encountered in walnut production necessitated the preference of alternative methods. In this case, micropropagation studies have become an important alternative as they both enable clonal reproduction and enable seasonal production in a short time in a narrow space. In this study, micropropagation studies were carried out on the "Paradox" variety, which is the most demanded rootstock. When the given information is examined, the best media for shoot induction and also growth were found as SP4 and SP2 media based DKW medium. Rooting in two stages as root induction and elongation increased the rooting efficiency in the study. The development of these methods with future studies is of great importance for the development of walnut agriculture.

ACKNOWLEDGEMENT

CONFLICT OF INTEREST

The authors declare no conflict of interest.

REFERENCES

Açıksöz, U. (2020). *Bandırma İlçesindeki Ceviz Fidanı Üretiminin Mevcut Durumunun İncelenmesi*. MSc Thesis, Bursa Uludağ University.

Aslansoy, B. (2012). *Sultandağı (Afyon) yöresi cevizlerinin (Juglans regia L.) seleksiyon yoluyla ıslahı üzerine araştırmalar*. . MSc Thesis, Selçuk University.

Bosela, M. J., & Michler, C. H. (2008). Media effects on black walnut (*Juglans nigra* L.) shoot culture growth *in vitro*: Evaluation of multiple nutrient formulations and cytokinin types. *In Vitro Cellular and Developmental Biology - Plant*, *44*(4), 316-329. doi:10.1007/s11627-008-9114-5

Budak, Y. (2010). *Ceviz Yetiştiriciliği*. Samsun İl Tarım Müdürlüğü, Çiftçi Eğitimi ve Yayım Şubesi Yayınları, 20 p., Samsun. PDF

Caboni, E., & Damiano, C. (2006). *In vitro* propagation of walnut (*Juglans regia* L.): Critical factors for the induction of the rooting response. *Acta Horticulturae*, 705, 329-333. doi:10.17660/ActaHortic.2005.705.44

Caboni, E., & Lauri, P. (1995). Effetto di fattori chimici, fisici e trasformazione localizzata sulla radicazione *in vitro* di noce. *Italus Hortus*, *4*(2), 49-53.

Dong, P., Lichai, Y., Qingming, W., & Ruisheng, G. (2007). Factors affecting rooting of *in vitro* shoots of walnut cultivars. *The Journal of Horticultural Science and Biotechnology*, *82*(2), 223-226. doi:10.1080/14620316.2007.11512223

Driver, J. A., & Kuniyuki, A. H. (1984). In vitro propagation of Paradox Walnut Rootstock. *Hortscience*, 19(4). 507-509.

Er, E., Akyüz, B., Öztürk, A., & Serdar, Ü. (2017). Cevizde Çeşit Değiştirme: Kabukaltı Aşısı. *Bahçe*, *46*(Special Issue-2), 307-312.

Fidancı, A. (2005). Şebin ve KR-2 ceviz çeşitlerinin *in vitro*'da hızlı çoğaltılma tekniklerinin belirlenmesi. *Bahçe*, *34*(1), 239-246.

Fu, Y., Gu, F., & Wu, W. (2003). Sterilization of *Carya illinoensis* Explants in Tissue Culture. *Journal of Anhui Agricultural University*, *31*(2), 169-172.

Gürel, A., Hayta, Ş., Nartop, P., Bayraktar, M., & Fedakar S. O. (2013). *Bitki Hücre, Doku ve Organ Kültürü Uygulamaları*. Ege Üniversitesi Yayınları Yayın No: 58.

Jay-Allemand, C., Capelli, P., & Cornu, D. (1992). Root development of *in vitro* hybrid walnut microcuttings in a vermiculite-containing gelrite medium. *Scientia Horticulturae*, *51*(3-4), 335-342. doi:10.1016/0304-4238(92)90132-V

Kamali, K., Majidi, E., & Zarghami, R. (2001). Micropropagation of GF-677 Rootstocks (*Prunus amygdalus* x P. persica). *Seed and Plant*, *17*, 175-177.

Kepenek, K., & Kolağası, Z. (2016). Micropropagation of Walnut (*Juglans regia* L.). *Acta Physica Polonica A*, *130*(1), 150-156. doi:10.12693/APhysPolA.130.150

Kumar, P. P., & Loh, C. S. (2012). Plant Tissue Culture for Biotechnology. In: A. Altman, & P. M. Hasegawa (Eds.), *Plant Biotechnology and Agriculture-Prospect for the 21st Century* (pp. 131-138) Academic Press. doi:10.1016/B978-0-12-381466-1.00009-2

Kyte, L. (1987). *Plants from Test Tubes. An Introduction to Micropropagation*. Timber.

Leal, D. R., Sánchez-Olate, M., Avilés, F., Materan, M. E., Uribe, M., Hasbún, R., & Rodríguez, R. (2007). Micropropagation of *Juglans regia* L. In: S. M. Jain, & H. Häggman (Eds.), *Protocols for Micropropagation of Woody Trees and Fruits* (pp. 381-390). Springer, Dordrecht. doi:10.1007/978-1-4020-6352-7_35

Leelavathy, S., & Sankar, P. D. (2016). Curbing the menace of contamination in plant tissue culture. *Journal of Pure and Applied Microbiology*, *10*(3), 2145-2152.

Licea-Moreno, R., Fira, A., & Chocov, G. (2020). Micropropagation of valuable walnut genotypes for timber production: new advances and insights. *Annals of Silvicultural Research*, *44*(1), 5-13. doi:10.12899/asr-1932

Lone, I. A. (2017). Effect of different growth regulator combinations on *in vitro* callusing of walnut (*J. regia* L.). *An Asian Journal of Soil Science*, *12*(1), 203-209. doi:10.15740/HAS/AJSS/12.1/203-209

Meier-Dinkel, A., & Wenzlitschke, I. (2015). *Micropropagation of mature Juglans hybrids*. In: M. Beruto, & E. A. Ozudogru (Eds.), Proceedings of the VI International Symposium on Production and Establishment of Micropropagated Plants, ISHS Acta Horticulturae 1155, (pp. 85-92). doi:10.17660/ActaHortic.2017.1155.11

Murashige, G., & Skoog, F. (1962). A Revised Medium for Rapid Growthand Bioassays With Tobacco Tissue Culture. *Physiologia Plantarum*, *15*(3), 473-497. doi:10.1111/j.1399-3054.1962.tb08052.x

Ray, S. S., & Ali, N. (2016). Biotic Contamination and Possible Ways of Sterilization: A Review with Reference to Bamboo Micropropagation. *Brazilian Archives of Biology and Technology*, *59*(e16160485). doi:10.1590/1678-4324-2016160485

Ripetti, V., Kevers, C. & Gaspar, T. (1994). Two successive media for the rooting of walnut shoots *in vitro*. Changes in peroxidase activity and in ethylene production. *Advances in Horticultural Science,* *8*(1), 29-32.

Revilla, M. A., Majada, J., & Rodriguez, R. (1989). Walnut (*Juglans regia* L.) micropropagation. *Annales des sciences forestières, INRA/EDP Sciences*, *46*(Suppl), 149s-151s. PDF

Rugini, E. (1984). *In Vitro* Propagation of Some Olive (*Olea europaea sativa* L.) Cultivars with Different Root-Ability and Medium Development Using Analytical Data from Developing Shoots and Embryos. *Scientia Hotriculturae,* *24*(2), 123-134. doi:10.1016/0304-4238(84)90143-2

Saadat, Y. A., & Hennerty, M. J. (2002). Factors Affecting the Shoot Multiplication of Persian Walnut (*Juglans regia* L.). *Scientia Horticulturae,* *95*(3), 251-260. doi:10.1016/S0304-4238(02)00003-1

Scaltsoyiannes, A., Tsoulpha, P., Panetsos, K. P., & Moulalis, D. (1997). Effect of Genotype on Micropropagation of Walnut Trees (*Juglans regia*). *Silvae Genetica*, *46*(6), 326-332.

Schader, M. (2019). The Definition of Necrosis in Plants (Accessed: 25/11/2019) URL

Stevens, M. E., & Pijut, P. M. (2018). Rapid *in vitro* shoot multiplication of the recalcitrant species *Juglans nigra* L. *In Vitro Cellular & Developmental Biology-Plant*, *54*(3), 309-317. doi:10.1007/s11627-018-9892-3

Şen, S. M. (2011). *Ceviz Yetiştiriciliği-Besin Değeri-Folklorü*. ÜÇM yayıncılık, Samsun.

Şirin, E. (2014). Kaman 1 ve Kaman 5 ceviz çeşitlerinin (*Juglans regia* L.) mikroçoğaltımı. MSc Thesis, Gaziosmanpaşa University.

Tarinejad, A. (2013). Effects of disinfectants and antibiotics on contamination during propagation of walnut (*Juglans regia* L.). *Research on Crops*, *14*(1), 219-225.

Tekielska, D., Peňázová, E., Kovács, T., Křižan, B., Čechová, J., & Eichmeier, A. (2019). Bacterial contamination of plant *in vitro* cultures in commercial production detected by high-throughput amplicon sequencing. *Acta Universitatis Agriculturae et Silviculturae Mendelianae Brunensis*, *67*(4), 1005-1014. doi:10.11118/actaun201967041005

Tetsumura, T., Tsukuda, K., & Kawase, K. (2002). Micropropagation of Shinano Walnut (*Juglans regia* L.). *Journal of the Japanese Society for Horticultural Science*, *71*(5), 661-663. doi:10.2503/jjshs.71.661

Tuan, P. N., Meier-Dinkel, A., Höltken, A. M., Wenzlitschke, I. & Winkelmann, T. (2017). *Factors affecting shoot multiplication and rooting of walnut (Juglans regia L.) in vitro*. In: M. Beruto, & E. A. Ozudogru (Eds.), Proceedings of the VI International Symposium on Production and Establishment of Micropropagated Plants, ISHS Acta Horticulturae 1155, (pp. 525-530). doi:10.17660/ActaHortic.2017.1155.77

Vahdati, K., Ashrafi, E. N., Ebrahimzadeh, H., & Mirmasoumi, M. (2009). *Improved micropropagation of walnut (Juglans regia L.) on media optimized for growth based upon mineral content of walnut seed*. In: M.-V. Hanke, F. Dunemann, & H. Flachowsky (Eds.), Proceedings of the I International Symposium on Biotechnology of Fruit Species: BIOTECHFRUIT2008, ISHS Acta Horticulturae 839, (pp. 117-124). doi:10.17660/ActaHortic.2009.839.13

Varghese, N., & Joy, P. P. (2016). Plant tissue culture contaminants identification and its response to fumigation. *Technical Report*, 1-10.

Yiğit, D., Yiğit, N., Aktaş, E., & Özgen, U. (2009). Ceviz (*Juglans regia* L.)'in antimikrobiyal aktivitesi. *Türk Mikrobiyoloji Cemiyeti Dergisi*, *39*(1-2), 7-11.

Prediction of Immediate Deflections for RC Beams Using Stress-varying Modulus of Elasticity

Eray ÖZBEK[1*] iD

[1]Gazi University, Engineering Faculty, Civil Engineering Department, 06570 Ankara, Türkiye

Keywords	Abstract
Beam	This paper discusses the immediate deflection calculation of reinforced concrete beams and their consistency with the experimental results. For this purpose, a total of six T-beams with low, medium, and high reinforcement ratios were tested and then, deflection behavior was compared with the well-known Branson (1965) and Bischoff (2005) approaches. Although both approaches could yield close results for the low reinforcement at service loads by using a constant modulus of elasticity, they underestimated the deflections of medium and highly reinforced beams. Thus, the nonlinear behavior of concrete that changes with stress was also considered in the subsequent analyzes. As a result, the developed new approach could predict the experimental deformations very accurately, especially at the level of service loads.
Deflection	
Serviceability	
Elastic Modulus	
Concrete Model	

1. INTRODUCTION

As known, reinforced concrete (RC) structural members are designed to resist loads without experiencing failure. On the other hand, RC members should also meet serviceability requirements to assure proper behavior and functionality under these loads. Deflections and cracking properties are the major concerns that can affect serviceability. Therefore, it is very crucial to predict these features with an estimate close to the actual behavior. However, this is not straightforward due to the specific behavior of RC. The flexural stiffness of a beam section depends on the moment of inertia normal to loading direction and the modulus of elasticity. However, the product of both variables is not constant for RC beams at any stage of the loading. Nonlinear and time-dependent stress-strain behavior of concrete results variability in the modulus of elasticity. On the other hand, the moment of inertia significantly changes after cracking and keeps changing due to crack propagation.

Accordingly, many research was conducted to calculate or predict immediate deflections of RC beams. They dealt with predicting the decreasing trend of moment of inertia due to cracked section properties. This behavior was taken into account by using different effective moment of inertia at corresponding load levels. Among these studies, Branson (1965) became very popular and conventional. This approach was also adopted by Turkish Standards TS500 (2000), American Concrete Institute, ACI 318-14 (2014), Canadian Standards CSA (2004), AASHTO (2005), Australian Standards, AS 3600-2009 (2009). American Concrete Institute Building Codes had been using this approach for more than 35 years (Mancuso & Bartlett, 2017). However, in 2019, ACI 318-19 (2019) removed the Branson (1965) equation, and instead adopted the Bischoff (2005) approach. The method proposed by Bischoff (2005) slightly better estimated the load-deflection of RC beams with a more rational approach of cracking behavior (Kalkan, 2010; Mancuso & Bartlett, 2017; Bischoff, 2020).

*Corresponding Author, e-mail: erayozbek@gazi.edu.tr

The current study was conducted to estimate the immediate deflection of RC beams. For this purpose, half-scaled and T-sectioned RC beams with the reinforcement ratios of high, medium, and low were tested under monotonic loads. Afterwards, obtained experimental load-deflection relationships were compared with analytical ones proposed by Branson (1965) and Bischoff (2005) in accordance with the ACI 318-14 (2014) and ACI 318-19 (2019), respectively. Both methods gave quite close results to experimental values for the beams with low reinforcement ratio. However, they underestimated the deflections of medium and highly reinforced beams especially at service load levels. In other words, this is on the unsafe side. The latest research are still mainly focused on cracking behavior of RC members and estimating the effective moment of inertia. Consequently, sophisticated methods have been developed (Ammash et al., 2018; Arabshahi et al., 2022). In these approaches, even shear deformations were considered and taken into account (Kim et al., 2021). On the other hand, the effect of the elastic modulus of the concrete, which shows non-linear behavior with stress, was omitted. In other words, the specific behavior for one of the two main parameters affecting flexural stiffness is neglected in the calculations as far as the author knows. ACI 318-14 (2014) and ACI 318-19 (2019) permit to use a constant modulus of elasticity for these analyses. Thus, the nonlinear behavior of concrete that changes with stress was also considered in the subsequent analyzes to predict deflections as accurately as possible. The widely-accepted Hognestad (1951) concrete model was implemented into the calculations in order to reflect the effect of an elasticity modulus that changes with stress. Obtained results were presented graphically and discussed in terms of accuracy.

2. MATERIAL AND METHOD

2.1 Experimental Research

A set of ½ scaled and T-sectioned six RC beams were tested under monotonic four-point bending. Table 1 indicates the basic properties of these specimens. Dimensions and materials of the beam specimens were designed considering common practice and the experimental test setup limits. Ratio of the longitudinal reinforcement and flange thicknesses were selected as research parameters. Concrete of the specimens were cast monolithically. Figure 1 shows the dimensions and reinforcement detailing of the test specimens. The length of the RC beams was 3000 mm. The beam width, depth, and flange width of beams were 125/250/725 mm, respectively. Flange thickness was 100 or 75 mm based on the specimen type. For each specimen, the upper flange region was reinforced by orthogonally placed Ø5/75 (rebar diameter is 5 mm and center to center spacing is 75 mm) rebars. On the other hand, while the bottom region of the flange was reinforced with Ø5/75 for the longitudinal direction, the transverse direction was Ø5/150. Five millimeters of net concrete cover distance was adopted for the flange reinforcement.

Table 1. *Test specimen properties*

Specimen	Flange thickness (mm)	Compression rebars	Tension rebars	Reinforcement ratio (%)	
L75	75	2Ø8	3Ø8	low	0.51
M75	75	2Ø10	4Ø10	medium	1.07
H75	75	2Ø12	4Ø12	high	1.55
L100	100	2Ø8	3Ø8	low	0.51
M100	100	2Ø10	4Ø10	medium	1.07
H100	100	2Ø12	4Ø12	high	1.55

RC beams in this study were formed with three main longitudinal tension reinforcement ratios, which are low, medium, and high. Accordingly, beams with low reinforcement had 3Ø8 (3 rebars with a diameter of 8 mm) tension and 2Ø8 compression, medium reinforcement had 4Ø10 tension and 2Ø10 compression, high reinforcement had 4Ø12 tension and 2Ø12 compression rebars. Numerical expression of these tension reinforcement ratios were indicated in Table 1. Ten millimeters of net concrete cover was left for longitudinal rebars. Transverse reinforcement was detailed by double-legged stirrups of Ø5/100 mm which had 60 mm long 135° bended hooks. Stirrup detailing was kept the same along the length of all specimens. Transverse reinforcement was designed to prevent shear failures in the experiments.
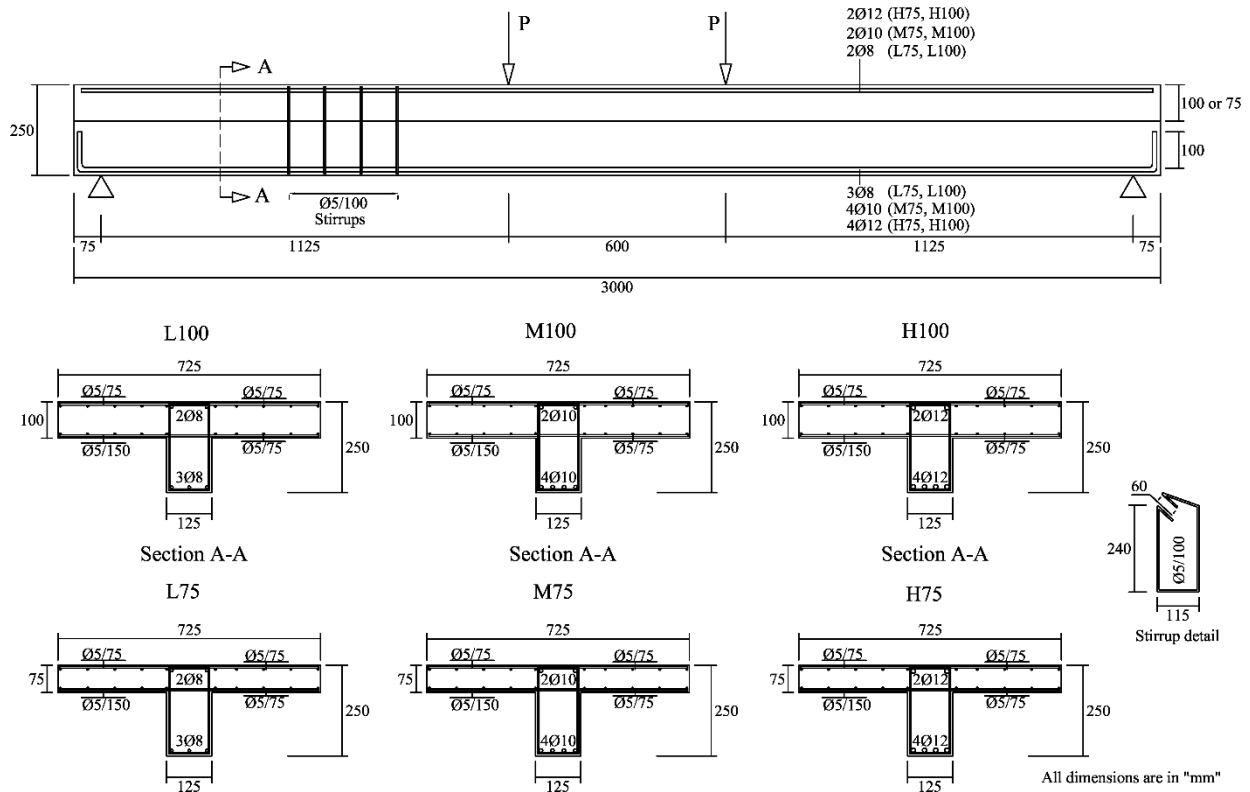
Figure 1. *Dimensions and detailing of test specimens*

Low and high longitudinal tension reinforcement ratios for the test specimens were designed according to TS500 (2000). While the low one corresponds to the minimum (ρ_{min}), the high one corresponds to the maximum (ρ_{max}) longitudinal reinforcing limits for flexural members and calculated by Eq. (1) and Eq. (2).

$$\rho_{min} = 0.8 \frac{f_{ctd}}{f_{yd}} \tag{1}$$

$$\rho_{max} = 0.85\rho_b \leq 0.02 \tag{2}$$

where f_{yd} is the design yield strength of longitudinal rebars and obtained by dividing characteristic strength to material factor of 1.15; f_{ctd} is the design tensile strength of concrete and obtained by dividing characteristic strength to material factor of 1.5; ρ_b is the reinforcement ratio for the balanced section. The medium reinforcement ratio was set by the arithmetic mean of these maximum and minimum boundaries.

The name of the specimens were determined to represent their test parameters. Accordingly, the first letter (H, M, or H) refers to the low, medium, and high reinforcement ratios by their initials. The following number indicates the flange thickness of the beam in millimeters as 75 or 100 (Table 1).

Concrete compressive strengths were determined based on standard 150×300 mm cylinder tests conducted on the 28th day of the casting. The same concrete mixing ratio was used for all specimens and there was not any chemical additives in it. At least ten concrete cylinder specimens were tested for each RC beam. Accordingly, the mean concrete compressive strength (f_c) of the concrete was calculated as 15.8 MPa, with a sample standard deviation of 0.63 MPa. Ribbed steel bars were used for the reinforcement. However, while Ø5 rebars were in S500 grade, Ø8, Ø10, and Ø12 rebars were in S420 grade. While S500 grade has a minimum yield strength (f_y) of 500 MPa and an ultimate strength (f_{su}) of 550 MPa, these values for S420 grade are 420 MPa and 500 MPa, respectively.

The experimental set-up was illustrated in Figure 2. Accordingly, RC beams were placed on simple supports. Tests were conducted in the closed steel frame. The load was acted by a hydraulic jack, and this load transmitted to the RC beam with the help of load-spreader steel shapes. The upper steel beam was utilized to divide the main load into halves. This simple supported steel beam had a clear span length of 600 mm and was standing on two steel shapes which were located on transverse direction of the RC beam. In this way, two uniformly distributed loads acted along the transverse direction of the test specimen. To ensure more even load distribution, rubber pads were also placed between the steel shapes and the RC beam. The acting force was measured by a canister type load cell which was attached to the hydraulic jack. The load cell had an accuracy of 0.25%. Linear variable differential transformers (LVDTs), which had an accuracy of 0.1%, were utilized to measure vertical displacements at the mid-span, loading projections, and supports. Since observed support settlements during the experiments were very close to zero, they were neglected during net displacement calculations. The vertical displacements measured from the loading projections were for curvature calculations and also a backup for the mid-span measurement. Monotonic quasi-static load was maintained up to 150 mm, which is the stroke length capacity of the hydraulic jack or a significant (at least 15%) decrease in the maximum load. All specimens experienced ductile flexural failure as expected. There was no sign of shear or bond damage. The experimental load-deflection diagrams of RC beams were plotted and shown in Figure 3 for comparison. In these diagrams, while the deflection axis corresponds to the net mid-span deflection, the load axis corresponds to the force measured by the load cell.
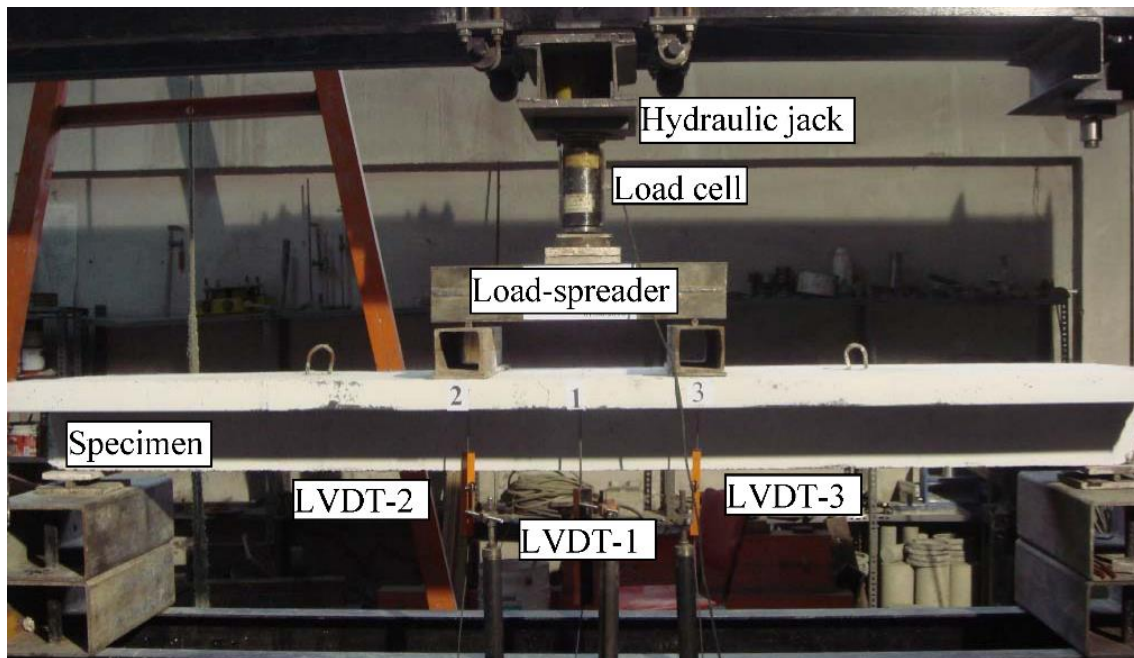
Figure 2. *Test set-up*

2.2 Analytical Study

Consecutively, the following steps were taken for predicting analytical load-deflection curves of the tested RC beams according to both methods developed by Branson (1965) and Bischoff (2005). Initially, the rupture modulus of concrete (f_r) was computed as 2.4 MPa by using the Eq. (3) according to (ACI 318-19, 2019):

$$f_r = 0.62\lambda\sqrt{f_c'} \qquad\qquad (3)$$

where λ is the lightweight concrete modification factor to account for the decreased mechanical properties and in this case $\lambda = 1$, f_c' is the specified compressive strength of concrete in MPa and was taken as 15 MPa based on cylinder tests.

The cracking moment (M_{cr}) was computed for the beams by the following Eq. (4) (ACI 318-19, 2019).

$$M_{cr} = \frac{f_r \, I_g}{y_t} \tag{4}$$

where y_t is the distance between gross section neutral axis and extreme fiber in tension, I_g is the gross-section moment of inertia by neglecting reinforcement. I_g was calculated as 325055499 mm⁴ and 328342608 mm⁴ for the beams with the flange thickness of 75 and 100 mm, respectively. Calculated M_{cr} values were explicitly given in Table 2.
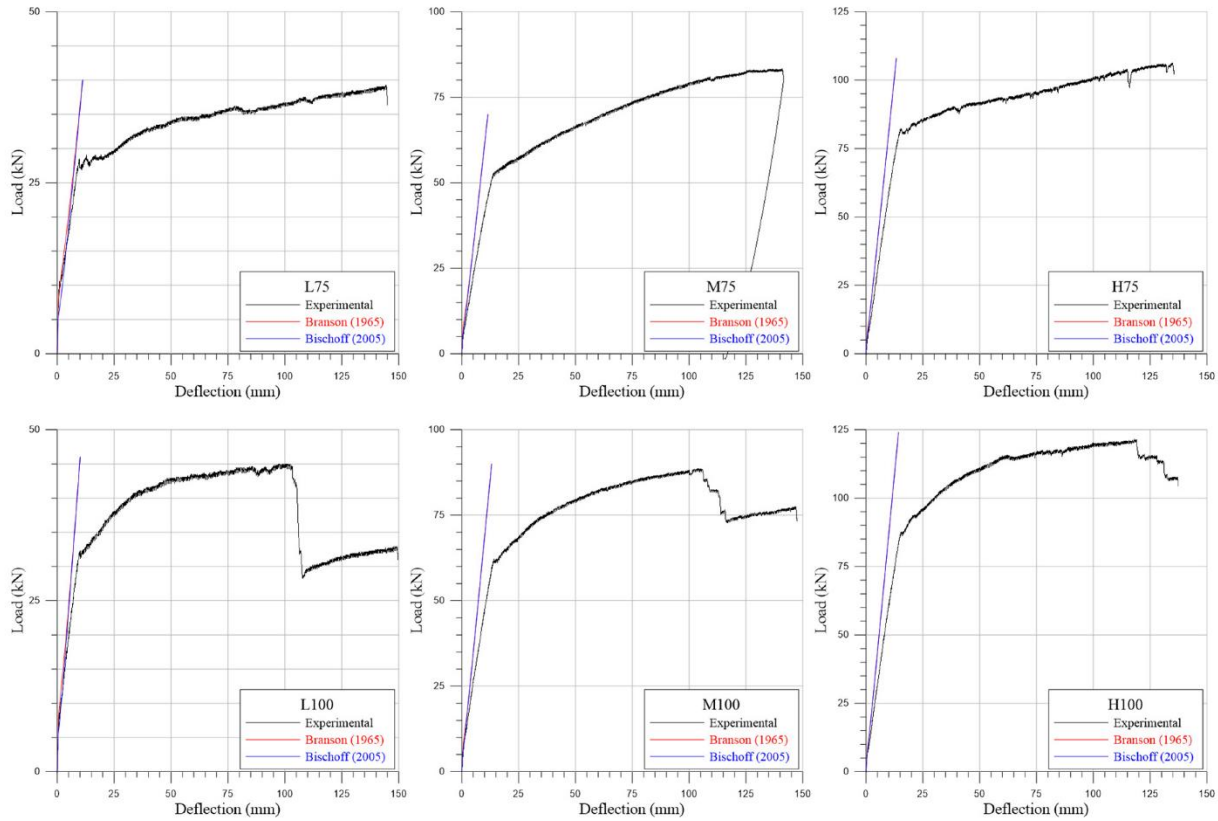

***Figure 3.** Analytical and experimental load-deflection diagrams*

***Table 2.** Used values for analytical approach*

Specimen	Tension reinforcement area (mm²)	Compression reinforcement area (mm²)	I_{cr} (mm⁴)	y_t (mm)	y_c (mm)	M_{cr} (kNmm)
L75	151	101	87601792	176.6	41.6	4416.5
M75	314	157	151440468	176.6	47.6	4416.5
H75	452	226	201074095	176.6	52.0	4416.5
L100	151	101	112361382	174.3	51.7	4520.7
M100	314	157	170151410	174.3	56.0	4520.7
H100	452	226	215662224	174.3	59.2	4520.7

The procedures for Branson (1965) and Bischoff (2005) methods are the same up to this stage. However, according to Branson (1965), if the RC member is cracked at one or more sections, immediate deflections should be calculated with the effective moment of inertia (I_e) given in Eq. (5) (ACI 318-14, 2014). On the other hand, according to Bischoff (2005), if the acting moment (M_a) is less than or equal to $2/3M_{cr}$, I_e can be taken equal to I_g. Otherwise, the following Eq. (6) should be used, if M_a is greater than $2/3M_{cr}$ (ACI 318-19, 2019).

$$I_e = \left(\frac{M_{cr}}{M_a}\right)^3 I_g + \left[1 - \left(\frac{M_{cr}}{M_a}\right)^3\right] I_{cr} \leq I_g \tag{5}$$

$$I_e = \frac{I_{cr}}{1 - \left(\frac{(2/3)M_{cr}}{M_a}\right)^2 \left(1 - \frac{I_{cr}}{I_g}\right)} \tag{6}$$

where I_{cr} is the cracked section moment of inertia which transformed in terms of concrete, I_g is the moment of inertia of gross concrete section about centroidal axis, neglecting reinforcement; M_a is the maximum moment acting on the RC member at stage deflection is calculated. I_{cr} was computed according to the derivations in ACI 435R-95 (2000) and shown for each specimen in Table 2. The elastic modulus of concrete (E_c) was computed according to ACI 318-19 (2019) and found as 18203 MPa by Eq. (7). Elastic modulus of the steel rebars (E_s) were taken as 200000 MPa.

$$E_c = 4700\sqrt{f_c'} \tag{7}$$

The following remaining procedures were applied to obtain the analytical load-deflection diagrams of the RC beams by both mentioned methods. Since measured deflections only include applied load, deflection resulted from self-weight was neglected. Acting load was started from zero and increased by 0.5 kN steps until the maximum load values in the experiments were achieved. Load steps were expressed in terms of M_a at the mid-span. Thus, I_e was computed for each M_a value by operating the protocols specific to each method.

Typical Eq. (8) was derived for computation of mid-span deflection (δ) for a simple supported beam subjected to two symmetrical concentrated loads. In the Eq. (8), P is one of the two acting concentrated loads and is equal to half of the total applied load; a is the shear span length which in this case equal to 1125 mm; L is the net span length and equal to 2850 mm for the current test set-up (Figure 1).

$$\delta = \frac{P\,a}{24\,E_c\,I_{ef}}(3L^2 - 4a^2) \tag{8}$$

Eventually, analytical load-deflection diagrams were drawn and presented with the experimental corresponding ones in Figure 3.

2.3 Proposed Method

In the proposed method, Eq. (6) which is adopted by ACI 318-19 (2019) was used as it is, except for the constant E_c assumption. As known, since the stress-strain behavior of concrete is nonlinear, it is possible to determine different E_c value for each point on the curve. The deviation from linearity becomes more obvious with increasing stress. Various models have been developed to express stress-strain relationship of concrete analytically (Hognestad, 1951; Hognestad et al., 1955; Desayi & Krishnan, 1964; Todeschini et al., 1964; Popovics, 1973; Carreira & Chu, 1985; Kumar, 2004). Among these, the widely-accepted Hognestad (1951) model with the Eq. (9) given below was selected for its convenience.

$$\sigma_c = f_c'\left[\frac{2\varepsilon_c}{\varepsilon_{co}} - \left(\frac{\varepsilon_c}{\varepsilon_{co}}\right)^2\right] \text{ for } \varepsilon_c \leq \varepsilon_{co} \tag{9}$$

where σ_c is the stress in concrete; ε_{co} is the strain corresponding with the maximum stress f_c'; ε_c is the stain in which the stress is computed. If $\varepsilon_c = \sigma_c/E_c$ is substituted in the Eq. (9), and then solved for E_c, following Eq. (10) can be obtained for the valid root. Thus, E_c could be defined as a secant modulus for each σ_c value.

$$E_c = \frac{f_c'[1 + \sqrt{1 - (\sigma_c/f_c')}\,]}{\varepsilon_{co}} \tag{10}$$

In Eq. (10), ε_{co} was taken as 0.002 which is valid for most of the cases (CEB-FIB, 1970). $f_c{}'$ was 15 MPa based on cylinder tests. σ_c was calculated for each M_a value according to the adopted practical approach by Eq. (11).

$$\sigma_c = \frac{M_a \, y_c}{I_e} \tag{11}$$

where y_c is the distance between neutral axis and the extreme fiber in compression. The value of y_c was calculated by the derivations of flanged sections with compression steel based on the ACI 435R-95 (2000) and given for each specimen explicitly in Table 2. I_e was computed by Eq. (6) which is Bischoff (2005) approach due its more rational results than the Branson (1965).

In this way, the analytical load-deflection diagram of the specimens plotted by using stress-varying modulus of elasticity were illustrated in Figure 4 with the previously drawn ones in Figure 3. Note that some portions of the post-yielding experimental curves were removed in order to make precise evaluations on a larger scale.
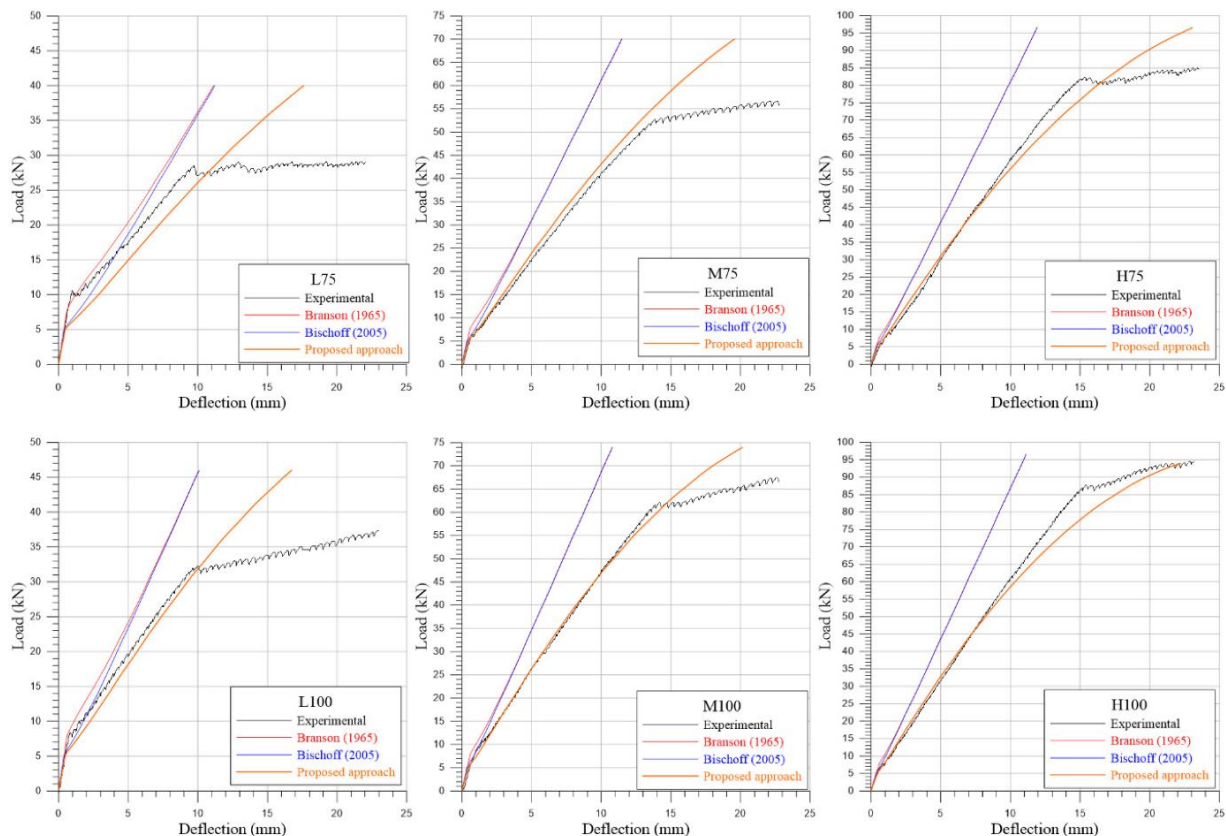
Figure 4. *Initial load-deflection curves including proposed ones*

3. RESULTS AND DISCUSSION

First point of the slope change in the load-deflection diagrams corresponds to the cracking load of the RC beams (Figure 4). Branson (1965) and Bischoff (2005) equations mostly underestimated the deflections after cracking. The deviation was more obvious for the medium and high reinforcement ratios (Figure 3). Exceptionally, Bischoff (2005) method slightly overestimated deformations up to approximately 1.5 times the experimental cracking load for beams with low reinforcement ratios (Figure 4). While Branson's (1965) approach was better for estimating the cracking behavior in RC beams with low reinforcement ratios, Bischoff's (2005) was better for medium and highly reinforced beams. Both methods resulted in almost equal deflections after about 2.5 times the experimental cracking loads. Therefore, the effects of the methods on behavior were dominant only for beams with low reinforcement. On the other hand, the proposed approach,

using stress-varying modulus of elasticity, had negligible impact on the cracking behavior even for beams with low reinforcement as expected. In other words, using stress-varying modulus of elasticity in Bischoff's (2005) equation did not make any difference from an engineering point of view (Figure 4).

Immediate deflections are mostly calculated under service loads. Therefore, the accuracy of deflection calculation is much more significant for loads at this level. The service load level for an RC beam approximately corresponds to 65% of the yielding load of the beam (P_y) when gravity load and flexural resistance factors are considered in the design codes (ACI 318-19, 2019). Experimental P_y values were apparent and directly obtained from load-deflection curves of the test specimens (Figure 3). Experimental and analytical deflections correspond to experimental $0.65P_y$ were considered service deflections (δ_s) and given in Table 3.

Branson (1965) and Bischoff (2005) equations gave the same results at the service loads for the RC beams with high and medium reinforcement ratios. On the other hand, Bischoff (2005) equation resulted slightly more deflections for the beams with low reinforcement. Nevertheless, both equations in their current form constantly underestimated the deflections for the service loads. They predicted almost 30% less than the experimental results for highly and medium reinforced beams. At low reinforcement ratios, this value was on average 22% and 14% less for Branson (1965) and Bischoff (2005), respectively. In other words, Bischoff (2005) correlated better with the experimental results. On the other hand, the proposed approach, using stress-varying modulus of elasticity, was in close agreement with the experimental results. The proposed approach estimated the deflection of the L75 specimen 23% more at service load levels. However, the overestimation was only 7% for specimen L100 which could be considered equivalent to L75. Thus, this contradiction was attributed to random causes arising from specific behavior of RC members. Nevertheless, it should not be disregarded that the deviation was in the safe region. When specimen L75 was excluded from the evaluation, the difference varied between +7% and -6%. Additionally, this range corresponded to deviations below 0.5 mm (Table 3).

Table 3. *Service load deflections of specimens*

Specimen	Experiment yield load, P_y (kN)	Experiment $0.65P_y$ (kN)	Experiment δ_s (mm)	Branson δ_s		Bischoff δ_s		δ_s of the proposed approach	
				mm	Rel.	mm	Rel.	mm	Rel.
L75	28	18.2	5.2	4.2	0.81	4.8	0.92	6.4	1.23
M75	52	33.8	8.0	5.5	0.69	5.5	0.69	7.5	0.94
H75	82	53.3	9.1	6.6	0.73	6.6	0.73	9.4	1.03
L100	32	20.8	5.5	4.1	0.75	4.4	0.80	5.9	1.07
M100	61	39.7	8.3	5.8	0.70	5.8	0.70	8.2	0.99
H100	86	55.9	9.1	6.4	0.70	6.4	0.70	9.4	1.03

Rel.: The ratio of the analytical deflection to the experimental deflection

In the proposed approach, the best fit was observed in the behavior of medium reinforced beams. The curves almost overlap to the yield point. A similar favorable consistency was valid for specimen L100. In specimen L75, while the current approaches mostly underestimate the deflection, the proposed approach overestimate in the same proximity (Figure 4). The agreement between the experimental curves gradually decreased as they got closer to yield in highly reinforced RC beams. However, the proposed approach resulted deflections much more close to the experimental ones even in the yield regions. Moreover, slight deviations were on the conservative side (Figure 4).

4. CONCLUSION

In this study, T-sectioned six RC beams with low, medium, and high reinforcements were tested and experimental load-deflection diagrams were obtained. Deflections were calculated according to Branson (1965) and Bischoff (2005) by using constant modulus of elasticity as it is recommended by ACI 318-14 (2014) and ACI 318-19 (2019), respectively. Afterwards, the nonlinear behavior of concrete that changes with stress was also taken into account for the Bischoff (2005) method to predict deflections as accurately as possible. The widely-accepted and practical Hognestad (1951) concrete stress-strain relationship was implemented in the proposed approach. Consistency between the analytical and experimental results was evaluated. In the current section, significant outcomes of the study were presented. On the other hand, it should be noted that the results are based on data from a limited number of test specimens. For this reason, solid and absolute judgements should be avoided.

When Branson (1965) and Bischoff (2005) equations were compared, Branson (1965) approach simulated the cracking behavior of RC beams with low reinforcement ratios better than Bischoff (2005). On the other hand, Bischoff (2005) approach was better for the tested medium and highly reinforced beams. Both deflection calculation methods did not result any significant difference under the assumed service loads and constantly underestimated the experimental deflections. The reached deviation was 30% less than the experimental results for high and medium reinforcement ratios.

Deflections could be calculated more accurately when non-linear stress-strain behavior of concrete was deployed in Bischoff (2005) approach. The proposed approach was able to estimate the experimental deflections under service loads with an average proximity of 5%. Moreover, this average value was on the safe side. The best fit to the experimental load-deflection curves was observed in medium reinforced beams which is valid for most of the case.

CONFLICT OF INTEREST

The author declares that there is no conflict of interest.

REFERENCES

AASHTO. (2005). LRFD bridge design specifications, American Association of State Highway and Transportation Officials, USA.

ACI 318-14. (2014). Building code requirements for structural concrete and commentary, American Concrete Institute, USA.

ACI 318-19. (2019). Building code requirements for structural concrete and commentary. American Concrete Institute, USA.

ACI 435R-95. (2000). Control of deflection in concrete structure. American Concrete Institute, USA.

AS 3600-2009. (2009). Australian standard for concrete structures. Standards Australia, Australia.

Ammash, H., Hemzah, S., & Al-Ramahee, M. (2018). Unified advanced model of effective moment of ınertia of reinforced concrete members. *International Journal of Applied Engineering Research*, *13*(1), 557-563.

Arabshahi, A., Tavakol, M., Sabzi, J., & Gharaei-Moghaddam, N. (2022). Prediction of the effective moment of inertia for concrete beams reinforced with FRP bars using an evolutionary algorithm. *Structures*, *35*, 684-705. doi:10.1016/j.istruc.2021.11.011

Bischoff, P. H. (2005). Revaluation of deflection prediction for concrete beams reinforced with steel and fiber reinforced polymer bars. *Journal of Structural Engineering*, *131*(5), 752-767. doi:10.1061/(ASCE)0733-9445(2005)131:5(752)

Bischoff, P. H. (2020). Comparison of existing approaches for computing deflection of reinforced concrete. *ACI Structural Journal*, *117*(1), 231-240. doi:10.14359/51718072

Branson, D. E. (1965). Instantaneous and time-dependent deflection on simple and continuous reinforced concrete beams (HPR Report No.7), Highway Department Bureau of Public Roads, USA.

Carreira, D. J. & Chu, K. D. (1985). Stress-strain relationship for plain concrete in compression. *ACI Journal Proceedings*, *82*(6), 797-804.

CEB-FIB. (1970). International recommendations for the design and construction of concrete structures: principles and recommendations, Comité Euro-International-Federation Internationale de la Précontrainte, London, UK.

CSA A23.3-04. (2004). Design of concrete structures, Canadian Standards Association, Canada.

Desayi, P. & Krishnan S. (1964). Equation for the stress strain curve of concrete. *ACI Journal Proceedings*, *61*(3), 345-350.

Hognestad, E. (1951). A study of combined bending axial load in reinforced concrete members. University of Illinois Bulletin Series No. 399. The University of Illinois Engineering Experimental Station, USA.

Hognestad, E., Hanson, N. W., & McHenry, D. (1955). Concrete stress distribution in ultimate strength design. *ACI Journal Proceedings*, *52*(4), 455-480. doi:10.14359/11609

Kalkan, İ. (2010). Deflection prediction for reinforced concrete beams through different effective moment of ınertia expressions. *International Journal of Engineering Research and Development*, *5*(1), 72-80.

Kim, S.-W., Han, D.-S., & Kim, K.-H. (2021). Evaluation of shear effect on deflection of RC beams. *Applied Sciences*, *11*(16), 7690. doi:10.3390/app11167690

Kumar, P. A. (2004). Compact analytical material model for unconfined concrete under uni-axial compression. *Materials and Structures*, *37*(9), 585-590. doi:10.1007/BF02483287

Mancuso, C., & Bartlett, F. M. (2017). ACI 318-14 criteria for computing instantaneous deflections. *ACI Structural Journal*, *114*(5), 1299-1310. doi:10.14359/51689726

Popovics, S. A. (1973). Numerical approach to the complete stress-strain curve of concrete. *Cement and Concrete Research*, *3*(5), 583-599. doi:10.1016/0008-8846(73)90096-3

Todeschini, C. E, Bianchini, A. C., & Kesler, C. E. (1964). Behavior of concrete columns reinforced with high strength steels. *ACI Journal Proceedings*, *61*(6), 701-716.

TS500. (2000). Requirements for design and construction of reinforced concrete structures, Turkish Standarts Institute, Turkey.

Gazi University
Journal of Science
PART A: ENGINEERING AND INNOVATION

Synthesis, Characterization, Optical and Thermal Properties of P(NVC-co-BZMA) Copolymer and Its ZnO Composites

Esra BARIM[1]

[1]Vocational School of Tunceli, University of Munzur, Tunceli, 62000, Türkiye

Keywords	Abstract
N-vinylcarbazole Benzyl Methacrylate (BZMA) Zinc Oxide Composite Optical Properties Thermal Analysis	Recent studies have paid particular attention to polymer-nanoparticle composite materials considering they have a number of interesting properties, which include optical, thermal, electrical, and others (Reyna-Gonzalez et al., 2009; Yakuphanoglu et al., 2010). In this study, a free radical polymerization process was used to create a copolymer of N-vinylcarbazole (NVC) and benzyl methacrylate (BZMA) at 25–75 mol% each. The procedure was conducted at 70°C with azobisisobutyronitrile (AIBN) acting as the initiator. Nano zinc oxide powders were then added to composites at three different ratios of 5%, 10%, and 15% weight of the copolymer. In order to better understand the structures of the P(NVC-co-BZMA) and its composites, FT-IR, ^{1}H NMR, and UV spectroscopic techniques were also implemented. The optical characteristics of both the pure copolymer and its composites were examined. In the visible region, the composite containing 15% nano ZnO had the highest optical absorbance value. Additionally, the thermal behaviours of the composites and copolymers were analysed.

1. INTRODUCTION

The presence of two monomers with different properties in a polymer chain with different compositions can give the polymer new properties (Saçak, 2012). Copolymerization is a method that can be used for this purpose and is of great technological importance. Furthermore, the structures obtained by adding nano- or macro-sized reinforcing materials to polymers and called polymer composites significantly change the properties of polymer materials.

NVC and BZMA monomers are among the polymers studied in copolymerization reactions in terms of some the properties that they exhibit. The high softening temperature of N-vinylcarbazole, an aromatic vinyl monomer, has caused it to become the subject of copolymerization studies with different monomers. One of the aims of these studies has been to obtain polymers with a lower softening temperature than P(NVC) (Isusi et al., 2006). Moreover, NVC has attracted attention due to its optical applications and is considered worthy of research in this field. There have also been composite studies with ZnO to improve the properties of P(NVC) (Ghosh & Biswas, 2009). Ghosh et al. (2010) studied the dielectric properties of P(NVC), a conducting polymer, by preparing its composites with acetylene black and ZnO separately and found that the nanocomposite of poly(N-vinylcarbazole) with acetylene black exhibited a negative dielectric constant at high frequency. Goumri et al. (2020) synthesized composites of P(NVC) with graphene oxide and emphasized that the electrical conductivity can be improved depending on the varying graphene oxide ratio. Benzyl Methacrylate (BZMA) is a methacrylic monomer containing the phenyl group in its structure. Although it has many applications (Aqel et al., 2013; Li et al., 2014), it has generally been used in

*Corresponding Author, e-mail: esrabarim@munzur.edu.tr

copolymerization studies to obtain thermal functionality (Ueno, 2018). For example, Liu et al. (2022) synthesized a series of copolymers with different BZMA and MMA compositions as microspheres and emphasized that some properties of the copolymer such as thermal stability and glass transition temperature (Tg) can be changed depending on the monomer compositions. There are also composite studies on BZMA in the literature. Demirelli et al. (2022a) prepared composites of BZMA with lactone end groups with graphene and reported that the composite material's thermal stability saw an increase that followed that of the amount of graphene doped, but the Tg value decreased.

Thermal degradation kinetic data of polymers is an important parameter to understand the degradation process of the polymer. Thermogravimetric analysis (TGA) is one of the most often used methods of analysis in the examination of the kinetics of polymer thermal degradation and it entails evaluating the activation energy of the thermal degradation of polymers. All kinetic studies are based on the assumption that the isothermal rate conversion dα/dt is a linear function of k(T), which is a temperature-dependent rate constant, and f(α), which is a function of conversion independent of temperature. This is written as follows:

$$\frac{d\alpha}{dt} = k(T)f(\alpha) \tag{1}$$

The activation energy is normally pinpointed through attaching kinetic data to various reaction models, yielding the Arrhenius parameters:

$$k(T) = A \exp\left(-\frac{Ea}{RT}\right) \tag{2}$$

Here, A is a pre-exponential factor assumed to be independent of temperature, E_a represents activation energy, T is absolute temperature, and R is the universal gas constant (R = 8.314 J/mol K). When these are combined, the following equation can be written:

$$\frac{d\alpha}{dt} = A \exp\left(-\frac{Ea}{RT}\right)f(\alpha) \tag{3}$$

For non-isothermal measurements at a constant heating rate of $\beta = \frac{dT}{dt}$ equation (3) transforms to the following:

$$\beta\left(\frac{d\alpha}{dT}\right) = A \exp\left(-\frac{Ea}{RT}\right)f(\alpha) \tag{4}$$

Activation energy E_a may be determined by a variety of techniques and, in particular, the Flynn-Wall-Ozawa (FWO) and Kissinger-Akahira-Sunose (KAS) models are frequently utilized in the calculation of the activation energy of polymer thermal degradation (Barim, 2021; Demirelli et al., 2022b). Both are integral methods that are independent of the reaction order. In the Flynn-Wall-Ozawa method, parallel lines are attained by plotting *Log β* against *1/T(K⁻¹)* various rates of heating. By calculating the slope of these lines, the activation energy (Ea) is achieved. The FWO method uses the following equation 5 (Ozawa, 1965; Flynn & Wall, 1966):

$$log(\beta) = \log\left[\frac{AEa}{g(a)R}\right] - 2.315 - \frac{0.457\,Ea}{RT} \tag{5}$$

In the equation above, g(α) is an unknown function of conversion. According to this equation, the activation energy *(–0.457 Ea/RT)* is calculated using the slope of the *Log β - 1/T(K⁻¹)* graph.

When implementing the KAS method to uncover the activation energy, ln*(β/T²)* is plotted against *1/T(K⁻¹)*. The Ea value is calculated from the slope of the linear line obtained from this graph. The equation of the KAS method is defined as follows (Kissinger, 1957):

$$\ln\left(\frac{\beta}{T^2}\right) = \ln\left(\frac{AR}{g(\alpha)Ea}\right) - \frac{Ea}{RT} \qquad (6)$$

The primary purpose of the present study was to synthesize, characterize, and make composites of a copolymer not encountered in the literature. Following this, it was to reveal the thermal degradation parameters, activation energies (with FWO and KAS method), and optical properties of both copolymer and composites. For this purpose, the P(NVC-co-BZMA) copolymer was synthesized, its structure was elucidated, and the composites of this copolymer with 5, 10 and 15 wt% nano ZnO were then prepared. Finally, the thermal and optical properties of copolymers and composites were investigated.

2. MATERIALS AND METHODS/EXPERIMENTAL METHODS

Benzyl methacrylate (BZMA) and N-vinylcarbazole (NVC) monomers were purchased commercially from Sigma-Aldrich. ZnO NPs a purity of 99.5% were obtained from Nanography Nanotechnology (Ankara, Turkey).

2.1. Preparation of P(NVC-co-BZMA) Copolymer

The P(NVC-co-BzMA) copolymer was synthesized by free radical polymerization method using 25 mol% NVC and 75 mol% BZMA monomers in the company of the AIBN initiator in 1,4-dioxane solvent submerged in a 70°C oil bath. Polymerization was performed for 12 hours. The copolymer was precipitated in ethyl alcohol solvent and this process was repeated 3 times. It was later dried in a vacuum oven at 40 °C for 24 hours. Structural characterization of the copolymer was performed by the spectroscopic methods of FT-IR and ^{1}H NMR. Thermal characterization was also carried out with a TGA-DTA system. UV spectra were recorded and optical properties were analysed. The reaction scheme for the poly(NVC-co-BZMA) copolymer system is shown in Figure 1.
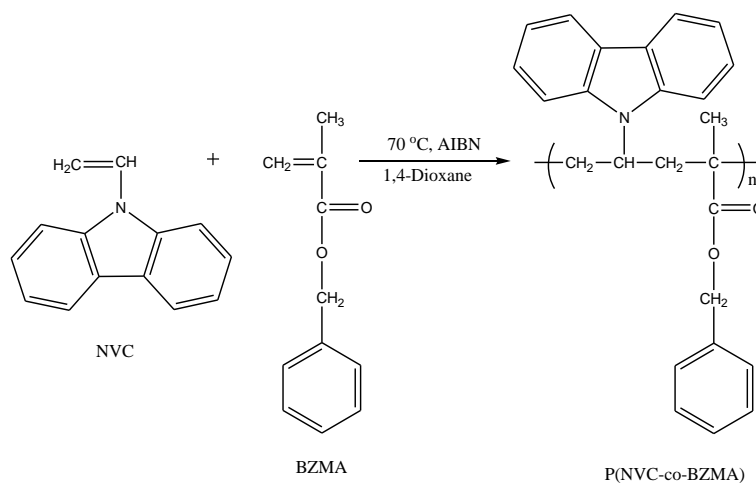
Figure. 1. Synthesis scheme of the poly(NVC-co-BZMA) copolymer

2.2. Preparation of P(NVC-co-BZMA) Copolymer Composites with Nano ZnO

Three composites of P(NVC-co-BZMA) copolymer containing 5, 10, and 15 wt% nano ZnO were prepared using the solvent casting method. Accordingly, certain amounts of P(NVC-co-BZMA) copolymers were dissolved in dichloromethane solvent in three separate beakers. Then 5, 10, and 15 wt% nano ZnO was weighed according to the amount of dissolved copolymer and dispersed in the dichloromethane solvent in three separate beakers for 2 h. Finally, the dispersed nano ZnO and copolymer solutions were mixed. The obtained nanocomposites were first mixed using an ultrasonic pen for two min and then the mixing process was continued with a magnetic stirrer overnight and the solvent of the composites was removed in a rotary evaporator. The composites were dried at a temperature of 40 °C inside a vacuum oven before determining the constant weight. Structural characterization of the composites was performed using the FT-IR spectroscopic method and thermal characterization by TGA-DTA dual system. UV spectra were taken and the optical properties were analyzed.

3. RESULTS AND DISCUSSIONS

3.1. FT-IR Spectroscopy

When the FT-IR spectrum of the P(NVC-co-BZMA) copolymer shown in Figure 2 was examined, the main peaks characterizing the copolymer were found as follows: peaks of aromatic C-H stretching vibrations between 2980–3048 cm^{-1}, peaks of aliphatic C-H stretching vibrations between 2840 and 2980 cm^{-1}, peak of ester carbonyl at 1723 cm^{-1}, peak of C=C stretching vibrations in the aromatic ring at 1450 cm^{-1}, peak of vinylidene at 1330 cm^{-1}, peaks of the (-C=O)-O-C group between 1156 and 1240 cm^{-1}, and peaks of C-H stretching vibrations of monosubstituted benzene at 695 cm^{-1}. The peak at 837 cm^{-1}, due to the nano ZnO, was below the peak at the same location in the composite structure and caused this peak to broaden (Haldar et al., 2011; Bashir et al., 2022).
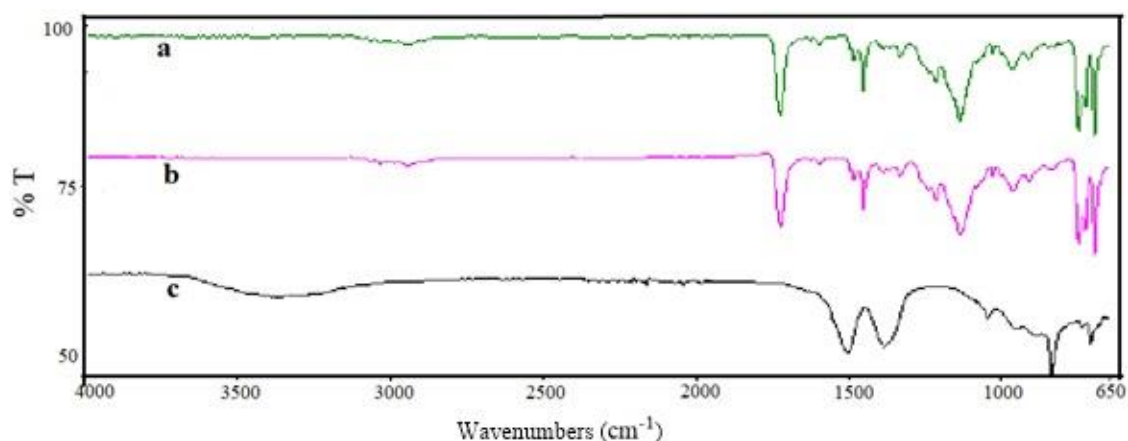
Figure. 2. FT-IR spectra of a) P(NVC-co-BZMA), b) P(NVC-co-BZMA)/ZnO 15%, and c) nano ZnO

3.2. ^{1}H-NMR Spectroscopy

The ^{1}H NMR spectrum of the copolymer which can be observed in Figure 3 was obtained using a Bruker 400 MHz AVIII 400 model NMR device in CDCl$_3$ solvent. In the ^{1}H NMR spectrum of the copolymer, the peaks between 0.5 and 2 ppm indicated CH$_3$ and CH$_2$ protons in the main chain of the polymer, the peak at 4.9 ppm indicated O-CH$_2$ protons belonging to the BZMA monomer, and the peaks between 6.8 and 7.9 ppm indicated protons originating from the aromatic ring in the NVC and BZMA monomers.
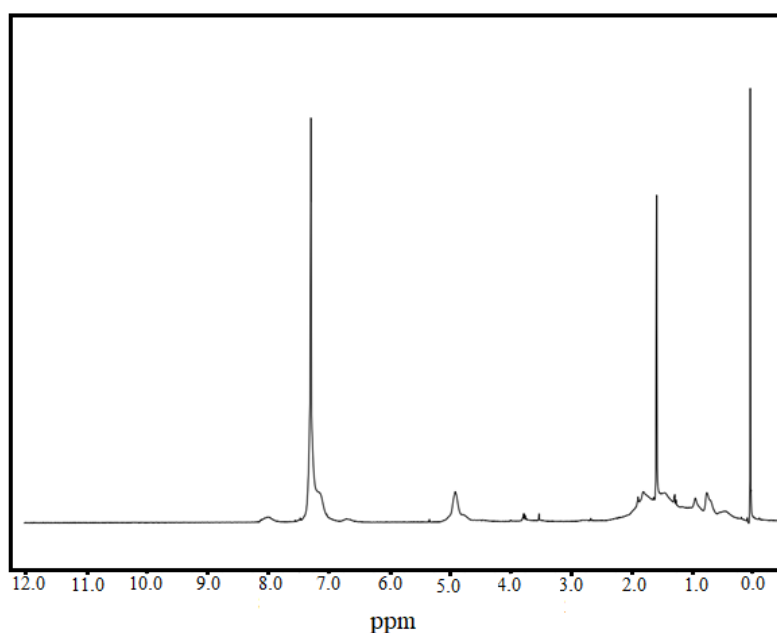
Figure. 3. ^{1}H NMR Spectrum of the P(NVC-co-BZMA)

3.3. Thermal Analyses of the Copolymers and Composites

Determination of the copolymer and composite TGA curves required the use of a Perkin Elmer SII 7300 model TGA/DTA dual system. The thermal analysis curves of the copolymers and composites were obtained by heating them to 500 °C in aluminium vessels at a rate of 20 °C/min in a nitrogen gas atmosphere and are shown in Figure 4. Initial degradation temperatures, glass transition temperatures (Tg), temperatures corresponding to a given degradation, and Table 1 shows the waste calculations taken from TGA thermograms.
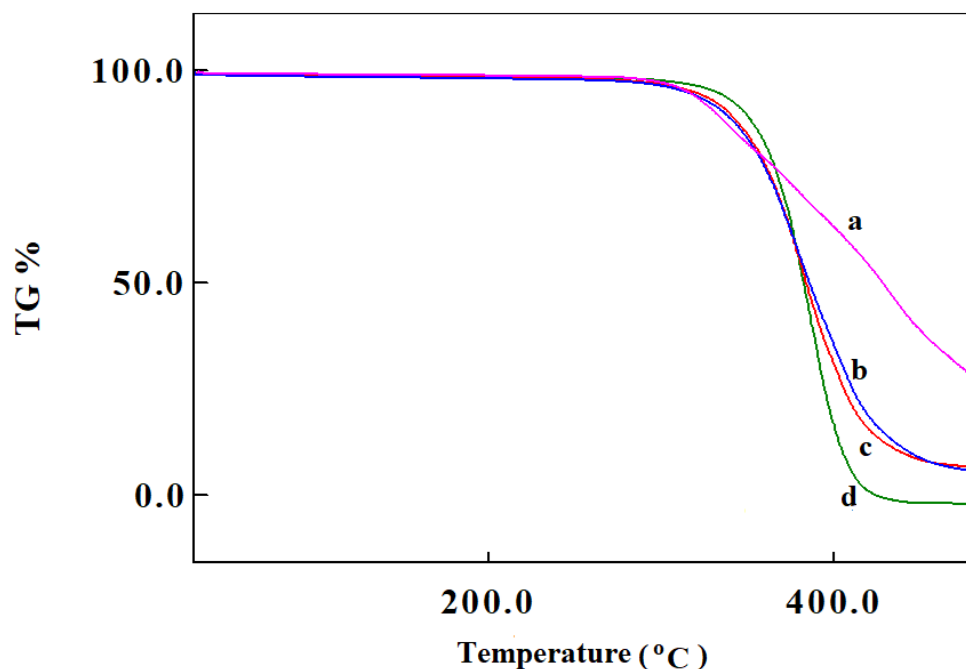
Figure. 4. *TGA curves of the copolymers and their composites; a) P(NVC-co-BZMA)/ZnO 15%, b) P(NVC-co-BZMA)/ZnO 10%, c) P(NVC-co-BZMA)/ZnO 5% and d) P(NVC-co-BZMA)*

Table 1. *The results of 20°C TGA for P(NVC-co-BZMA) and composite systems (Decomposition characteristics of copolymer and its composites with ZnO)*

Polymer / Composite	Tg (°C)	IDT[a] (°C)	Temperatures (°C) at certain % weight losses					
			10	30	50	70	90	% Residue at 500°C
P(NVC-co-BZMA)	94	310	348.5	371	382	392	404.5	-
P(NVC-co-BZMA)/ZnO 5%	96	299	339	368.2	383.5	400	-	6.5
P(NVC-co-BZMA)/ ZnO 10%	98	300	336	367.7	385	405	443	5.5
P(NVC-co-BZMA)/ ZnO 15%	99	302	331.4	382.5	427	473.7	-	27

a: Initial decomposition temperature

3.3.1. Calculation of the Activation Energy of P(NVC-co-BZMA) and P(NVC-co-BZMA)/ZnO 10%

The thermal degradation kinetics of the P(NVC-co-BZMA) and P(NVC-co-BZMA)/ZnO 10% were examined by means of TGA thermograms. For this purpose, both the copolymer and composite samples were heated under nitrogen atmosphere from 30 °C to 500 °C; the rate was 10, 15, 20, and 25 °C/min for copolymer samples and 10, 15, 25, and 35 °C/min for composite samples. From the obtained thermograms, the degradation temperatures of the polymer with different transformations were determined. Using these data, the thermal degradation activation energies of the copolymer and composite samples were calculated according to the FWO and KAS methods. Thermal degradation activation energy plots of the P(NVC-co-

BZMA) copolymer calculated based on the FWO and KAS methods have been provided in Figure 5 and 6. The calculated values for activation energy according to these methods are shown in Table 2.
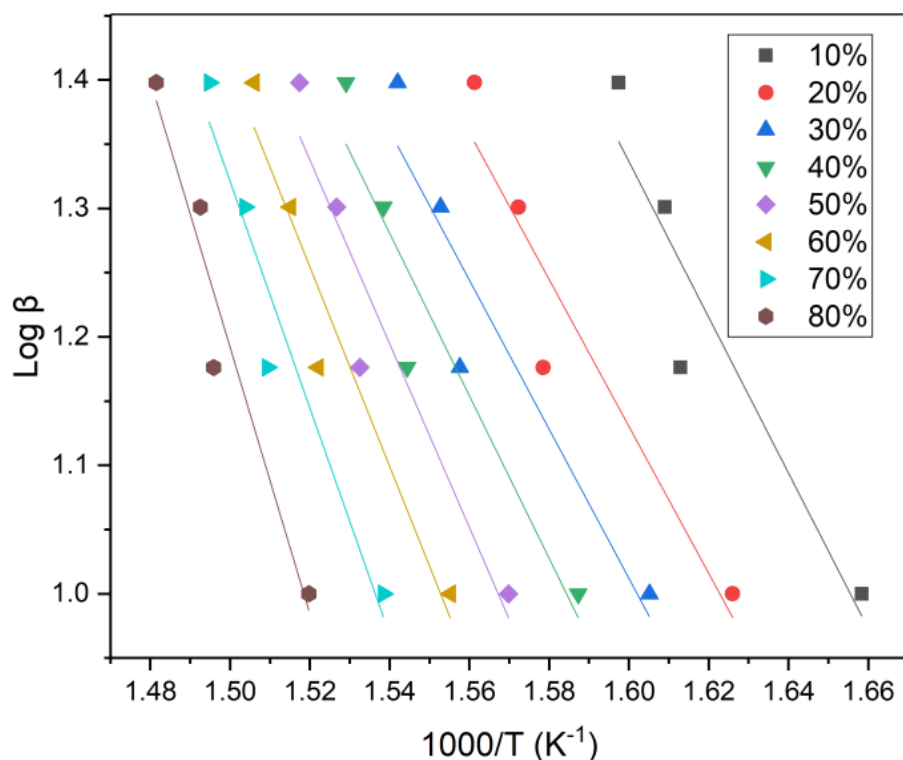
Figure. 5. *Determination of the activation energy of P(NVC-co-BZMA) calculated by FWO models*
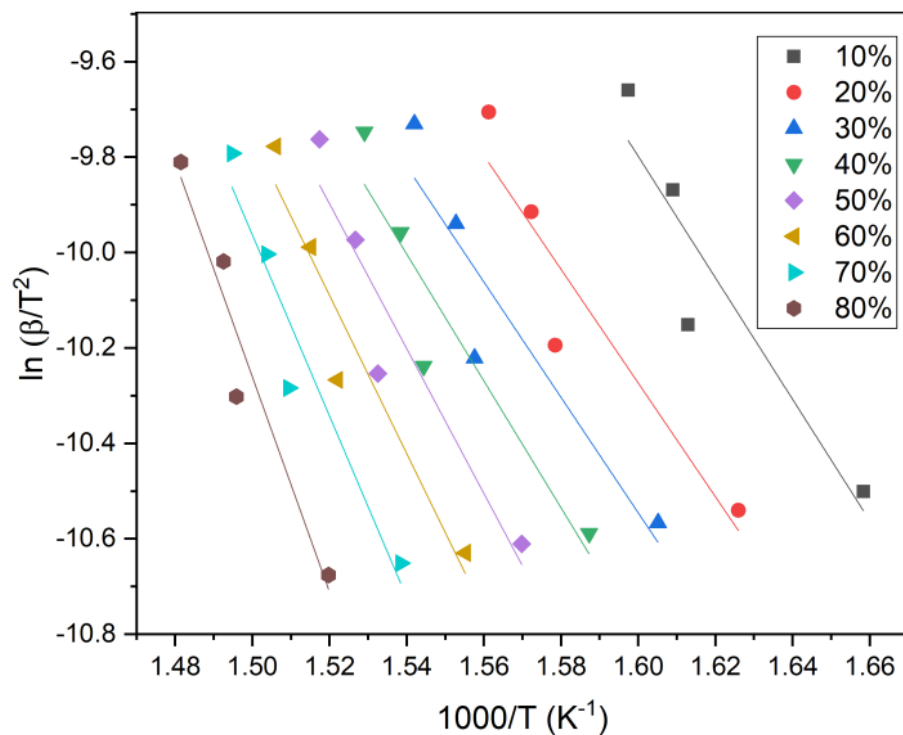
***Figure. 6.*** *Determination of the activation energy of P(NVC-co-BZMA) calculated by KAS models*

Thermal degradation activation energy plots of the P(NVC-co-BZMA)/ZnO 10% composite calculated according to the FWO and KAS methods can be observed in Figure 7 and 8, while calculated values for activation energy according to both methods are highlighted in Table 3.

Table 2. *Activation energy values estimated by FWO and KAS Methods for P(NVC-co-BZMA)*

Flynn–Wall–Ozawa (FWO) Method		Kissinger–Akahira–Sunose (KAS) Method	
Conversion/α	Ea (kJ/mol)	Conversion/α	Ea (kJ/mol)
0.1	110.257	0.1	105.820
0.2	104.025	0.2	99.044
0.3	105.602	0.3	100.574
0.4	115.144	0.4	110.509
0.5	130.105	0.5	126.148
0.6	141.214	0.6	137.746
0.7	160.431	0.7	157.866
0.8	188.620	0.8	187.414
Average	131.924	Average	128.140
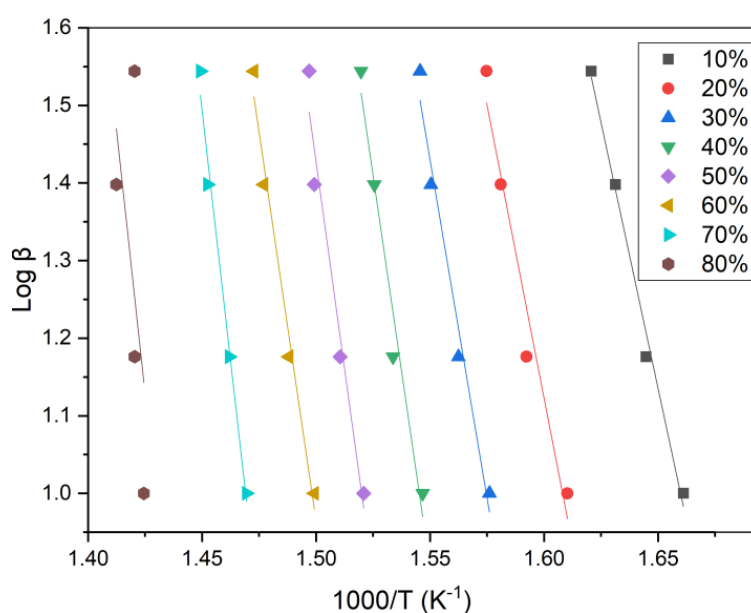
Figure. 7. *Determination of the activation energy of P(NVC-co-BZMA)/ZnO 10% calculated by FWO models*
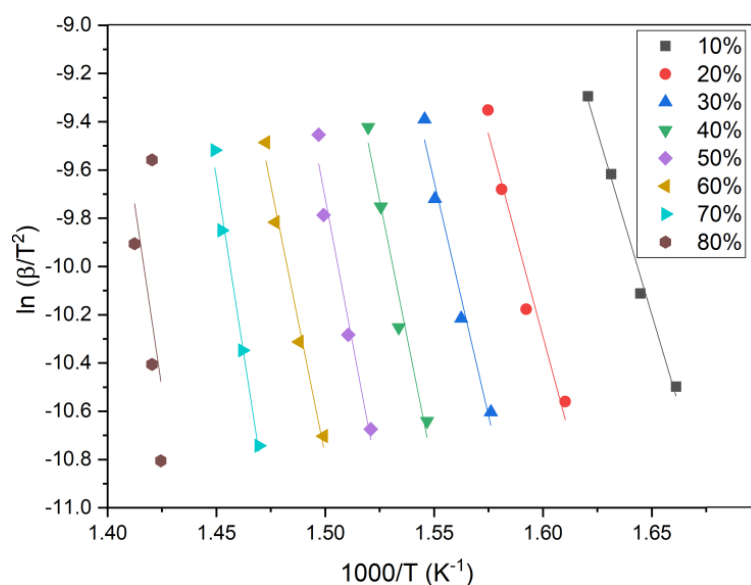
Figure. 8. *Determination of the activation energy of P(NVC-co-BZMA)/ ZnO 10% calculated by KAS models*

Table 3. *Activation energy values estimated by FWO and KAS Methods for P(NVC-co-BZMA)/ ZnO 10%*

Flynn–Wall–Ozawa (FWO) Method		Kissinger–Akahira–Sunose (KAS) Method	
Conversion/α	**Ea (kJ/mol)**	**Conversion/α**	**Ea (kJ/mol)**
0.1	249.183	**0.1**	242.080
0.2	274.653	**0.2**	268.580
0.3	317.096	**0.3**	313.015
0.4	367.162	**0.4**	361.518
0.5	388.447	**0.5**	383.725
0.6	364.633	**0.6**	360.500
0.7	470.459	**0.7**	470.658
0.8	492.927	**0.8**	493.982
Average	**365.573**	**Average**	**361.757**

3.4. Optical Properties

P(NVC-co-BZMA) films doped with 5, 10, 15 wt% ZnO were prepared using the sol gel drop coating method. UV measurements on the thin film samples were taken with a UV3600 SHIMADZU UV-VIS-NIR spectrophotometer. Transmittance and absorbance graphs were drawn using the data obtained from UV measurements. UV spectra of P(NVC-co-BZMA) copolymer and composites were examined. Results are shown in Figure 9 and 10.

The transmittance-wavelength spectra revealed that the undoped P(NVC-co-BZMA) copolymer had the highest optical transmittance in the visible region when compared to its nano ZnO-doped composites. In the same region, the P(NVC-co-BZMA)/ZnO 15% composite with the highest doping ratio was found to have the lowest optical transmittance.
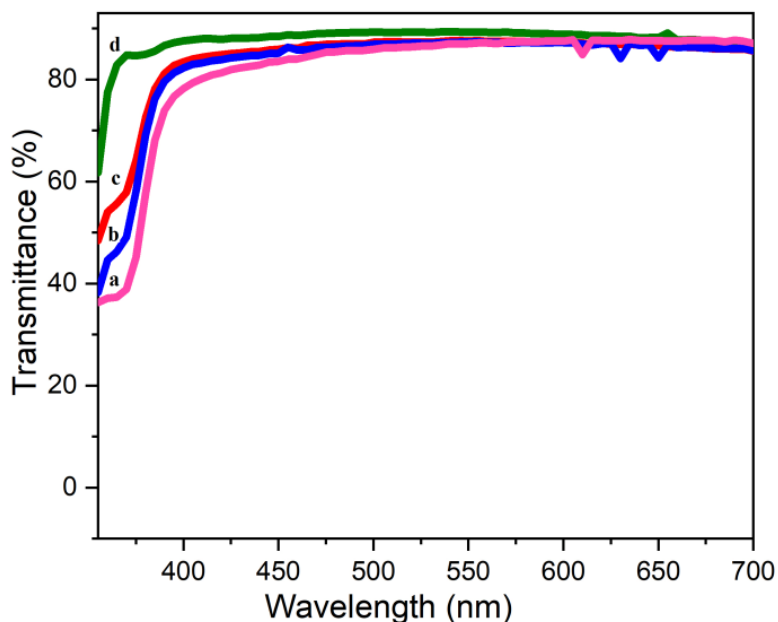
Figure. 9. *The transmittance spectra of P(NVC-co-BZMA) and it's composites; a) P(NVC-co-BZMA)/ZnO 15%, b) P(NVC-co-BZMA)/ZnO 10%, c) P(NVC-co-BZMA)/ZnO 5% and d) P(NVC-co-BZMA)*

When the absorbance-wavelength spectra of the P(NVC-co-BZMA) copolymer and composite samples were analysed, it was found that the absorption value of the P(NVC-co-BZMA) copolymer without any doping in the visible region was the lowest. The P(NVC-co-BZMA)/ZnO 15% composite with the highest doping ratio was found to have the highest absorption value. P(NVC-co-BZMA)/ZnO 5% and P(NVC-co-BZMA)/ZnO 10% composites were observed to exhibit absorption directly proportional to the doping amounts.
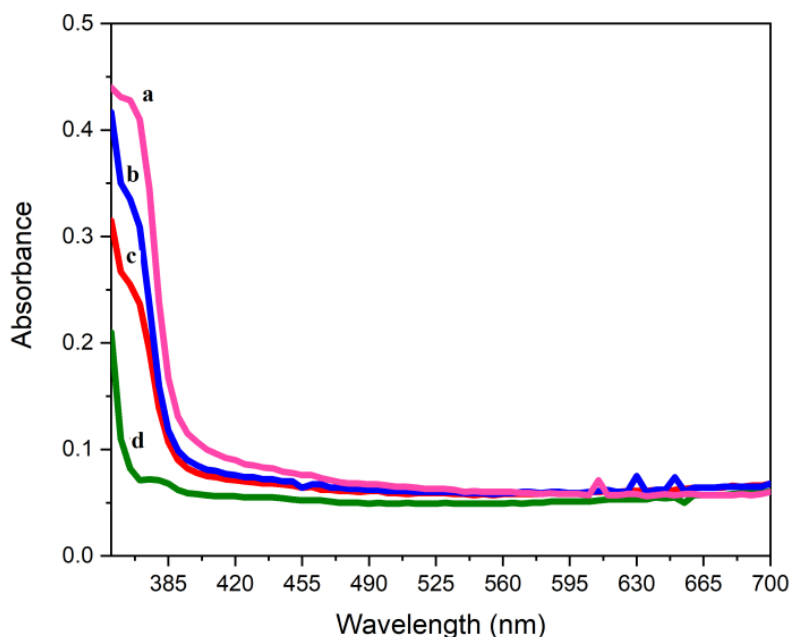
Figure. 10. *The absorption spectra of P(NVC-co-BZMA) and it's composites; a) P(NVC-co-BZMA)/ZnO 15%, b) P(NVC-co-BZMA)/ZnO 10%, c) P(NVC-co-BZMA)/ZnO 5% and d) P(NVC-co-BZMA)*

4. CONCLUSION

In this study, 25%-75% by mole copolymer of N-vinyl carbazole and benzyl methacrylate monomers and composites of this copolymer with nano ZnO in three different weight ratios were prepared. Thermal and optical properties of the synthesized samples were examined. The fact that the peak of the ester carbonyl was observed at 1723 cm^{-1} in the FT-IR spectrum of the copolymer and the absence of the peaks of the vinylic protons at 6.5 and 5.5 ppm in the ^{1}H NMR spectrum was important evidence that the copolymer was synthesized. All of the peaks belonging to the copolymer were also observed in the FT-IR spectrum of the composite. Thermal degradation behaviors and glass transition temperatures of the copolymer were determined by thermograms obtained from the TGA-DTA dual system. While the glass transition temperature for benzyl methacrylate polymer is 59°C in the literature, this value was determined as 227 °C for P(NVC) (Pearson & Stolka, 1981; Worzakowska, 2016). Glass transition temperatures of P(NVC-co-BZMA) copolymer were found in the range of those of P(NVC) and P(BZMA) homopolymers. The Tg value of P(NVC-co-BZMA) copolymer was 94.6 °C while the Tg values of the composites made with 5%, 10%, 15% ZnO doping were determined as 96, 98.4 and 99 °C, respectively. The Tg of the composites was higher than the Tg of the pure copolymer and it was determined that the softening temperatures increased as the nano ZnO ratio in the composites increased. This behavior shows that nano ZnO reduces the mobility of the chain in the copolymer chain, thus reducing the free volume of the polymer and increasing the softening temperature of the composites. While 310 °C defined the base temperature of the copolymer, the initial degradation temperatures of the composites decreased with the doping of nano zinc oxide into the polymer. In general, when the temperature values corresponding to 50% weight loss for the thermal stability of polymeric materials are evaluated, this value was determined as 382 ^{0}C for the copolymer, while it was 383.5, 385, and 427 °C for composites doped with 5%, 10% and 15% zinc oxide, respectively. Zinc oxide doped into the copolymer increased the thermal stability of the composites between 1.5 and 44 °C. The activation energy calculations of the P(NVC-co-BZMA) copolymer synthesized in the study were examined by employing the FWO and KAS methods. The activation energies for the copolymer were determined as 131.924 and 128.139 kJ/mol according to the FWO and KAS methods, respectively. The closest value to the average activation energy for the copolymer was obtained at a conversion value of 0.5. Activation energies of the P(NVC-co-BZMA)/ZnO 10% composite according to FWO and KAS method were calculated as 365.57 and 361.757 kJ/mol, respectively. The closest value to the average activation energy for this composite was obtained at a conversion value of 0.4. The UV spectra of the P(NVC-co-BZMA) copolymer and composites were analyzed in the visible region and it was observed that the undoped P(NVC-co-BZMA) copolymer had the highest optical transmittance and the lowest absorption value. As for the composites, it

was determined that the optical transmittance values decreased with the increase in the amount of doped nano ZnO, while the optical absorption increased. In conclusion, it was observed that the absorption spectra were in agreement with the optical transmittance spectra.

ACKNOWLEDGEMENT

REFERENCES

Aqel, A., ALOthman, Z. A., Yusuf, K., Badjah-Hadj-Ahmed, A. Y., & Alwarthan, A. A. (2013). Preparation and evaluation of benzyl methacrylate monoliths for capillary chromatography. *Journal of Chromatographic Science*, *52*(3), 1–10. doi:10.1093/chromsci/bmt011

Barim, G. (2021). Synthesis and thermal degradation kinetics of poly(benzyl methacrylate)/graphite composites. *Journal of Materials and Electronic Devices*, *2*(1), 30-35.

Bashir, S., Awan, M. S., Farrukh, M. A., Naidu, R., Khan, S. A., Rafique, N., Ali, S., Hayat, I., Hussain, I. & Khan, M. Z. (2022). In-vivo (Albino Mice) and in-vitro Assimilation and Toxicity of Zinc Oxide Nanoparticles in Food Materials. *International Journal of Nanomedicine*, *17*, 4073-4085. doi:10.2147/IJN.S372343

Demirelli, K., Abubakar, A. M., Ahmad, A. A. & Bağcı, E. (2022a). The effect of end group and graphene on dielectric properties and thermal degradation of poly(benzyl methacrylate) prepared by ATRP method. *Polymer Bulletin*. doi:10.1007/s00289-021-04003-2

Demirelli, K., Barim, E., Tuncer, H., Barim, G,. & Abubakar, A. M. (2022b). Synthesis and characterization of N-(2-acetylbenzofuran-3-yl)methacryl-amide and ethyl methacrylate copolymer/graphite oxide composites and study of their kinetic and electrical properties. *Polymer Bulletin*, *79*, 4721-4743. doi:10.1007/s00289-021-03730-w

Flynn, J. H., & Wall, L. A. (1966). General treatment of the thermogravimetry of polymers. *Journal of Research of the National Bureau of Standards – A. Physics and Chemistry*, *70A*(6), 487-523. doi:10.6028/jres.070a.043

Ghosh, D., & Biswas, M. (2009). NanoZnO initiated polymerization of N-vinylcarbazole (NVC) and evaluation of a poly(N-vinylcarbazole)–ZnO nanocomposite. *Journal of Polymer Research*, *16*, 245-254. doi:10.1007/s10965-008-9223-1

Ghosh, D., Sardar, P. S., Biswas, M., Mondal, A., & Mukherjee, N. (2010). Dielectric characteristics of poly(N-vinylcarbazole) and its nanocomposites with ZnO and acetylene black. *Materials Chemistry and Physics*, *123*(1), 9-12. doi:10.1016/j.matchemphys.2010.04.019

Goumri, M., Hatel, R., Ratier, B., & Baitoul, M. (2020). Optical and electrical properties of poly (*N*-vinylcarbazole)/grapheneoxide nanocomposites for organic semiconductor devices. *Applied Physics A*, *126*, 647. doi:10.1007/s00339-020-03812-y

Haldar, I., Kundu, A., Biswas, M., & Nayak, A. (2011). Preparation and evaluation of a poly(N-vinylcarbazole)–Fe3O4 (PNVC–Fe3O4) nanocomposite. *Materials Chemistry and Physics*, *128*(1-2), 256-264. doi:10.1016/j.matchemphys.2011.03.008

Isusi, M., Rodríguez, M., Garay, T., Vilas, J. L. & León, L. M. (2006). Thermal properties of copolymers of N-vinylcarbazole with acrylic and methacrylic monomers. *Journal of Macromolecular Science Part B*, Physics, *41*(2), 241-253. doi:10.1081/MB-120003083

Kissinger, H. E. (1957). Reaction kinetics in differential thermal analysis. *Analytical Chemistry*, *29*(11), 1702-1706. doi:10.1021/ac60131a045

Li, H., Liu, J., Lin, L., Mu, Q., Sun, X., & Liu, X. (2014). Preparation and characterization of UV-curable copolymers containing alkali soluble carboxyl pendant for negative photoresist. *Polymer Science Series B*, *56*, 855-862. doi:10.1134/S1560090414770024

Liu, X., Dai, X., Boyko, W., Fleischer, A. S., & Feng, G. (2022). Surfactant-mediated synthesis of monodisperse Poly(benzyl methacrylate)-based copolymer microspheres. *Colloids and Surfaces A: Physicochemical and Engineering Aspects*, *633*(Part 2), 127870. doi:10.1016/j.colsurfa.2021.127870

Ozawa, T. (1965). A new method of analyzing thermogravimetric data. *Bulletin of the Chemical Society of Japan*, *38*(11), 1881-1886. doi:10.1246/bcsj.38.1881

Pearson, J. M., & Stolka, M. (1981). *Poly(N-vinylcarbazole)*. Gordon and Breach Science Publishers.

Reyna-Gonzalez, J. M., Roquero P., & Rivera, E. (2009). A Comparative investigation between poly(N-vinylcarbazole) and poly(3,6-N-vinylcarbazole): spectroscopy, conductivity, thermal and optical Properties. *Designed Monomers and Polymers*, *12*(3), 233-245. doi:10.1163/156855509X436058

Saçak, M. (2012). *Polimer Kimyası*. Ankara, Gazi Kitabevi.

Ueno, K. (2018). Soft materials based on colloidal self-assembly in ionic liquids. *Polymer Journal*, *50*, 951-958. doi:10.1038/s41428-018-0083-1

Worzakowska, M. (2016). Starch-g-poly(benzyl methacrylate) copolymers, Characterization and thermal properties. *Journal of Thermal Analysis and Calorimetry*, *124*, 1309-1318. doi:10.1007/s10973-016-5328-7

Yakuphanoglu, F., Yahia, I. S., Barim, G., & Şenkal, B. F. (2010). Double-walled carbon nanotube/polymer composites: Electrical properties under dc and ac fields. *Synthetic Metals*, *160*(15-16), 1718-1726. doi:10.1016/j.synthmet.2010.06.007

Flood Control of Ulupinar Stream (Kemer/Antalya) and Evaluation of Geological Data

Sinan Emre ÇAKIR[1*] (iD) Mustafa Gürhan YALÇIN[1] (iD)

[1]Department of Geological Engineering, Akdeniz University, 07058, Antalya, Türkiye

Keywords	Abstract
Antalya Climate Kemer Ulupinar Stream Flood	Antalya province, the study area, is located in the south of Türkiye, and it is one of the regions where flood disasters frequently occur, particularly due to excessive precipitation in the autumn and winter months. Therefore, it is extremely important to carry out the necessary engineering studies. Deluges and floods damage buildings, agricultural and residential areas, human life, and social and economic activities in the vicinity according to their flow rate. The study aims to evaluate the general geological structure of the region considering the reclamation of Ulupinar Stream in the Kemer district of Antalya, to determine a rock pit where resistant and impermeable rock material can be obtained to use in the construction of the masonry stone wall during the reclamation work, and also offer a reference study for future studies. The geological structure of the region was interpreted by using the general geological maps and studies conducted in the study area. The general geological map of the study area was edited and a generalized stratigraphic section was generated using geographical information system (GIS) methods and software. According to the results of the assessment of the studies and geological data on the flood control of Ulupinar Stream, which is one of the regions posing flood risk, the region was found to be a susceptible environment for flood considering the determining criteria such as the location of the basin and the average rainfall, and the reclamation of the stream has been suggested as part of the flood prevention plan. A rock pit where rock material can be obtained for constructing the masonry stone wall has been found 11 km from the region. The material in the rock pit is at a shallow depth and suitable for mining. All scientific studies related to the rock material and the rock pit determined in the study should be carried out before using the rock.

1. INTRODUCTION

In Türkiye, the Mediterranean, Black Sea, and Western Anatolia geographical regions are known to be susceptible to deluges and floods. The settlement type, distribution of the vegetation, and topography of these regions are observed to be compatible with the precipitation regime. Precipitation in these regions occurs under the influence of South, South-West, and North-West depression. In the Mediterranean and Black Sea Regions, the severity of depression precipitation increases since the range of mountains extend parallel to the coasts. Moreover, the melting of snow at high elevations, convective heavy rainfall in the inner regions, and the magnitude and frequency of floods in these regions affect the occurrence of floods in the spring (Demirbas, 2002).

Scientific studies have been made on medical geology, beach sands, and various river networks in the region (Yalcin M. G. et al., 2016; Cengiz et al., 2017; Unal et al., 2018; Yalcin et al., 2019). However, no study has been previously conducted on the study area. This emphasizes the originality of the study. The site location map (Figure 1) prepared in detail to be used in flood prevention studies of the Ulupinar Stream

*Corresponding Author, e-mail: sinanemrec@gmail.com

(Kemer/Antalya) is included in the study. The area indicated by the yellow line represents the risky area in the flood prevention study of the Ulupinar Stream in Kemer.
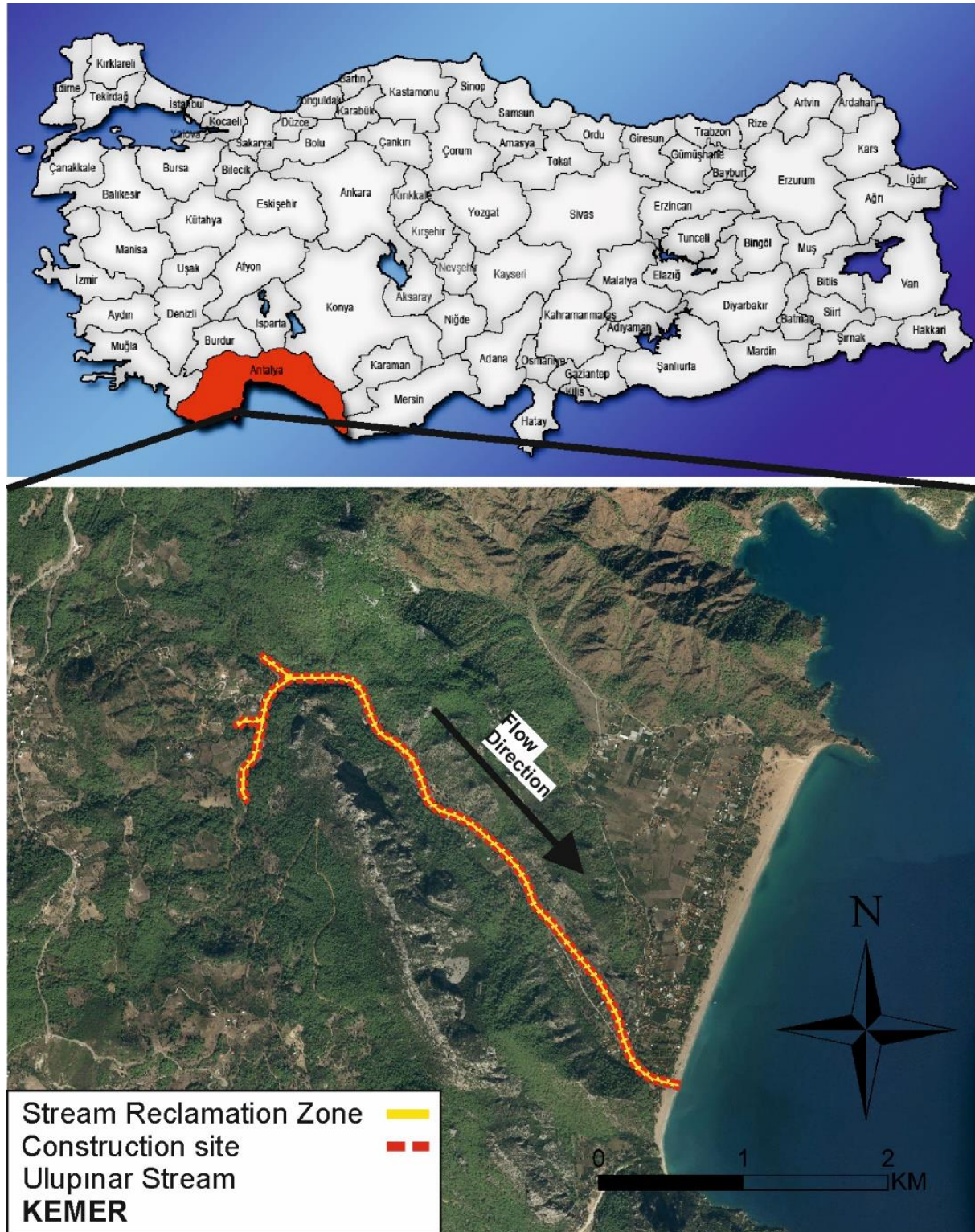
***Figure 1.** Site location map*

The precipitation and temperature chart of Antalya (Figure 2) reveals that the amount of precipitation decreases very much and the temperature increases in the summer while it is warm and rainy in the winter. The temperature chart reveals that the average temperature in summer is above 25°C, the highest temperatures are observed in July (28.5°C) and August (28.4°C) while the lowest temperatures are observed in December,

January, and February. The lowest average temperature has been measured in January (10°C). According to the precipitation chart, the amount of precipitation has been at the lowest level in summer while the amount of precipitation in winter has been higher compared to other months. The highest average precipitation (262.1 mm) has been observed in December (MGM, 2022).
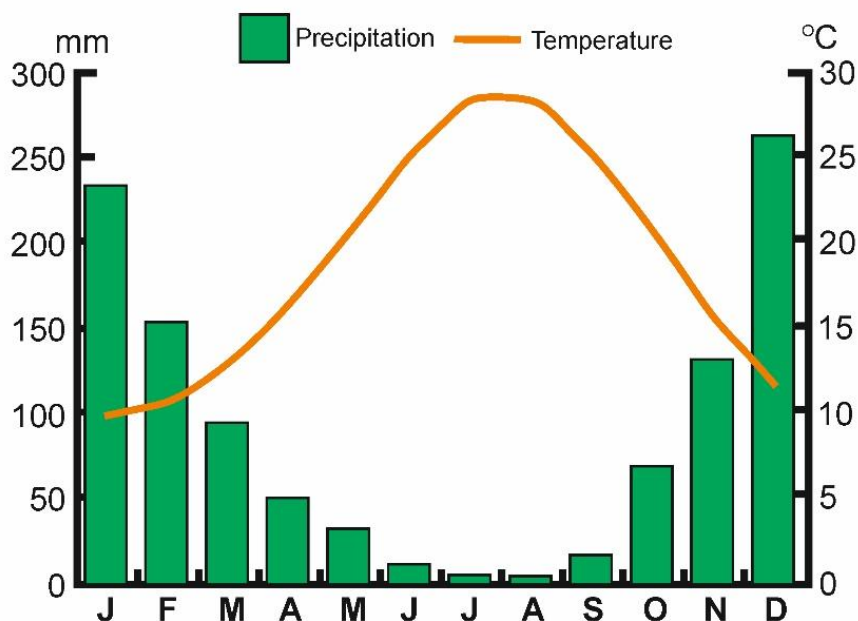
Figure 2. *Temperature and precipitation data of Antalya province for 1930-2020*
(prepared using the 2022 dataset of MGM)

Moisture added to the atmosphere with the evaporation in the Mediterranean creates unstable local precipitation around Antalya, especially in the summer. It is known that the humid air passing over the Mediterranean region creates heavy rainfalls due to factors such as the fact that the mountains extend parallel to the coast and the wind rises along the slopes. The fact that Antalya has heavy rainfalls creates flood risks and dangers.

Flood estimation studies are carried out using two methods before the occurrence of flood studies. These methods are as follows:

Deterministic (Analytical) Methods: Analytical relationships between the flood basins and climate parameters are established, and possible floods are estimated using these relationships (Yuksek et al., 2013).

Statistical Methods: Deluges and floods are examined as variables and possible floods are estimated using various probability distribution functions (Yuksek et al., 2013).

Flood risk assessment has been defined as the analysis of the most possible negative effects of the flood on people, buildings, agricultural areas, and infrastructure. The main purpose of flood risk assessment is to ensure human safety, support flood management and management decisions, and prevent damage to public and private sector infrastructure, and commercial and other economic activities (OSIB, 2015).

Deluges and floods occur at any time and place in nature due to usual or unusual meteorological events or due to climate change. However, artificial interventions performed by people play a significant role in causing destruction and human-life loss in settlements (Demircan et al., 2017).

Antalya has a high risk of deluges and floods due to heavy rainfalls; moreover, it is a suitable location for the formation of mineral deposits in terms of geological processes. In the region, quartzite, sand and gravel, manganese, lead and zinc, chromium mineralization and marble formation, as well as aluminum and barite

mineralization, are observed (Yalcin F. et al., 2016; Tarinc et al., 2019; Ozer & Yalcin, 2020; Atakoglu et al., 2021; Atakoglu & Yalcin, 2021; MTA, 2022). Barite, lead, and zinc deposits, which are above the mining limit, are generally located in the Alanya and Gazipaşa districts in the east of Antalya. The region has barite deposits containing $BaSO_4$ with almost 95-100% purity (Kursun & Yalcin, 2020).

In areas such as the Ulupinar Stream, where the flow rate is high and the height and strength of the stream slope are low, it poses a flood risk due to heavy rains in cases where the gutter is insufficient. This causes material and moral damages, particularly in settlements such as greenhouses, agricultural fields, roads, and households. In order to prevent the flood risk, it is aimed to raise the stream slope by constructing an appropriate engineering structure and making it resistant to flow, thus reducing the damage it will cause. Therefore, a geological study was conducted before the project to meet the impermeable and stable rock material required for the construction of the flood prevention structure for the stream from a rock pit closest to the study area.

The general geological map and generalized stratigraphic section of the study area were generated using a geographical information system (GIS) software (ArcGIS 10.0.4), drawing software (Corel Draw 7.0), and 1:25,000 scale geological map data of the General Directorate of Mineral Exploration and Research.

2. MATERIAL AND METHOD

Geological units in the region are listed from the oldest to the youngest as follows (Figure 3):

Carbonates and Clastic Rocks - Carboniferous (p2): Tectonic slices of Hocalar and Sinat Mountain Nappes, which are examined in the regions can be examined as part of the Bolkar Mountain Unit and are located on tectonic slices belonging to the Bozkır Union. The outcrops of the Hocalar Nappe in the Hadim region consist of the Zindancık meta-olistostrome, which is thought to be Triassic-aged and contains meta-shale slate, meta-sandstone, and phyllite and includes Late Devonian, Late Permian, and Carboniferous limestone olistoliths, and Kayraklitepe quartzites, which cover it conformably (Ozgul, 1976).

Sandstone and shale limestone are identified as Middle-Upper Triassic (t2-3) age while the Middle-Upper Triassic aged sediments are identified as Sapadere formation. The name of radiolarite member was used for red-brown radiolarite, cherts, and shales in the formation (Ozgul, 1984a, 1984b).

Carbonates and Clastic Rocks - Triassic (t): The formation, which is represented by Megalodon limestones to the south of Anamas Mountain, was named by Gutnic et al. (1979). The unit consists of a thick-medium layer, light gray, pink, gray, cream, and dirty yellow limestones with plenty of megalodons. There is dolomitic limestone at the base and sand-clay limestones at the upper level. It has abundant algae and gastropod traces and stromatolite layers. Leylek limestone, which is compatible with Üzümdere formation on top, is approximately 250 meters thick and found to be of Rhaetian age. Shallow carbonate is the unit that deposits in the shelf environments and has a regressive feature at the top (Gutnic et al., 1979).

Neritic Limestone - Jurassic-Cretaceous (jka): The formation, which was named by Senel (1984), consists of neritic limestones. In the study area, several small crops with block appearance belonging to Tekedagi formation, which is the typical formation of Tahtalıdağ nappe, have been outcropped. The unit consists of limestones with medium-thick stratification, occasionally massive, beige, cream, gray, and white color, recrystallized limestones, and dolomitic limestones. Local dolomitizations are observed widely in the unit. The lower relationship of limestones in small cubes is observed to be tectonic while the upper relationship is not observed in this area. The unit in the area has a thickness of a few tens of meters. The Jurassic-Cretaceous formation was deposited in offshore platforms.

Dunite - Mesozoic (y1): Bolkar Mountain Unit, which was named by Ozgul (1976), contains Permian-Cretaceous aged rocks. It starts with the upper Permian carbonate rock and schist; the lower Triassic shale is compliant with the sandstone and marble intercalation. Middle Triassic diabase cuts these units and is all covered incompatibly by Jurassic-Cretaceous carbonate rocks. These units have been eroded by Cretaceous ophiolites (Yalcin & Temur, 2006).

Unseparated Quaternary Sediments (Qa): Quaternary alluvial sediments consist of loose, slightly round, or angular sand, gravel, and silt fillings. They are easily uncompacted dispersible rocks. The alluvium is observed along the stream valleys. Alluvial series, which are the cover layers, consist of limestones, metamorphic base, and clastic units (Cobanoglu et al., 2007).
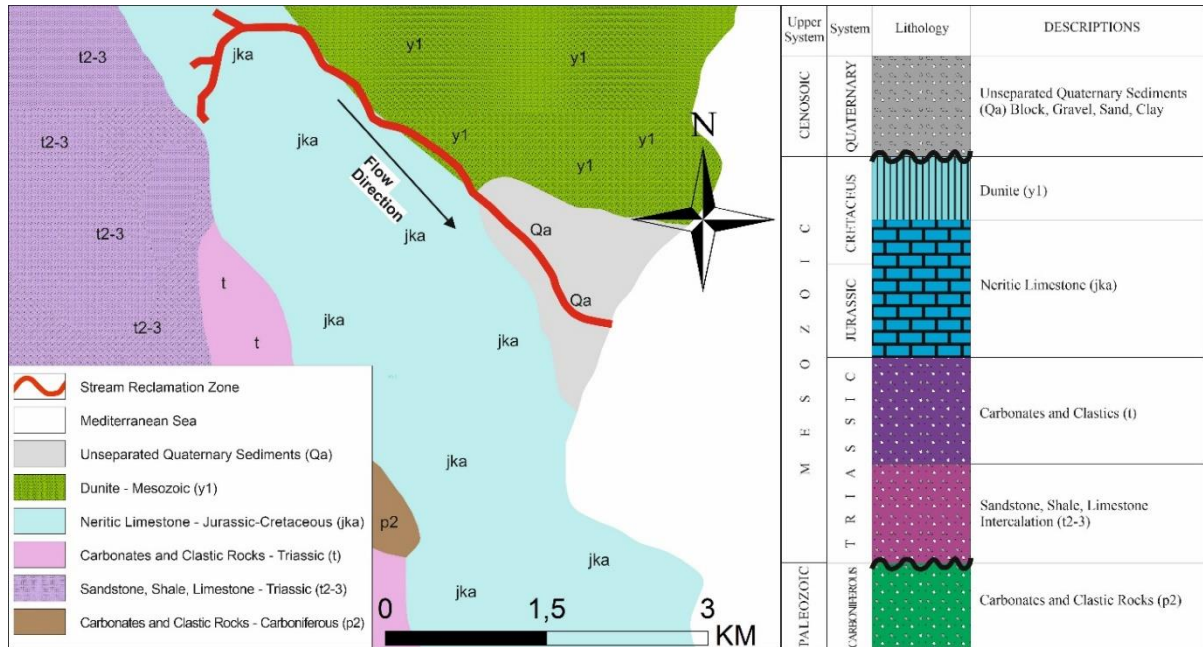
Figure3. a) *Geological map of Ulupinar Stream and vicinity in Cirali Neighborhood of Kemer (prepared by editing the data of MTA (Akbaş et al., 2011)),* ***b)*** *Generalized stratigraphic section of Ulupinar Stream in Cirali Neighborhood of Kemer (prepared by editing the data of MTA (Akbaş et al., 2011))*

Photographs indicating the land and flow directions in the area are presented in Figure 4. Considering the geological map, stratigraphy, and general geology of Ulupinar Stream/Kemer and its vicinity, it is usually observed that there are carbonates and clastic rocks, sandstone-shale-limestone intercalation, limestones, and alluvial sediments in the study area. Since the geological units in the area will create a susceptible environment for deluges and flooding, research studies have been carried out to determine a rock pit of stable and impermeable rock material to be used in the construction of masonry stone wall for the reclamation of the stream and prevent the material and moral damage due to floods.

Figure 4. *Photographs and flow directions in the study area of Ulupinar Stream in Kemer*

3. RESULTS AND DISCUSSION

Considering the geological data of the Ulupinar Stream and its vicinity covered by the study area, it was determined that it generally posed a flood hazard under heavy rainfall or precipitation conditions. Therefore, the reclamation of the Ulupinar Stream/Kemer was decided against flood hazards. The rock pit for the rock material required for the flood prevention measures in line with the data obtained from the General Directorate for State Hydraulic Works was determined, and the required filling volume was calculated.

The rock pit where rock material required for the construction of various flood protection and prevention structures on the course of the Ulupinar Stream/Kemer can be obtained is located 11 km southwest of the region. It is public property in the north of the Kilise location. It was found that 106,090 m^3 of rock material can be obtained with a mining depth of 4 meters. The site was investigated in terms of the required rock materials and the nature, reserve, and ground of the examined rock pit and its distance to the structure are given in the following tables (Table 1, 2).

The rock pit is located in the area covered by the 1:25.000 scale topographic map sheet of ANTALYA P24-b3. The rock pit, which is located approximately 1 km southeast of the Dükmendibi Neighborhood, is located on the western slopes of the Orta Hill in Kiliseyaka Location (Figure 5).
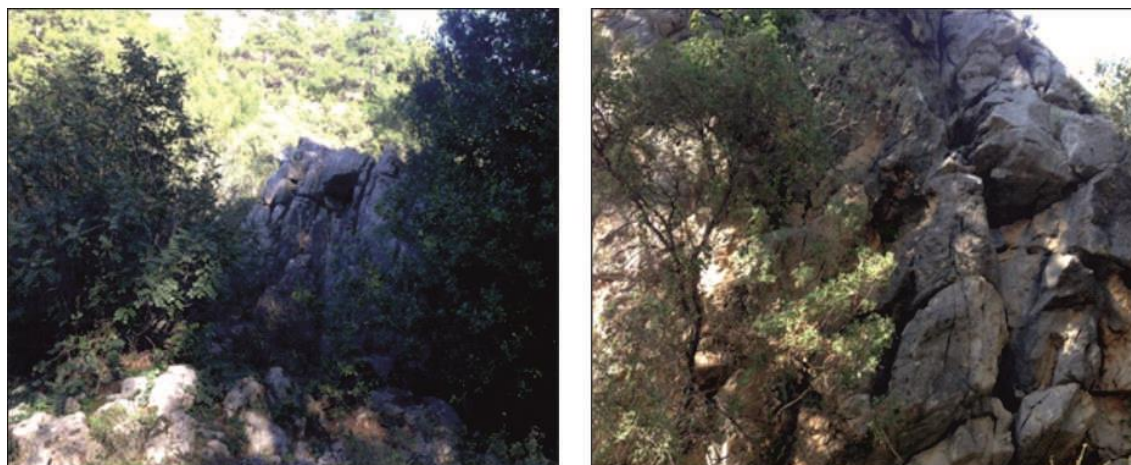
Figure 5. *Images of Rock Pit*

Table 1. *Details about the Rock Pit, its reserve, and distance to the construction site*

NAME OF THE AREA	DISTANCE TO STRUCTURE (m)	ROAD STATUS	AREA OF THE ROCK PIT (m^2)	MINING DEPTH (m)	RESERVE OF THE ROCK MATERIAL (m^3)	AMOUNT OF MATERIAL NEEDED (m^3)
ROCK PIT	11,000	Earth road has to be improved	26,524	4	106,096	67,000

Table 2. *UTM Coordinates of the Rock Pit (ITRF96-6°)*

POINT	Y= (EAST) E	X= (NORTH) N
1	271578.73	4030194.04
2	271665.18	4030175.23
3	271580.29	4029961.54
4	271458.93	4030010.62

All scientific studies should be carried out for the rock material to be extracted from the proposed rock pit before use.

4. CONCLUSION

Considering the geological and stratigraphic properties of Ulupinar Stream/Kemer, it was thought that there might be flood risk and it might damage farming and residential areas. Therefore, the reclamation of the stream was suggested. According to the results of the investigations, the researchers found that there were Upper Triassic Period Formations, Upper Cretaceous Period Formations, Quaternary Period Formations, Upper Cretaceous Formations (Bey Daglari Autochthon), and Quaternary Formations in the study area. Quaternary unseparated sediments, quaternary travertine, beach sand formations, limestone-shale intercalation, alluvial range, neritic and pelagic limestones, carbonates, and clastic rocks were also observed in the study area and its vicinity.

The geological map and stratigraphic section of the study area, Ulupinar Stream/Kemer and its vicinity, were generated. The rock material required for the construction of flood protection and prevention structures was investigated. Examining the geological maps and ambient conditions of the study area, it was first determined that the environment was susceptible to floods; thus, the reclamation of the stream was suggested by constructing a masonry stone wall using impermeable and strong rocks extracted from the rock pit.

REFERENCES

Akbaş, B., Akdeniz, N., Aksay, A., Altun, İ. E., Balcı, V., Bilginer, E., Bilgiç, T., Duru, M., Ercan, T., Gedik, İ., Günay, Y., Güven, İ. H., Hakyemez, H. Y., Konak, N., Papak, İ., Pehlivan, Ş., Sevin, M., Şenel, M., Tarhan, N., Turhan, N., Türkecan, A., Ulu, Ü., Uğuz, M. F., Yurtsever, A. et al. (2011). 1:1.250.000 ölçekli Türkiye Jeoloji Haritası. Maden Tetkik ve Arama (MTA) Genel Müdürlüğü Yayını, Ankara. Geological Map Viewer. (Accessed: 08/10/2022) URL

Atakoglu, O. O., & Yalcin, M. G. (2021). Geochemical characterization of the Sutlegen bauxite deposit, SW Antalya. *Mining of Mineral Deposits*, *15*(3), 108-121. doi:10.33271/mining15.03.108

Atakoglu, O. O., Yalcin, M. G., & Ozmen, S. F. (2021). Determination of radiological hazard parameters and radioactivity concentrations in bauxite samples: the case of the Sutlegen Mine Region (Antalya, Turkey). *Journal of Radioanalytical and Nuclear Chemistry*, *329*(2), 701-715. doi:10.1007/s10967-021-07826-5

Cengiz, M. F., Kilic, S., Yalcin, F., Kilic, M., & Yalcin, M. G. (2017). Evaluation of heavy metal risk potential in Bogacayi River water (Antalya, Turkey). *Environmental Monitoring and Assessment*, *189*(6), 248, doi:10.1007/s10661-017-5925-3

Cobanoglu, I., Ozbek, A., Gül, M. (2007). Geotechnically Evaluations of Buildings over the Pleistocene-Recent Loose Deposits: A Case Study from Mersin. *J. Fac.Eng.Arch. Selcuk Univ*, *23*(3), 85-94.

Demirbas, E. (2002). Floods in Türkiye. Disaster and Emergency Management Presidency Education News and Science Journal. Antalya, (pp. 3-12).

Demircan, M., Gürkan, H., Eskioglu, O., Arabaci, H., & Coskun, M. (2017). Climate Change Projections for Turkey. Three Models and Two Scenarios. *Turkish Journal of Water Science & Management*, *1*(1), 22-43 doi:10.31807/tjwsm.297183

Gutnic, M., Monod, O., Poisson, A., & Dumont, J. (1979). Geology of the Western Taurides (Türkiye). Mémoires de la Société Géologique de France (Nouvelle Série). Mémoire, 137, 109.

MGM, Turkish State Meteorological Service. (2022). Precipitation and Temperature data of Antalya province between 1930-2020. (Accessed: 08/11/2022) URL

MTA, General Directorate of Mineral Research and Exploration. (2022). Barite. (Accessed: 26/09/2022) URL

Kursun, G. B., & Yalcin, M. G. (2020). Origin of barite deposits in dolomite-limestone units Gazipasa Eastern of Antalya. geology, geochemistry, statistics, sulfur isotope composition. *Mining of Mineral Deposits*, *14*(1), 62-71. doi:10.33271/mining14.01.062

OSIB, Ministry of Forestry and Water Affairs. (2015). Basin Monitoring and Determination of Reference Points Project. Küçük Menderes Basin. Ankara. *(Havza İzleme ve Referans Noktalarının Belirlenmesi Projesi, Küçük Menderes Havzası. Ankara.)*

Ozer, O., & Yalcin, M. G. (2020). Correlation of chemical contents of Sutlegen (Antalya) bauxites and regression analysis. *AIP Conference Proceedings*, *2293*(1), 180008 doi:10.1063/5.0026731

Ozgul, N. (1976). Some geological aspects of the Taunts orogenic belt (Turkey) (1). *Bulletin of the Geological Society of Turkey*, *19*(1), 65-78.

Ozgul, N. (1984a). Geology of the Alanya region. Türkiye Geology Institute Ketin Simp., (pp. 97-120).

Ozgul, N. (1984b). Stratigraphy of the Mesozoic carbonate sequence of the Munzur Mountains (Eastern Taurides): In: Tekelli, O. and Goncuoglu, M.C. (Eds.) Geology of the Taurus Belt. Ankara, (pp. 173-181).

Senel, M. (1984). Discussion on the Antalya nappes. Geology of the Taurus Belt. (Ed. by O. Tekeli and C. Goncuoglu). Ankara, (pp. 41-51).

Tarinc, O. K., Ozer, O., Aydin, B., & Yalcin, M. G. (2019). Comparison of physical-mechanical properties of Clova and Lyca marbles in Akcay (Antalya) region by using independent-samples T-test statistics. In the 2nd Mediterranean International Conference of Pure Applied Mathematics and Related Areas, Paris, France (pp. 28-31).

Unal, S., Yalcin, M. G., Ocak, S., Yalcin, R., & Ozmen, S. F. (2018). Computation of gamma radioactivity of natural rocks in the vicinity of Antalya province and its effect on health. *Kerntechnik*, *83*(2), 112-120. doi:10.3139/124.110895

Yalcin, F., Ozer, O., Nyamsari, D. G., & Yalcin, M. G. (2019). Statistical evaluation of the geochemical content of beach sand along the Sarisu-Kemer coastline of Antalya, Turkey. *AIP Conference Proceedings*, *2116*(1), 100005. doi:10.1063/1.5114081

Yalcin, F., Nyamsari, D. G., Paksu, E., & Yalcin, M. G. (2016). Statistical assessment of heavy metal distribution and contamination of beach sands of Antalya-Turkey: an approach to the multivariate analysis techniques. *Filomat*, *30*(4), 945-952. doi:10.2298/FIL1604945Y

Yalcin, M. G., Akturk, O., & Paksu, E. (2016). The contribution of west mediterranean cities (Antalya, Isparta and Burdur) to Turkey's natural stones-marble export. International Multidisciplinary Scientific GeoConference (SGEM), vol. 2, 875-880.

Yalcin, M. G., & Temur, S. (2006). Geochemistry of the terra rossa from Ayrancı, Central Turkey. *Geochimica et Cosmochimica Acta*, *70*(18), A716. doi:10.1016/j.gca.2006.06.1285

Yuksek, O., Serencam, U., Ucuncu, O., & Anilan, T. (2013). Disaster and Flood Management and the Case of Degirmendere. IMO Flood and Landslide Symposium Proceedings. Trabzon.

A Computational Study of the Adsorptive Separation of Methane and Hydrogen in Zeolite Templated Carbons

Celal Utku DENİZ[1]* 🆔

[1]Hitit University, Faculty of Engineering, Department of Chemical Engineering, 19030, Çorum, Türkiye

Keywords	Abstract
Hydrogen Methane Gas Separation GCMC Zeolite Templated Carbons	Combustion of conventional energy sources produces pollutants such as SO_x, NO_x, and CO; the use of hydrogen and methane can eliminate these harmful emissions. In fuel cell technology and other uses, hydrogen must be refined by extracting methane from the methane/hydrogen combination, produced via dry or steam reforming. This study investigates the adsorption and separation capabilities of recently discovered zeolite-templated carbons (ZTCs) for binary mixtures consisting of hydrogen and methane. To assess the adsorption and separation performances of these carbon-based nanostructures, grand canonical Monte Carlo (GCMC) simulations were used. The simulation results revealed that AFY ($|(C_6H_{15}N)_3(H_2O)_7|[Co_3Al_5P_8O_{32}]$) and RWY ($|(C_6H_{18}N_4)_{16}|$ $[Ga_{32}Ge_{16}S_{96}]$) structures could be viable alternatives for applications involving adsorptive gas separation based on selectivity and the CH_4 uptake capacity. The selectivity of AFY was calculated to be 176, while its capacity to uptake CH_4 was found to be 2.57 mmol/g, the selectivity of RWY was calculated to be 132, and its CH_4 uptake was 3.49 mmol/g.

1. INTRODUCTION

Compared to traditional energy sources, which create pollutants during combustion (such as SO_x, NO_x, CO, etc.), hydrogen and methane are more desirable options. Dry reforming and steam reforming processes are used in industry to produce hydrogen. In some applications, such as fuel cell technology, the hydrogen must be purified by separating methane from the methane/hydrogen mixture. Cryogenic distillation and chemical adsorption, two traditional methods for separating gases, have drawbacks such as high costs, poor safety, and difficult operating conditions (Niaz et al., 2015). Gas adsorption/separation using porous materials has recently been identified as a possible solution (Li et al., 2022).

Various porous adsorbents, including covalent organic materials, zeolites, and metal-organic materials, have been proposed for gas storage applications (Zhang et al., 2013). Currently, these materials have demonstrated highly promising storage performance for pure gases. In contrast, most industrial processes involve gas mixtures instead of pure gases. Consequently, evaluating these materials' mixed gas adsorption performance is crucial. Evaluating the adsorption characteristics of gas mixtures indicates the selectivity of the adsorbent and, thus, its applicability in adsorptive gas separation for various applications (Kosinov et al., 2016).

The principle behind the adsorptive separation of gas mixtures is the selective adsorption of a component on the adsorbent compared to the others. The selectivity is determined by several factors, such as the adsorbent and the adsorbate molecule interaction, the pore size of the adsorbent, and the geometry of the molecule being adsorbed. A high specific surface area is a crucial parameter for adsorption capacity, but a pore size that

matches the diameter of one of the gas mixture components can improve the framework's interaction with that molecule. In such a system, the framework selectively adsorp some molecules and reject others. Activated carbons, polymers, and metal-organic materials are a few of the adsorbents proposed for adsorptive gas separation applications (Attia et al., 2020).

Using numerical analysis methods, carbon-based nanostructures' single-gas storage capacities have been widely explored (Ozturk et al., 2015; Mert et al., 2020). However, there is limited research on gas mixtures' separation performance in the literature. Majumdar et al. (2018) employed the GCMC method to study the adsorptive separation of CO_2 from H_2S, SO_2, and N_2 multicomponent gas combinations in carbon nanotube arrays. Sha and Faller (2016) employed GCMC simulations to assess the carbon-based nanostructures in the separation performance of pure noble gases. GCMC and molecular dynamic simulations are used by Wang and Cao (2015) to evaluate the separation capabilities of the covalent organic frameworks (COFs) for binary mixtures of H_2S, N_2, CO_2, CH_4, SO_2, and CO_2 gases.

Zeolite-templated carbons (ZTCs) were developed from the concept of creating microporous carbon-based materials with a porosity similar to that of the original zeolite templates. Their substantial specific surface area and distinctive microporous structure can make them effective gas adsorbents. Furthermore, ZTCs can be produced in large amounts effectively (Nishihara & Kyotani, 2018). Recent work by Braun et al. (2018) provided an analytical groundwork for obtaining a ZTC starting from a zeolite, outlined the basics of forming ZTCs, and discovered 68 ZTCs. As previously indicated, even though ZTCs have a very high potential for use as an adsorbent in gas storage applications (Deniz, 2022), there has been no research on how effectively these structures separate methane and hydrogen gas mixture.

Motivated by these facts, adsorptive separation performances of the zeolite-templated carbons identified by Braun et al. (2018) are investigated for the hydrogen/methane equimolar mixture. The efficiency of methane/hydrogen separation is evaluated employing the grand canonical Monte Carlo (GCMC) approach. In order to interpret the results, selectivity and the differential enthalpy of adsorption (ΔH_{Ads}) were used along with the structural parameters of the ZTCs. According to the findings of the simulations, some of the ZTCs has the potential as a promising option for applications involving adsorptive gas separation.

2. MATERIAL AND METHOD

The GCMC simulations for adsorption and separation were run with the RASPA molecular simulation software tool (Dubbeldam et al., 2016). The simulations were run for 2×10^5 iterations, the first 10^5 of which were utilized to achieve system equilibrium and the second 10^5 to ensure statistical reproducibility. The results showed that further increasing the number of cycles had a minimal impact on findings. Four types of Monte Carlo (MC) move, including swap, reinsertion, translation, and identity change, were considered for simulations. All simulation results were obtained between 0.1 and 100 kPa pressure and a temperature of 298 K.

Lorentz-Berthelot combining approach given in Eqs. 1 and 2 were used to calculate the interactions between individual species. Attraction and repulsion forces between gas molecules and ZTCs were modeled using the Lennard Jones (LJ) potential given in Eq 3, and the electrostatic interactions were also considered employing the Ewald summation.

$$\varepsilon_{ij} = \sqrt{\varepsilon_i \varepsilon_j} \tag{1}$$

$$\sigma_{ij} = \frac{1}{2}\left(\sigma_i + \sigma_j\right) \tag{2}$$

$$U_{ij} = 4\varepsilon_{ij}\left[\left(\frac{\sigma_{ij}}{r_{ij}}\right)^{12} - \left(\frac{\sigma_{ij}}{r_{ij}}\right)^{6}\right] + \frac{q_i q_j}{4\pi\varepsilon_0 r_{ij}} \tag{3}$$

where interacting species are i and j, the representative distance between species is expressed with σ_{ij} while the potential of the interactions is denoted as ε_{ij}. The distance between species i and j is denoted by r_{ij}; ε_0 is the dielectric constant, and partial charges for species i and j are expressed as q_i and qj, respectively.

Carbon-Carbon interactions in ZTC structure are considered sp2-hybridized, and suitable potential parameters were selected from the literature (Lithoxoos et al., 2010) and employed in simulations. A rigid spherical model was used to represent hydrogen molecules with a fixed hydrogen bond length (0.74 Å), and the potential parameters reported by Michels et al. (1960) were used. The united-atom model (Peng et al., 2010) was adopted and used in simulations for the methane molecule. Parameters for the potentials in the GCMC simulations are given in Table 1.

Table 1. The LJ parameters of framework and adsorbate molecules

Molecule	Reference Study	σ (Å)	ε (K)
C – C (Framework)	(Lithoxoos et al., 2010)	3.40	28.2
H_2	(Michels et al., 1960)	2.96	36.7
CH_4	(Peng et al., 2010)	3.81	148.2

To save computing costs, it was assumed that ZTC frameworks were static. This was also the case in earlier studies (Ozturk et al., 2015). Additionally, periodic boundary conditions were also imposed. After a spherical cutoff of 12.8 Å, the LJ interactions were neglected. The differential enthalpy of adsorption (ΔH_{Ads}), a numerical indicator for adsorption strength between gas molecules and adsorbent, was determined using the energy/particle fluctuations (Vlugt et al., 2008).

Selectivity is utilized to measure the performance of the frameworks in adsorbing hydrogen and methane during the computational gas separation process. Eq. (4) describes the selectivity parameter.

$$S = \frac{X_{H_2} Y_{CH_4}}{X_{CH_4} Y_{H_2}}$$

(4)

where S represents the selectivity, X_{H_2} and X_{CH_4} represent the molar adsorption amount of adsorbate molecule species in the adsorption phase, and Y_{H_2} and Y_{CH_4} indicate the concentrations of adsorbate molecule species in the bulk phase, respectively.

Density, specific surface area (SSA), and accessible pore volume (APV) were computed for the ZTC structures using a visualization package called iRASPA (Dubbeldam et al., 2018). Pore-size distribution (PSD) was also determined using RASPA for the chosen ZTC structures (Dubbeldam et al., 2016). In this study, when naming ZTC structures, original zeolite-template code names were used.

3. RESULTS AND DISCUSSION

Selectivity is one of the most important metrics for assessing the gas separation capability of nanostructures. Consequently, the selectivity of ZTC structures considered within the scope of this study is evaluated, and a more detailed assessment based on APV, SSA, pore-size distribution, and adsorption isotherm is carried out on selected ZTC structures following the initial assessment. First, the CH_4/H_2 selectivities of 68 ZTCs are estimated at 298 K and 100 kPa conditions to determine the most promising ZTC structures for methane/hydrogen adsorptive separation. The selectivities of the ZTC structures are given in Figure 1.

As seen in Figure 1, AFY, BOG (($|Ca_7Na_4(H_2O)_{74}|[Al_{18}Si_{78}O_{192}]$)), JSR_1 ($|(Ni(C_3H_{10}N_2)_3)_{36}Ni_{4.7}|_3$ $[Ga_{27.1}Ge_{68.9}O_{192}]_3$), JSR_3, and RWY structures differ in selectivity. The selectivities for AFY, BOG, JSR_1, JSR_3, and RWY structures were calculated as 176, 95, 93, 97, and 132, respectively. In the following parts of the study, a detailed examination of these structures will be carried out. In this context, calculated densities, APV, and SSA of the promising structures are given in Table 2. The representative structures are also given in Figure 2.
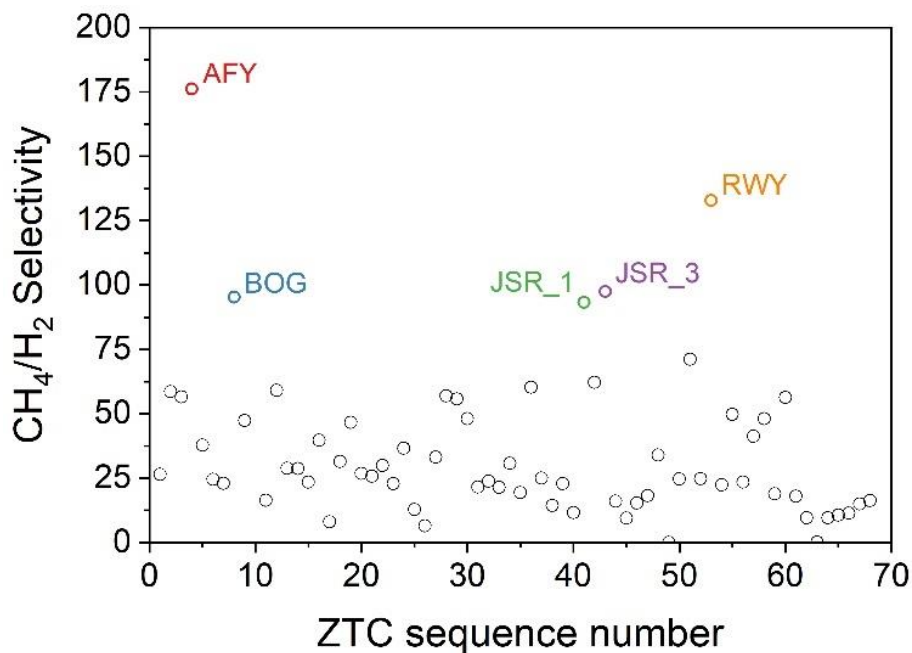
Figure 1. *Selectivity of 68 ZTCs at 298K and 100 kPa*
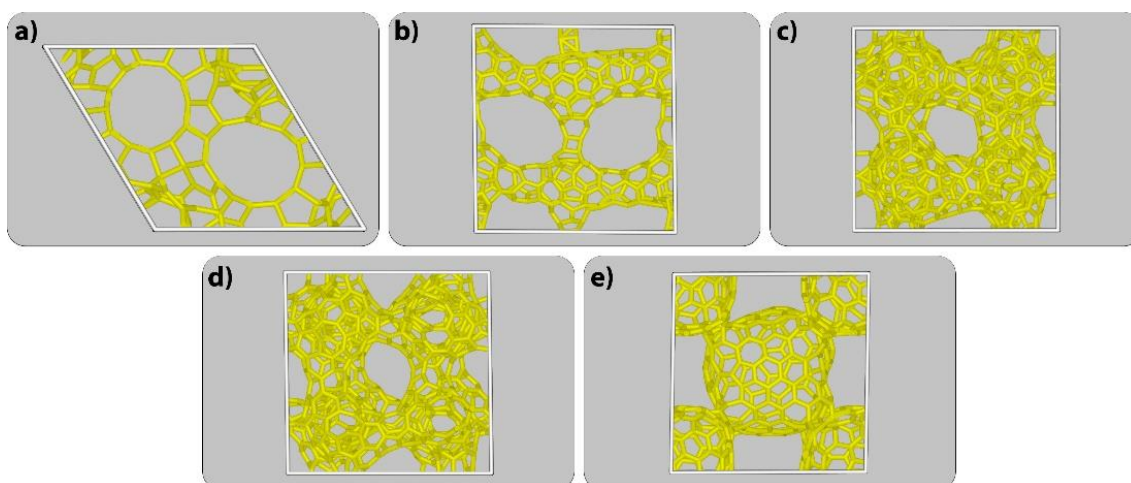
Figure 2. *The representative structures of **a)** AFY **b)** BOG **c)** JSR_1 **d)** JSR_3 **e)** RWY*

When Table 2 is examined, it can be said that the RWY structure has a lower density and higher surface area than the others. On the other hand, it is expected that the BOG, JSR_1, and JSR_3 structures would exhibit comparable adsorption characteristics due to the similarities between their SSA and APV.

Table 2. *Structural properties of ZTCs*

Structure	SSA (m^2/g)	APV (cm^3/g)	Density (g/cm^3)
AFY	1107.7	0.5033	1.432
BOG	1018.9	0.3843	1.406
JSR_1	953.7	0.4408	1.489
JSR_3	893.2	0.4186	1.514
RWY	1681.3	0.7620	1.233

The pore size of carbon-based nanomaterials (CBNs) is critical in determining their adsorption performance. Figure 3 displays the PSDs for the AFY, BOG, JSR_1, JSR_3, and RWY structures, and only micropores exist in the specified ZTC structures. The gas storage ability of CBNs is known to be poor if their pores are smaller than 5 Å (Mert et al., 2020). Notably, the selected ZTC structures all have pore sizes that fall within the range of what is considered an appropriate pore size for adsorbents (Deniz, 2022), with the smallest pore size being around 2 Å and the largest being around 8 Å.
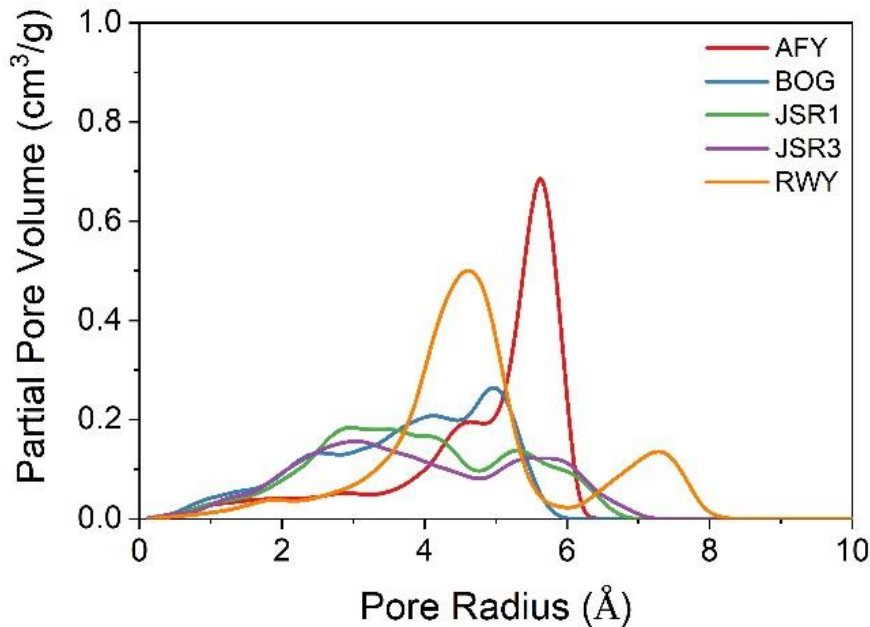
Figure 3. *Pore size distribution of ZTC structures*

Figure 4a shows that H_2 uptake capabilities grow linearly with increasing pressure from 0.1 to 100 kPa at 298 K. Hydrogen adsorption capacity of five ZTCs is shown to be more closely related to pore volume than surface area and ΔH_{Ads} at 298 K, as shown by the highly linear isotherms. According to Table 2 and Figure 4a, the order of the APV and hydrogen adsorption capacity of five ZTCs is RWY > AFY > JSR_1 > JSR_3 > BOG. Furthermore, the pore size distribution seen in Figure 3 can be used to justify RWY and AFY storing more H_2 as pressure increases. Considering that the kinetic diameter of hydrogen molecules is around 2.89 Å (Dal-Cin et al., 2008), it can be stated that these two structures with larger pores and sharper distribution establish better contact with the surface and increase their surface area. On the other hand, JSR_1, JSR_3, and BOG structures have relatively small pores to enhance the surface area. Figure 4b also shows the ΔH_{Ads} of ZTCs. From the perspective of gas separation performance, it is advantageous that the ΔH_{Ads} of hydrogen for ZTCs are less than 15 kJ/mol, which is regarded as an appropriate value for hydrogen adsorption in porous materials (van den Berg & Areán, 2008).
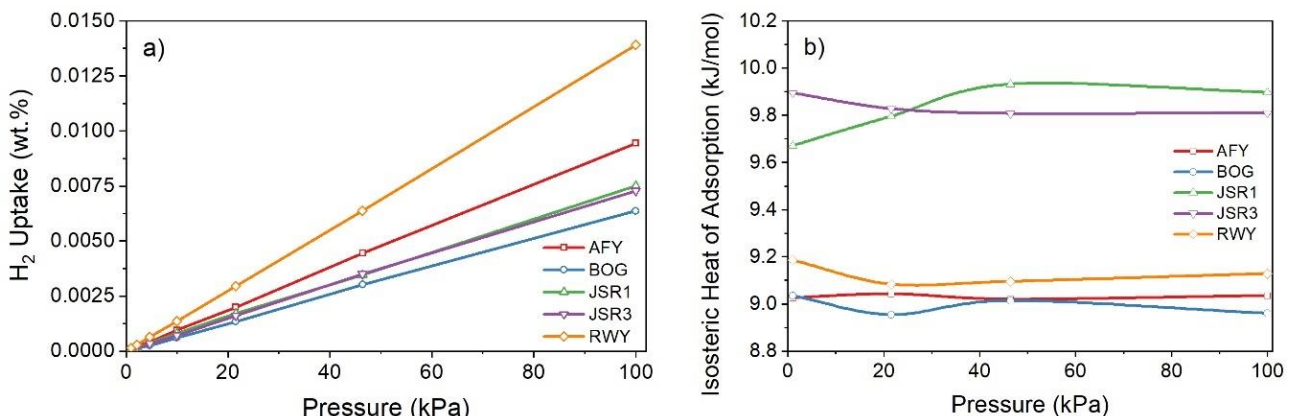
Figure 4. a) *H_2 uptake capacities and **b)** ΔH_{Ads} values*

Figure 5a depicts the adsorption isotherms, while Figure 5b shows ΔH_{Ads} of methane in ZTCs at 298 K. The non-linear pressure-dependency of CH_4 adsorption capacity is visible in Figure 5a at 298 K. This is a distinct trend from that observed in Figure 4a for H_2 uptake capacity at 298 K. This indicates the fact that at 298 K, five ZTCs can adsorp enough methane to reach saturation, and it is due to the higher adsorption affinity of CH_4 relative to H_2. The comparatively limited pore volume of JSR_1, JSR_3, and BOG, results in the CH_4 adsorption capabilities at low pressure being close to saturation. For 100 kPa and 298 K, the CH_4 adsorption capacities of AFY, BOG, JSR_1, JSR_3, and RWY are 4.13, 2.34, 2.74, 2.45, and 5.59 wt.%, respectively. Comparing Figure 4b and Figure 5b, one can conclude that the ΔH_{Ads} for CH_4 (23.4–26 kJ/mol) in five ZTCs are significantly higher compared to H_2 (9–10 kJ/mol). Similar ΔH_{Ads} values have also been reported by Li et al. (2022) for covalent organic frameworks. In this context, these ZTCs have the potential to effectively separate CH_4/H_2 mixtures according to their higher adsorption capacity and ΔH_{Ads} for CH_4.
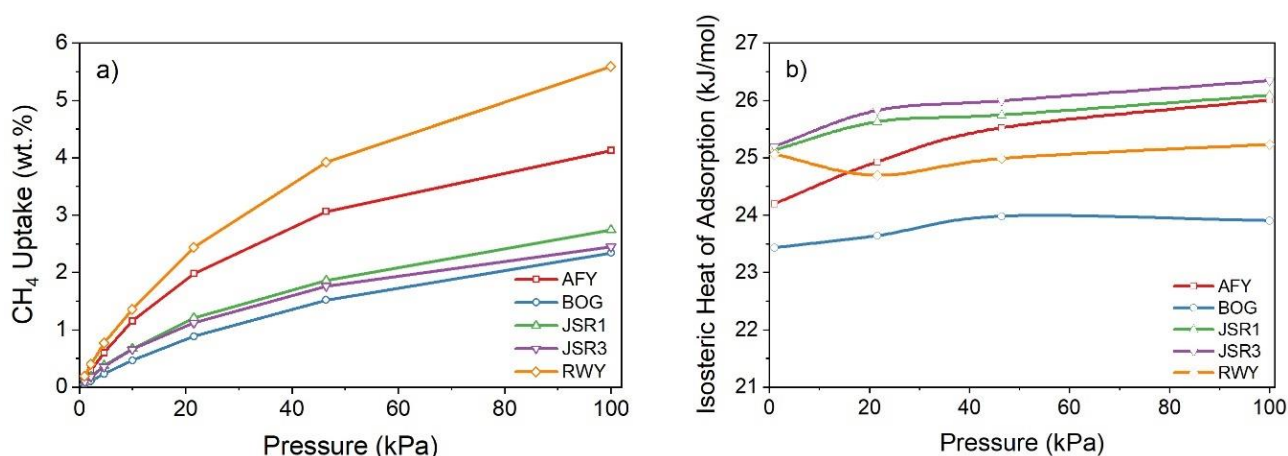
Figure 5. a) CH_4 uptake capacities and b) ΔH_{Ads} values

The adsorption selectivity of ZTCs at 298 K is evaluated for different pressures considering the binary mixture of CH_4 and H_2 with the same molar ratio. Figure 6 depicts the influence of pressure (0.1–100 kPa) on selectivity at a constant temperature. As shown in Figure 6, the selectivity of all structures decreases with increasing pressure. For the 100 kPa and 298 K conditions, the CH_4/H_2 selectivities of AFY, BOG, JSR_1, JSR_3, and RWY were calculated as 176, 95, 93, 97, and 132, respectively.
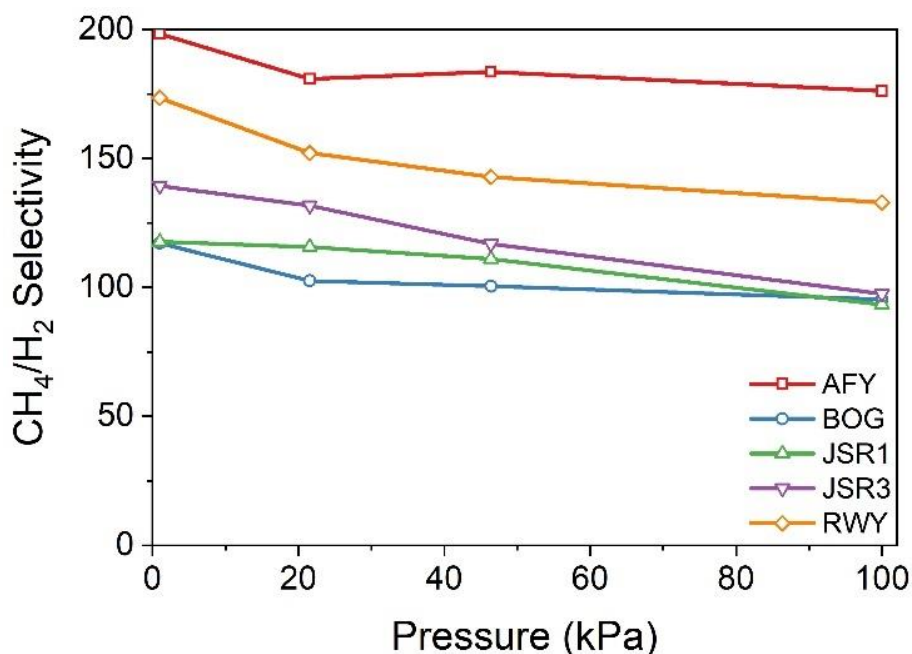
Figure 6. Effect of pressure on CH_4/H_2 selectivity of ZTC structures

Numerous aspects must be considered to understand the dependency of selectivity on pressure, such as the structural properties of ZTCs, the diameter of adsorbates, and the ΔH_{Ads} for adsorbates in the host material. It can be observed in Figure 4b and 5b that CH_4 has higher ΔH_{Ads} in ZTCs than H_2, allowing it to interact with the frameworks more strongly than H_2. As a result, the CH_4 to H_2 ratio is always higher than 1. Under mild pressure, adsorbates interact with the host material and are primarily adsorbed on the framework surface. Therefore, the methane/hydrogen selectivity is quite strong at low pressures because CH_4 has an even greater ΔH_{Ads} than H_2. When the pressure increases, the gas molecules are started to spread out throughout the framework and cover its accessible surface completely. In this instance, because of the difference in molecule size between hydrogen (2.89 Å) and methane (3.8 Å) (Dal-Cin et al., 2008), hydrogen can reach places that methane cannot; hence the selectivity between the two gases begins to decrease.

The performance of CH_4/H_2 separation is primarily determined by two factors: selectivity and methane uptake capability. AFY (Selectivity: 176 and CH_4 Uptake: 2.57 mmol/g) and RWY (Selectivity: 132 and CH_4 Uptake: 3.49 mmol/g) are more suitable compared to BOG, JSR_1, and JSR_3 for separating methane from the mixture.

In the literature, different researchers have used different temperature and pressure conditions when calculating selectivity and methane uptake capacity. For this reason, unfortunately, most of the data in the literature are not comparable with each other. However, a comparison was made with the data in the literature obtained under similar working conditions. Zhou et al. (2017) reported that a recently synthesized metal-organic framework had a selectivity value of about 206 under the same conditions as in this study and a CH_4 storage capacity of approximately 1.1 mmol/g. Li et al. (2022) described that the CH_4/H_2 selectivity for borophosphonate-based covalent organic frameworks (BP-COFs) was about 120 and CH_4 storage capacity was about 4 mmol/g under 100 kPa at 298 K. Yuan et al. (2021) reported that the CH_4/H_2 selectivity for hybrid ultra-microporous materials was about 90 for the same conditions, and the CH_4 uptake was 1.6 mmol/g. As it is understood in the studies in the literature, materials with high selectivity offer low CH_4 storage capacity, and materials with high CH_4 storage properties offer low selectivity.

When the results are compared with previous studies in terms of ΔH_{Ads}, it is seen that the values calculated for methane (23.4–26 kJ/mol) and hydrogen (9–10 kJ/mol) are consistent with previous studies in the literature. For instance, Zhou et al. (2017) noted these values as 24 - 27 kJ/mol for methane and about 9 kJ/mol for hydrogen. Similarly, Li et al. (2022) reported ΔH_{Ads} for hydrogen (9 - 10 kJ/mol) and (14 - 26 kJ/mol) for methane in BP-COFs structures. It should be noted here that the selectivity of the material, with the low ΔH_{Ads} (14 kJ/mol), is also relatively low (about 10). When materials are evaluated in terms of ΔH_{Ads}, it can be said that to achieve high CH_4/H_2 selectivity and high methane storage together, it should be as low as possible for hydrogen and vice versa for methane. Today's economic materials are, unfortunately, somewhat limited in this respect. Moreover, it seems unlikely that this can be achieved only with the structural properties of materials such as SSA and APV. It may be possible to overcome this limitation by identifying and incorporating functional groups with high methane and low hydrogen affinity into the structures. All these results reveal that the AFY and RWY structures are comparable with the materials in the literature for adsorbing methane from the mixture and can be used for purifying hydrogen or capturing methane.

4. CONCLUSION

In this work, ZTC structures that were recently discovered were investigated for their potential use as an adsorbent in an application involving the separation of methane and hydrogen. First, there were 68 ZTCs initially; however, this number was cut down to five so that they could be investigated in greater depth, taking into account their selectivity performance. GCMC method was employed to assess the adsorptive separation capabilities of the ZTCs for methane and hydrogen mixture. Depending on the results, five ZTCs offer favorable characteristics for separating methane/hydrogen gas mixture, including a large APV (0.38 - 0.76 cm^3/g), an appropriate pore size distribution (2 - 8 Å), and a specific surface area (893 - 1681 cm^2/g). At ambient temperature, the GCMC simulation reveals that the ZTCs can adsorp a more significant amount of CH_4 than H_2. The separation simulations demonstrate that AFY and RWY are more suited for adsorbing methane from the mixture in terms of selectivity and methane uptake capacity. The performance of five ZTCs in gas adsorption and separation is comprehensively related to structural factors such as APV, SSA, and PSD,

and the pressure also influences it. According to the findings of this research, ZTC structures, especially AFY and RWY, are potentially applicable host materials for the purpose of separating methane and hydrogen.

CONFLICT OF INTEREST

The author declares no conflict of interest.

REFERENCES

Attia, N. F., Jung, M., Park, J., Jang, H., Lee, K., & Oh, H. (2020). Flexible nanoporous activated carbon cloth for achieving high H_2, CH_4, and CO_2 storage capacities and selective CO_2/CH_4 separation. *Chemical Engineering Journal, 379*, 122367. doi:10.1016/j.cej.2019.122367

Braun, E., Lee, Y., Moosavi, S. M., Barthel, S., Mercado, R., Baburin, I. A., Proserpio, D. M., & Smit, B. (2018). Generating carbon schwarzites via zeolite-templating. *Proceedings of the National Academy of Sciences of the United States of America, 115*(35), E8116-E8124. doi:10.1073/pnas.1805062115

Dal-Cin, M. M., Kumar, A., & Layton, L. (2008). Revisiting the experimental and theoretical upper bounds of light pure gas selectivity–permeability for polymeric membranes. *Journal of Membrane Science, 323*(2), 299-308. doi:10.1016/j.memsci.2008.06.027

Deniz, C. U. (2022). Computational screening of zeolite templated carbons for hydrogen storage. *Computational Materials Science, 202*, 110950. doi:10.1016/j.commatsci.2021.110950

Dubbeldam, D., Calero, S., Ellis, D. E., & Snurr, R. Q. (2016). RASPA: Molecular simulation software for adsorption and diffusion in flexible nanoporous materials. *Molecular Simulation, 42*(2), 81-101. doi:10.1080/08927022.2015.1010082

Dubbeldam, D., Calero, S., & Vlugt, T. J. H. (2018). iRASPA: GPU-accelerated visualization software for materials scientists. *Molecular Simulation, 44*(8), 653-676. doi:10.1080/08927022.2018.1426855

Kosinov, N., Gascon, J., Kapteijn, F., & Hensen, E. J. M. (2016). Recent developments in zeolite membranes for gas separation. *Journal of Membrane Science, 499*, 65-79. doi:10.1016/j.memsci.2015.10.049

Li, X.-D., Yang, P., Huang, X.-Y., Liu, X.-Y., Yu, J.-X., & Chen, Z. (2022). Computational simulation study on adsorption and separation of CH4/H2 in five higher-valency covalent organic frameworks. *Materials Today Communications, 33*, 104374. doi:10.1016/j.mtcomm.2022.104374

Lithoxoos, G. P., Labropoulos, A., Peristeras, L. D., Kanellopoulos, N., Samios, J., & Economou, I. G. (2010). Adsorption of N2, CH4, CO and CO2 gases in single walled carbon nanotubes: A combined experimental and Monte Carlo molecular simulation study. *Journal of Supercritical Fluids, 55*(2), 510-523. doi:10.1016/j.supflu.2010.09.017

Majumdar, S., Maurya, M., & Singh, J. K. (2018). Adsorptive Separation of CO2 from Multicomponent Mixtures of Flue Gas in Carbon Nanotube Arrays: A Grand Canonical Monte Carlo Study. *Energy & Fuels, 32*(5), 6090-6097. doi:10.1021/acs.energyfuels.8b00649

Mert, H., Deniz, C. U., & Baykasoglu, C. (2020). Monte Carlo simulations of hydrogen adsorption in fullerene pillared graphene nanocomposites. *Molecular Simulation, 46*(8), 650-659. doi:10.1080/08927022.2020.1758696

Michels, A., de Graaff, W., & Ten Seldam, C. A. (1960). Virial coefficients of hydrogen and deuterium at temperatures between −175°C and +150°C. Conclusions from the second virial coefficient with regards to the intermolecular potential. *Physica, 26*(6), 393-408. doi:10.1016/0031-8914(60)90029-X

Niaz, S., Manzoor, T., & Pandith, A. H. (2015). Hydrogen storage: Materials, methods and perspectives. *Renewable and Sustainable Energy Reviews, 50*, 457-469. doi:10.1016/j.rser.2015.05.011

Nishihara, H., & Kyotani, T. (2018). Zeolite-templated carbons-three-dimensional microporous graphene frameworks. *Chemical Communications, 54*(45), 5648-5673. doi:10.1039/c8cc01932k

Ozturk, Z., Baykasoglu, C., Celebi, A. T., Kirca, M., Mugan, A., & To, A. C. (2015). Hydrogen storage in heat welded random CNT network structures. *International Journal of Hydrogen Energy, 40*(1), 403-411. doi:10.1016/j.ijhydene.2014.10.148

Peng, X., Zhou, J., Wang, W., & Cao, D. (2010). Computer simulation for storage of methane and capture of carbon dioxide in carbon nanoscrolls by expansion of interlayer spacing. *Carbon, 48*(13), 3760-3768. doi:10.1016/j.carbon.2010.06.038

Sha, H., & Faller, R. (2016). Molecular simulation of adsorption and separation of pure noble gases and noble gas mixtures on single wall carbon nanotubes. *Computational Materials Science, 114*, 160-166. doi:10.1016/j.commatsci.2015.12.031

van den Berg, A. W. C., & Areán, C. O. (2008). Materials for hydrogen storage: current research trends and perspectives. *Chemical Communications, 6*, 668-681. doi:10.1039/B712576N

Vlugt, T. J. H., García-Pérez, E., Dubbeldam, D., Ban, S., & Calero, S. (2008). Computing the Heat of Adsorption using Molecular Simulations: The Effect of Strong Coulombic Interactions. *Journal of Chemical Theory and Computation, 4*(7), 1107-1118. doi:10.1021/ct700342k

Wang, H., & Cao, D. (2015). Diffusion and Separation of H2, CH4, CO2, and N2 in Diamond-Like Frameworks. *The Journal of Physical Chemistry C, 119*(11), 6324-6330. doi:10.1021/jp512275p

Yuan, J., Liu, X., Li, X., & Yu, J. (2021). Computer simulations for the adsorption and separation of CH4/H2/CO2/N2 gases by hybrid ultramicroporous materials. *Materials Today Communications, 26*, 101987. doi:10.1016/j.mtcomm.2020.101987

Zhang, Q., Uchaker, E., Candelaria, S. L., & Cao, G. (2013). Nanomaterials for energy conversion and storage. *Chemical Society Reviews, 42*(7), 3127-3171. doi:10.1039/C3CS00009E

Zhou B., Li W., & Zhang J. (2017). *The Journal of Physical Chemistry C*, *121*(37), 20197-20204. doi:10.1021/acs.jpcc.7b07108

Effectuality of the Frequency Levels on the C&G/ω–V Data of the Polymer Interlayered Metal-Semiconductor Structure

Jaafar Abdulkareem Mustafa ALSMAEL[1] 🆔 Nuray URGUN[2] 🆔 Serhat Orkun TAN[3*] 🆔 Habibe Uslu TECİMER[4] 🆔

[1]Karabük University, Department of Electrical and Electronics Engineering, 78050, Karabük, Türkiye
[2]Karabük University, Faculty of Technology, Department of Mechatronics Engineering, 78050, Karabük, Türkiye
[3]Karabük University, Faculty of Technology, Department of Electrical Engineering, 78050, Karabük, Türkiye
[4]Karabük University, Faculty of Engineering, Department of Medical Engineering, 78050, Karabük, Türkiye

Keywords	Abstract
Metal-Polymer-Semiconductor Structures Surface States Negative Capacitance Series Resistance Frequency	Voltage and frequency dependent of capacitance and conductivity versus voltage (C&G/ω–V) qualifications of Al/(ZnFe$_2$O$_4$-PVA)/p-Si structure was compared and examined at lower and higher frequencies as 10 kHz and 1 MHz, respectively. The negative capacitance (NC) is a phenomenon that occurs at low frequencies and is primarily caused by minority carrier injection, series resistance (R$_s$), and surface states (N$_{ss}$). Because of the specific density distribution and relaxation times of N$_{ss}$, NC acts different behavior at lower and higher frequency levels and loses its effectiveness with increasing frequency. Also, the fluctuations in C and G/ω were ascribed to doping concentration, surface states loss charges, and interlayer thickness. N$_{ss}$ was acquired using the low-high frequency capacitance method (C$_{LF}$-C$_{HF}$), and the forward biased C^{-2} vs V graphs (at 10 kHz to 1 MHz) were used to determine the Fermi level (E$_F$), barrier height (Φ$_B$), and concentration of doped acceptor atoms (N$_A$). Accordingly, it has been detected that C and G/ω are highly dependence on biases and frequencies. Then again, the polarizations and surface states effect are barely perceptible at extremely higher frequency levels. Thus, polarization and R$_s$ stand out as important parameters that should be taken into account when examining the basic parameters of electronic devices.

1. INTRODUCTION

Metal and semiconductors are often used together in electronic technology, and metal-semiconductor (MS) structures or Schottky junctions are used in electronic/semiconductor devices, especially as switching elements (Sze, 1981; Bakkaloğlu et al., 2021). MS structures are used in different ways, and MIS, MPS and MFS structures are obtained by using insulator, polymer, and ferroelectric interlayers, respectively. Thereby, an organic/polymer interlayer between the metal and semiconductor forms the MPS structure. A semi-crystalline polymer that is water soluble is called polyvinyl alcohol (PVA), which has a hydroxyl group (OH-) and many hydrogen bonds in its structure. An all-purpose material, PVA, can be utilized in distinct kind of applications such as cements, mortars, films, fibers, and polymerization stabilizers. Since it has a very stable chemical and physical structure, many researchers have confirmed its qualities, and it has a variety of applications in nanotechnology (Gaaz et al., 2015; Aziz, 2016). Furthermore, organic/polymer doped nanocomposite material can be easily coated on a semiconductor layer at average temperature by using electrospinning technique which is provided by a collector and a high voltage power supply also with some equipment of nozzle and syringe pump (Unnithan et al., 2015). At the same time, PVA, which has a high dielectric strength but low electrical conductivity, increases its electrical and optical features when it is doped with a dopant material with high

555

Jaafar Abdulkareem Mustafa ALSMAEL, Nuray URGUN, Serhat Orkun TAN, Habibe Uslu TECİMER
GU J Sci, Part A, 9(4): 554-561 (2022)

conductivity (Subba Reddy et al., 2006). Zinc ferrite ($ZnFe_2O_4$) was chosen as a dopant material in this study due to its properties that can contribute to the charge transitions between metal and semiconductor.
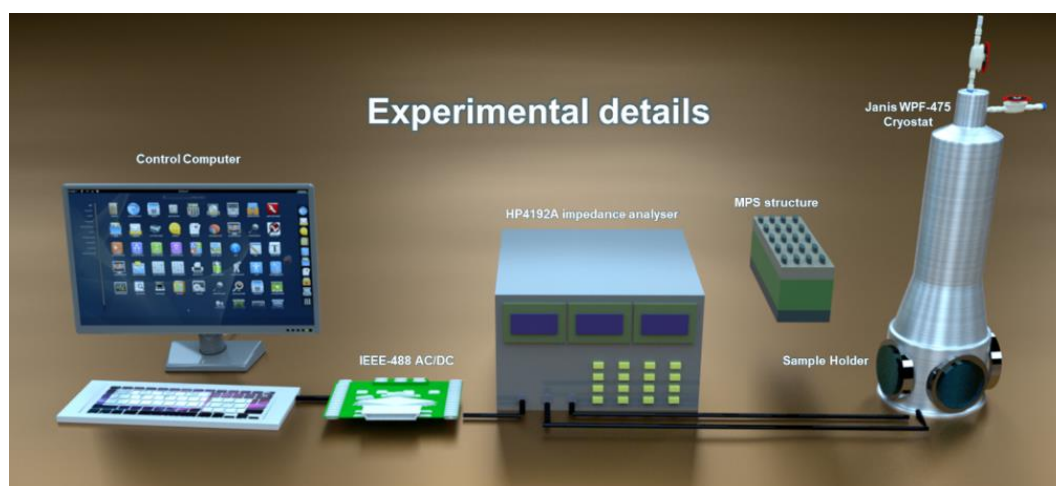
Zinc ferrite is not only of interest for essential examination in magnetization, but ferrites also have low-hole semiconductors and separators at low temperatures; they have been utilized in various technologically significant applications, for example, gas sensors (Patil et al., 2014), magnetization materials (Vijatović-Petrović et al., 2020), photocatalysis (Hou et al., 2018), catalysts (Zhang et al., 2015), and absorbance materials (Shultz et al., 2006). Moreover, for medical and industrial purposes, zinc ferrite has been developing immensely since the most recent decade. Zinc ferrite nanoparticles have additionally been utilized for media capacity, ferrofluids, spintronic, magnetic refrigeration, drug conveyance to specific areas of the body, hyperthermia, and biosensors, etc. (Slavu et al., 2021).

The structure's series resistance, the interface states between the metal and the semiconductor, and the barrier height are considered among the performance factors of the polymer interlayered junction. The resistance and doped-polymer interlayer are essential components of the MPS structure. Because both the series resistance and the depletion layer share the total voltage applied to the structures (Tecimer et al., 2018). As a result, the quality of the interlayer and the series resistance were an essential impact on the dependability and usefulness of these devices (Zeyrek et al., 2013).

In this study, considering its possible future mass production, it is aimed to fabricate a low-cost electronic circuit element with easy production techniques, instead of conventional (MS) structures with insulator (interface oxide) interlayer, which is widely researched in the literature. For this purpose, the operation of this circuit element at low and high frequencies was examined in the light of parameters such as series resistance and interface conditions, and the most appropriate frequency-operation range was tried to be determined. Thanks to this research, it has been interpreted that, how the electrical parameters of the fabricated semiconductor-based circuit element varied by frequency. Inferences were made about how the positive and negative effects of the relevant parameters affect the performance of the structure at the related frequencies. The comparison of low and high frequencies in this study is important to better understand the operation of Schottky structures operating at high frequencies and known for their rapid response to forward and reverse biases.

2. MATERIALS AND METHODS/EXPERIMENTAL METHODS

In order to prepare the Al/($ZnFe_2O_4$ -PVA)/p-Si structure, the Zinc ferrite nanoparticles doped PVA solution is precipitated on the wafer employing the electro-spinning process. In the earlier study (Alsmael et al., 2022) specifications of the deposition and manufacturing process are provided. Impedance Analyzer (4192A LF) (5 Hz–13 MHz) was employed to acquire C-V and G/ω-V data. In addition, Janis vpf-475, which was designed to minimize the influence of external factors on the measured values, was used throughout the experimental process. Figure 1 depicts the schematic diagram of the measurement setup as below.

Figure 1. *The schematic presentation of the experimental setup (Alsmael et al., 2022)*

556

Jaafar Abdulkareem Mustafa ALSMAEL, Nuray URGUN, Serhat Orkun TAN, Habibe Uslu TECİMER
GU J Sci, Part A, 9(4): 554-561 (2022)

3. RESULTS AND DISCUSSIONS

As generally known, MS-type and MIS or MPS-type contacts indicate different properties from each other. This difference is a result of the interlayer formation with a wide variety of production techniques, which helps regulate charge transitions and provide more stable conduction/isolation states. The presence of an interlayer between the metal and the semiconductor significantly changes the structure's C-V and G/ω-V properties compared to the ideal or Schottky barrier diodes MS type. Figure 2 and 3 presents the (C and G/ω) versus voltage data for Al/(ZnFe$_2$O$_4$ -PVA)/p-Si type at ordinary room temperatures, respectively. Three distinct regions are clearly seen in Figure 2, as a region of reflection (4 V to 0V), depletion (0 V to -1V), and accumulation (-1 V to -4 V) for low frequencies in the ±4 V voltage range. C values increase with decreasing voltage. The capacitance values display three peaks starting in the forward bias region with negative capacitance and continuing with two peaks in the reverse bias. Peaks in capacitance signal the presence of interface states. The cause for this characteristic behavior can be referred to the ZnFe$_2$O$_4$ -PVA interface and the presence of series resistors. G/ω values peak at the depletion zone and reduce with increasing frequency due to the density distribution at the device interface (Çetinkaya et al., 2019).

As demonstrated in Figure 2 and 3 the C and G/ω values were nearly constant at 1 MHz high frequency compared to 10KHz low frequency because interface charges cannot be tracking the AC signal at high frequencies and do not make a contribution to the observed capacitance values (Neamen, 1992).
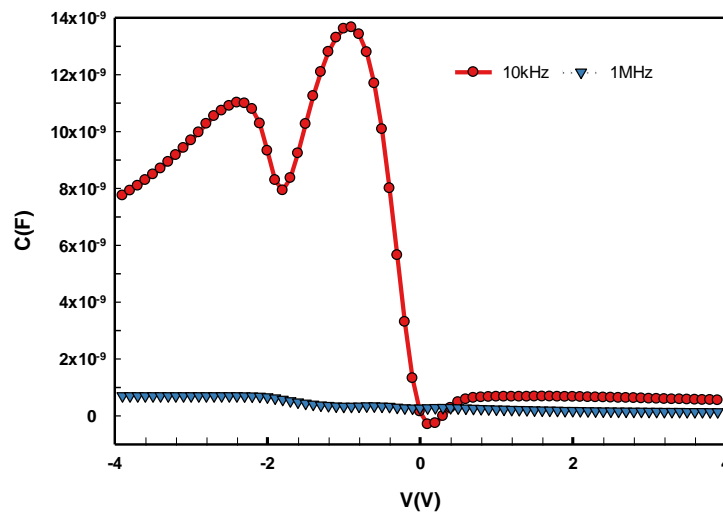
Figure 2. *C-V curves for the low and high frequencies*
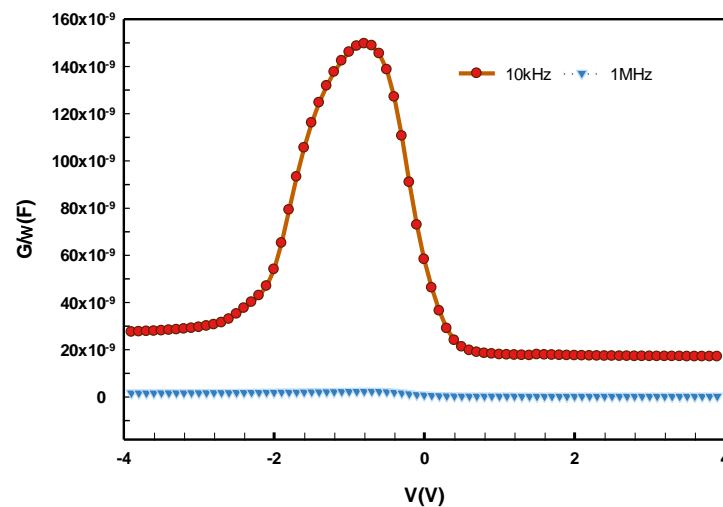
Figure 3. *G/ω-V curves for the low and high frequencies*

Using the conductance approach, it was capable to determine the R_s of the contacts by the admittance measuring, where C_m and G_m stand for the experimentally measured capacitance and conductance, respectively.

$$R_s = \frac{G_m/\omega}{\omega[(G_m/\omega)^2 + C_m^2]} \tag{1}$$

As shown in the equation, the series resistance is reversely proportional with the sum of the square of the C_m and G_m/ω multiplied by the angular frequency(ω). On the other hand, it is directly proportional to the conductance, so the series resistance decreases through the increased capacitance with the conductivity. As observed, the values of capacitance and conductivity in the forward biases are lower than in the reverse biases.

Among the reasons for the series resistance formation, the semiconductor's bulk resistance, the contact resistance between the semiconductor and the metal, the rectifier and ohmic contact resistances and possible resistances of the metal electrodes are effective.

Figure 4 represents the R_s-V curves for lower (10 kHz) and higher (1 MHz) frequency with reverse and forward bias voltages variations. While the R_s value stayed steady in the reverse bias region at 1 MHz frequency, the R_s value at 10kHz increases with increasing forward and reverse biases.
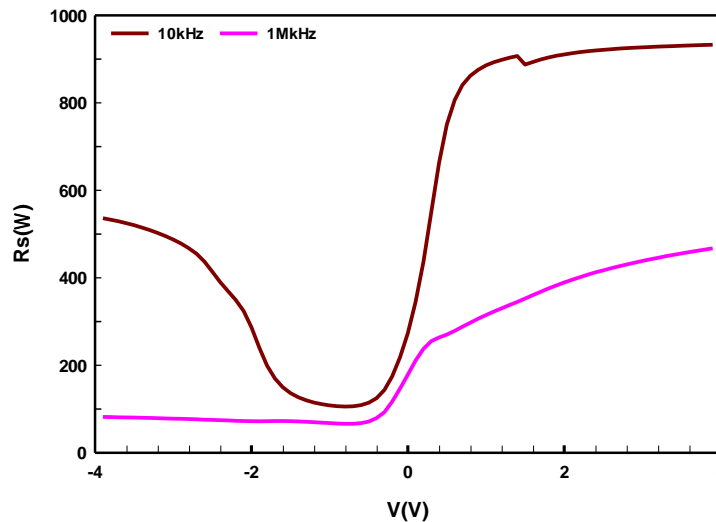
Figure 4. *R_s-V curves for the low and high frequencies*

The (C_{LF}-C_{HF}) method is useful for obtaining the voltage-dependent distribution of the interface state density, N_{ss} (V). This method allows easy calculation of many features of the interface layer and semiconductor interface (Ata et al., 2022). The following equation can be used to get N_{ss} (V) values of $ZnFe_2O_4$ -PVA interlayered Al/p-Si structure. N_{ss}(V)-V graphs for the structure was formed utilizing high-frequency (1 MHz) and low-frequency (10 kHz) values.

$$N_{ss} = (\frac{1}{qA})[\left(\frac{1}{C_{LF}} - \frac{1}{C_{ox}}\right)^{-1} - \left(\frac{1}{C_{HF}} - \frac{1}{C_{ox}}\right)^{-1}] \tag{2}$$

The explanations of each abbreviation are given as; A; the area of the MPS structure, q; the electronic charge, C_{ox}; the capacitance of the insulating layer, and d; the thickness of the polymer film. 10 kHz and 1 MHz were performed in this situation as the low and high frequencies. Figure 5 illustrates the N_{ss}-V curve, which has two peaks at around 1 V and 2.4 V at reverse biases. The disruption of the periodic lattice structure on the crystal surface and the density distribution in the finite band gap of the semiconductor may be related to the causes of these peak formations (Ata et al., 2022). The density of the interface states in the C and G_m/ω graphs acquired at high frequency (1MHz) may be ignored since interface states can only track AC signals at frequencies below 500 kHz (Neamen, 1992).
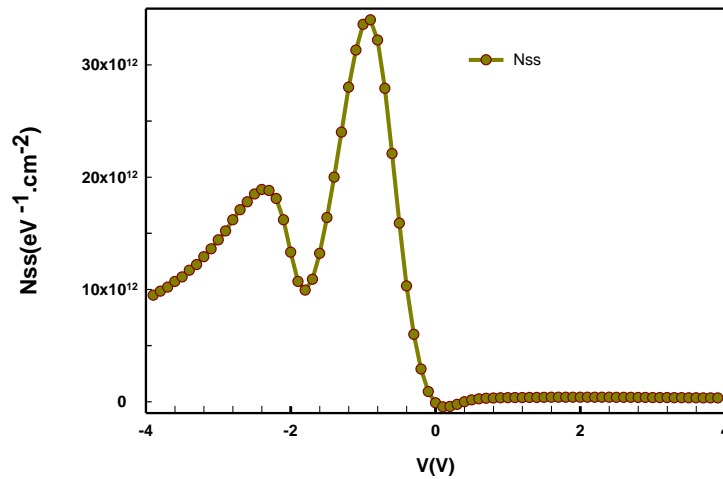
Figure 5. N_{ss}-V curve of the MPS structure

The graph for $1/C^2$ of the related structure was drawn for the low and high frequencies, 10 kHz and 1 MHz level, and presented below in Figure 6.

$$C^{-2} = \frac{2(V_0 + V_F)}{q\varepsilon_s\varepsilon_0 A^2 N_A} \tag{3}$$

Here, V_F is the forward bias voltage, ε_s is the relative permittivity of the semiconductor, ε_0 is the permittivity of free space or vacuum, and V_0 is the cut-off voltage at zero volts. It is evident that these curves behave linearly well in the forward bias range of 1.5 to 3 V.
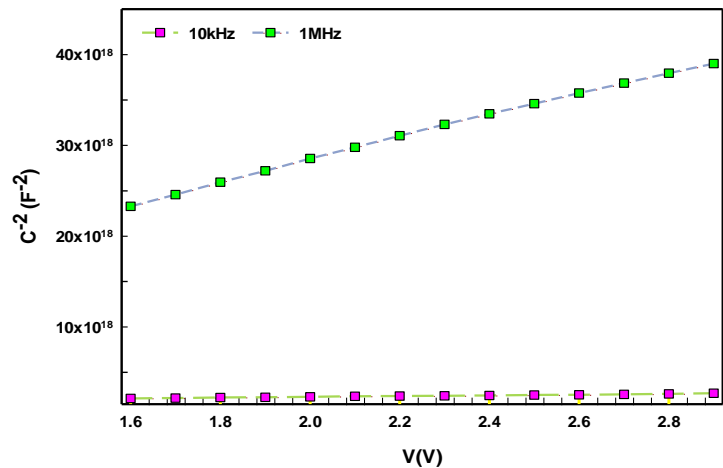
Figure 6. $1/C^2$ -V curves for the low and high frequencies

Based on the voltage evolution of $1/C^2$ for the device presented in Figure 7 and 8, the Fermi-energy level $E_F(eV)$ ln(f), barrier height (Φ_B) ln(f), and concentration of doped acceptor atoms (N_A) ln(f) were determined by using following equation:

$$E_F = \frac{kT}{q}Ln(\frac{N_V}{N_A}) \tag{4}$$

Here, the density of active states in Si valence band is symbolized with N_V. The following equation were used to get $\Phi_B(C-V)$ values:

$$\Phi_B(C-V) = \left(V_0 + \frac{kT}{q}\right) + E_F \tag{5}$$

559

Jaafar Abdulkareem Mustafa ALSMAEL, Nuray URGUN, Serhat Orkun TAN, Habibe Uslu TECİMER
GU J Sci, Part A, 9(4): 554-561 (2022)
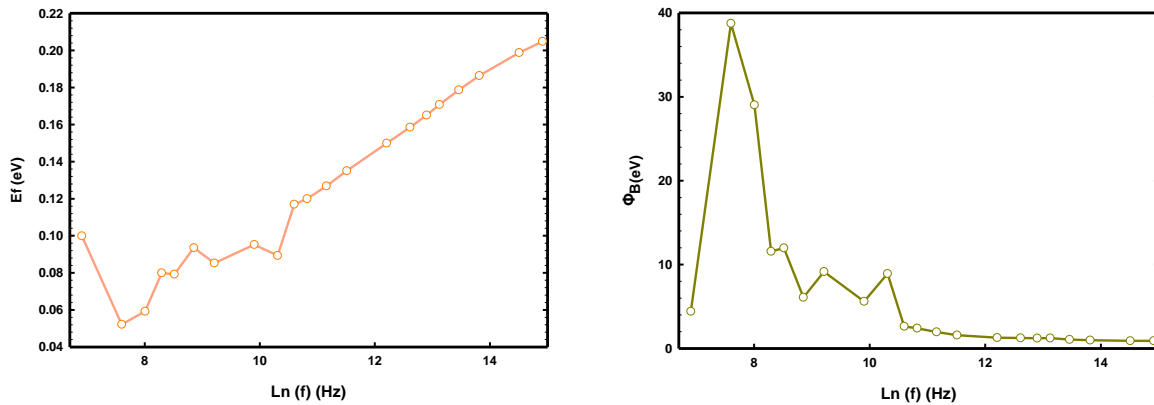
Figure 7. *Ln frequency dependent a) $E_f(eV)$ and b) Φ_B curves of the device*

Concentration of doped acceptor atoms (N_A) values were obtained using the following equation.

$$N_A = \frac{2}{q\varepsilon_S\varepsilon_0 A^2 \tan(\theta)} \qquad (6)$$
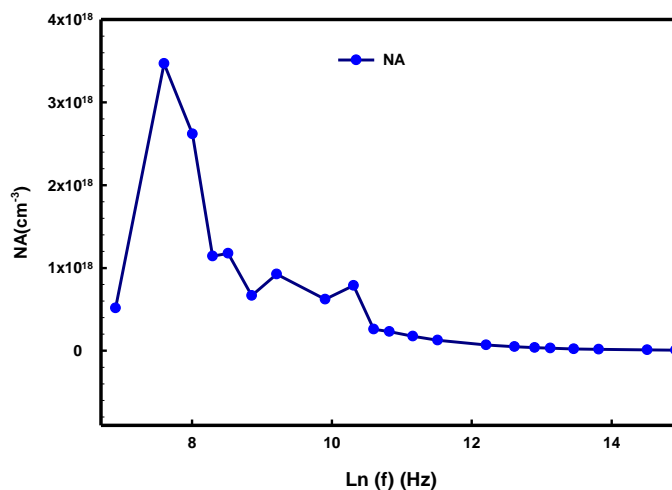
Figure 8. *Ln frequency dependent $N_A\,(cm^{-3})$ curve of the device*

4. CONCLUSION

Electrical measurements of the PVA interlayered MS device were made by utilizing C&G/ ω-V data at frequency and voltage ranges of 10 kHz–1 MHz and -4V– +4V, respectively. The capacitance, conductance, series resistance, and the voltage evolution of $1/C^2$ were compared between low frequency (10KHz) and high frequency (1 MHz) as a function of biasing voltage. From the plot of C-V, the structure showed a negative capacitance characteristic behavior. Estimation of electrical parameters of the structure such as Fermi-energy level $E_F(eV)$ ln(f), barrier height (Φ_B) ln(f) and concentration of doped acceptor atoms (N_A)(cm^{-3}) ln(f) was performed by utilizing the $1/C^2$ voltage evolution. In order to better interpret the performance of the structure on the basis of frequencies, it would be more accurate to interpret the experimental results by considering the behavior in the reverse and forward polarization regions. Especially for the reverse polarity, higher capacitance and conductance values are seen for low frequency, while the capacitance and conductance values at forward polarization region are almost close to each other for both frequencies. Looking at the series resistance values; higher series resistance values were obtained at low frequency in both reverse and forward polarizations. In addition to these, the fact that the interface states are higher in the reverse polarity region can be interpreted as the performance of the structure in this region, especially for low frequency, is more inadequate. The effects of the increase in frequency are observed as a decrease on the capacitance, conductance, and series resistance values, especially in the reverse bias region. Experimental results point out that, the electrical qualifications of

the device are very sensitive to the applied biases and especially to the frequency levels. Considering signal tracking difficulty at high frequencies, such effects of series resistance, interface states, negative capacitance have been decreased for the fabricated device. In terms of devices operating at high frequencies, the effects of the parameters obtained for this fabricated contact structure at low frequency and in the reverse polarization region may have a negative effect in terms of rapid response to polarization variations. On the other hand, the decrease in the effect of these parameters at high frequency is evaluated positively in terms of fast switching performance.

ACKNOWLEDGEMENT

REFERENCES

Alsmael, J. A. M., Tan, S. O., Tecimer, H. U., Altındal, Ş., & Kalandaragh, Y. A. (2022). The Impact of Dopant on the Dielectric Properties of Metal-Semiconductor With ZnFe2O4 Doped Organic Polymer Nanocomposites Interlayer. *IEEE Transactions on Nanotechnology*, *21*, 528-533. doi:10.1109/TNANO.2022.3207900

Ata, D., Altındal Yeriskin, S., Tataroğlu, A., & Balbasi, M. (2022). Analysis of admittance measurements of Al/Gr-PVA/p-Si (MPS) structure. *Journal of Physics and Chemistry of Solids*, *169*, 110861. doi:10.1016/j.jpcs.2022.110861

Aziz, S. B. (2016). Modifying Poly(Vinyl Alcohol) (PVA) from Insulator to Small-Bandgap Polymer: A Novel Approach for Organic Solar Cells and Optoelectronic Devices. *Journal of Electronic Materials*, *45*(1), 736-745. doi:10.1007/s11664-015-4191-9

Bakkaloğlu, Ö. F., Ejderha, K., Efeoğlu, H., Karataş, Ş., & Türüt, A. (2021). Temperature dependence of electrical parameters of the Cu/n-Si metal semiconductor Schottky structures. *Journal of Molecular Structure*, *1224*, 129057. doi:10.1016/j.molstruc.2020.129057

Çetinkaya, H. G., Sevgili, Ö., & Altındal, Ş. (2019). The fabrication of Al/p-Si (MS) type photodiode with (%2 ZnO-doped CuO) interfacial layer by sol gel method and their electrical characteristics. *Physica B: Condensed Matter*, *560*, 91-96. doi:10.1016/j.physb.2019.02.038

Gaaz, T. S., Sulong, A. B., Akhtar, M. N., Kadhum, A. A. H., Mohamad, A. B., Al-Amiery, A. A., & McPhee, D. J. (2015). Properties and applications of polyvinyl alcohol, halloysite nanotubes and their nanocomposites. *Molecules*, *20*(12), 22833-22847. doi:10.3390/molecules201219884

Hou, G., Li, Y., & Wang, X. (2018). Research Progress of Zinc Ferrite as Photocatalyst. *Cailiao Daobao/Materials Review*, *32*(1), 51-57. doi:10.11896/j.issn.1005-023X.2018.01.006

Neamen, D. A. (1992). *Semiconductor Physics and Devices, Basic Principles*. McGraw-Hill.

Patil, J. Y., Nadargi, D. Y., Gurav, J. L., Mulla, I. S., & Suryavanshi, S. S. (2014). Glycine combusted $ZnFe_2O_4$ gas sensor: Evaluation of structural, morphological and gas response properties. *Ceramics International*, *40*(7) Part B, 10607-10613. doi:10.1016/j.ceramint.2014.03.041

Shultz, M. D., Carpenter, E. E., Morrison, S. A., & Calvin, S. (2006). Cation occupancy determination in manganese zinc ferrites using Fourier transform infrared spectroscopy. *Journal of Applied Physics*, *99*(8), 08M901. doi:10.1063/1.2151831

Slavu, L. M., Rinaldi, R., & Di Corato, R. (2021). Application in nanomedicine of manganese-Zinc ferrite nanoparticles. *Applied Sciences*, *11*(23), 11183. doi:10.3390/app112311183

Subba Reddy, C. V., Han, X., Zhu, Q.-Y., Mai, L.-Q., & Chen, W. (2006). Dielectric spectroscopy studies on (PVP + PVA) polyblend film. *Microelectronic Engineering*, *83*(2), 281-285. doi:10.1016/j.mee.2005.08.010

Sze, S. M. (1981). *Physics of Semiconductor Devices*. (2nd edition). Wiley–Blackwell.

Tecimer, H. U., Alper, M. A., Tecimer, H., Tan, S. O., & Altındal, Ş., (2018). Integration of Zn-doped organic polymer nanocomposites between metal semiconductor structure to reveal the electrical qualifications of the diodes. *Polymer Bulletin*, *75*(9), 4257-4271. doi:10.1007/s00289-018-2274-5

561

Jaafar Abdulkareem Mustafa ALSMAEL, Nuray URGUN, Serhat Orkun TAN, Habibe Uslu TECİMER
GU J Sci, Part A, 9(4): 554-561 (2022)

Unnithan, A. R., Arathyram, R. S., & Kim, C. S. (2015). Chapter 3 - Electrospinning of Polymers for Tissue Engineering. In: S. Thomas, Y. Grohens, & N. Ninan (Eds.), *Nanotechnology Applications for Tissue Engineering* (pp. 45-55). William Andrew Publishing. doi:10.1016/B978-0-323-32889-0.00003-0

Vijatović-Petrović, M. M., Džunuzović, A., Bobić, J. D., Ilić, N., Stijepović, I., & Stojanović, B. D. (2020). Study of barium titanate/nickel-zinc ferrite based composites: Electrical and magnetic properties and humidity sensitivity. *Processing and Application of Ceramics*, *14*(1), 9-18. doi:10.2298/PAC2001009V

Zeyrek, S., Acaroğlu, E., Altindal, Ş., Birdoğan, S., & Bülbül, M. M. (2013). The effect of series resistance and interface states on the frequency dependent C-V and G/w-V characteristics of Al/perylene/p-Si MPS type Schottky barrier diodes. *Current Applied Physics*, *13*(7), 1225-1230. doi:10.1016/j.cap.2013.03.014

Zhang, F., Wei, C., Hu, Y., & Wu, H. (2015). Zinc ferrite catalysts for ozonation of aqueous organic contaminants: Phenol and bio-treated coking wastewater. *Separation and Purification Technology*, *156*, Part 2, 625-635. doi:10.1016/j.seppur.2015.10.058

Investigation of Microstructure and Tribological behavior of WE43/nano B₄C Composites Produced by Spark Plasma Sintering

Ufuk TAŞCI[1*] Bülent BOSTAN[2]

[1]Department of Graduate School of Natural and Applied Sciences, Gazi University, 06500 Ankara, Türkiye
[2]Department of Metallurgy and Materials Eng., Gazi University, 06500 Ankara, Türkiye

Keywords	Abstract
Spark Plasma Sintering WE43 B₄C Tribology Behavior Mechanical Properties	In this study, composite samples of WE43 (Mg-4Y-3RE-Zr) reinforced with nano-B₄C particles in different ratios (0.5 and 2 wt.%) were prepared by spark plasma sintering (SPS). The powders were mixed in a 3-dimensional ball mill at 300 rpm. The mixed powders were then hot pressed under 35 MPa pressure at 525 °C for 6 min. XRD and FESEM-EDS instruments were used to characterize the composite samples. Microhardness and wear tests were performed to designate the mechanical properties. It was found that the highest hardness occurred in the composite sample with 2% nano-B₄C composites. It was also found that tribological properties improved with the increase of nano-B₄C content.

1. INTRODUCTION

Metal matrix composites (MMC) exhibit excellent mechanical properties compared to their conventional, non-reinforced counterparts. In particular, magnesium (Mg)-based MMCs occupy an important position due to their lightweight advantage (Nimityongskul et al., 2010). By reinforcing the Mg matrix with a hard ceramic phase, properties for example high hardness, high strength, and low wear resistance can be improved. Therefore, Mg, which has the lowest density among metals, is increasingly used in aerospace, automotive, and medical applications (Ghasali et al., 2017a). Among Mg alloys, WE43 alloy, which have stand out the attention of researchers in recent years, are preferred because of their superior mechanical and microstructural properties compared to other Mg alloys, as they contain rare earth elements. Despite neodymium, yttrium and other rare earth elements exhibit properties such as good mechanical performance at high temperatures, flame retardancy and high temperature creep resistance, studies are continuing to improve the problems in wear properties (Banijamali et al., 2022).

Studies have long been conducted to reinforce Mg-based alloys with ceramic particles to increase their strength. It is well known that various ceramics such as SiC, Al₂O₃, ZrB₂, TiB₂, and B₄C are dispersed in the matrix phase as reinforcing materials during the fabrication of MMC. B₄C is a very hard ceramic with low density, high chemical resistance and abrasion resistance. It is well known that B₄C reinforcement of the Mg matrix increases the interfacial bonding strength, hardness and wear resistance of the composite (Taşcı et al., 2013). Ceramic reinforced metal matrix composites (MMCs) can show very good mechanical and wear properties when compared to non-reinforced metals (Yadav et al., 2022). It is extremely important that the composites have a defect-free microstructure and maintain their mechanical properties. For this purpose, it is necessary to distribute the reinforced ceramics homogeneously in the matrix phase. It is very difficult to

*Corresponding Author, e-mail: ufuktasci@gazi.edu.tr

achieve such homogeneous distribution, especially in the casting process. Therefore, it is possible to produce a fine and non-porous microstructure using the powder metallurgy (P/M) technique (Ghasali et al., 2017b). Spark plasma sintering (SPS), which has occupied an important place in the P/M technique in the last decade, makes it possible to produce metal alloys and MMCs under vacuum, at very low pressing pressure and in a very short time (Saheb et al., 2012).

In this study, nano-B_4C (nB_4C) was added to the WE43 alloy in amounts of 0.5% and 2% using the SPS technique to provide homogeneous mixing of the powders. Microstructure characterization and mechanical properties of these produced composites focused on improving their wear performance.

2. MATERIAL AND METHOD

2.1. Production Method of Composite Specimens

The matrix WE43 powder with an average diameter of 45 μm was supplied by Magnesium Elektron™ ltd. The nB_4C (55 nm) was provided by Nanografi Nanotechnology™ and used for 0.5 and 2% nB_4C to prepare the composite powders. In order to mix the starting powders homogeneously, the mixing process was carried out for 4 hours at 300 rpm in a 3D ball mill with an atmospherically controlled chamber. Table 1 shows the chemical composition of WE43.

Table 1. WE43 Chemical Composition

Element	Mg	Y	Nd	Gd	Z
WE43	Bal	3.72	2.13	1.11	0.41

Powders with different ratios of nB_4C in the WE43 alloy were prepared by SPS. A custom-made graphite mold was used to press the powders. The powders placed in the mold were first recompressed at a pressure of 5 MPa at room temperature. The mixed composite powders were then pressed under a load of 35 MPa at 525 °C for 6 minutes.

3. RESULTS AND DISCUSSION

3.1. Examination of Powders

The images of the initial WE43, nB_4C, and mixed WE43/nB_4C composite powders used in the study are shown in Figure 1. Mixing of the composite powders was performed in a 3D high energy mixer. Figure 1a shows that the WE43 powder used as matrix alloy has a spherical shape. In Figure 1b, the nB_4C particles were found to have a complex shape with sharp corners. By examining the images, a series of grooves and micro ploughing, plastic deformations parallel to the sliding direction, debris and significant crater areas were visible on the worn surface of the unreinforced WE43 matrix alloy. It can also be seen that the morphology of the matrix powder does not change and remains spherical during the mixing process.

3.2. Microstructure Characterization

The XRD patterns of the WE43/%2 nB_4C composites produced by SPS are shown in Figure 2. Examination of the XRD peaks shows that the produced composites contain $Mg_{41}Nd_5$ intermetallic phase and α Mg matrix phase. It was found that the rare earth elements yttrium and neodymium form compounds with the matrix phase Mg to different extents. Since the crystal structures of these phases are compatible with the matrix, they are believed to increase the obstacle of the composite by preventing dislocation movement. The matrix alloy in the XRD patterns was found to increase slightly with the addition of nB_4C particles, along with additional peaks corresponding to nB_4C (Tang et al., 2022).
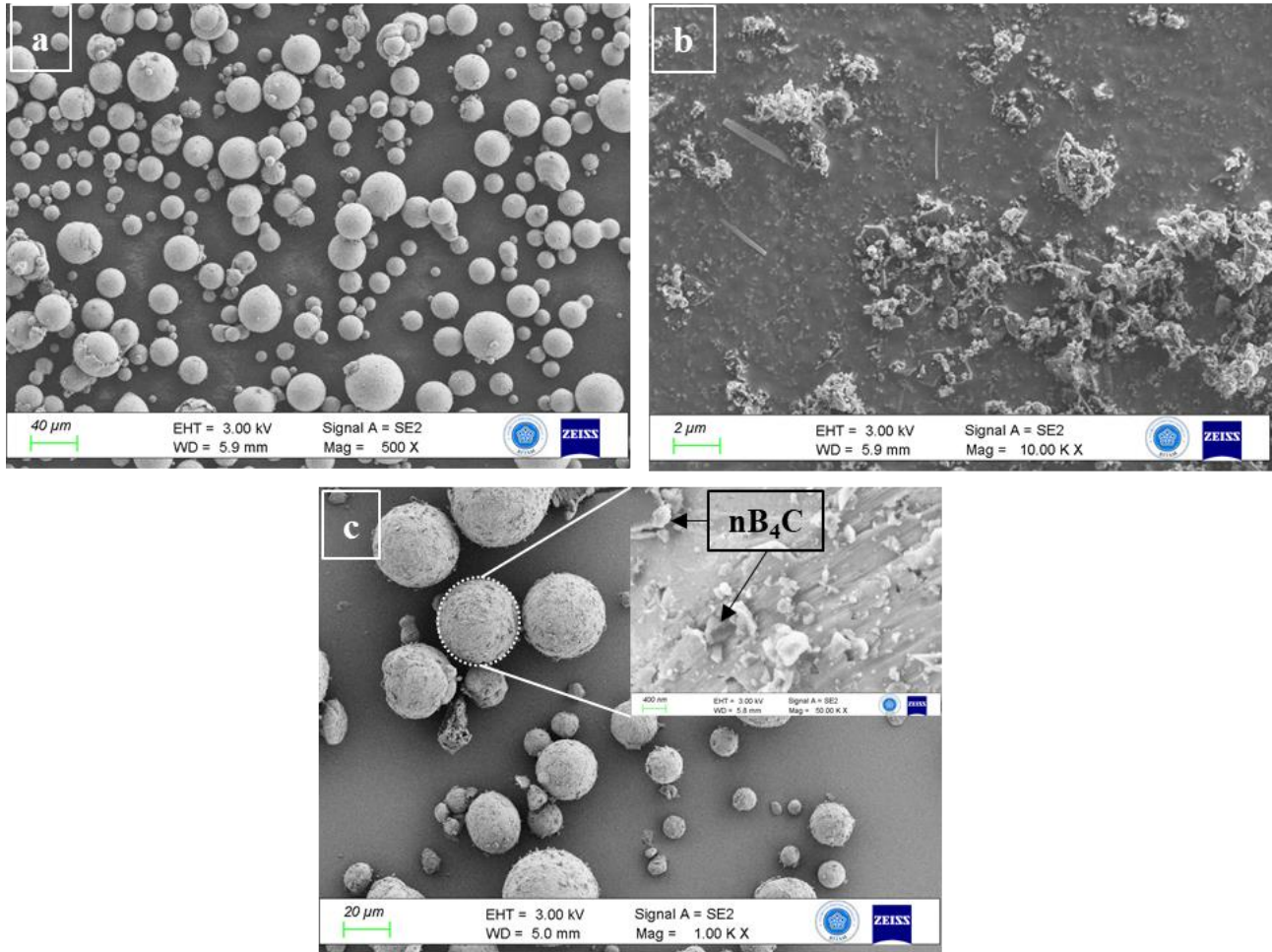
Figure 1. a) *WE43 powder morphology,* **b)** *nB$_4$C ceramic reinforcement powder,* **c)** *WE43/nB$_4$C composite powder*
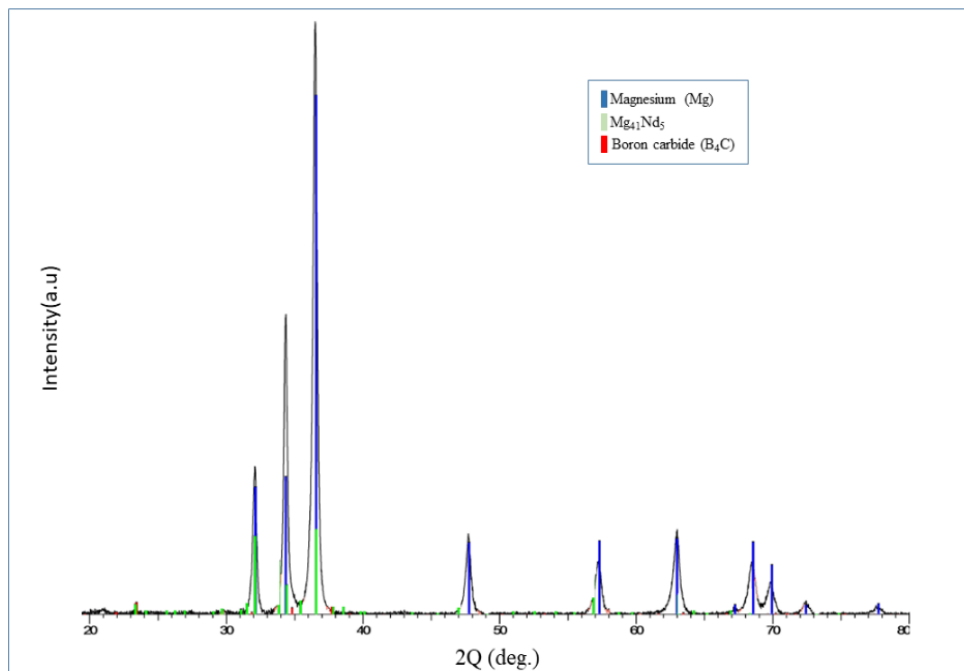
Figure 2. *XRD analysis of WE43 alloy and WE43/nB$_4$C composites*

After the spherical powders were subjected to 35 MPa pressing in the SPS device and sintered at 525 °C, the surface images of all samples were examined using FESEM to characterise the microstructure. Figure 3a shows the unreinforced WE43 alloy, Figure 3b indicates the 0.5% nB_4C composite, and Figure 3c reveals the microstructure images of these samples fabricated with 2% nB_4C ceramic reinforcement. When the images were examined, no significant difference was found in the grain sizes of these unreinforced and composite specimens. This is because the driving force required for grain size growth and the absence of deformation in the powder morphologies during the mixing process play a certain role (Shuai et al., 2021). It is desirable that the grain sizes are close to each other during the sintering process. It was found that nB_4C reinforcement ceramics are generally formed at grain boundaries. It was found that the phases that appear as white dots in the grains are phases such as $Mg_{41}Nd_5$, Y_2O_3. It is therefore suspected that the WE43 alloy contains a rare earth element that affects the growth kinetics of the intermetallics.
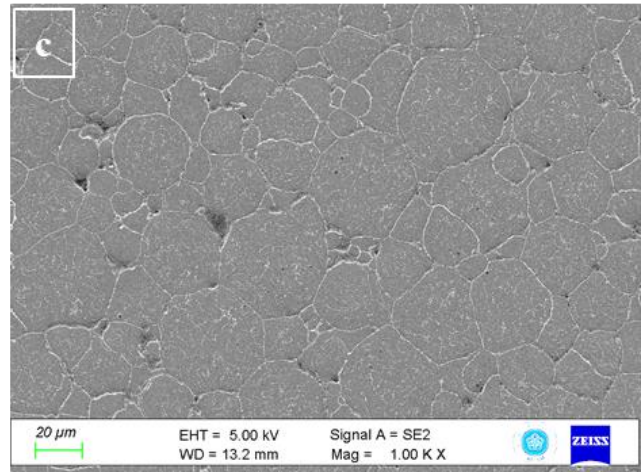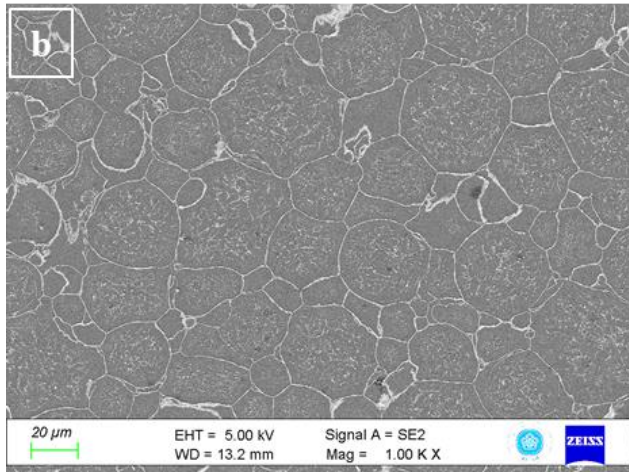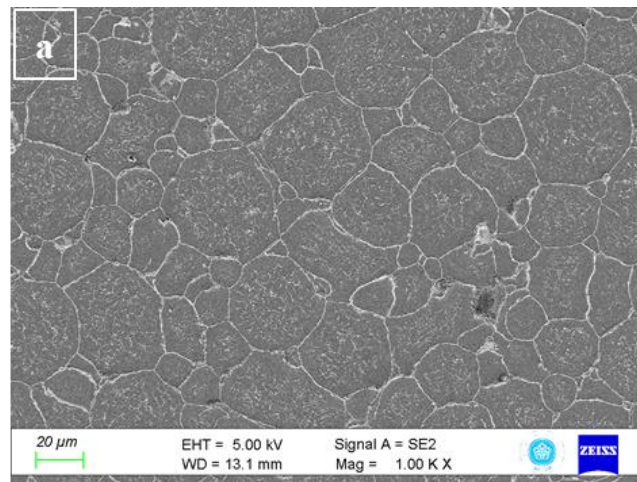
Figure 3. a) WE43 alloy, b) WE43/0.5% nB_4C composite, c) WE43/2% nB_4C

By studying the microstructure of WE43 by FESEM/EDS (Figure 4), it was found that the precipitates at the grain boundaries are rich in neodymium and yttrium, which are determined and homogeneously distributed in the matrix structure of the nB_4C ceramic particles.
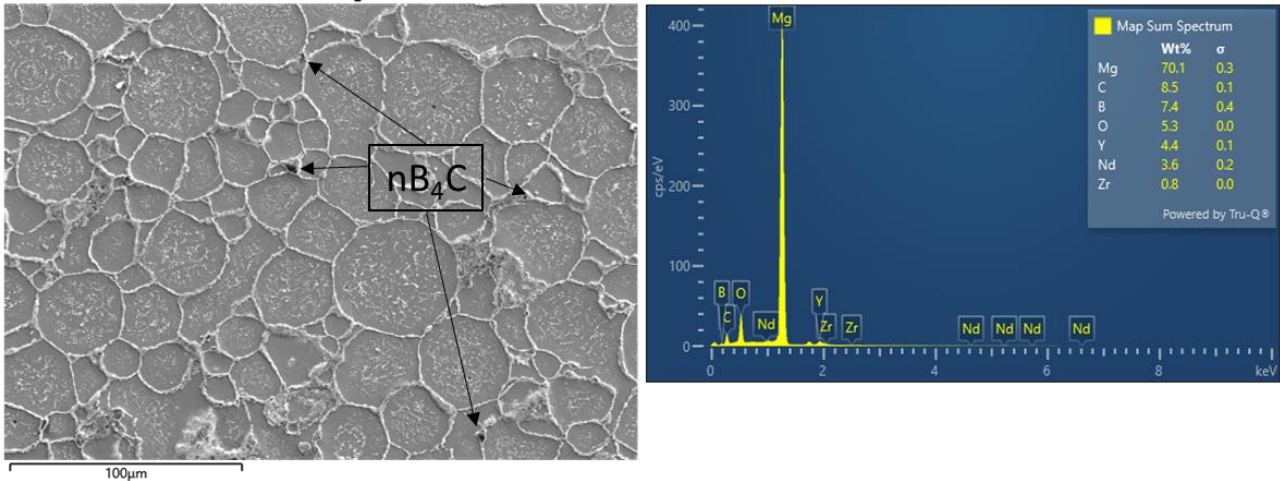
Figure 4. *FESEM/EDS analysis result of WE43/2% nB$_4$C composite material*

3.3 Mechanical Properties

By examining the density graph (Figure 5a) of WE43 alloy and WE43/ nB$_4$C composites, it was seen that the highest density occurred in WE43 alloy (99.00%) and the lowest density in WE43/2 nB$_4$C composite (97.8%). It is known that composites reinforced with ceramic particles have lower density compared to unreinforced matrix specimens. Also, by looking at the hardness graphs in Figure 5b, it can be seen that the sample with the highest hardness is WE43/2 nB$_4$C and the sample with the lowest hardness is the unreinforced WE43 alloy. The B$_4$Cs in the matrix phase, which is soft along with the ceramic particle reinforcement, accumulate at the grain boundaries and prevent dislocation movement. Therefore, an increase in the strength values of the composites is observed. Comparing the hardness value with that of the unreinforced WE43 alloy, it is found that it increases by about 5% at 0.5% nB$_4$C. Similarly, when comparing the hardness values of the unreinforced WE43 alloy and the composite reinforced with 2% nB$_4$C, it was found that there was an increase of about 12%. The reinforcement by nB$_4$C ceramic particles was homogeneously distributed in the structure and increased the strength.
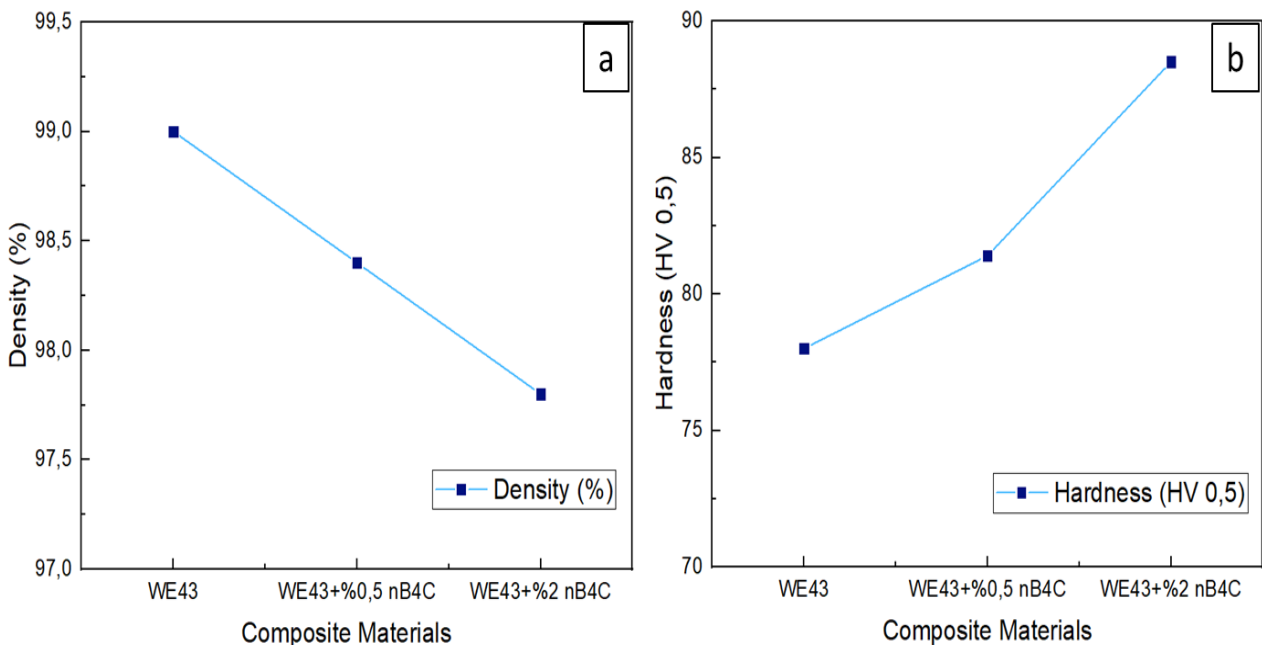

Figure 5. a) *Density,* ***b)*** *Hardness*

3.4. Tribological Behavior

3.4.1. Weight loss

Figure 6 shows the weight loss of the unreinforced WE43 matrix alloy and the WE43/nB_4C composites with different reinforcements under 15 N load. The weight loss decreases with increasing reinforcement ratio compared to the matrix material. It is known that various properties such as grain size, porosity in the structure, strength and hardness affect the wear behavior of materials. It is believed that the reinforcement particles act as a coercive factor at the grain boundaries, leading to the development of wear resistance (Moheimani et al., 2021).
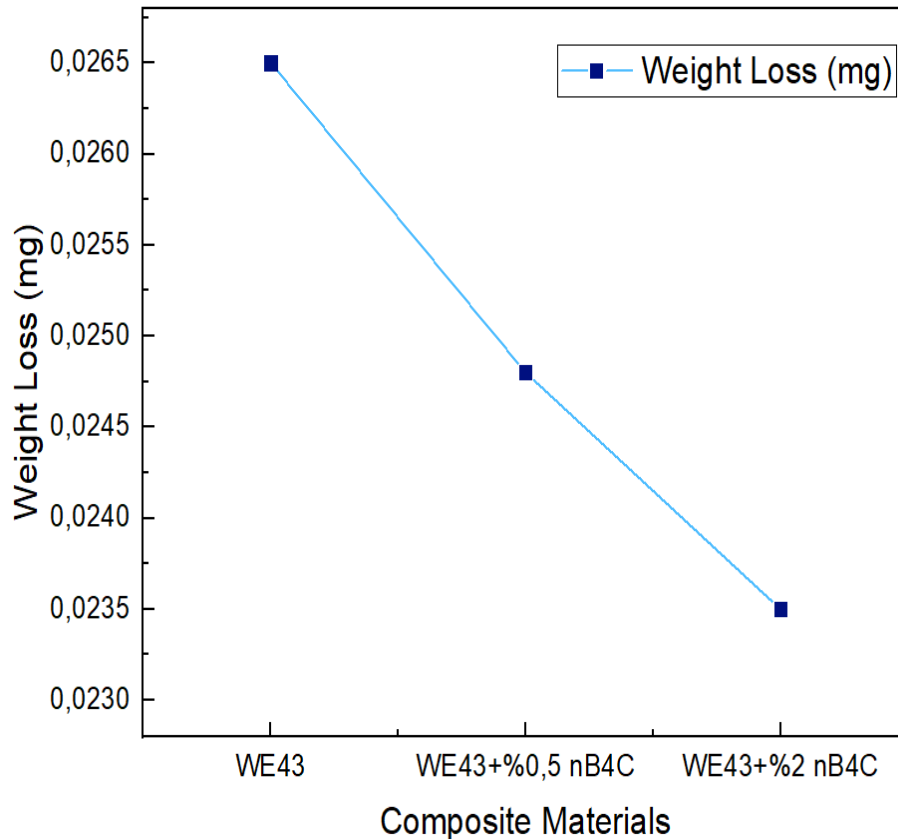
Figure 6. *Weight loss*

3.4.2. Wear mechanisms

FESEM analysis was performed to investigate the wear mechanisms of WE43 alloy and WE43/ nB_4C composites during wear testing and the effects of the presence of nB_4C particles in different proportions on wear behavior. Figure 7. SEM shows images of the worn surfaces of the WE43 alloy and WE43/nB_4C composites subjected to the wear test under 15N load. By examining the images, a series of grooves parallel to the sliding direction, debris, plastic deformations and significant crater areas were visible on the worn surface of the unreinforced WE43 matrix alloy. It is assumed that this situation exhibits typical characteristics of abrasive wear.

4. CONCLUSION

In this study, powder-metal composites were produced by the SPS method after homogeneously mixing WE43 alloy and WE43/nano B_4C powder in a 3D ball mixer. The microstructure, hardness and wear properties of the composites were investigated. The following conclusions can be drawn from the results.

The mixing process in an atmospherically controlled 3D ball mill showed that the nB_4C particles were homogeneously distributed at the grain boundaries. While the highest density value was observed in the

unreinforced WE43 alloy, the density values decreased with increasing nB_4C particle addition. The lowest density value was found in the WE43/2% nB_4C composite. While the lowest hardness occurred in the unreinforced WE43 alloy, the highest hardness was observed in the WE43/ 2% nB_4C composite. It was observed that the hardness values increased with increasing nB_4C ratio. The addition of nB_4C particles improved wear resistance and minimized weight loss.
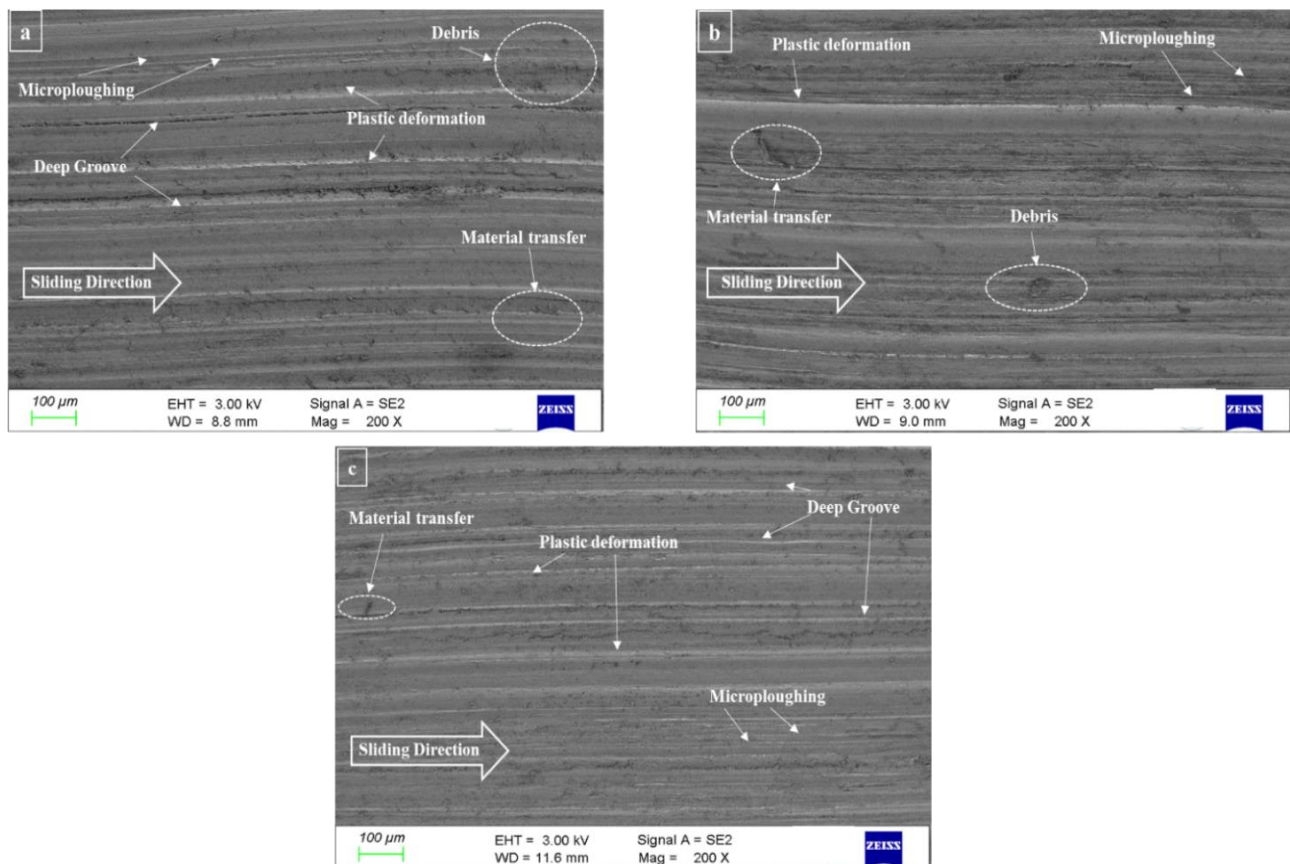
Figure 7. *Worn surface SEM pictures **a)** WE43 alloy, **b)** WE43/0.5% nB₄C composite, **c)** WE43/2% nB₄C*

ACKNOWLEDGEMENT

CONFLICT OF INTEREST

The authors declare no conflict of interest.

REFERENCES

Banijamali, S. M., Palizdar, Y., Nekouee, K. A., Najafi, S., & Shariat Razavi, M. (2022). Effect of B_4C reinforcement and hot rolling on microstructure and mechanical properties of WE43 magnesium matrix composite. *Proceedings of the Institution of Mechanical Engineers, Part L: Journal of Materials: Design and Applications*, 236(9), 1854-1868. doi:10.1177/14644207221085939

Ghasali, E., Alizadeh, M., Niazmand, M., & Ebadzadeh, T. (2017a). Fabrication of magnesium-boron carbide metal matrix composite by powder metallurgy route: comparison between microwave and spark plasma sintering. *Journal of Alloys and Compounds*, *697*, 200-207. doi:10.1016/j.jallcom.2016.12.146

Ghasali, E., Yazdani-rad, R., Asadian, K., & Ebadzadeh, T. (2017b). Production of Al-SiC-TiC hybrid composites using pure and 1056 aluminum powders prepared through microwave and conventional heating methods. *Journal of Alloys and Compounds*, *690*, 512-518. doi:10.1016/j.jallcom.2016.08.145

Moheimani, S. K., Keshtgar, A., Khademzadeh, S., Tayebi, M., Rajaee, A., & Saboori, A. (2021). Tribological behaviour of AZ31 magnesium alloy reinforced by bimodal size B_4C after precipitation hardening. *Journal of Magnesium and Alloys*, *10*(11), 3267-3280. doi:10.1016/j.jma.2021.05.016

Nimityongskul, S., Jones, M., Choi, H., Lakes, R., Kou, S., & Li, X. (2010). Grain refining mechanisms in Mg–Al alloys with Al_4C_3 microparticles. *Materials Science and Engineering: A*, *527*(7-8), 2104-2111. doi:10.1016/j.msea.2009.12.030

Saheb, N., Iqbal, Z., Khalil, A., Hakeem, A. S., Al Aqeeli, N., Laoui, T., Al-Qutub, A., & Kirchner, R. (2012). Spark plasma sintering of metals and metal matrix nanocomposites: a review. *Journal of Nanomaterials*, *2012*, 983470. doi:10.1155/2012/983470

Shuai, C., He, C., Peng, S., Qi, F., Wang, G., Min, A., Yang, W., & Wang, W. (2021). Mechanical alloying of immiscible metallic systems: process, microstructure, and mechanism. *Advanced Engineering Materials*, *23*(4), 2001098. doi:10.1002/adem.202001098

Tang, B., Li, J., Wang, Y., Luo, H., Ye, J., Chen, X., Chen, X., Zheng, K., & Pan, F. (2022). Mechanical properties and microstructural characteristics of Ti/WE43 composites. *Vacuum*, *206*, 111534. doi:10.1016/j.vacuum.2022.111534

Taşcı, U., Gökmeşe, H., & Bostan, B (2013). AA 2014 Al Matrisli B4C Parçacık Takviyeli Kompozitlerin Mikro Yapı ve Aşınma Davranışının İncelenmesi. *Gazi Üniversitesi Fen Bilimleri Dergisi Part C: Tasarım ve Teknoloji*, *1*(4), 161-168.

Yadav, M., Kumaraswamidhas, L. A., & Singh, S. K. (2022). Investigation of solid particle erosion behavior of $Al-Al_2O_3$ and $Al-ZrO_2$ metal matrix composites fabricated through powder metallurgy technique. *Tribology International*, *172*, 107636. doi:10.1016/j.triboint.2022.107636

JOURNAL OF SCIENCE